

Technical Program Committee

P. Lampariello, University of Rome La Sapienza, Workshop Co-Chairman
R. Sorrentino, University of Perugia, Workshop Co-Chairman
V. Fouad-Hanna, CNET, France
H. L. Hartnagel, Technische Hochschule, Darmstadt, Germany

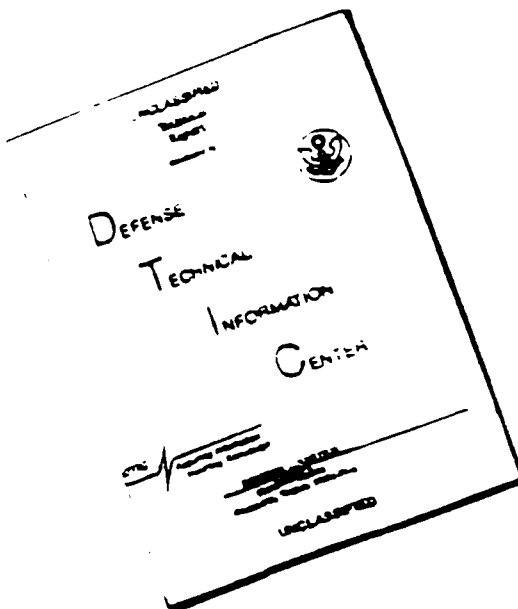
Organizing Committee

R. Giorgini, Itelco S.p.a.
V. Alleva, Itelco S.p.a.
S. Monelli, Itelco S.p.a.
S. Catena, University of Perugia

Secretariat

V. Papini, University of Perugia
L. Castellani, University of Perugia
C. Paolotti, University of Rome "La Sapienza"

DISCLAIMER NOTICE



THIS DOCUMENT IS BEST
QUALITY AVAILABLE. THE COPY
FURNISHED TO DTIC CONTAINED
A SIGNIFICANT NUMBER OF
PAGES WHICH DO NOT
REPRODUCE LEGIBLY.



Microwave Theory and Techniques Society
C&S, Italy, France and Germany MTT Chapters

1992 International Workshop on Millimeter Waves

April 22-24, 1992

Palazzo del Capitano del Popolo
Orvieto, Italy

Organized by:

Central and South Italy MTT Chapter
France MTT Chapter
Germany MTT Chapter
University of Perugia
ITELCO S.p.a., Orvieto

Sponsored by:

CNR, Italy
CNET, France
USARDG European Research Office, UK
IEEE Microwave Theory and Technique Society
University of Perugia, Italy
Contraves Italiana S.p.a., Italy
Itelco S.p.a., Italy
Alenia S.p.a., Italy

Technical Program Committee

P. Lampariello, University of Rome La Sapienza, Workshop Co-Chairman
R. Sorrentino, University of Perugia, Workshop Co-Chairman
V. Fouad-Hanna, CNET, France
H. L. Hartnagel, Technische Hochschule, Darmstadt, Germany

Organizing Committee

R. Giorgini, Itelco S.p.a.
V. Alleva, Itelco S.p.a.
S. Monelli, Itelco S.p.a.
S. Catena, University of Perugia

Secretariat

V. Papini, University of Perugia
L. Castellani, University of Perugia
C. Paolotti, University of Rome "La Sapienza"

6

| | |
|--------------------|--------------------------|
| Accession For | |
| NTIS | ORAL |
| DATA TAB | <input type="checkbox"/> |
| Unannounced | <input type="checkbox"/> |
| Justification | |
| By Doc Room 50 | |
| Distribution/ | |
| Availability Codes | |
| Avail and/or | |
| Dist | Special |
| A-1 | 23 |

23

FOREWORD

Welcome to third edition of the International workshop on Millimeter Waves, being held at the *Palazzo del Capitano del Popolo* in Orvieto. After the encouraging success of the previous editions at the University of Rome "Tor Vergata" in 1986 and at the University of Perugia in 1989, it was decided to organize a new workshop as a cooperation between the Central and South Italy Chapter with the France and Germany Chapters of the IEEE Microwave Theory and Techniques Society.

The city of Orvieto has been chosen as the venue for this event not simply because it is located midway between Rome and Perugia, but mainly for its unique charm due to its suggestive medieval appearance and the rich artistic patrimony dating back to the Etruscan period. The *Palazzo del Capitano del Popolo* is no doubt an extraordinary combination between a historical medieval *palazzo* and a modern and efficient Congress Center.

ITELCO S.p.a. enthusiastically agreed to sponsor the workshop and has been a fundamental partner in the organization. The social program is also very attractive, including a very nice concert of two Canadian artists, T. Goudie and D. Lawton.

We would like to thank all the invited speakers who kindly agreed to participate in the workshop and the many others who have worked for its success. We are deeply grateful to Professor Carrara, one of the *fathers* of microwaves in Italy, who accepted our invitation to welcome the participants at the opening session.

Paolo Lampariello and Roberto Sorrentino

Workshop Co-Chairmen

CONTENTS

H. Meinel, Millimeter-Wave Applications and Technology Trends

K. Gruener, A New Passive Microwave Scanner for Airborne Measurements of Maritime Oil Pollution

M. Aikawa, MMIC Technology for Communication Systems

R. Funck, New Integrated Subsystems for Millimeter-Wave Applications

D. Pous, New Millimeter-Wave Devices: Realization and Performance

G. Salmer, Field-Effect Transistors for the Millimeter-Wave Range: Physical Analysis, Modelling and Expected Performance

J. Freyer, Two-Terminal Millimeter-Wave Devices

H. L. Hartnagel, Technology Developments towards Nanometric Structures

T. Itoh, Optical Control of Millimeter-Wave Circuits

T. Yoneyama, Recent Developments of NRD-Guide Technology

R. H. Jansen, Advanced Design Techniques for Linear and Nonlinear MMIC's into the Millimeter-Wave Region

V. Fouad Hanna, CAD of Millimeter-Wave Passive Components in Suspended Microstrip Technology

A. A. Oliner, Leakage and Crosstalk Effects in Millimeter-Wave Integrated Circuits

N. Alexopoulos, JD Modeling of Millimeter-Wave Circuits and Antennas

MILLENNIUM-ERA AIRCRAFT APPLICATIONS
ANALYSIS AND TECHNOLOGY TRENDS

H. Meinel

Deutsche Aerospace • Germany

1992

INTERNATIONAL WORKSHOP

on

MILLIMETER WAVES

Palazzo del Capitano del Popolo

Orvieto, Italy

MILLIMETER WAVE APPLICATIONS
AND TECHNOLOGY TRENDS

Holger H. Meinel

Deutsche Aerospace AG
Leopoldstrasse 175
D-8000 München
Germany

ABSTRACT

The advantages and new application areas being offered by millimeter-wave systems have been known for a long time. But only the advent of reliable and efficient solid-state sources as well as the progress in low-cost integration procedures, i.e. Hybrid- and Monolithic-Integration Techniques, respectively, has made millimeter-wave technology mature, opening a wide field of employment areas today. It is widely accepted, that the solution to traffic congestion, being a serious problem worldwide, does not lie in the construction of more roads, but in the application of advanced technologies to control the flow of vehicles. The efficiency of the already existing infrastructure will be increased, incorporating RTI (road traffic informatics) in the millimeter-wave range.

APPLICATIONS

Three major application areas have to be distinguished in this field today, communications, radar, and automotive traffic control, the latter combining the earlier two. Apart from the unique propagation behaviour, millimeter-wave applications take advantage of the highly directive nature of the millimeter-wave beam, i.e. Good angular resolution can be achieved with moderately small antennas, thus millimeter-wave systems are small in size and light in weight, compared to their microwave counterparts. The lack of frequencies in the microwave bands commonly used today, is an additional important reason.

COMMUNICATIONS

Atmospheric propagation effects strongly influence considerations related to the application of millimeter-wave transmission. Normally such systems will be operated in the atmospheric windows around 35 and 94 GHz; for specific applications, the maximum absorption range around 60 GHz will be taken.

The employment of the 40 - 50 GHz band for EHF military satellite up-links has been very important for the development of millimeter-wave technology. This frequency band offers increased bandwidth over the UHF and SHF bands being in current use today and permits the construction of small terminals; thus covert operation for various military platforms is achieved. The SKYNET 4 series of satellites in the U.K. and the MILSTAR program in the US are such applications.

As new services emerge for LAN (local area network) and PCN (personal communication network) systems as well as for traffic control, the demand for a new generation of high data rate radio links has fostered the worldwide development of commercial millimeter-wave POINT-TO-POINT transmission link equipment.

VIDEO-CONFERENCE-SERVICES or SATSTREAM and MEGASTREAM are application examples for high data rate radio links, while remote telephone- or 'cable'-TV-subscriber connection is another; here with special emphasize on 'low cost and effort' infrastructure enhancement. The safety control of high speed trains with velocities up to 400 km/h, like the German ICE (Inter City Express) and the French TGV (Train à Grande Vitesse) as well as LCRN-services (local cellular radio network) are mobile millimeter-wave applications.

- POINT-TO-POINT transmission links, using portable equipment can be installed very rapidly on maximum hop lengths of up to about 10 km, the equipment, due to size and weight, can be mounted easily.

The main employment area for such millimeter-wave equipment is in connecting subscribers, for example in private data-, TV-, and telephone circuits. More than 1,000 systems have become operational since the late 1970's, mostly in Japan, but also in Europe.

Besides these point-to-point and area type connections, the millimeter-wave range has been used and is further investigated for mobile communication purposes.

- Local Cellular Radio Networks (LCRN), for wideband mobile services, are a major investigation effort, for instance in England.

The demand for mobile radio has been such, that severe spectrum congestion is occurring within the today allocated bands. Thus a region of radio spectrum has been sought, which could accommodate the future LCRN bands. The application of millimeter-waves could be the solution.

RADAR

The widest spread employments of millimeter-waves are found in radar, having fostered the development of millimeter-wave technology during the last two decades. Seekers for terminal guided submunitions or battlefield and terrain mapping radars are military application examples, while the contact measurement of distances or velocity in industry and traffic control are typical civilian employments.

The most important application in this area were seekers for terminal guided submunitions. Besides stringent performance and low cost constraints a high production volume was required; thus the world-wide seeker development has stimulated millimeter-wave development efforts and secured today's technology status. Such seekers, engineered to production status, are available from various manufacturers.

Millimeter-wave radar is advantageous for applications, where high resolution is a major requirement. Short range surveillance radars, like the Helicopter Obstacle Warning Radar in the lower frequency regime (40 - 60 GHz), is an example of this type. Wire like obstacles with diameters as small as 3 mm have been detected under flight conditions. Being a military necessity at first, helicopter obstacle warning today is an important civilian application, concerning the safety of airport commuter traffic.

In industry millimeter-wave radar can be employed in any situation, where movements, length or height have to be measured in a contactless manner. Doppler sensing is taken to gain information for automatic process control. An example of the latter is the top-dead-center measurement system for combustion engines, while the controlled glue application on windows in car manufacturing is an example of the earlier.

RECONNAISSANCE

Millimeter-wave technology has matured and operational systems are deployed in the military arena; thus millimeter-wave reconnaissance has become an urgent necessity today. Different systems, including millimeter-wave superhet- and DIFM-receivers, have been built.

TRAFFIC CONTROL

Millimeter-wave techniques offer the means of sensing vehicles and communicating with them, while they have the advantage of being immune to changing weather conditions. Four major areas of applications have to be distinguished: Automatic Debiting Systems (ADS) and Road traffic Informatics (RTI) are communication type applications, while true motion- and collision avoidance sensors are radar type approaches. Especially millimeter-wave systems have found an increasing interest for such purposes due to their specific advantages: to be small in size and light in weight. The lack of frequencies in the microwave bands commonly used today, is another very important reason. The frequency allocations for European road transport applications, as suggested by CEPT, clearly identifies the importance of millimeter-wave techniques in this field.

ADS TELEPASS is an ADS installed along the Autostrade Italiane - Naples in Italy. Communication is achieved at 5.72 GHz between a roadside transceiver at the toll plaza and a transponder within the vehicle. Such an ADS approach will also be taken to reduce city traffic significantly, e.g. in Cambridge, England, as city entrance debiting is the second major ADS application. In the future such systems will be operated in the 60 GHz range.

RTI A major concern of RTI is vehicle-to-vehicle and vehicle-to-roadsideside communication. An example of this type is the DACAR system within the DRIVE programme. Communication occurs at 61 GHz over a taken prototype bandwidth of 500 MHz. DPSK Differential Phase Shift Keying) with error detecting and correcting coding was applied. This leads to a bit error rate (BER) of 5×10^{-10} after demodulation, as multiple tests trials, being carried out in May/June '91 have shown. Further systems, like the improved German AVES (AEG Verkehr Erfassung System) at 61 GHz are under test and development, respectively, for the same purpose.

REFERENCES

Applications:

- [1] Van der Forst, A.: millimeter-wave Atmospheric Propagation and System Implications. 16th EuMC, Dublin, Sept 1986, 19 - 30.
- [2] Meinel, H.: System design, applications and development trends in the millimeter-wave range, 18th EuMC 1989, Stockholm.
- [3] Ron Schneiderman: Millimeter-waves find commercial markets. Microwaves & RF, July 1991, 35-39.
- [4] Meinel, H.: Millimetre-wave technology advances since 1985 and future trends. IEEE Trans. MTT 39, No. 5, May 1991, 759 - 767.
- [5] Dawson, T.W.G., et al.: Skynet 4 defense communication satellite project. MM 182, London Oct. 1982, 94-103.
- [6] Briginshaw, P. M.; Resnick, A. S.: 60 GHz covert communication link in binoculars. MM '86 Conference, Brighton Jun. 1986.
- [7] Plattner, A.; Meinel, H.: A 60 GHz hand-held LPI transceiver. 12th EuMC, Helsinki, Sept 1982, 540-594..
- [8] Meinel, H.: The current status of mmwave communication systems, melecon '89 conf., Lisbon, Portugal, March 1989, 680-686.
- [9] Dooi, Y.; Kurematsu, H.; Furuhama, Y.: A 50 GHz band millimeter-wave radio system, Links for the future, Science systems and services for communication, IEEE publication: CH 2028 - 9/64, 955-958.

[10] Watanabe, S.; Kasuga, O.; Kaneko, K.: General purpose 50 GHz Transmitter-Receiver. Links for the future. *Science systems and services for communication*. IEEE publication: CH 2028 - 9184 - 251-954.

[11] Ogawa, K.; Ishizaki, T.; Hashimoto, K.; Sakakura, M.; Uwano, T.: A 50 GHz GaAs FET MMIC transmitter/receiver using hemispherical miniature probe transitions. *IEEE MTT-Trans., Vol. 37, No. 9, Sept. 1989, 1434-1441.*

[12] Barnes, B.C.; Bates, R.N.; Clarke, I.M.: Integrated E-plane millimeter-wave 29 GHz transceiver. *MSN & CT, Sept. 1988, 93-103.*

[13] Barnes, B.C.; O'Sullivan, P.J.; Rose, A.; Pilgrim, M.; Wilson, P.G.: Monolithic circuits for mm-wave multichannel TV system. *MIOP '90, Stuttgart, Germany, April 24-26, 1990, 426-430.*

[14] Huish, P.W.; Johnson, I.T.; Li, T.A.; Nicholls, M.J.: mm-wave length microcellular mobile radio systems - a solution to spectrum congestion for high user densities. *Int. conf. on Mobile Radio, Cambridge, UK, Dec. 1995.*

[15] Thomas, H.J.; Siqueira, G.L.; Cole, R.S.: Millimeter-waves sh: / merit for mobile Cellular Radio. *Microwaves and RF, Feb. 1937, 67-70.*

[16] Bansebti, M.; Davies, R.; McGehee, J.P.; Beach, M.A.; Rickard, D.C.: Short range propagation measurements and modelling at 60 GHz for LANs. *MIOP '90, Stuttgart, Germany, April 24-26, 1990, 431-437.*

Radar:

[17] Wilke, K.-H.: Microwave sensors for intelligent ammunitions MILTECH. *No. 5, 1986 May 1986, 32-42.*

[18] Burnett, C. E.: 94 GHz integrated monopulse radar demonstrator. *IEEE MTT-S Symp., Las Vegas July 1987.*

[19] Williams, M. B.; Clarks, I. M.: Radar transceiver for smart-munitions applications. *MSN & CT Oct. 1987, 43-89.*

[20] Greenhalgh, D.: Millimeter wave radar for short range air defenses. *MIOP '90, Brighton, U.K., July 1990, 205-210.*

[21] Bischoff, M.; Dreier, J.; Dreher, H.; Patzwahl, M.: An airborne solid state U-band pulse compression radar. *WIM 1981, Wembley July 1981, Symp. Dig. 455-459.*

[22] Meinel, H.; Wigisch, H.G., et al.: LPI-radar for helicopter obstacle warning. *AGARD Conf. Proc. No. 359, Monterey, CA, 1984, 17-1 to 7.*

[23] Anthouard, P.: Millimetric wave ROMEO for obstacle avoidance (in French). *Conference de Radar, Paris 1983. Communication AV.3, 192-196.*

Reconnaissance:

[24] Stammier, W.; Boheim, M.; Lins, W.: mm-wave sensor for traffic data acquisition systems. *Proc. Int. Microwave Symp. (Sao Paulo, Brazil), July 1989, 24-27.*

[25] Newton, B.H.; Dodds, A.F.; Nugent, D.M.; Body, D.H.: A sensitive K-band receiver for ESM applications. *NIM (86), Brighton June 1986.*

[26] Meier, P.J.; Brauer, K.D.; Cohen, L.D.; Vorontzoff, N.; Lesprie, J.; Günther, J.: Channelized receiver covering 26 to 60 GHz with planar integrated circuit components. *Eaton Corp. All Div., Print 81 - 17.*

Traffic control:

[27] Panel discussion on: "Microwaves and Optronics in Vehicular Technology". *MIOP '90, April 24-26 1990, Stuttgart, Germany.*

[28] Workshop on: "Advanced car electronics and future traffic control systems related to microwaves". *21st EUMC 1991, Sept. 13 1991, Stuttgart, Germany, Workshop Proc., 97-153.*

[29] Glathe, H.-P.: Contribution to a future European traffic structure - progress report. *8th Int. Conf. on Automotive Electronics, Oct. 1991, London, England, 112 - 119.*

[30] Zandbergen, A.: Evaluation of different transmission media for use in automotive debating systems. *DACAR Conf., May 1991, Roma, Italy.*

[31] Autostrade S.p.A.: TELEPASS, toll-payment without stopping. central department for information, Florence, Italy - 1991.

[32] The Cambridgeshire County Council: Congestion Metering in Cambridge City. *Information Brochure 1992.*

[33] Blythe, P. T.: The use of transponder technology in road traffic control. *8th Int. Workshop 21st EUMC, Stuttgart 1991, in 129, 112 - 121.*

[34] Fischer, H.-J.: Digital beacon vehicle communication at 61 GHz for interactive dynamic traffic management. *8th Int. Conf. on Automotive Electronics, Oct. 1991, London, England, 120 - 124.*

[35] Moss, C. R.: The DACAR millimetre wave vehicle communications link. *Information Brochure 1992.*

[36] Anthouard, P.: Millimetric wave ROMEO for obstacle avoidance (in French). *Conference de Radar, Paris 1983. Communication AV.3, 192-196.*

[37] Kehlbeck, J.; Heidrich, E.; Wiesbeck, W.: Planar microwave Doppler-sensors for car speed monitoring. *Workshop 21st EUMC, Stuttgart 1991, in 129, 129-134.*

1992 International Workshop on Millimeter Waves
Applications & Technology Trends

- [38] Lissel, E.: Geschwindigkeits- und Wegsensor nach dem Mikrowellen-Doppler-Prinzip, VDI Berichte No. 687, 1988, 257 - 275.
- [39] Lowbridge, P.L.: Brigginshaw, P.M., Kumar, B.: Millimetre wave technology for collision avoidance and cruise control, 8th Int. Conf. on Automotive Electronics, Oct. 1991, London, England, 150 -154.
- [40] Stove, A.: 80 GHz automotive radar, 8th Int. Conf. on Automotive Electronics, Oct. 1991, London, England, 145 - 149.
- [41] Rolland, P.A.: Haese, N.: Beniamini, M.: Quasi optical technology for mm wave car electronics, Workshop 21st EuMC 1991, Stuttgart, in [29], 141-146.
- [42] Riahieli, L.: Stewart, E.: mmWave monolithic components for automotive applications, Alpha Industries Reprint, 1992.

LPI - COMMUNICATION

Performance Data

| MANUFACT. | FREQ. | OUTPUT POWER | MODULATION | DATA RATE | HOP LENGTH | YEAR | FCC Authorization | |
|-----------|-------|--------------|------------|--------------|------------|------|---|----|
| | | | | | | | Model | km |
| Hughes | 33 | 150 (max) | FM | 5 | 8 | 1975 | NCL/STAR NCL/air Strategic/Tactical Air & Radar | |
| MA-COM | 33 | 70 | NCFSK | 20 | | | Tactical Air & Radar 9000, 45000 6000, 30000 45000, 150000 | |
| Philips | 62 | 150 | FM | | 4 | 1975 | ECL/CS-1 Tactical Air & Radar 45000, 150000 15000, 45000 15000, 45000 | |
| WTI | 63 | 70 | FM | 8K | 5 MHz | | ECL/CS-1 Tactical Air & Radar 45000, 150000 15000, 45000 | |
| NOSC | 63 | 50 | FM | | 1332 | | ECL/CS-1 Tactical Air & Radar 45000, 150000 | |
| AEG | 53 | 17 | FM | B.W. 220 kHz | 1.5 | 1981 | ECL/CS-1 Tactical Air & Radar 45000, 150000 | |
| TRW | 70 | 10 (max) | PCM / FM | B.W. 150 kHz | 7.3 | 1979 | ECL/CS-1 Tactical Air & Radar 45000, 150000 | |
| MARCONI | 60 | 50 | AM | | | 1935 | Tactical Air & Radar 45000, 150000 15000, 45000 | |

LPI : Low Probability of Intercept

FM = Frequency Modulation

AM = Amplitude Modulation

PCM = Pulse Code Modulation

PSK = Phase Shift Keying

NCFSK = Non-Continuous Frequency Shift Keying

ECL = Electronic Countermeasures

CS-1 = Countermeasures System

Tactical Air & Radar

45000, 150000

15000, 45000

45000, 150000

15000, 45000

45000, 150000

15000, 45000

45000, 150000

15000, 45000

45000, 150000

15000, 45000

45000, 150000

15000, 45000

45000, 150000

15000, 45000

45000, 150000

15000, 45000

45000, 150000

15000, 45000

45000, 150000

15000, 45000

45000, 150000

15000, 45000

45000, 150000

15000, 45000

45000, 150000

15000, 45000

45000, 150000

15000, 45000

45000, 150000

15000, 45000

45000, 150000

15000, 45000

45000, 150000

15000, 45000

45000, 150000

15000, 45000

45000, 150000

15000, 45000

45000, 150000

15000, 45000

45000, 150000

15000, 45000

45000, 150000

15000, 45000

45000, 150000

15000, 45000

45000, 150000

15000, 45000

45000, 150000

15000, 45000

45000, 150000

15000, 45000

45000, 150000

15000, 45000

45000, 150000

15000, 45000

45000, 150000

15000, 45000

45000, 150000

15000, 45000

45000, 150000

15000, 45000

45000, 150000

15000, 45000

45000, 150000

15000, 45000

45000, 150000

15000, 45000

45000, 150000

15000, 45000

45000, 150000

15000, 45000

45000, 150000

15000, 45000

45000, 150000

15000, 45000

45000, 150000

15000, 45000

45000, 150000

15000, 45000

45000, 150000

15000, 45000

45000, 150000

15000, 45000

45000, 150000

15000, 45000

45000, 150000

15000, 45000

45000, 150000

15000, 45000

45000, 150000

15000, 45000

45000, 150000

15000, 45000

45000, 150000

15000, 45000

45000, 150000

15000, 45000

45000, 150000

15000, 45000

45000, 150000

15000, 45000

45000, 150000

15000, 45000

45000, 150000

15000, 45000

45000, 150000

15000, 45000

45000, 150000

15000, 45000

45000, 150000

15000, 45000

45000, 150000

15000, 45000

45000, 150000

15000, 45000

45000, 150000

15000, 45000

45000, 150000

15000, 45000

45000, 150000

15000, 45000

45000, 150000

15000, 45000

45000, 150000

15000, 45000

45000, 150000

15000, 45000

45000, 150000

15000, 45000

45000, 150000

15000, 45000

45000, 150000

15000, 45000

45000, 150000

15000, 45000

45000, 150000

15000, 45000

45000, 150000

15000, 45000

45000, 150000

15000, 45000

45000, 150000

15000, 45000

45000, 150000

15000, 45000

45000, 150000

15000, 45000

45000, 150000

15000, 45000

45000, 150000

15000, 45000

45000, 150000

15000, 45000

45000, 150000

15000, 45000

45000, 150000

15000, 45000

45000, 150000

15000, 45000

45000, 150000

15000, 45000

45000, 150000

15000, 45000

45000, 150000

15000, 45000

45000, 150000

15000, 45000

45000, 150000

15000, 45000

45000, 150000

15000, 45000

45000, 150000

15000, 45000

45000, 150000

15000, 45000

45000, 150000

15000, 45000

45000, 150000

15000, 45000

45000, 150000

15000, 45000

45000, 150000

15000, 45000

45000, 150000

15000, 45000

45000, 150000

15000, 45000

45000, 150000

15000, 45000

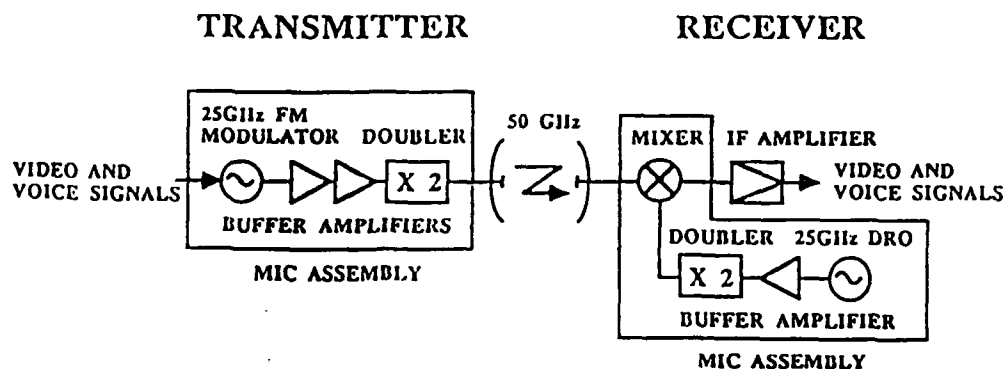
45000, 150000

15000, 45000

45000, 150000

15000, 45000

**BLOCK DIAGRAM OF A 50 GHz
TRANSMITTER AND A RECEIVER**



MATSUSHITA
Electric Industrial Company, Ltd.

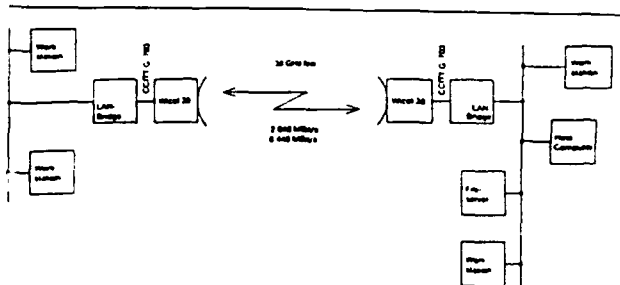
MATSUSHITA
Electric Industrial Company, Ltd.

Major characteristics of the 50 GHz communication system

| | |
|------------------------|----------------------|
| Frequency | 50.46 GHz |
| Transmitting power | 10 dBm |
| Noise figure | 13 dB |
| Frequency stability | ±100 ppm (-20-60 °C) |
| Modulation | FM |
| Frequency deviation | 16 MHz pp |
| Intermediate frequency | 960 MHz |
| IF bandwidth | 27 MHz |
| Video signal bandwidth | 4 MHz |
| Audio signal bandwidth | 15 kHz |

Wicol 38
38 GHz Wireless Link
for Digital Data Transmission

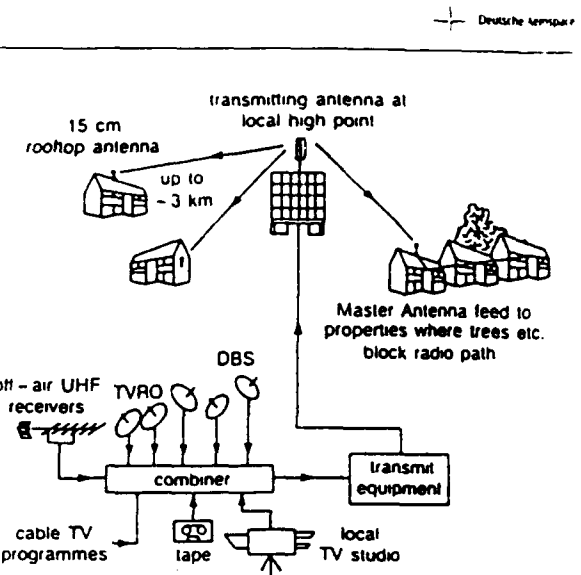
TELEFUNKEN
Sendertechnik



bridge channel configuration using Wicol 38

| Technical data | Application |
|--------------------|--|
| Frequency range | unites interconnection of data networks e.g. Ethernet, IEEE 802.3, token ring FDDI |
| Frequency tuning | Wicol 38 is equipped with an interface corresponding to CCITT G.703 and may thus be easily used in telecommunications area |
| Antenna beam width | in the range 37.5 GHz to 38.5 GHz |
| Bit rate | channel selection by means of incorporated keyboard |
| Interface | approx. 2° |
| Hop length | 2 048 Mbit/s or 8 448 Mbit/s |
| Power supply | corresponding to CCITT G.703 |
| Power consumption | high transmission reliability up to 4 km |
| Temperature range | 20 V to 60 V DC |
| Dimensions | 230/110 V AC optional |
| Weight | -20 °C to +50 °C (for ranges up to 8 km) |
| | approx. 50 W |
| | approx. 290 mm |
| | W x H x D: approx. 290 mm |
| | W x H x D: approx. 450 mm |
| | approx. 18 kg |

TELEFUNKEN Sendertechnik GmbH
Postfach 1000
D-7430 Ellwangen (Jagst)
Telephone (0 71 21) 10 18 19 Telex 10 432 14



System Concept

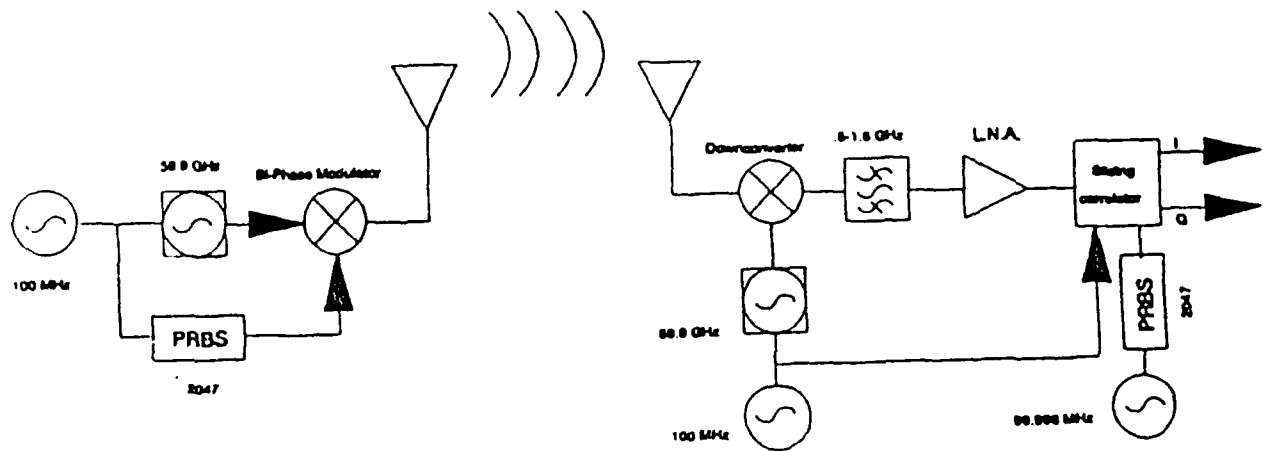
38 GHz MULTICHANNEL TV SYSTEM
FROM BTRL, MABLESHAM HEATH, ENGLAND



| Manufact. | Type | Freq. | Output | Modulation | Data Rate | | Hoplength |
|------------|----------|-------|--------|------------|-----------|----------|-----------|
| | | | | | GHz | power mW | |
| Alc.-Th. | TM 440 | 40 | 50 | FM | BW:15MHz | | 15 |
| BTRL | | 29 | 120 | FSK/PSK | 8k/70k | | 10 |
| Telefunken | Wicol 38 | 38 | | | 8,000 | | 4 |
| NEC | PL 50 | 50 | 15 | FSK | 1,544 | | 2 |
| FUJITSU | FC2160 | 50 | 10 | FM/FSK | 20,000 | | 2 |
| MATSUSHITA | | 50 | 10 | FM | BW:15MHz | | |
| SONY | | 50 | 20 | FSK | 30,000 | | |

POINT-TO-POINT Millimeter-Wave Communication systems
Performance Data

System 1

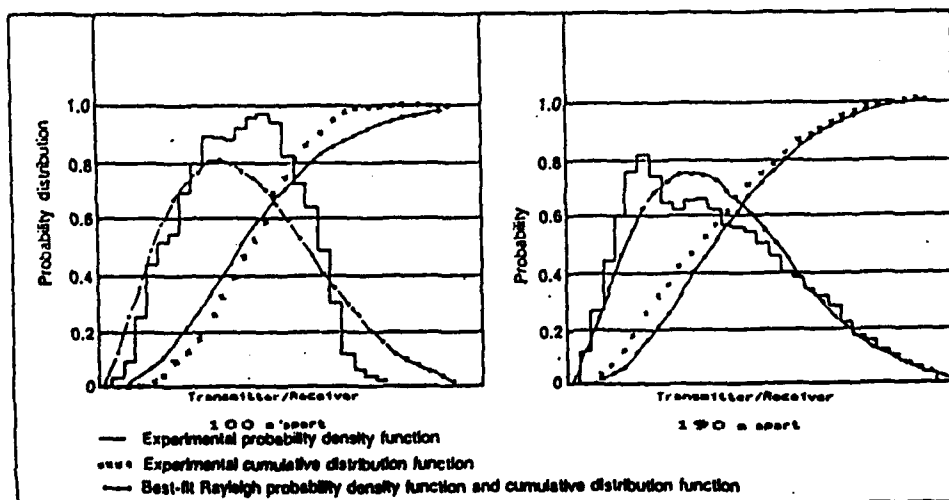


Sounder Diagram

60 GHZ LAN PROPAGATION MEASUREMENTS
FROM: UNIVERSITY OF BRISTOL, UK

Radio and Radar Systems Division

AEG

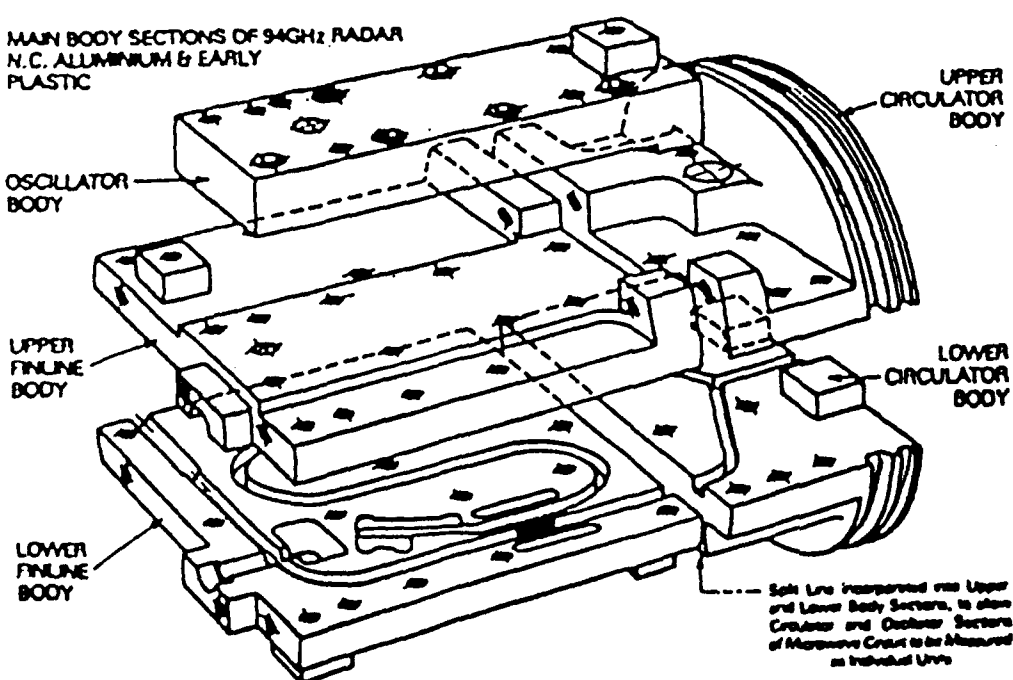


from: H.J. Thomas, S.L. Bigueiro, R.B. Cole
UNIVERSITY COLLEGE LONDON,
London, England

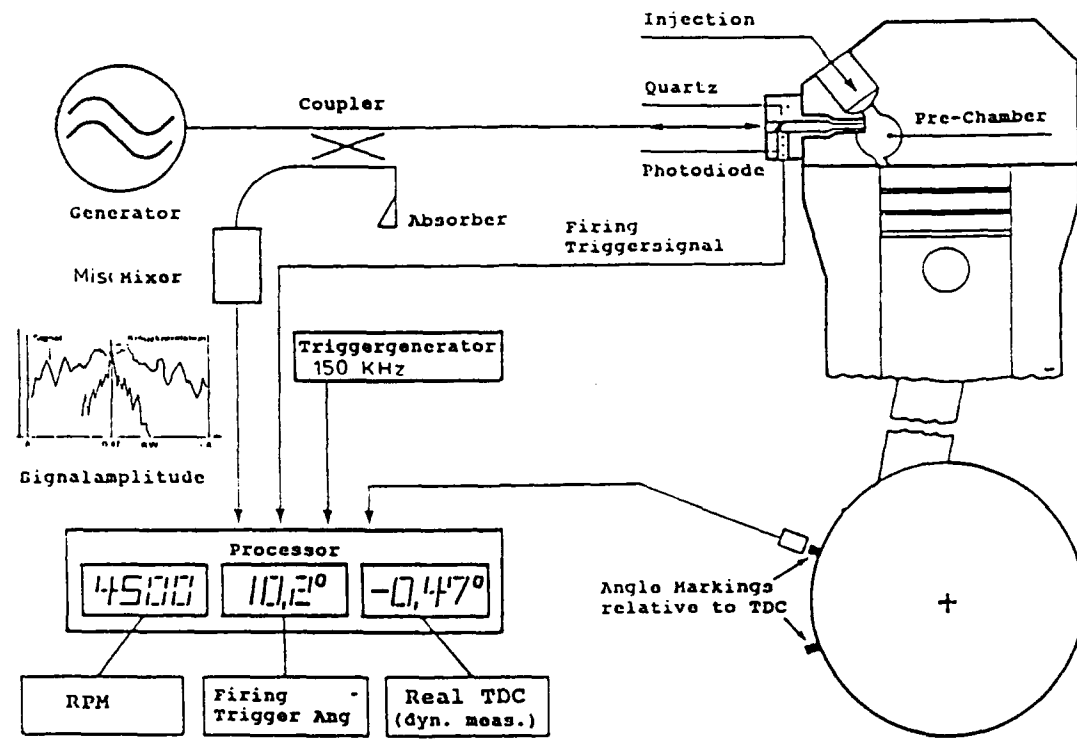
| Manufact. | Freq. | Output | Modulation | Bandwidth | Runlength |
|--------------------|-------|-------------|------------|-----------|--------------|
| | GHz | Power mW | | MHz | m |
| Univ. Col. Ldn. | 55 | 60 | | 5 | 150 |
| Univ. Bristol | 60 | 20 | PRBS | 2 | L-O-S 200 |

 Experimental Millimeter-Wave System for Mobile Braodband Services (MBS)
 Performance Data

PHILIPS MICROWAVE

 MAIN BODY SECTIONS OF 94GHZ RADAR
 N.C. ALUMINUM & EARLY
 PLASTIC


TDC measurement
Schematic diagram



10.03.82 DASA - U1 11 b/pb

16



| | |
|----------------------|----------------|
| Output power | 35 mW |
| Frequency | 94 GHz |
| Sweep range | 800 MHz |
| Linearity | less than 1 % |
| Mixer NF | 8 db |
| Weight | less than 50 g |
| Price * (housing) | less than 5 £ |

| | REQUIREMENTS FOR AN OBSTACLE WARNING SYSTEM | AEG |
|--|---|-----|
| | <ul style="list-style-type: none"> • DETECTION OF CABLES AND WIRES WITH DIAMETERS \geq 3mm • RANGE OF CA. 500m • ALL WEATHER CAPABILITY • LIGHT WEIGHT AND SMALL VOLUME • COOPERATION WITH EXISTING NAVIGATION AIDS | |

*) polymer injection moulding process
more than 10,000 units
Cu-plating applied

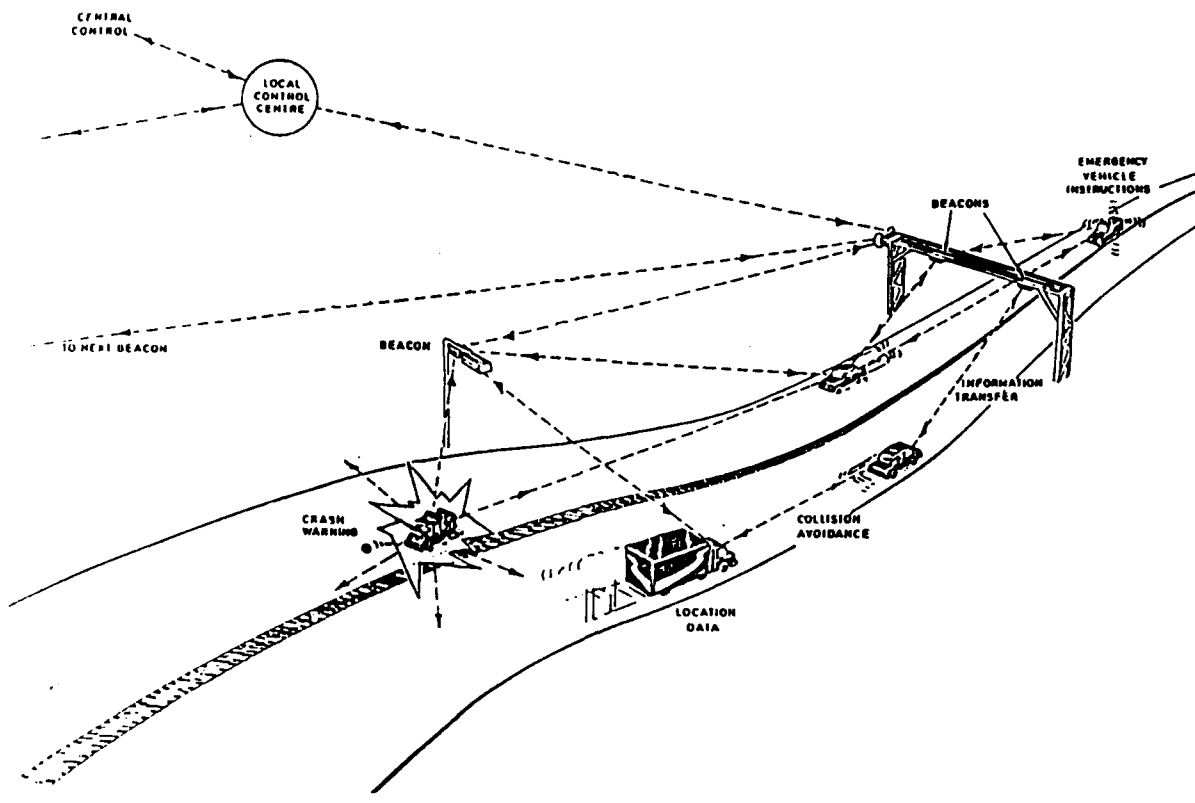


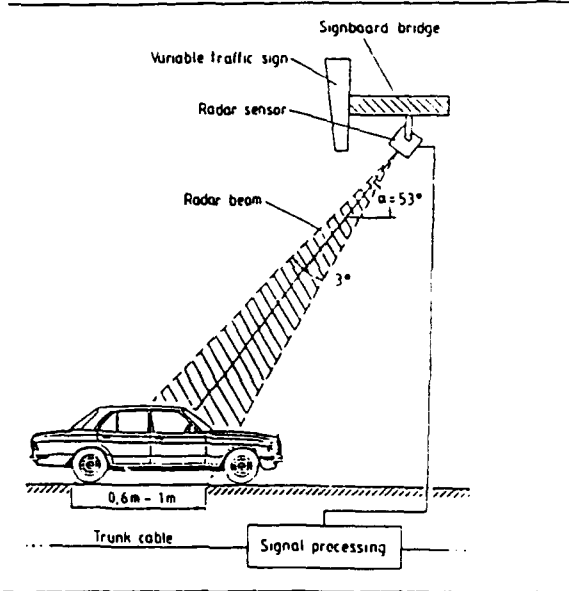
Figure 2.1: Operational system for RTI applications

JR

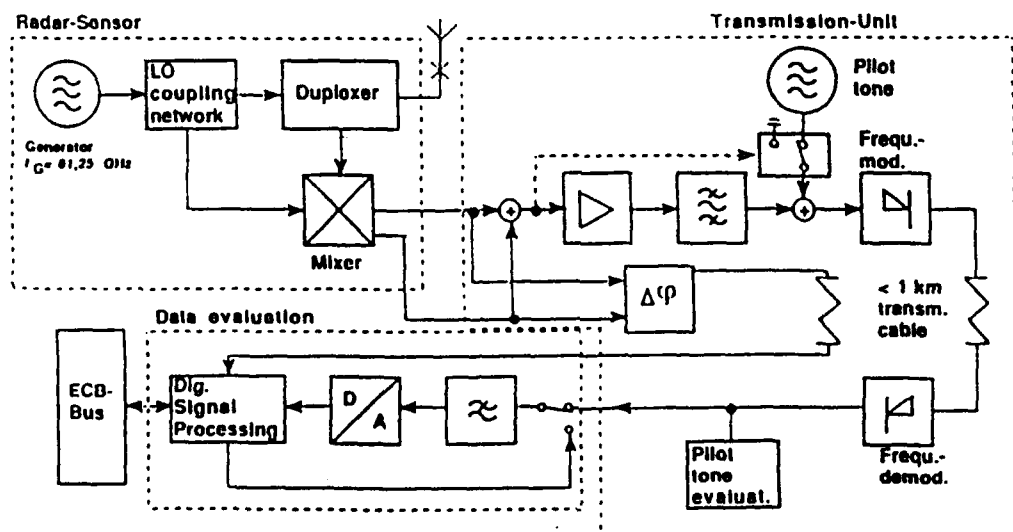


| Bands GHz | 5.795 - 5.805 5.805 - 5.815 | 63 - 64 | 76 - 77 |
|-----------------------------|--------------------------------------|-------------------------------------|-------------------------------------|
| Applications | Automatic toll debiting systems | Transmissions Road ↔ V V ↔ V | Anticollision radars |
| Bandwidth | 2*10MHz or 4 channels of 5 MHz | 1 GHz Channels of 5 to 20 MHz | FM/CW : 100 MHz Pulsed : 500 MHz |
| Allowed power | 3 dBw | 3 - 16 dBw | 16 - 20 dBw |
| Recommended antenna gain | 10 - 15 dB | 10 - 30 dB | 30 - 35 dB |
| Rate | 1 - 3 Mbits/sec | Few Mbits/sec | |
| Modulation | FSK, PSK, ASK | FSK, PSK | FM/CW Pulsed |

from: HESS, President of the CEPT frequency group - DRIVE Conference, 4 - 6/2/91



Application of AVES - Millimeterwave Radar Sensor



AVES - AEG VERKEHRS ERFASSUNGS SYSTEM
SCHEMATIC BLOCK DIAGRAM

| | |
|---|------------|
| Output power | 5 mW |
| Frequency (2nd harm. Gunn) | 61.25 GHz |
| Harmonic suppression (H-irises) | > 25 dB |
| Antenna beamwidth | |
| azimuth | 13 degrees |
| elevation | 3 degrees |
| (asymmetric lens) | |
| gain | 25 dB |
| Mixer NF | dB |
| (Ku-Band diodes) | |

CONFIRMED.

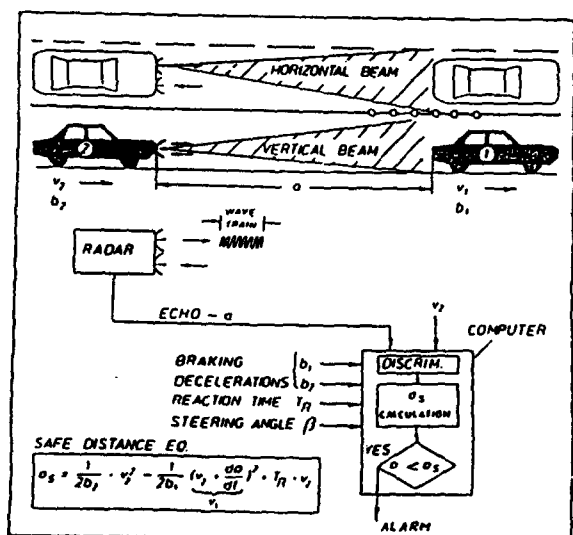
- 2) OPERATES SATISFACTORILY IN PRESENCE OF MULTIPATH EFFECTS.
- 3) OPERATES IN PRESENCE OF OTHER VEHICLES.
- 4) OPERATES WHEN DIRECT PATH IS OBSCURED BY OTHER VEHICLES.
- 5) ERROR RATE BEFORE ERROR CORRECTION $\approx 10^{-4}$.
- 6) ERROR RATE AFTER ERROR CORRECTION SO LOW THAT IT IS DIFFICULT TO MEASURE (PROBABLY LESS THAN 10^{-9}).

Telefunken Systemtechnik
AVES sensor data

DRIVE - DACAR - Program Road test results

100

Radio and Radar Systems Group



5 GHz collision avoidance radar principle of operation

TOYOTA MOTOR CORPORATION, JAPAN

PERFORMANCE DATA

STAND ALONE 'SKIN TRACKING' UNIT

FREQUENCY **10.5.02**

NOTIFICATION

FM-TRIANGULAR 75 MHz

RATE 750 Hz

OUTPUT POWER 30 mW

MEASUREMENT RANGE 3 mm-60 mm

150-mm/h RAIN TO 50%

ACCURACY

ANTENNA DESIGN

SEPARATE TRANSMIT AND RECEIVE ANTENNA

2 DEGREES BEAM WIDTH

CROSS POLARIZED

POLARIZED 45 DEGREES TO ROADWAY

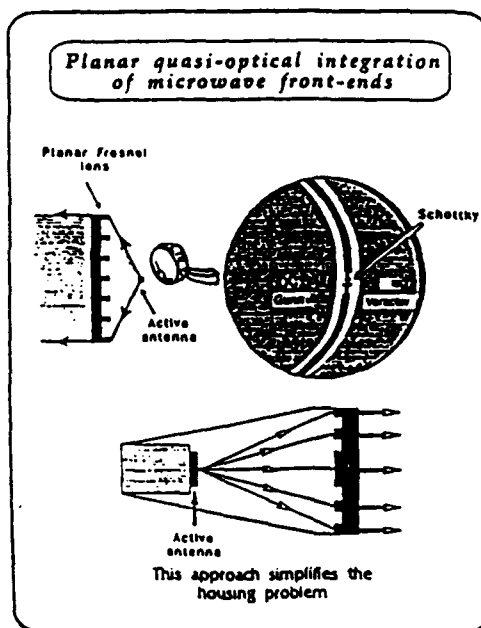
49.5 GHz AUTO MOTIVE RADAR

64



Deutsche Aerospace

WORKSHOP ON: ADVANCED CAR ELECTRONICS AND FUTURE TRAFFIC CONTROL SYSTEMS RELATED TO MICROWAVES



Quelle: P.A. Roland, C.H.S. - Université de Lille

Abstandswarnradar

Quasi-optischer Aufbau bei 60 und 86 GHz

| | Collision Avoidance | Doppler Sensing | Beacon Systems | |
|------|---------------------|----------------------|----------------|--------------------------------|
| 1970 | Bendix | 16 GHz duplex CW | | |
| 1972 | RCA | 10 GHz FM-CW | TI | 55 GHz Speedometer |
| 1974 | AEG-TfK | 35 GHz pulsed | | |
| | Lucas Ltd. | 32 GHz FM-CW | | |
| 1975 | SEL | 16.5 GHz FM-CW | | |
| 1976 | AEG-TfK | 50 GHz pulsed | Philips | 10 GHz antenna sensor |
| 1977 | Bendix | 36 GHz duplex CW | AEG-TfK | 35 GHz vsb-Radar |
| 1978 | SEL | 35 GHz FM-CW | Japan | Stad control sensor |
| | Nissan | 24 GHz pulsed/FM | | |
| 1980 | Toyota/ Fujitsu | 50 GHz FM-CW | | Vehicular Communication 60 GHz |
| 1982 | Nissan | 60 GHz pulsed/FM | | |
| 1984 | | | | |
| 1986 | | | | |
| 1988 | Philips | 94 GHz L/C Hybrid | AEG | 60 GHz AVES |
| 1990 | Uni Lille | 94 GHz Quasi-optical | | MCCS / SEL |
| | | | | TST 60 GHz AVES-COM |

23



Deutsche Aerospace

Millimeter-wave technology is mature today

- covert communication systems
- LAN radios (PCN, MBS)
- Terminal guidance systems
- collision avoidance sensors

have been built and tested successfully

Low cost techniques

for high rate production,
hybrid and monolithic, are available and
prototype production has been launched

Commercial applications

have gained momentum

- RTI-Road Traffic Informatics
- LAN radio

are today's driving forces

Conclusion

Millimetre-wave applications

Millimetre-wave commercial applications and technologies

As the microwave spectrum becomes more crowded the need for application of the millimetre spectrum becomes more acute. Holger Melin from Deutsche Aerospace, Munich has collected together some of the most likely applications of parts of the spectrum and the technologies that are an essential part of the successful application.

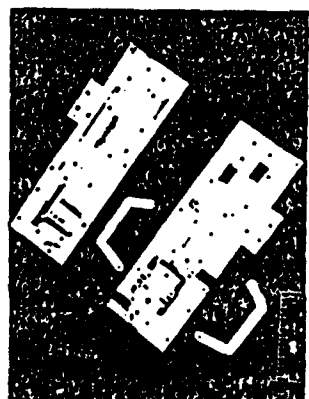


Figure 1 A 3.7GHz matched channel radio integrated transmitter module fabricated using M-A-COM's 4.0µm-deep-micromachining technique (Courtesy of M-A-COM)

Millimetre-wave technology is available and mature today, and it is explored in various applications. In the commercial arena, two major types of applications have to be distinguished: communications and traffic-control systems. The former being either point-to-point or LAN (local area network) systems, the latter incorporating radar and beacon (short hop link) systems [1].

Apart from the atmosphere's unique propagation behaviour [2], all mm-wave applications take advantage of the highly directive nature of the mm-wave beam; good angular resolution can be achieved with moderately small antennas, thus mm-wave systems are small in size and light in weight, compared to their microwave counterparts. The lack of frequencies in the microwave bands is a common usage problem, especially for communication purposes, in an important reason to take advantage of mm-wave techniques.

Atmospheric propagation effects strongly influence considerations related to the application of mm-wave transmission links. Normally, such systems will be operated in the atmospheric windows around 35 and

40 GHz. Beyond that, existing in-house component technology is heavily influencing this decision and thus the system design. The physical set-up for a particular application might differ significantly from company to company, as seen in the following. Based on promising measurement results customized digital distribution radios have been developed worldwide. About 700 mm-wave point-to-point radio links are already installed in Japan alone [8].

Being either usable for digital data transmission up to 20Mbit/s or for wide-band analogue signals such as colour TV, the FACOM 160/50GHz system built by Fujitsu of Kawasaki, Japan [7], features 2.5km of hop-length, depending on circuit performance being required.

Typical configuration is with a parabolic antenna with 40dBi gain (from) output power and a receiver noise figure of 17dB. In order to prevent interference problems, if two or more transmitters on the same frequency are used in the same neighbourhood, the FACOM 2160 features a unique, but simple solution. It has chosen a linear technology for the realization of this 29GHz system, which has been extensively used but two who developed a 70GHz system for transmission of data and fullband video traffic. Output power here is 150mW, receiver noise figure is 10dB and antenna gain is 41dBi. Philips Research at Redhill, England, who developed the RF components of this 29GHz system, has chosen linear technology for the realization. It has emerged as a front runner for frequencies of about 25-100GHz [15].

10

radio module was designed to be used with existing host radios. System parameters for the host radio include 60mW output power at 70GHz, an antenna gain of 41dB and 8.5dB receiver noise figure.

The integrated 37GHz transmitter assembly of this mm-wave radio module, figure 1, within the Gunn/VCO, isolator source being incorporated as a 'bolt on' unit, illustrates the system complexity. M-A-COM's integrated circuit technology for chip equipment in production at 100µm/micromachining would reduce by approximately 30%.

Waveguide Integration

The VWR (Waveguide Integrated Package) technique for integrating several different waveguide components into one compact, unicellular integrated assembly has been developed and used at M-A-COM of Burlington, MA, USA, for many years in the microwave range. It has been used as a cost-effective method for high-volume production, providing size and weight reduction without sacrificing performance. VWR techniques use waveguide as the primary transmission medium and computerized NC milling combined with laser welding for fabrication.

15

November 1991

ductor technology is the 50GHz system built by Matsushita Electric Ltd of Osaka, Japan [8]. In this example the output power is 10mW and the receiver noise figure is 13dB.

This system employs 3-terminal devices only and takes advantage of hybrid MIC technology at 25GHz with double-buried circuits following. This approach will reduce production costs significantly. Figure 3 depicts the assembled 25GHz FM modulator, including a dielectric resonator.

An example of a European point-to-point transmission link is the 28GHz BTI SYSTEM [10]. Early work at British Telecom Laboratories (BTL) in Martlesham, UK, concentrated on developing a 70GHz system for transmission of data and fullband video traffic. Output power here is 150mW, receiver noise figure is 10dB and antenna gain is 41dBi.

Philipps Research at Redhill, England, who developed the RF components of this 29GHz system, has chosen linear technology for the realization. It has emerged as a front runner for frequencies of about 25-100GHz [15].

Linear techniques achieve relatively low loss and the conductor patterns on circuit boards, which can be made reproducible using photolithographic techniques.

The RF front end contains the integrated finline modulator, to which the Gunn diode local oscillator and the transmitter sources are mounted on circuit boards. This transmitter unit, includes a bipolar modulator, a voltage-controlled attenuator, and a modulator coupler for checking power and frequency. The receiver unit shown in figure 4, contains a low noise amplifier for receiving power and frequency. A good example for a transmission link making use of modern semiconductor technology is the 25GHz

Figure 2 FACOM 2160 Cross coupling filter (CCF) design (From Doer et al [7]) (Courtesy of M-A-COM) (Courtesy of M-A-COM)

Figure 3 25GHz FM modulator (From Ogawa et al [8])

Figure 4 29GHz BTI communication system (Integrated receiver module (Courtesy of Philips Research))

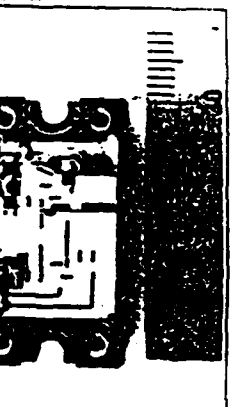


Figure 4 29GHz BTI communication system (Integrated receiver module (Courtesy of Philips Research))

systems as soon as it becomes available; after several years of operation, the frequency of the BTI system was reallocated to 41GHz and the entire front end will now be redesigned incorporating MMICs [10].

Local Cellular

Demand for communication services that can be provided without the need for cable connections is growing rapidly as potential users become aware of services such as cordless telephones and mobile cellular radio.

Trans 45GHz and 90GHz bands have been extensively used but two namely H. J. Thomas et al [11] and P. McGehee et al [12] from the Universities of London and Bristol respectively, have investigated the 55-60GHz range for LCRN applications. Figure 5 shows the power profile of 60GHz transmission measurements carried out in Bristol.

Based on these initial measurements it appears possible to establish LCRN's (local cellular radio networks) in the mm-wave range. This is the commercial exploitation of this gravity under utilised region of the spectrum is anticipated. So far both groups have used



Figure 5 60GHz transmission measurements in Bristol (Courtesy of P. McGehee et al [12])

hybrid MMIC technology is the 50GHz system built by Matsushita Electric Ltd of Osaka, Japan [8]. In this example the output power is 10mW and the receiver noise figure is 13dB.

This system employs 3-terminal devices only and takes advantage of hybrid MIC technology at 25GHz with double-buried circuits following. This approach will be incorporated into such

systems as soon as it becomes available. After several years of operation, the frequency of the BTI system was reallocated to 41GHz and the entire front end will now be redesigned incorporating MMICs [10].



Figure 6 25GHz MMIC assembly (Courtesy of Matsushita Electric Ltd)

Millimetre-wave applications

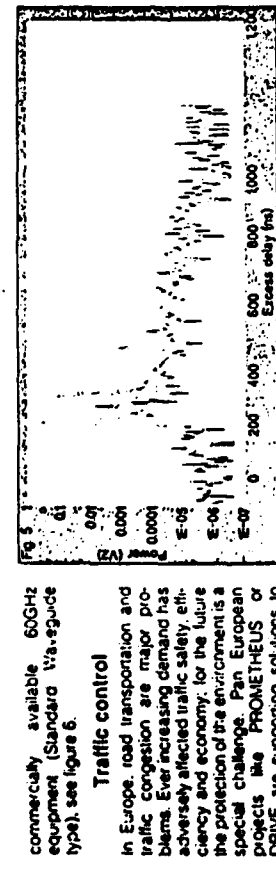


Figure 5: 60GHz transmission experiments Power profile (From McGeehan [17])

commercially available, 60GHz equipment (Standard Vivaldi-antennas type), see figure 6.

Traffic control

In Europe road transportation and traffic congestion are major problems. Ever increasing demand has adversely affected traffic safety, efficiency and economy; for the future the protection of the environment is a special challenge. Pan European projects like PROMETHEUS or DRIVE are supporting solutions to control and assist the traffic flow using Road Traffic Informatics (RTI), such as route guidance, road pricing, incident detection, for example. Thus mm-wave systems have found an increasing interest [13]. Doppler radar systems for true motion control and traffic monitoring as well as FMCW- or pulse-radar for collision avoidance purposes, and beacon systems for road pricing and advanced road infrastructures are suggested by the European frequency allocations for European road transport applications [14], as suggested by the CEPT. This clearly demonstrates the importance of mm-wave techniques in this field.

Not taking into account the very early research in this field, hybrid and monolithic mm-wave inte-

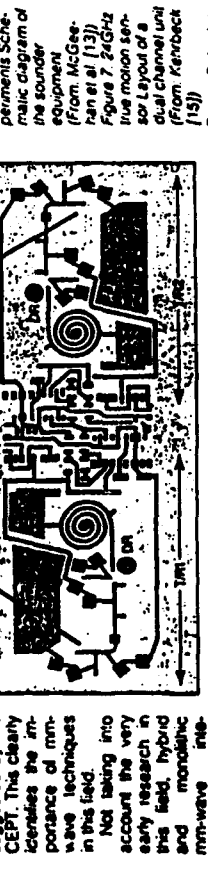


Figure 6: 60GHz transmission experiments Schematic diagram of the sounder equipment (From McGeehan [13])

has been shown, that at least two independent sensors have to be employed - looking forward and backward - in order to correct the systematic measurement error due to atmospheric fluctuations. However, quasi-optical techniques, i.e. the optical integration of planar MMICs, is being studied as an option.

Future traffic control systems require true ground speed information for ABS, ASC or car navigation systems, using microwave Doppler systems for this purpose.

Table 1: CEPT frequency allocation for European road transport applications

| Region | Frequency Range (GHz) | Antennas | Antennas | Antennas |
|--------|-----------------------|----------|----------|----------|
| 1 | 24 | 100 | 100 | 100 |
| 2 | 24 | 100 | 100 | 100 |
| 3 | 24 | 100 | 100 | 100 |
| 4 | 24 | 100 | 100 | 100 |
| 5 | 24 | 100 | 100 | 100 |
| 6 | 24 | 100 | 100 | 100 |
| 7 | 24 | 100 | 100 | 100 |
| 8 | 24 | 100 | 100 | 100 |
| 9 | 24 | 100 | 100 | 100 |
| 10 | 24 | 100 | 100 | 100 |
| 11 | 24 | 100 | 100 | 100 |
| 12 | 24 | 100 | 100 | 100 |
| 13 | 24 | 100 | 100 | 100 |
| 14 | 24 | 100 | 100 | 100 |
| 15 | 24 | 100 | 100 | 100 |
| 16 | 24 | 100 | 100 | 100 |
| 17 | 24 | 100 | 100 | 100 |
| 18 | 24 | 100 | 100 | 100 |
| 19 | 24 | 100 | 100 | 100 |
| 20 | 24 | 100 | 100 | 100 |
| 21 | 24 | 100 | 100 | 100 |
| 22 | 24 | 100 | 100 | 100 |
| 23 | 24 | 100 | 100 | 100 |
| 24 | 24 | 100 | 100 | 100 |
| 25 | 24 | 100 | 100 | 100 |
| 26 | 24 | 100 | 100 | 100 |
| 27 | 24 | 100 | 100 | 100 |
| 28 | 24 | 100 | 100 | 100 |
| 29 | 24 | 100 | 100 | 100 |
| 30 | 24 | 100 | 100 | 100 |
| 31 | 24 | 100 | 100 | 100 |
| 32 | 24 | 100 | 100 | 100 |
| 33 | 24 | 100 | 100 | 100 |
| 34 | 24 | 100 | 100 | 100 |
| 35 | 24 | 100 | 100 | 100 |
| 36 | 24 | 100 | 100 | 100 |
| 37 | 24 | 100 | 100 | 100 |
| 38 | 24 | 100 | 100 | 100 |
| 39 | 24 | 100 | 100 | 100 |
| 40 | 24 | 100 | 100 | 100 |
| 41 | 24 | 100 | 100 | 100 |
| 42 | 24 | 100 | 100 | 100 |
| 43 | 24 | 100 | 100 | 100 |
| 44 | 24 | 100 | 100 | 100 |
| 45 | 24 | 100 | 100 | 100 |
| 46 | 24 | 100 | 100 | 100 |
| 47 | 24 | 100 | 100 | 100 |
| 48 | 24 | 100 | 100 | 100 |
| 49 | 24 | 100 | 100 | 100 |
| 50 | 24 | 100 | 100 | 100 |
| 51 | 24 | 100 | 100 | 100 |
| 52 | 24 | 100 | 100 | 100 |
| 53 | 24 | 100 | 100 | 100 |
| 54 | 24 | 100 | 100 | 100 |
| 55 | 24 | 100 | 100 | 100 |
| 56 | 24 | 100 | 100 | 100 |
| 57 | 24 | 100 | 100 | 100 |
| 58 | 24 | 100 | 100 | 100 |
| 59 | 24 | 100 | 100 | 100 |
| 60 | 24 | 100 | 100 | 100 |
| 61 | 24 | 100 | 100 | 100 |
| 62 | 24 | 100 | 100 | 100 |
| 63 | 24 | 100 | 100 | 100 |
| 64 | 24 | 100 | 100 | 100 |
| 65 | 24 | 100 | 100 | 100 |
| 66 | 24 | 100 | 100 | 100 |
| 67 | 24 | 100 | 100 | 100 |
| 68 | 24 | 100 | 100 | 100 |
| 69 | 24 | 100 | 100 | 100 |
| 70 | 24 | 100 | 100 | 100 |
| 71 | 24 | 100 | 100 | 100 |
| 72 | 24 | 100 | 100 | 100 |
| 73 | 24 | 100 | 100 | 100 |
| 74 | 24 | 100 | 100 | 100 |
| 75 | 24 | 100 | 100 | 100 |
| 76 | 24 | 100 | 100 | 100 |
| 77 | 24 | 100 | 100 | 100 |
| 78 | 24 | 100 | 100 | 100 |
| 79 | 24 | 100 | 100 | 100 |
| 80 | 24 | 100 | 100 | 100 |
| 81 | 24 | 100 | 100 | 100 |
| 82 | 24 | 100 | 100 | 100 |
| 83 | 24 | 100 | 100 | 100 |
| 84 | 24 | 100 | 100 | 100 |
| 85 | 24 | 100 | 100 | 100 |
| 86 | 24 | 100 | 100 | 100 |
| 87 | 24 | 100 | 100 | 100 |
| 88 | 24 | 100 | 100 | 100 |
| 89 | 24 | 100 | 100 | 100 |
| 90 | 24 | 100 | 100 | 100 |
| 91 | 24 | 100 | 100 | 100 |
| 92 | 24 | 100 | 100 | 100 |
| 93 | 24 | 100 | 100 | 100 |
| 94 | 24 | 100 | 100 | 100 |
| 95 | 24 | 100 | 100 | 100 |
| 96 | 24 | 100 | 100 | 100 |
| 97 | 24 | 100 | 100 | 100 |
| 98 | 24 | 100 | 100 | 100 |
| 99 | 24 | 100 | 100 | 100 |
| 100 | 24 | 100 | 100 | 100 |
| 101 | 24 | 100 | 100 | 100 |
| 102 | 24 | 100 | 100 | 100 |
| 103 | 24 | 100 | 100 | 100 |
| 104 | 24 | 100 | 100 | 100 |
| 105 | 24 | 100 | 100 | 100 |
| 106 | 24 | 100 | 100 | 100 |
| 107 | 24 | 100 | 100 | 100 |
| 108 | 24 | 100 | 100 | 100 |
| 109 | 24 | 100 | 100 | 100 |
| 110 | 24 | 100 | 100 | 100 |
| 111 | 24 | 100 | 100 | 100 |
| 112 | 24 | 100 | 100 | 100 |
| 113 | 24 | 100 | 100 | 100 |
| 114 | 24 | 100 | 100 | 100 |
| 115 | 24 | 100 | 100 | 100 |
| 116 | 24 | 100 | 100 | 100 |
| 117 | 24 | 100 | 100 | 100 |
| 118 | 24 | 100 | 100 | 100 |
| 119 | 24 | 100 | 100 | 100 |
| 120 | 24 | 100 | 100 | 100 |
| 121 | 24 | 100 | 100 | 100 |
| 122 | 24 | 100 | 100 | 100 |
| 123 | 24 | 100 | 100 | 100 |
| 124 | 24 | 100 | 100 | 100 |
| 125 | 24 | 100 | 100 | 100 |
| 126 | 24 | 100 | 100 | 100 |
| 127 | 24 | 100 | 100 | 100 |
| 128 | 24 | 100 | 100 | 100 |
| 129 | 24 | 100 | 100 | 100 |
| 130 | 24 | 100 | 100 | 100 |
| 131 | 24 | 100 | 100 | 100 |
| 132 | 24 | 100 | 100 | 100 |
| 133 | 24 | 100 | 100 | 100 |
| 134 | 24 | 100 | 100 | 100 |
| 135 | 24 | 100 | 100 | 100 |
| 136 | 24 | 100 | 100 | 100 |
| 137 | 24 | 100 | 100 | 100 |
| 138 | 24 | 100 | 100 | 100 |
| 139 | 24 | 100 | 100 | 100 |
| 140 | 24 | 100 | 100 | 100 |
| 141 | 24 | 100 | 100 | 100 |
| 142 | 24 | 100 | 100 | 100 |
| 143 | 24 | 100 | 100 | 100 |
| 144 | 24 | 100 | 100 | 100 |
| 145 | 24 | 100 | 100 | 100 |
| 146 | 24 | 100 | 100 | 100 |
| 147 | 24 | 100 | 100 | 100 |
| 148 | 24 | 100 | 100 | 100 |
| 149 | 24 | 100 | 100 | 100 |
| 150 | 24 | 100 | 100 | 100 |
| 151 | 24 | 100 | 100 | 100 |
| 152 | 24 | 100 | 100 | 100 |
| 153 | 24 | 100 | 100 | 100 |
| 154 | 24 | 100 | 100 | 100 |
| 155 | 24 | 100 | 100 | 100 |
| 156 | 24 | 100 | 100 | 100 |
| 157 | 24 | 100 | 100 | 100 |
| 158 | 24 | 100 | 100 | 100 |
| 159 | 24 | 100 | 100 | 100 |
| 160 | 24 | 100 | 100 | 100 |
| 161 | 24 | 100 | 100 | 100 |
| 162 | 24 | 100 | 100 | 100 |
| 163 | 24 | 100 | 100 | 100 |
| 164 | 24 | 100 | 100 | 100 |
| 165 | 24 | 100 | 100 | 100 |
| 166 | 24 | 100 | 100 | 100 |
| 167 | 24 | 100 | 100 | 100 |
| 168 | 24 | 100 | 100 | 100 |
| 169 | 24 | 100 | 100 | 100 |
| 170 | 24 | 100 | 100 | 100 |
| 171 | 24 | 100 | 100 | 100 |
| 172 | 24 | 100 | 100 | 100 |
| 173 | 24 | 100 | 100 | 100 |
| 174 | 24 | 100 | 100 | 100 |
| 175 | 24 | 100 | 100 | 100 |
| 176 | 24 | 100 | 100 | 100 |
| 177 | 24 | 100 | 100 | 100 |
| 178 | 24 | 100 | 100 | 100 |
| 179 | 24 | 100 | 100 | 100 |
| 180 | 24 | 100 | 100 | 100 |
| 181 | 24 | 100 | 100 | 100 |
| 182 | 24 | 100 | 100 | 100 |
| 183 | 24 | 100 | 100 | 100 |
| 184 | 24 | 100 | 100 | 100 |
| 185 | 24 | 100 | 100 | 100 |
| 186 | 24 | 100 | 100 | 100 |
| 187 | 24 | 100 | 100 | 100 |
| 188 | 24 | 100 | 100 | 100 |
| 189 | 24 | 100 | 100 | 100 |
| 190 | 24 | 100 | 100 | 100 |
| 191 | 24 | 100 | 100 | 100 |
| 192 | 24 | 100 | 100 | 100 |
| 193 | 24 | 100 | 100 | 100 |
| 194 | 24 | 100 | 100 | 100 |
| 195 | 24 | 100 | 100 | 100 |
| 196 | 24 | 100 | 100 | 100 |
| 197 | 24 | 100 | 100 | 100 |
| 198 | 24 | 100 | 100 | 100 |
| 199 | 24 | 100 | 100 | 100 |
| 200 | 24 | 100 | 100 | 100 |
| 201 | 24 | 100 | 100 | 100 |
| 202 | 24 | 100 | 100 | 100 |
| 203 | 24 | 100 | 100 | 100 |
| 204 | 24 | 100 | 100 | 100 |
| 205 | 24 | 100 | 100 | 100 |
| 206 | 24 | 100 | 100 | 100 |
| 207 | 24 | 100 | 100 | 100 |
| 208 | 24 | 100 | 100 | 100 |
| 209 | 24 | 100 | 100 | 100 |
| 210 | 24 | 100 | 100 | 100 |
| 211 | 24 | 100 | 100 | 100 |
| 212 | 24 | 100 | 100 | 100 |
| 213 | 24 | 100 | 100 | 100 |
| 214 | 24 | 100 | 100 | 100 |
| 215 | 24 | 100 | 100 | 100 |
| 216 | 24 | 100 | 100 | 100 |
| 217 | 24 | 100 | 100 | 100 |
| 218 | 24 | 100 | 100 | 100 |
| 219 | 24 | 100 | 100 | 100 |
| 220 | 24 | 100 | 100 | 100 |
| 221 | 24 | 100 | 100 | 100 |
| 222 | 24 | 100 | 100 | 100 |
| 223 | 24 | 100 | 100 | 100 |
| 224 | 24 | 100 | 100 | 100 |
| 225 | 24 | 100 | 100 | 100 |
| 226 | 24 | 100 | 100 | 100 |
| 227 | 24 | 100 | 100 | 100 |
| 228 | 24 | 100 | 100 | 100 |
| 229 | 24 | 100 | 100 | 100 |
| 230 | 24 | 100 | 100 | 100</td |

**A NEW PASSIVE MICROWAVE SCANNER FOR
AIRBORNE MEASUREMENTS OF MARITIM OIL
POLLUTIONS**

K. Gruener

DLR, Oberpfaffenhofen • Germany

A New Passive Microwave Linescanner for Airborne Measurements of Maritime Oil Pollutions

K. Grüner, G. Kahlisch, H. Schreiber, P. Sliwinski
* B. Vowinkel

German Aerospace Research Establishment (DLR), Oberpfaffenhofen, FRG
* University of Cologne, Cologne, FRG

Abstract

A new passive microwave linescanner has been developed that will be used for airborne operational measurements of maritime oil pollutions. The system consists of two offset rotating parabolic mirrors and two radiometer sets, where each set contains three radiometers at 18.7, 36.5 and 89 GHz center frequency. A further 89 GHz radiometer is used for the measurement of the average radiometric sky temperature. The system is continuously calibrated by the use of a "hot load" at ambient temperature and a peltier cooled "cold load". A computer system allows online data reduction for the estimation of the amount of oil on the sea surface.

I. Introduction

Pollution of the sea has increased up to levels which can result in severe risks for the marine ecosystem. High loads of oil have been observed in many coastal waters. In addition to the procurement of "oil combating ships", this situation has led to the demand for airborne surveying methods for providing helpful data for oil spill clean-up operations following accidental discharges, and to monitor the legal aspects of permanent contributions to maritime oil pollutions.

In Europe, aircraft equipped with remote sensing instruments have been provided in various countries in the period 1983-1988 for a regular survey of coastal waters and, in view of a sensor system of second generation, for the purpose of basic research. Since 1986, for example, two Dornier Do28 aircrafts equipped with an IR/UV-Linescanner, a Side Looking Airborne Radar (SLAR) and a scanning 35GHz-Radiometer have been flown in the German-responsibility areas of the North Sea and the Baltic Sea, aiming at a continuous surveillance of maritime pollution and an improved guidance of oil combating operations. In 1983, 1985 and 1988, under the sponsorship of the European Community, a series of international airborne exercises took place in the North Sea (Archimedes Campaigns [1-3]). Different institutions

operated optical and active microwave sensors in parallel to a multitude of microwave radiometers (linescanners and profilers). The general aim of these exercises was to establish specifications for an improved operational sensor package for quantitative registration of oil pollution at sea under nearly all-weather conditions.

In 1989, the German Ministry of Traffic decided, to realize a new maritime surveillance system on board a modern Do228 aircraft [4]. In addition to improved sensors utilized up to this time in the first generation aircraft, the new system will include newly developed sensors, a Laser Fluorosensor and a multiple frequency microwave radiometer which allow a more thorough analysis of oil spills. This includes a quantification of the spilled volume over a range covering small discharges up to accidental events, and the classification of oil types.

II. The New Radiometer

A. Requirements

The Archimedes exercises offered a unique chance to study radiometer outputs in the 5GHz to 90GHz range for different types of oil and oilwater emulsions of varying thickness (up to several millimeter) during a variety of realistic environmental conditions. A series of findings resulted which, together with some operational restraints are now forming the basis for the development of the new radiometer. In detail, basic requirements for a radiometer of second generation are:

- simultaneous measurements at several frequencies to avoid ambiguity problems during the determination of layer thickness and, above all, the oil volume; an error of volume estimation smaller than 50% is tolerated,
- selection of frequency bands with reference to possible interferences due to man-made noise and registration of oil layer thickness in the 50µm to 3mm range,
- simultaneous registration of the sky radiation at least at the highest frequency band which is the most sensitive one with respect to variation of weather conditions,

- a scan angle as large as possible to realize wide scan widths,
- a spatial resolution as high as possible under the proviso of the maximum tolerable dimensions for the radiometer package (length:88cm, width:50cm),
- consideration of typical flight altitudes of 300m to 1000m and aircraft velocities near 70m/s.

B. Frequency Ranges

All requirements, listed above, have been considered during the development of the new radiometer. The construction of the linescanner was achieved with a compact configuration that realizes simultaneous imaging at 18.7, 36.5 and 89GHz. The frequency bands selected are reserved for passive measurements. During the Archimedes campaigns, measurements at 17GHz regularly resulted in the best volume estimations for thicker layers. A frequency around 35GHz seems to be the best compromise with respect to geometrical resolution and bad weather capability. 90GHz images are highly resolved and comparable in quality to IR images (Fig. 1). A sensitivity down to a layer thickness of 50 μ m exists. Oil-in-water emulsions and white caps (false alarm) can be determined qualitatively well in this frequency range.

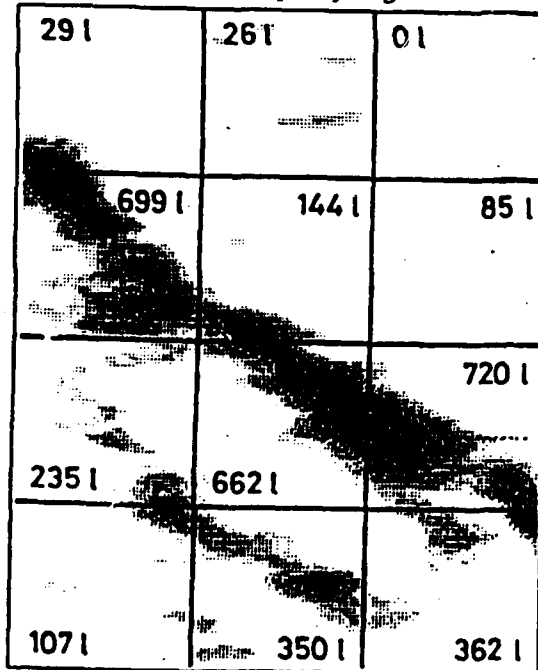


Fig. 1. Example for the representation of passive microwave oil spill measurements. Oil slick taken at 90GHz during night time together with volume estimations (liter); altitude 4000 ft, scan width 440 m, maximum variation of brightness temperature 21 K.

In general, for optimum data evaluation, the sky radiation which influences the linescanner output should also be constantly mapped with a separate system in all frequency bands. But for simplification and cost reduction only one further 89GHz radiometer with a fixed sector-horn antenna has been designed for the sky radiation measurement. Its output delivers a mean-value of the relevant sky radiation which is the optimum basis for numerical estimation of the corresponding values at 36.5 and 18.7 GHz. The errors resulting from that procedure are expected to be smaller than 50%.

C. The Scanning Principle

Scanning happens with the aid of two parabolic mirrors installed in a continuously rotating cylinder (Fig.2). Beyond both front sides of the cylinder, identical three-channel-receivers are placed which are coupled to the parabolic mirrors via plane reflectors and through holes at the front sides. This scanning principle should be particularly advantageous with respect to operational use. It avoids oscillating movements of the main reflectors, rotational switches and guarantees redundancy in the case of a failure of receiver channels. Further it supports a simple method for continuous calibration. A swath width of 476m is achieved for an altitude of 308m (1000ft).

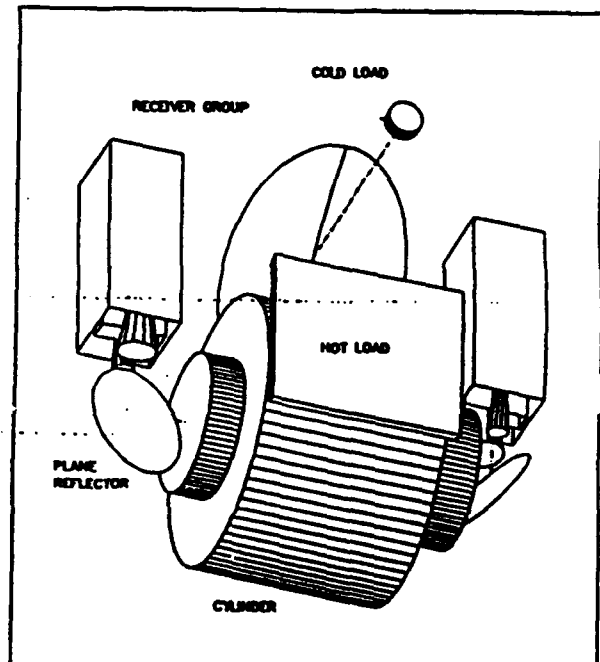


Fig. 2. Perspective representation of the MWR configuration developed. Two parabolic reflectors in a rotating cylinder and two receiver groups realize two scanlines per revolution. Thermal hot/cold sources are used for a continuous calibration.

D. The Calibration Principle

The calibration of the radiometer output signals is done by using a hot load at ambient temperature and a peltier-cooled cold load. The hot load consists of a sheet of absorbing material that is mounted on the inner wall of the radiometer main rack. As the effective area of the cold load is much smaller, a further mirror is used for focussing the beams of the rotating antennas onto the cold load. During each revolution of the cylinder a complete series of hot/cold measurements for all frequency channels is accomplished.

A cross sectional view of the cold load is shown in Fig. 3. The absorber is cooled by a 3-stage Peltier element that has a power consumption of 45W, this results in a temperature difference of 51K with reference to the case temperature. The core of the cooled absorber is made of aluminum in order to get a nearly constant temperature distribution up to the tips of the pyramids. The surface is covered with a layer of absorbing material. The reflecting inner wall of the load case has a conical shape resulting in an increased effective area of the cold load. This is important for the 18GHz channels which have the largest beam waist that is also somewhat off axis. The space between the inner wall of the case and the cold load is filled with small balls of expanded polystyrene in order to prevent convection of the surrounding air and condensation of water. The overall efficiency of the cold load has been determined with an external cold load consisting of a large sheet of absorbing material cooled with liquid nitrogen.

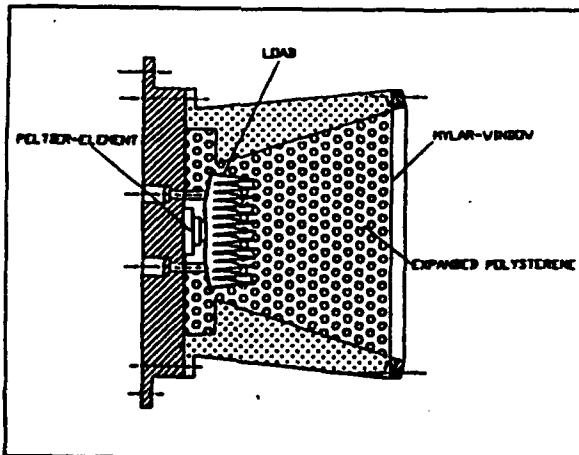


Fig. 3. Principal configuration of the cold load.

The sky-radiometer is calibrated by the same principle. However here we are using waveguide ferrite switches to switch the radiometer input to the loads. The cold load consists of a waveguide absorber that is also cooled by a 3-stage Peltier element.

E. Receiver Front- and Back-End Characteristics

To realize optimum radiometric resolution total power and heterodyne principles are applied to all channels. Balanced mixers are used throughout. They show the lowest noise figures which are, presently, obtainable with commercial devices at room temperature. The receiver housings shown in Fig.2 only contain the single front-end modules which can be simply removed like a drawer for better access during repair. The adjustment of a single radiometer channel for calibration happens by the use of a variable offset amplifier which is placed in a separate back-end housing. Low pass filtering and A/D conversion follow after low frequency amplification.

The whole radiometer system is completely computer controlled. Not only calibration is done automatically but also a system configuration on the basis of a priority list (after switching on the radiometer). Further, during the measurements, a numerical correction of the antenna beam squint angles which result from the displacement of the feedhorns is realized. Digital processing, in addition, allows a continuous observation of the operational conditions of the system by monitoring and storing data such as the physical temperatures of the housings and calibration loads, the noise figures of the front-ends, and the gain and offset voltages of the variable amplifiers. Finally, in the case of oil spill measurements, layer-thickness and volume is directly processed from the received signals.

Different spatial resolutions are obtained for the single frequency bands by optimum utilization of the antenna apertures especially at 89GHz. However an identical resolution which would be important for an automatic unambiguous estimation of the volume, could be achieved numerically.

In table 1, the most important radiometer characteristics are listed.

III. First Airborne Measurements

After integration and installation into the aircraft, the new system has been flown for the first time in November 1991 in the Oberpfaffenhofen area. A special quick-look system had been developed for image representation, to qualify the radiometer. The first results showed that the concept of the new system works very well and that the resolutions meet the specified values (Fig. 4). On the other hand, a deeper analysis revealed some spurious interferences, among other things, due to local-oscillator radiation in the 18.7 and 36.5GHz ranges. These problems arise from the absence of unilines at the receiver inputs which normally results in higher sensitivities for well adjusted devices. In view of the first measurements above oilpolluted sea that are scheduled for April 1992, additional filtering in the 18.7GHz channels will be a short term solution. It is planned, however, to replace the het-

Tab. 1. Microwave Radiometer Characteristics

| Antennas | | | | |
|----------------------|-------------------------------------|--------------|----------------|-------------|
| Sensor : | linescanner | | sky-radiometer | |
| type : | rotating offset parabolic reflector | | sector horn | |
| angular resolution : | 0.8° / 2.0° / 4.0° | | 8° • 80° | |
| scan-with utilized : | 76° | | . / . | |
| scan-frequency : | 10 revolutions/sec = 20 lines/sec | | . / . | |
| Receiver front-ends | | | | |
| channel | type | center freq. | i.f. | noise temp. |
| 1, 1' | heterodyne DSB | 89.0 GHz | 1-3 GHz | 590 K |
| 2, 2' | heterodyne DSB | 36.5 GHz | 1-5 GHz | 565 K |
| 3, 3' | heterodyne SSB | 18.7 GHz | 6-8 GHz | 550 K |
| sky | heterodyne DSB | 89.0 GHz | 1-1 GHz | 590 K |

erodyne principle by direct receiver principle, at an appropriate time, by using HEMT amplifiers in the 18.7 and 36.5GHz ranges.



Fig. 4. First airborne measurements with the new radiometer. 89GHz (left) and 36.5GHz (right) quick-look representation of a section with different types of vegetation or soils and water surfaces (black colour, storage lake). Demonstration of resolution capability and brightness temperature range awaited for polluted sea surfaces. Spurious interferences by external electronics. Altitude 3000ft.

Acknowledgement

We wish to express our thanks to our industrial partners "Krupp MaK Maschinenbau" and "Wissenschaftlich-technische Beratungen, Dr. Hoffmann". Development of the Microwave Radiometer is financed by grants from the "Bundesministerium für Technologie", FRG. We thank O. Krause from "DLR Projektträgerschaft Umweltschutztechnik", for his continued support and encouragement.

References

- [1] Gillot, R.H., Toselli, F., "The Archimedes 1 Experiment", Commission of the European Communities, Series: Environment and Quality of Life. EUR 10216 EN, 228 pp. Luxembourg 1985.
- [2] Gillot, R.H., "The Archimedes 2 Experiment", Commission of the European Communities, Series: Environment and Quality of Life. EUR 11249 EN, 238 pp. Luxembourg 1987.
- [3] Bekkering, J.A., "The Archimedes 2A Experiment", Commission of the European Communities, Series: Environment and Quality of Life. EUR 12674 EN, 83 pp. Luxembourg 1990.
- [4] Grüner, K., Reuter, R., Smid, H., "A New Sensor System for Airborne Measurements of Maritime Pollution and of Hydrographic Parameters", GeoJournal 24.1 pp 103-117, 1991 (May), Kluwer Academic Publishers.

MMIC TECHNOLOGY FOR COMMUNICATION SYSTEMS

M. Aikawa

NTT • Japan

MMIC Technology for Communication Systems

MMICs are potentially very suited to high frequency bands (microwave band to millimeter-wave band), due to

- (1) mass productivity with high repeatability and excellent accuracy in the fabrication process,

and

April 22, 1992

Masayoshi Aikawa, Nobuyuki Imai

NTT Radio Communication Systems Laboratories
1-2355 Yodogawa-5-ch, Kanagawa, 223-003 Japan

TECHNICAL PROBLEMS IN APPLYING MMICs TO COMMUNICATION SYSTEMS

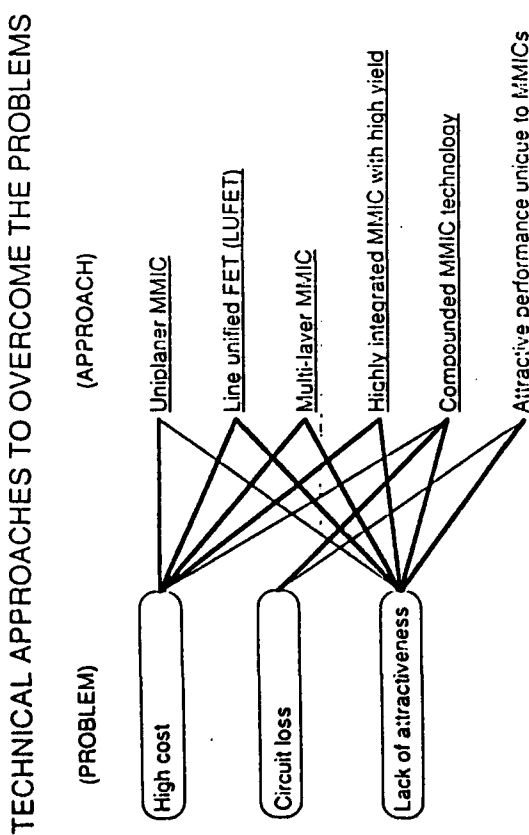
OUTLINE

1. Problems in Applying MMICs to Communication Systems
2. MMIC Technology for Low Cost
3. Technology for Overcoming Disadvantages and Increasing Attractiveness of MMICs
4. MMICs Applications in Radio Communication Systems
 - Digital Microwave Radio
 - Subscriber Radio
5. Conclusion

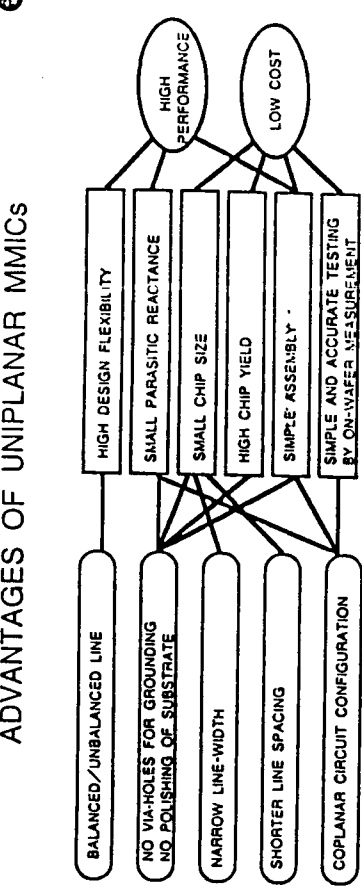
(1) High cost at present
because of the small market size and specialized needs,

(2) Circuit loss
because of the small chip size
⇒ high Q resonator, filter, power efficiency, NF, etc.

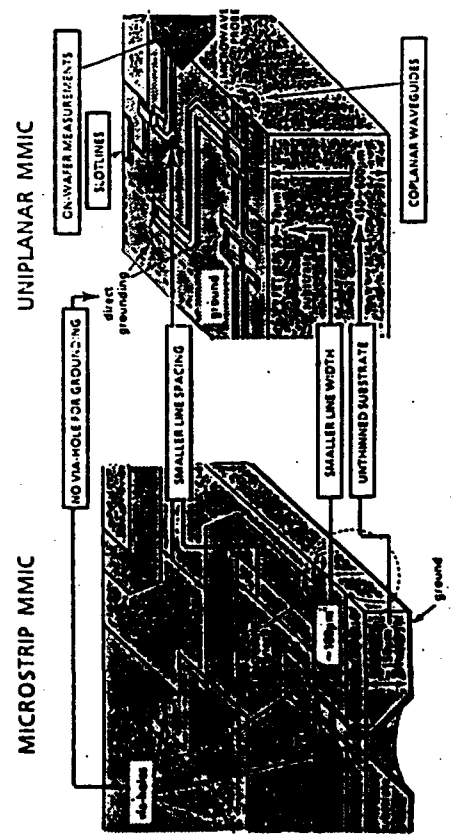
(3) Lack of MMIC attractiveness for systems to which MMICs are applied



TECHNICAL APPROACHES TO OVERCOME THE PROBLEMS

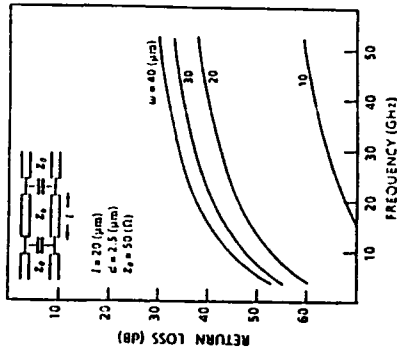


ADVANTAGES OF UNIPLANAR MMICs



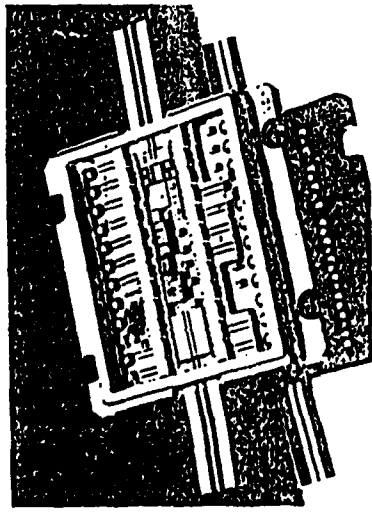
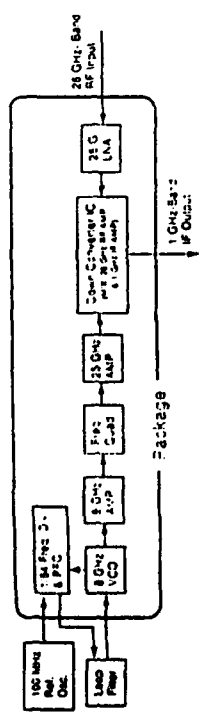
UNIPLANAR MMIC

MICROSTRIP MMIC



Characteristics of Air-Bridge

26 GHz-Band LiMIC RECEIVER MODULE

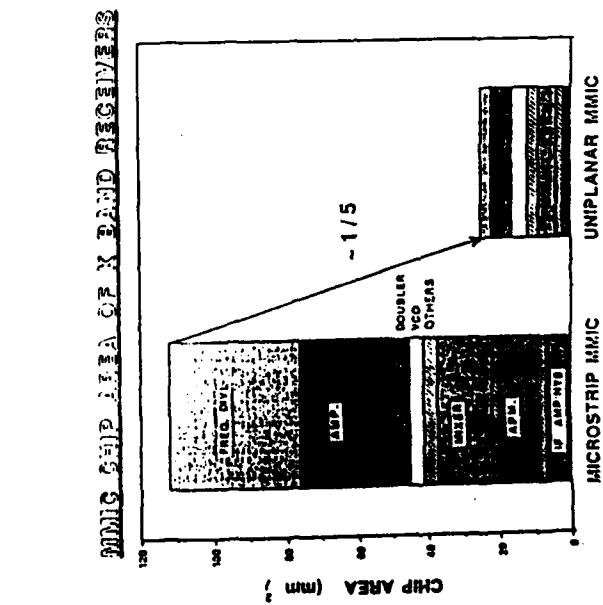
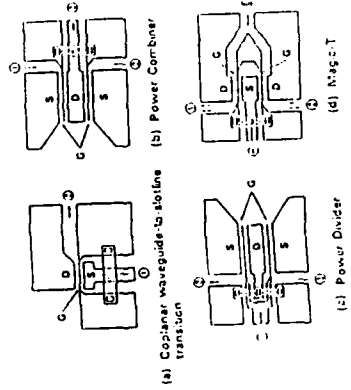


Package size
(except range):
2.500 x 1.750 x 2.500

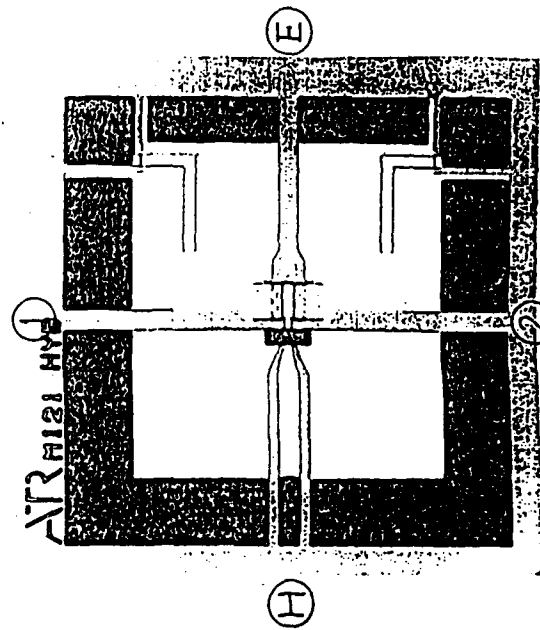
LINE-UNIFIED FET (LUFET)

Features

- (1) Super-compact functional circuits with transistor size,
- (2) Remarkably wide frequency performance.

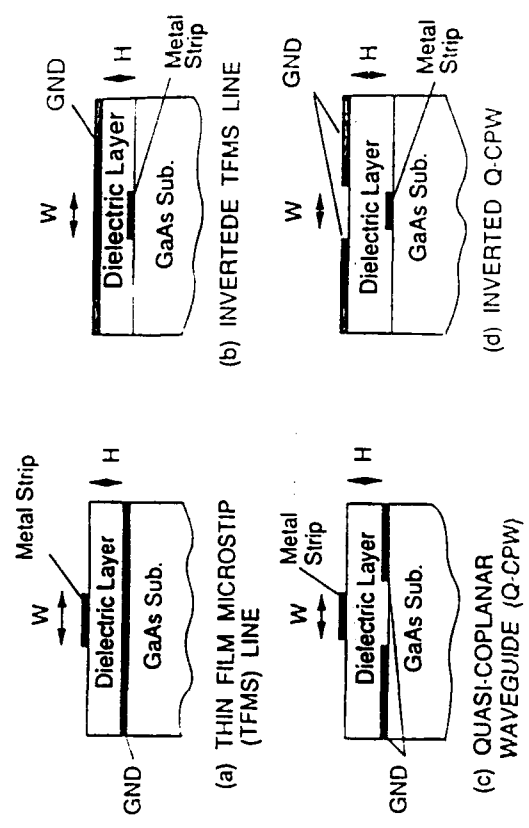
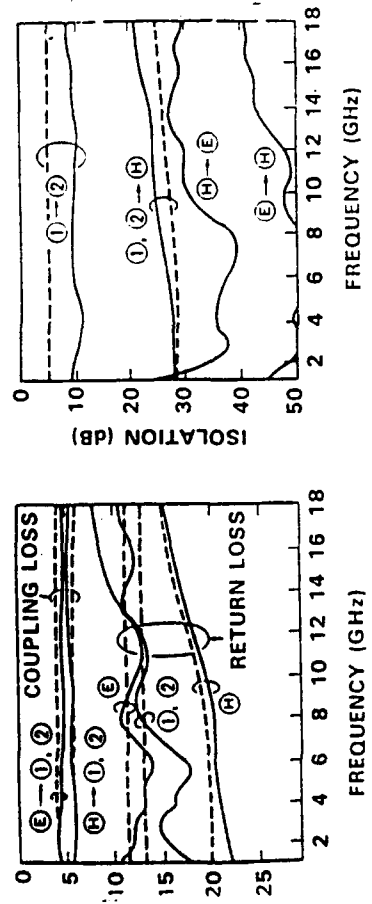


Photograph of Magic T LUFET



MINIATURE TRANSMISSION LINES FABRICATED USING A THIN DIELECTRIC FILM

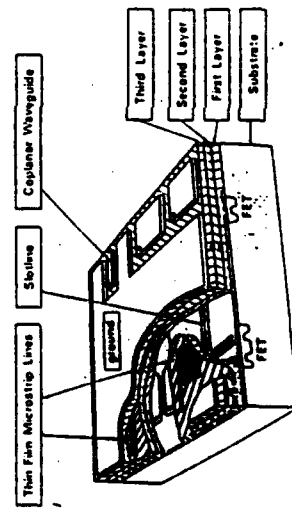
Line-Unified FET MMIC Magic-T Performance



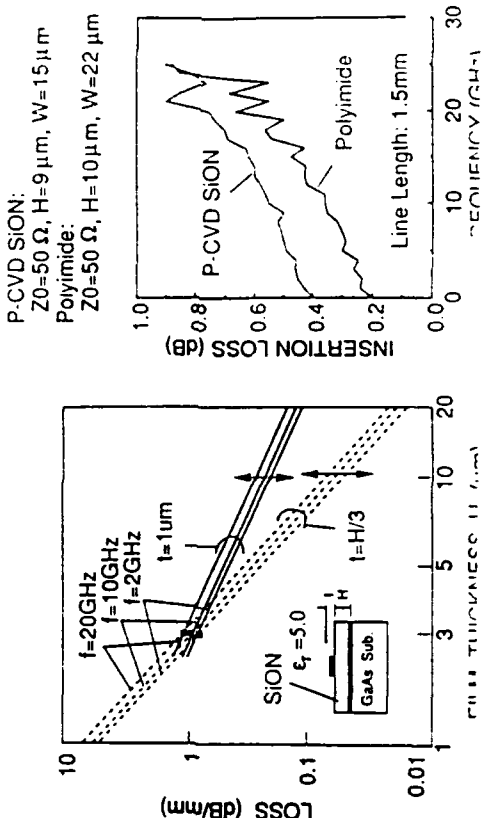
MULTI-LAYER MMIC

Purposes are as follows:

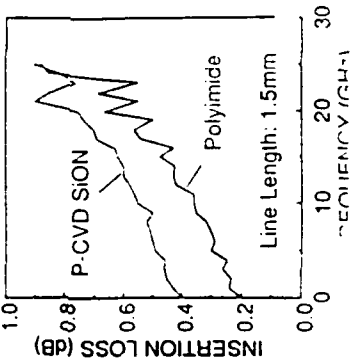
- (1) Substantially reducing MMIC chip size,
- (2) Making high design flexibility for advanced MMICs possible,
- (3) Achieving highly integrated MMICs.



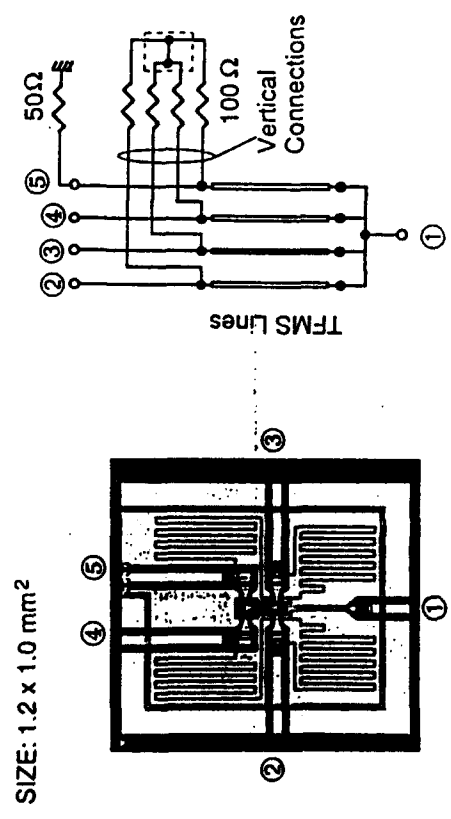
LOSS CHARACTERISTICS OF TFMS LINE



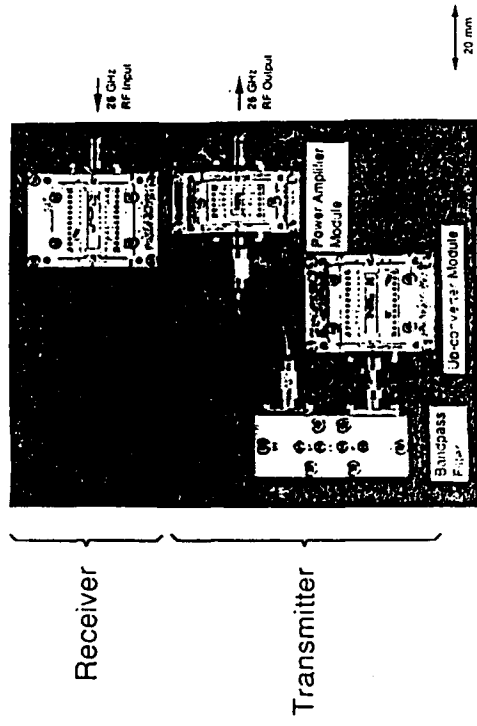
P-CVD SiON:
 $Z_0=50 \Omega$, $H=9 \mu\text{m}$, $W=15 \mu\text{m}$
 Polyimide:
 $Z_0=50 \Omega$, $H=10 \mu\text{m}$, $W=22 \mu\text{m}$



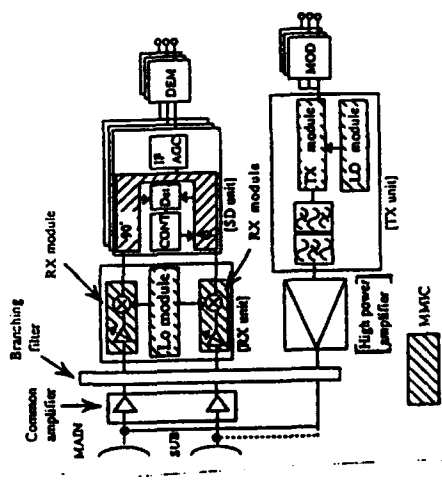
**A 12GHZ, 4-PORT WILKINSON DIVIDER MMIC
USING VERTICAL CONNECTIONS**



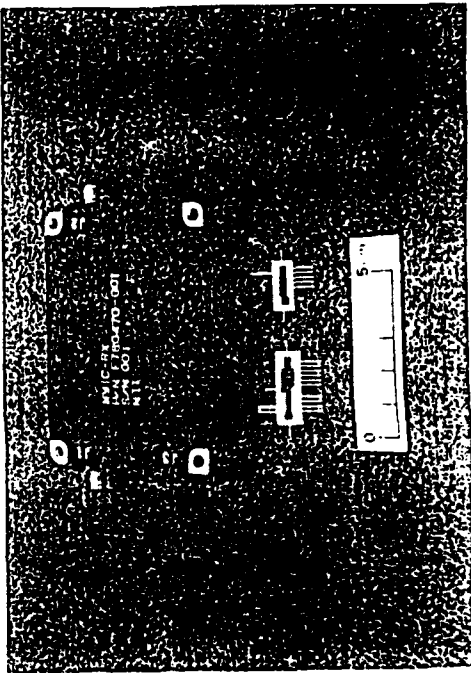
26 GHz-Band Full MMIC T/R Board Model



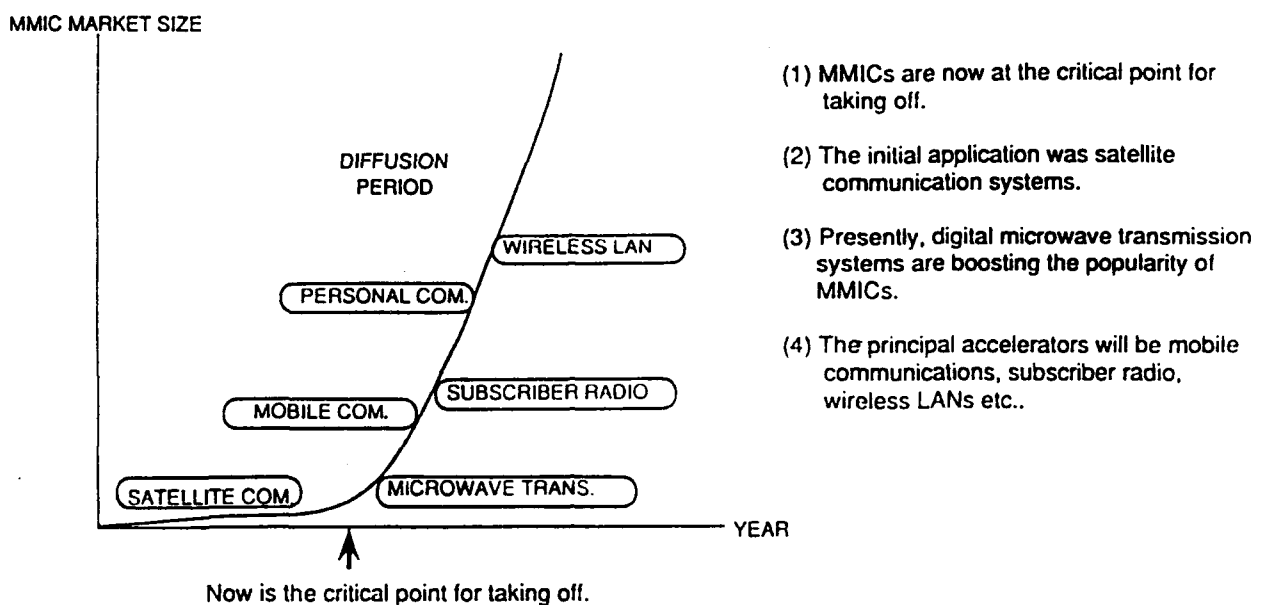
**4/5/6 GHz-Band MMIC Transmitter & Receiver
for 16QAM Digital Microwave System**



30 GHz-Band Full MMIC RECEIVER FOR ETSE-VI



Prospects for MMIC Applications in the Communication Field



CONCLUSION

1. Uniplanar MMICs and LUFET MMICs as well as highly-integrated MMICs are remarkably effective for the cost problem, and multi-layer MMICs are also very promising for the next generation.
2. In addition, the uniplanar-, LUFET- and multi-layer MMICs are very suited to high-frequency-band applications.
3. Performances / functions unique to MMICs and Compounded MMIC technology should be studied and developed more eagerly in order to overcome the disadvantages of MMICs, and to promote wider, more active MMIC applications in the communication field.

**NEW INTEGRATED SUBSYSTEMS FOR MILLIMETER -
WAVE APPLICATIONS**

R. Funck

Dassault Electronique • France

NEW INTEGRATED SUBSYSTEMS FOR MILLIMETER-WAVES APPLICATIONS

Ronald FUNCK

Dassault Electronique
55 Quai Marcel Dassault
92214 Saint-Cloud, France

INTRODUCTION

The technology of millimeter wave circuits has been developing for many years and is now available for the realization of complex subsystems to be used in various applications. The classical technologies are waveguide technology, finline or E-plane circuits, microstrip circuits, and are often used jointly in the same subsystem, depending on the performance and cost objectives.

Historically, the first millimeter wave applications have been for military (radars, sensors, seekers) and space (communications) purposes. They have allowed, after the use of waveguide components, the development of planar and quasi-planar hybrid integration technologies (microstrip, finline or E-plane circuits). We can observe that, today, the development of new integrated subsystems using these basic technologies is still continuing, especially civilian, and the search for cost reductions, have favoured the appearance of new principles of integration, among which the most promising are quasiclitical techniques.

Beside the development of hybrid circuits, much work is ongoing in the field of monolithic millimeter wave circuits development. Two types of technologies are concerned : **Monolithic Wave Integrated Circuits (SiMMICs)** and **Si/SiGe Monolithic Millimeter Wave Integrated Circuits (SiMMICs)**, silicon having very interesting properties at such high frequencies.

This paper will first describe the new developments of millimeter wave subsystems for specific applications. After that it will be focussing on more general or multi-applications developments

RADARS AND SENSORS

The integrated subassemblies developed for these applications generally use a combination of waveguide, E-plane and microstrip circuits.

The finline or E-plane technology was one of the most promising hybrid integration techniques and research was being carried out worldwide [1], as this technology had emerged as a front-runner. The finline structure, which is a planar printed circuit enclosed in a waveguide like a spilt-block housing, has relatively low loss, and the conductor patterns are on circuit boards, which can be made reproducible using conventional photolithographic techniques. Entire systems were designed and realized using finline technology. We will describe some recent developments made at **Telefunken System Technik** of Ulm, Germany [2,3,4].

The block diagram of a polarization agile 94 GHz monopulse radar front-end for interrupted FMCW operation with 600 MHz bandwidth [2] is given in fig. 1. The transmitter part of the radar front-end is formed by a 500 mW pulsed IMPATT oscillator, which is injection synchronized by bias tuned CW Gunn oscillator. A high isolation SPST switch with 60 dB isolation and 1.6 dB insertion loss is inserted between Gunn and IMPATT oscillators in order to ensure maximum receiver sensitivity during pulse intervals. Transmit-receive switching is carried out by E-plane circulators, integrated in common housings with finline balanced receiver mixers and IF amplifiers. The technology used for the design of the front-end is a combination of E-plane and integrated waveguide milled block technology, enabling straight forward design and manufacturing of integrated subsystems in the frequency range 30-150 GHz. The front-end overall design and its separation into modules suitable for easy production and testing is shown in fig. 2. The global front-end performances are : 270 mW output power, 4 dB receiver conversion gain.

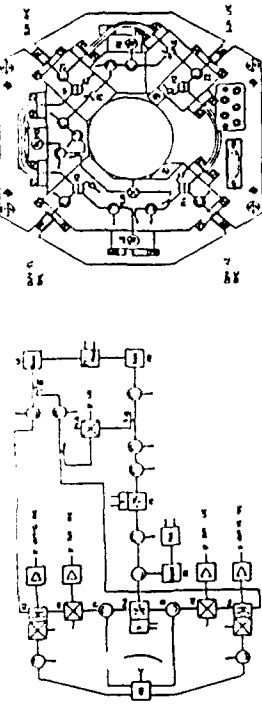


Fig. 1: Block diagram of a polarization agile 94 GHz monopulse radar front-end [2].

The integrated milled block technology has been used for the design of an active passive sensor front-end in the 90 GHz range [4]. This combined radar/radiometer sensor, the block-diagram of which is given in fig. 3 and its photography in fig. 4, has been developed for a low cost application. The Gunn oscillator provides transmitting power (30 mW) as well as local oscillator power for the mixer. The received signal is converted down to video frequency which can, after being amplified, be separated by filtering into radar and radio-tear channels. The entire RF unit is very compact and measures only 20 mm x 20 mm x 23 mm, and has a mass of 16 g. A number of complete subsystems have been successfully tested at accelerations reaching 1500 g.

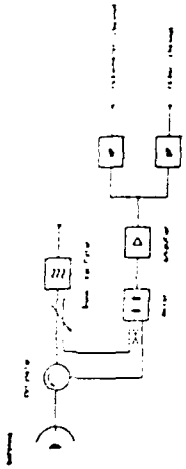


Fig. 2: Block diagram of a 94 GHz monopulse radar front-end [1].

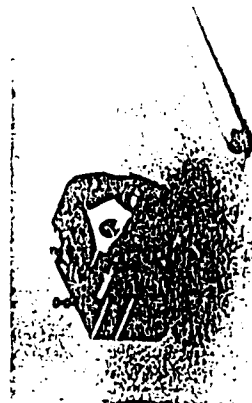
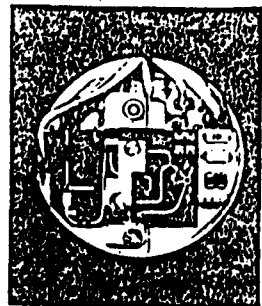


Fig. 3: Block diagram of an active-passive sensor [4].

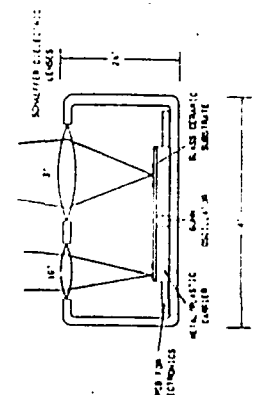
These sensors were originally developed for military purposes. Today they are under consideration for automotive radar applications, due to their potential low cost. Microstrip technology has been used by GEC, U.K. for the production of millimeter wave circuits for more than 10 years. Its development progressed upward in frequency, with 35 GHz components

being developed in the mid-1970's and 84 GHz components in the 1980's. This technology uses hard substrates such as single crystal quartz or glass ceramics, which allows the insertion of ferrie patches for iso-circulators and provide compact, rugged assemblies.

The Fig. 5 gives an example of a 32-bit integrated SiGe HBT- SiO_2 transceiver using this microstrip technology [6], which has been designed specifically for an anti-armour sensor requirement. The transceiver is realised in a volume of 1 cubic inch. A single quartz-microstrip circuit contains all the millimetre wave components, except the VCO, which is in a waveguide cavity. The transmit power is approximately +8 dBm, and the system overall noise figure is less than 16 dB.

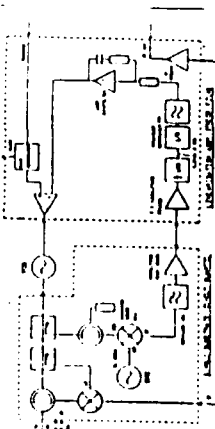


卷之三



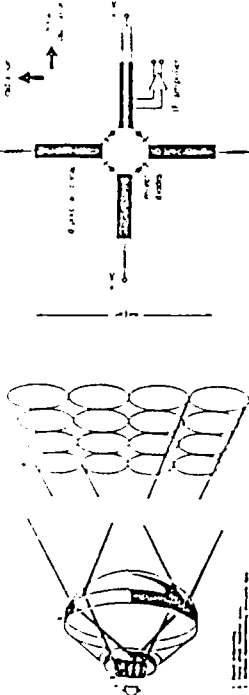
thin film microstrip circuit. A quasi optical concept is used for the antenna : patch antennas on the microstrip circuit are used to illuminate a dielectric lens. By illuminating the lens from diffraction foci, a beam steering effect can be achieved. The dielectric lens forms an hemispherical beam that can be produced as part of the housing.

A very interesting concept has been described by the RSRE UK [5]. This paper describes a steerable, multi-beam, local-plane array technology and radar development which has resulted from research into lens-fed microwave and millimeter wave receivers with integral antennas. The key components are a high permittivity dielectric lens and a local-plane array of receivers in intimate contact with the lens (Fig. 8). The lens generates a multiplicity of simultaneously narrow beams, each with its own direction of look, covering between them the local field of view. Each beam is focussed to a unique position on the lens local-plane. Combining this with an array of receivers in the focal-plane creates an array of high gain receivers which collectively stare across a wide field of view with no moving parts and without separate beam forming circuitry. Each receiver is built round a crossed-dipole antenna in which one dipole receives the signal and the other the local oscillator. This provides a convenient means to drive a quad quadrature mixer (Fig. 9). Receiver noise figures of dipole coupled mixers replicated on a single glass ferrite substrate have been realized at 3.5 GHz, 4.4 GHz and the silicon array and 5.5 hybrid arrays on thin-film have been realized. Typical noise figure characteristics of the type were measured to be 8.5 dB including 2.0 dB IF noise. A 25 GHz wideband radar demodulator has been built incorporating an array of nine 5x5 thick-film receivers. As can be seen, this is a good example of a system combining different technological concepts - microwave circuits on silicon and quasi-optical techniques.



FCC: 5000 designations (1970-1980) 33

The same technology has been used to design a millimeter wave system for cruise control on automobiles [7]. This system is operating at 77 GHz and comprises an FMCW radar realized in thin film microstrip technology and a switched beam quasi optical antenna. Active cruise control enables the driver to engage cruise control when travelling at a "driver determined" set distance behind a vehicle. As the selected vehicle speeds up or slows down, your vehicle tracks this change by accelerating or decelerating. A proposed structure of the control unit is given in fig. 6. The system (fig. 7) is a basic FMCW radar based on a varactor tuned waveguide Gunn oscillator using the radial flat geometry with extraction of the second harmonic (31 mV output power, 1 GHz tuning range, -85 dBc/Hz phase noise at 100 kHz of carrier). The received signal is mixed with the oscillator sampled with a 10 dB coupler to additive LO power. A further sampling coupler is used in a FIM feedback loop which is used to linearize the ramped output of the oscillator. The 77 GHz output signal is downconverted in the 850 - 1150 MHz range with a subharmonic mixer driven by a 14 GHz DRO and applied to a 10 MHz frequency discriminator through a 1/100 frequency divider. All the microwave components are located on a single



COMMUNICATIONS

and for satellite communicators. The technologies which are used are on the same type as previously described.

T.S.T. has designed a 2 W solid state transmitter for short range data communication at 80 GHz. It is composed of 3 stages of amplification. The first uses a reflection type Gunn diode [12] followed by the second an injection locked Gunn diode oscillator [13] and the third, an injection locked Gunn diode oscillator [14] to give a total power of 2 W.

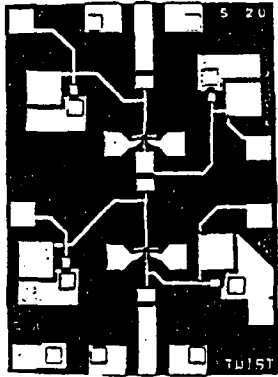


Fig. 13 : 30 GHz MMIC Amplifier [19]

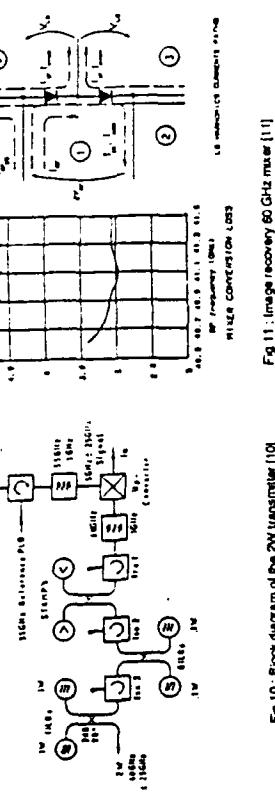


Fig. 10 : Block diagram of the 2W transverter [10]

The European AIMS/ESPRIT programme, led by Thomson-CSF, France, addresses components up to subsystems level for applications between 20 and 30 GHz. System parts are from short-hop land links and ultra-small aperture satellite terminals (USAAT). A range of generic MMICs are being developed, covering switches, VCOs, solid-state amplifiers. Apart from the T/R switch, which makes use of MESFETs, all other circuits are based on the use of heterojunction transistors, HEMT, P-HEMT, HBT. These activities will be briefly described in a next paragraph. Within this project, Thomson-CSF/TCM is developing a 27.5-30 GHz synthesiser. The fig. 12 and 13 represent respectively the microwave part of the synthesiser and the 30 GHz MMIC amplifier chip. The main performances are : 10 dBm output power, less than -70 dBc/Hz phase noise at 100 kHz off carrier, and 27 MHz frequency steps. The subassembly consists in cascaded buffer, frequency divider, buffer, VCO, power divider, frequency multiplier, amplifier. At this step, the functionality has been proven with conventional thin-film hybrid technology to interconnect individual MMIC chips. Later on, compact versions will be designed together with comparing improvements gained from advanced MMIC technology.

GaAs IMPATT oscillator (12 W). The block-diagram of this amplifier is given in fig. 10. The breadboard has been realized in waveguide technology.

The work done by Siemens Telecommunications in Italy [11] concerns commercial inter-orbit and inter-satellite communication applications. In this sense, advanced studies are in progress in order to evaluate a possible experimental mission of a 50/84 GHz communication payload. Their work demonstrates that resistive mixers present a reliable and performing solution for mm-wave low noise mixers. The mixer which has been realized uses a cross-bar configuration which allows a clear separation of the various LO sidebands and harmonics, as well as image recovery. Tests have been made at 40 GHz with a 4 GHz IF. Insertion loss is about 3.2 dB in 1 GHz bandwidth (fig. 11), showing clearly the performance improvement due to image frequency recovery. It is expected that at 65 GHz, the conversion loss would be 3.7 dB.

AUTOMOTIVE APPLICATIONS

Many programs related to automotive applications are now under study in Europe. In particular, there are European projects like DRIVE and EUREKA. The main applications are : automatics debiting systems, Doppler speedometers, vehicle-vehicle and vehicle-road communications, obstacle detection. These programs could lead to large microwave applications if two conditions are satisfied : low cost technology compatible with mass production, low size and low weight design to fulfill the implementation requirements.

The search for low cost and low volume at millimeter wave frequencies may force the engineer to simplify components and to combine functions whenever possible. The use of MMICs could be appropriate, but these components doesn't solve the problem of circuit integration.

Rather than scaling low frequency techniques to shorter wavelengths, a completely new approach is often needed. Quasi-optical components provide a solution to this problem. An example of realization of a radar sensor for automobile cruise control, directly derived from radar developments, has been described above [7]. T.S.T. Germany, has developed a very simple radar sensor for traffic data acquisition system, named AVES [12]. This system obtains specific traffic information from appropriate Doppler frequency. The chosen frequency of operation, 61.5 GHz, offers several advantages : the band is available for this application in Europe (ISM-band, Industrial, Scientific and Medical). Due to the high frequency, small antenna dimensions allow good focussing, short range application and economic reuse of frequencies due to high atmospheric absorption. The sensor is relatively small (150x150x150 mm³), and can be mounted on existing sign posts and bridges. The schematic set up of the mm-wave front end is presented in figure 14. Hybrid integration was implemented, combining fringing and waveguide to reduce cost ; this unit is composed of a cavity second-harmonic type Gunn oscillator, a waveguide filter and a finline mixer. Vehicle speed, vehicle length and the distance between vehicles is obtained by the AVES sensor. A future application of this type of sensor can be seen in vehicle-roadsida communications

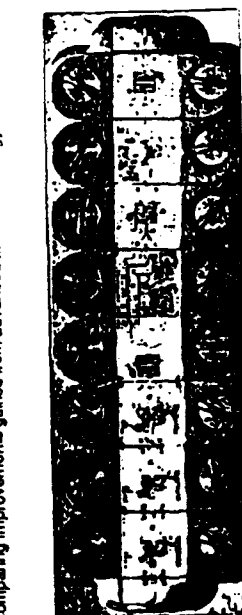


Fig. 12 : 30 GHz synthesizer for AIMS

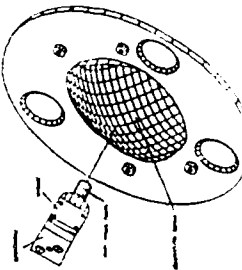


Fig. 14 : The AVES system [11]

A first example of the quasi-optical approach is given by the design of ALDER from the RSRE [9].

The University of Lille, France, presents an other circuit approach based on a quasi-optical planar integration [13] which suppresses the physical connections between junctions, the transfer of energy being achieved either by electromagnetic radiation or by electromagnetic coupling. This allows the realization of low cost active antennas which can be coupled to Fresnel lenses to fulfill the various directivity requirements. The concept of this antenna is given in fig. 15. The transmitter is composed of a circular patch fed by two terminal devices (Gunn or IMPATT diode) in a TM_{11} radiating mode. The insertion location of the diode is chosen to optimize its matching. Electronic frequency tuning is provided by a varactor which is implemented inside the circular patch cavity, the value of the coupling depending on the distance from the disc center. The receiver is realized by the means of a Schottky diode mixer integrated on the patch. The principle is to isolate a strip following the TM_{11} mode current lines, the receiver diode being connected in series on this strip. The concept has been demonstrated at X-band. Some modifications have been implemented for mm-wave applications, in order to increase the size of the antenna to allow the use of packaged Gunn or IMPATT diodes. This is achieved by coupling a TM_{11} circular patch antenna to a TM_{12} annular patch antenna by means of a circular slot antenna as illustrated in fig. 16. In addition, simple electronic beam forming can be obtained by proper perturbation of the electromagnetic fields : scanning of the beam can be achieved at $4/10^\circ$. Two anticolision radar prototypes have been developed : a pulsed 60 GHz Gunn radar which gave excellent results for a 150 m range, and a 86 GHz FM-CW IMPATT radar which exhibited lower sensitivity due to the IMPATT diode noise.

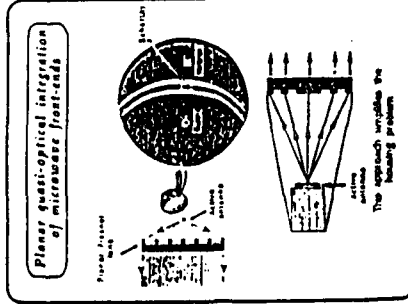


Fig. 15. [13]

QUASI-OPTICAL

Quasi-optical techniques can also be used as an elegant way to improve the power handling by coupling many devices distributed over a surface several wavelengths in dimensions [14]. This technique is referred to as quasi-optical array or grid technique. This technique can be applied to oscillators, multipliers, phase shifters and mixers. The LEST, France [15].

Theoretical modeling of grid power combiners is being made by the LEST, France [15]. Quasi-optical techniques are also well adapted to the realization of filters. The LEST is studying planar grating-reflector antennas [16] on a theoretical point of view. Dicroic filtering structures are being realized for radionavigation applications by MATRA ESPACE, France [17]. Such structures are transparent or reflective depending on the wavelength of the incident electromagnetic wave. A dicroic

triplexer using resonant grid structures etched on a fused silica substrate has been realized demonstrating very low loss : insertion loss at 90 and 157 GHz is 0.2 and 0.3 dB, reflection loss at 183 GHz is 0.2 dB. A different approach is used by the Institut National de Télécommunications and the Observatoire de Meudon, France, to be used for Météosat satellite [18]. The dicroic triplexer are realized by using perforated screens. The performances obtained are : 0.54 dB insertion loss at 183 GHz, 0.05 and 0.11 dB reflection loss at 150 GHz and 110 GHz respectively.

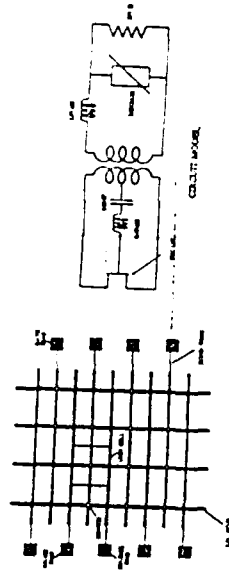


Fig. 17. Planar grid oscillator

MONOLITHIC INTEGRATION

Two technologies are used for the realization of monolithic integrated circuits and subsystems : Microwave Monolithic Integrated Circuits on GaAs (MMICs) and Silicon Monolithic Millimeter Wave Integrated Circuits (SMMWICs).

MMICs

Three ESPRIT programs are concerned with MMICs developments for mm-wave applications. AIMS addresses components and subsystems for applications between 20 and 30 GHz. The fig. 13 shows a 22-40 GHz amplifier from Thomson, which is used in the synthesizer described above. The gain is 15 dB, noise figure 14 dB and size 1.5 mm². This amplifier uses a 0.25 μ m pseudomorphic noise technology [19]. The same laboratory has designed a 60 GHz LNA having a 12 dB gain and a 5 dB noise figure.

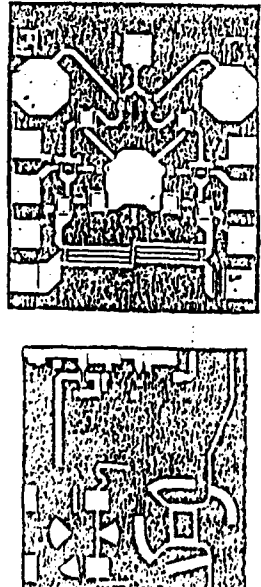
MONOFAST is focussed at 44 GHz. The overall aim of this project is to integrate unfamiliar technologies and new design tools into a high proven methodology for high frequency MMICs. An MMIC LNA at 44 GHz based on sub-micron MESFET, and coplanar waveguide technology is being simulated by Alcatel Espace, France [20] : a gain of 15 dB and a noise figure less than 4 dB have been simulated.

GIANTS is concerned with the development of InGaAs based transistors where one of the aims is to demonstrate a low noise MMIC amplifier at 60 GHz.

Philips Microwave Linel, France, has developed several mm-wave MMICs using a pseudomorphic HEMT technology [21, 22]. A push-push oscillator using a 0.5 μ m HEMT has been realized demonstrating a -3 dBm output power and a phase noise of -75 dBc/Hz at 1 MHz off carrier at 52 GHz. An image rejection mixer (fig. 18) designed in the 52-60 GHz frequency range and using a 0.25 μ m HEMT has a typical conversion loss of 14 dB and an image rejection higher than 30 dB for a 2-4 GHz IF frequency range.

In Germany, Telefunken System Technik is also engaged in an important mm-wave MMICs development program [23, 24, 25]. Using the integration of MESFET devices (f_{max} = 90 GHz), and Schottky diodes (f₁ = 2300 GHz) on the same chip, mixers working at 35 GHz and 60 GHz have been realized. The 35 GHz mixer, integrating a 2-stage IF amplifier, has a 6 dB conversion gain with a 9 dB DSB noise figure. The 60 GHz receiver chip has a 2-stage IF amplifier : the conversion gain of this chip is 12.5 dB with an associated DSB noise figure of 9.5 dB. The fig. 19 represents the 60 GHz receiver chip with a chip size of 3x3.5 mm². The mixer itself consists of a Lange-coupler feeding two Schottky

diodes and LO and signal band structures in the chip. The diodes have a finger width of 0.3 μ m. The low noise IF amplifiers and MESFETs with a gate length of 0.75 μ m. First, carrier accumulations have been made using a P-EMIT technology which has proven to be superior to all other available monolithic technologies for both advanced low noise and power circuits in the mm-wave frequency range. Carrier-mixing HBTs with a F_{1dB} of 200 GHz have been developed and fabricated using these devices. A 2-stage low noise amplifier has been fabricated having a gain of 5 dB at 5.3 GHz.



卷之三

SILVANICS

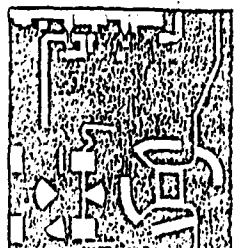
This arrangement of wave system has been tested on high intensity station (5000 C-meters) is dominated by convection currents around 40°C. On the other hand, when stations are in the integration of two thermal currents such as heat islands, Sutro and ECE cities, provides, therefore, silicon is also a good material for the design of mobile integrated circuit in the millimeter wave range.

In reviewing the progress made in the last years in multihop wireless networking, we have seen that the search for low cost and large volume quantities for commercial applications such as communications, basic control, collision avoidance, etc., has favored the emergence of raw principles of integration in parallel with the development of more complex and complete multihop wireless architectures, which have been improved and pushed by mainly research first, and now available for commercial applications.

CONCLUSION

Planar millimeter wave silicon detector circuits have been realized by the same laboratory [27]. Schottky barrier diodes have been monolithically integrated with planar antenna structures on high resistivity silicon. The Schottky barrier diodes were fabricated by MEC [28]. Low series resistance (≤ 5 ohms), low Miller capacitance (≤ 1.1 pF) and cut-off frequency up to 1 GHz have been achieved. The figure 21 gives the layout of two types of receiver which have been realized with the two antenna structure. Detection efficiencies of 4.9 mV/mV \cdot Hz without bias, and of 50 mV/mV \cdot Hz with 200 mV bias, have been achieved at 4 GHz.

diodes and LO and signal band switchable IF output. The diodes have a finger width of 0.3 μm . The low noise IF amplifier employs two MESFETs with a gate length of 0.75 μm . Further developments have been made using a PHEMT technology which has proven to be superior to all other available monolithic technologies for both advanced low noise and power circuits in the mm-wave frequency range. Quarter-micron HEMTs with a finger of 200 nm have been developed and fabricated using



卷之三

卷之三

Range [MHz] Frequency [GHz] Frequency [GHz] Frequency [GHz]

[1] D. A. WILHELM, "Time-Wave Correlations and Subsystems," *IEEE Trans. Veh. Technol.*, p. 2

[2] J. T. TECHELOGY, "IEEE Trans. Aerospace & Electronic Propagation," Vol. 41, No. 7, 733-774, May 1992

[3] P. L. WILBERDGE, "Low-Cost 91 GHz FMCW Radar for Precision Range Measurements," *IEEE Trans. Microwaves*, Vol. 42, pp. 1311-1319

[4] P. L. WILBERDGE, "A Reaserach Clock Cost-UMatter Wave Course," *Cent. Scientific Automobile Applications*, Private comm.

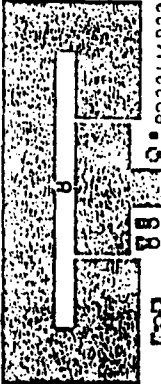
[5] B. M. R. NICHOLLS, "A Numerical Sensor for Stand-off Weapons," *Memory Measurements*, Vol. 20, pp. 167-175

[6] J. C. ALBER, et al., "Microwave and Millimeter-Wave Standing Acousto-Technique," *1991 IEEE WIT-S Digest*, pp. 1243-1252

[7] C. H. BARTH and M. R. KIRK, "A 2 W SSB Side Transmitter for Short-Range Data Communication," *IEEE Trans. Consumer Electronics*, Vol. 39, No. 1, pp. 931-933

[8] J. M. HOPKINS and G. CARPENTER, "DO-160C Draft Compendium," *Software Configuration Management*, European Network, 9, Com. 92, pp. 145-150

[9] W. STAMMLER, et al., "High-Wave Sensors for Traffic Data Acquisition System," *Proc. Int. Conference on Recent Advances in Mechatronics*, 1992, pp. 101-104



ECONOMIC INTEGRATION IN THE EEC 23

- [13] P.A.ROLLAND, *et al.*, "Quasi optical Technology for MM-Wave Car Electronics", *Workshop 21st EuMC 91*
- [14] E.KOLLBERG, "New Solid State Devices and Circuits For Millimeter Wave Applications", *European Microwave Conf. 1991*, pp.36-54
- [15] A.TCHAMENI, "Surfaces sélectives en fréquence", *Journées d'études sur les composants millimétriques, Carry-le Rouet (France)*, pp.57-60
- [16] H.CAM, "Addition de puissance en ondes millimétriques", *Journées d'études sur les composants millimétriques, Carry-le Rouet (France)*, pp.65-68
- [17] J.M.GOUTOULE, "Dichroïque millimétrique à grande incidence réalisé en photogravure", *Journées d'études sur les composants millimétriques, Carry-le Rouet (France)*, pp.69
- [18] C.LETROU, "Conception de filtres dichroïques pour le millimétrique et le submillimétrique", *Journées d'études sur les composants millimétriques, Carry-le Rouet (France)*, pp.84-87
- [19] P.BOURNE, "Amplificateurs faible bruit à 35 et 60 GHz", *Journées d'études sur les composants millimétriques, Carry-le Rouet (France)*, pp. 39-42
- [20] C.TRONCHE, "Fonctions millimétriques à 30 GHz, 44 GHz, et 90 GHz pour applications spatiales", *Journées d'études sur les composants millimétriques, Carry-le Rouet (France)*, pp.1-16
- [21] P.GAMAND, "L'intégration monolithique dans le domaine millimétrique", *Journées d'études sur les composants millimétriques, Carry-le Rouet (France)*, pp.43-46
- [22] P.GAMAND, "Développement des MMICs en gamme millimétrique", *2èmes Journées d'étude Micro-ondes et Espace, Toulouse, France*, Jan 1992, pp.153-156
- [23] B.ADELSECK, A.CLOQUHOUN, "MMIC Receiver Modules for Frequencies up to 100 GHz", *Military Microwave 90*, pp.305-310
- [24] B.ADELSECK, *et al.*, "Monolithic 60 GHz Amplifier using Low Noise pseudomorphic HEMTs", *European Microwave Conf. 1991*, pp.341-345
- [25] B.HUDER, *et al.*, "Recent MMIC Developments and Concepts Leading to Advanced Microwave and Millimeter Wave Phased Array Antennas", *ESA Workshop on Advanced Beamforming Networks for Space Applications*, nov.91
- [26] J.BUECHLER, *et al.*, "Coplanar Monolithic Silicon IMPATT Transmitter", *European Microwave Conf. 1991*, pp.352-356
- [27] K.M.STROHM, *et al.*, "Planar 100 GHz Silicon Doctor Circuits", *ESSDERC'91*, Lausanne, sept. 1991.

**NEW MILLIMETER - WAVE DEVICES REALIZATION
AND PERFORMANCE**

D. Pons

Thomson - CSF LCR • France

**FIELD - EFFECT TRANSISTORS FOR THE MILLIMETER -
WAVE RANGE: PHYSICAL ANALYSIS, MODELING AND
EXPECTED PERFORMANCE**

G. Salmer

Université de Lille • France

jean
lamb

FIELD EFFECT TRANSISTORS FOR THE MILLIMETER WAVE RANGE

Physical Analysis - Modelling and Expected Performance

G. SALMER

I.E.M.N. - U.M.R. CNRS 9929

Département Hyperfréquences
et Semiconducteurs
Université des Sciences et Techniques de Lille
Villeneuve d'Ascq - France.

With the help of
- E. CONSTANT
- Y. CROSNIER
- A. CAPPY
- R. FAUQUEMBERGUE
- P. BOURREL

C.H.S.

jean
lamb

OUTLINE

• PHYSICAL DEVICE MODELS

• LOW NOISE DEVICES

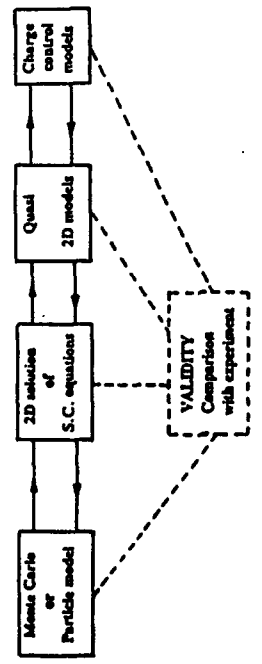
- Noise simulation
- MESFETs
- MODFETs on GaAs Substrate
- MODFETs on InP Substrate
- Discussion

• POWER DEVICES

- Power requirements
- Breakdown phenomena
- Power FETs.

C.H.S.

PHYSICAL MODELLING OF F.E.T.: METHODOLOGY



C.H.S.

MONTE CARLO OR PARTICLE MODELS

Principle

The stochastic motion of the carriers is studied simultaneously:

• in the $3Dk$ space: for each time step Δt , are considered

- the effect of the electric field: $\vec{a} = \frac{q}{m} \vec{E} A$
- the effect of scattering mechanisms.

• in the $2D r$ space: that gives the two dimensional description of

- electric fields
- carrier concentrations
- carrier velocities

from which can be deduced

- external currents and voltages
- equivalent circuits

Remark: other possibilities: Direct solution of the Boltzmann transport equation.

C.H.S.

MONTE CARLO OR PARTICLE MODELS

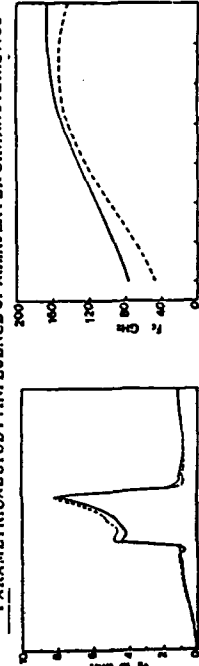
- **Advantages:**
 - S.C. Equations automatically solved
 - All physical effects can be included
 - transport properties
 - Determination of all device properties.
- **Requirements:**
 - Accurate description of energy band diagram
 - Knowledge of various scattering mechanisms
 - Transport properties unknown for several ternary or quaternary compounds
 - Introduction of quantum effects
- **Problems:**
 - Bad knowledge of several effects: screening, ionization
 - Transport properties unknown for several ternary or quaternary compounds
 - Introduction of quantum effects
- **Drawback:**
 - Very long computational time
 - Powerful computers
 - Difficult to study dynamic regimes.

C.H.S.

MONTE CARLO SIMULATION

OF A AlInAs/GaInAs MODFET:

PARAMETRICAL STUDY: INFLUENCE OF AlInAs LAYER CHARACTERISTICS



Longitudinal velocity
AlInAs layer:

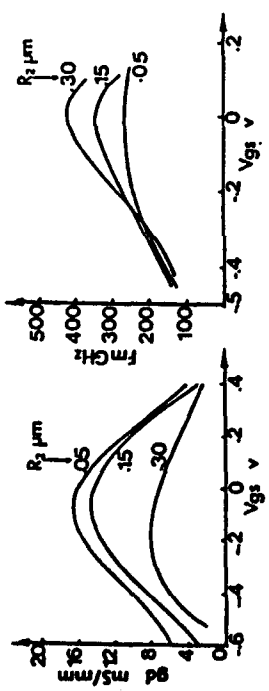
- $a = 410\text{ \AA}$ —
- $a = 210\text{ \AA}$ - - -

Internal cut-off frequency:

from Bourrel and Faquembergue, 1991

C.H.S.

lem
INFLUENCE OF GATE TO DRAIN
CAP LAYER SPACING R_2



Output Conductance
for $L_g = 0.3 \mu$ $R_1 = 0.05 \mu\text{m}$

Following Shawki and Salmer (1990)

lem

QUASI TWO DIMENSIONAL MODELS: ONE DIMENSIONAL SOLUTION
OF SEMICONDUCTOR EQUATIONS

• Main assumptions:

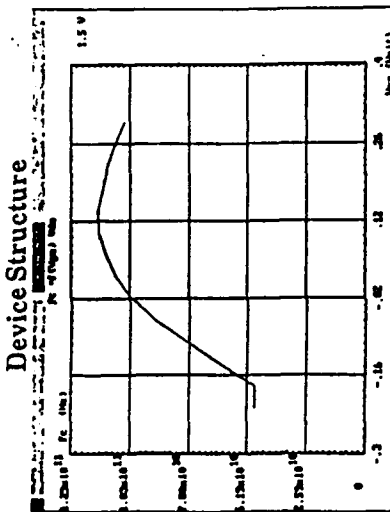
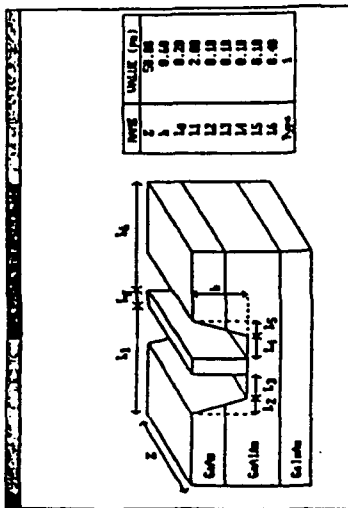
- Equipotential lines perpendicular to the source to drain axis
→ one dimensional treatment
- Depletion regions are fully depleted.

• Main advantages:

- Computational effort is strongly reduced
- Main physical effects can be account for: overshoot, surface, buffer injection, ionization...
- Parametrical studies are easy
- Large signal behaviour and noise properties can be deduced.
- Problems:
 - Difficulty to treat very complicated structures or two dimensional effects
 - Validity for very short gate devices.

lem
EXAMPLE OF QUASI 2D MODEL

HELENA SOFTWARE



Current gain cut-off frequencies predicted

H. Happy, A. Cappy, G. Dambrine, 1991.

C.H.S.

C.H.S.

Two Dimensional Solutions of Semiconductor Equations

Principles:

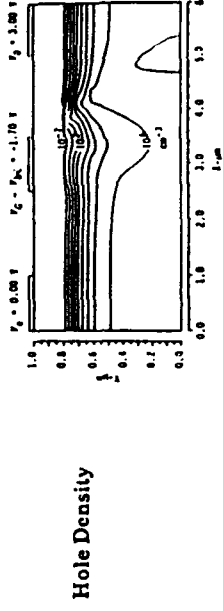
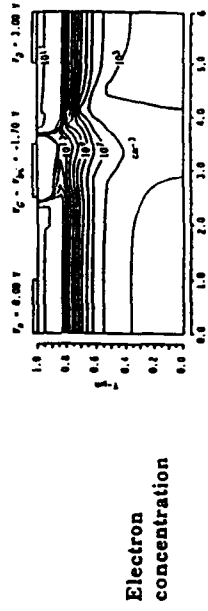
- Two dimensional solution of:
 - Equations deduced from B.T.E.: continuity, momentum relaxation, energy relaxation.
 - Poisson equation
- By taking into account
 - Physical effects and material properties: trapping in the substrate, surface potential, ionization effects
 - Parameter values deduced from Monte Carlo simulation: τ, μ
- Remarks:
 - Various kinds of models corresponding to various degrees of assumptions: single electron gas, drift diffusion models.
 - Possibility to account for quantum effects by partially coupling with Schrödinger equations
 - Finite difference methods are generally used.

C.H.S.

2D Solutions of Semiconductor Equations

Equations - Typical Results:

MESFET SIMULATION



from

Advantages:

- The most complete equations allow to account for non steady state transport phenomena and other physical effects (trapping, surface, ionization...).
- Dynamic characteristics, transient response and microwave performance can be deduced
- Parametrical studies can be made

Problems:

- Validity of semiconductor equations or simplified assumptions (drift diffuses for submicrometer gates)
- Inclusion of quantum effects
- Treatment of Schottky diodes
 - Highly doped regions: mesh dimensions
 - Computation time remains long.

C.H.S.

From Ghione et al, 1990.

C.H.S.

Effect of substrate electron injection
on acceptor deep trap level occupancy.

CHARGE CONTROL AND ANALYTICAL MODELS

- Principle:

- One dimensional solution of equilibrium equations (Schrödinger or current continuity equations) following the transversal direction
- Analytical formulations of drain current such as very simplified one: $J_D = qn_e \langle v \rangle$

- Interest:

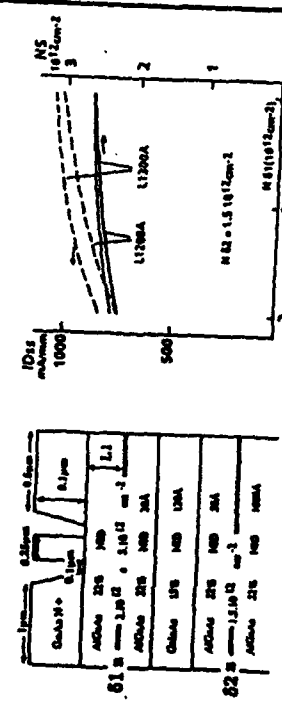
- Usable for first order optimization
- Allows to point out interesting physical dependances
- Needs very small computation times.

- Problem:

- Validity of simplified assumptions : unrealistic values of saturation velocity
- Unable to treat complicated structures.

C.H.S.

APPLICATIONS OF SIMPLIFIED CHARGE CONTROL MODEL: COMPARISONS WITH QUASI 2D MODEL



Considered structure

— Charge control model
- - - Quasi 2D model
From Cressler et al. 1992
ESPAIT MSSAIMS

C.H.S.

LOW NOISE DEVICES

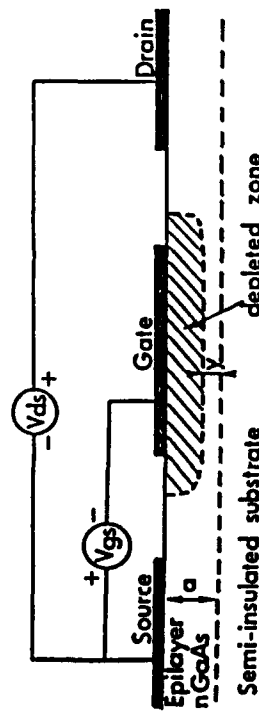
C.H.S.

LOW NOISE DEVICES

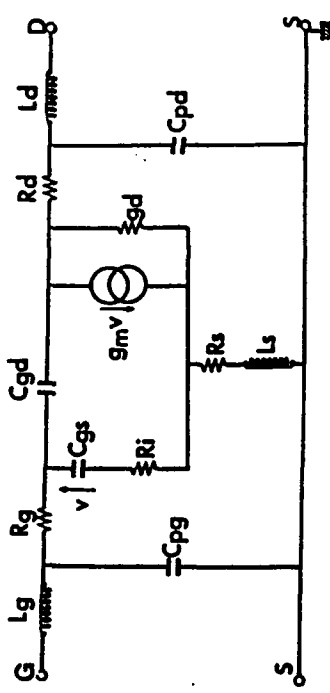
C.H.S.

C.H.S.

GaAs MESFET: Basic principle.



Electrical equivalent circuit.



iemm

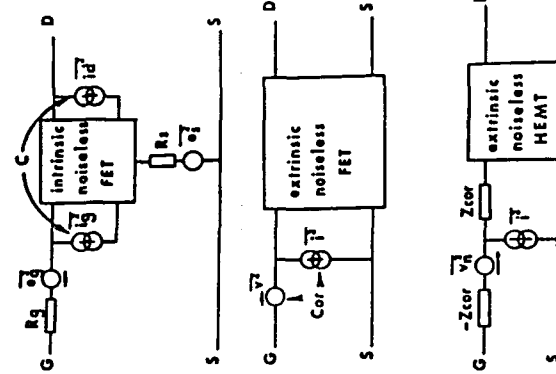
NOISE CALCULATIONS FOR F.E.T.

Noise origins:

- Carriers velocity fluctuations in the channel that induce - drain current fluctuations $\langle i_d \rangle^2$
- gate current fluctuations $\langle i_g \rangle^2$ that are correlated

- Noise in the access resistances R_s and R_g .

Circuit transformations for the noise determination



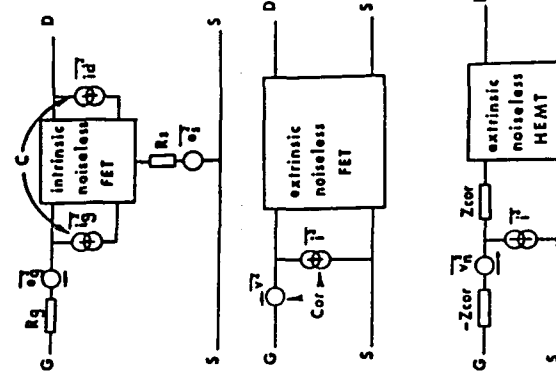
C.H.S.

Noise origins:

- Carriers velocity fluctuations in the channel that induce - drain current fluctuations $\langle i_d \rangle^2$
- gate current fluctuations $\langle i_g \rangle^2$ that are correlated

- Noise in the access resistances R_s and R_g .

Circuit transformations for the noise determination



C.H.S.

ANALYTICAL FORMULATIONS OF NOISE FIGURE following Cappy

When neglecting gate noise $\langle i_g^2 \rangle$:

$$F_{min} = 1 + 2 \sqrt{P} \frac{f}{f_c} \sqrt{g_m (R_s + R_g)}$$

with $P = \frac{\langle i_d^2 \rangle}{4kTg_m A_f}$ close to "Fukui" formula

According to Delagebeaudeuf: $P \# \frac{I_{ds}}{E_c L_g g_m}$

$$F_{min} = 1 + 2 \sqrt{\frac{I_{ds}}{E_c L_g}} \times \frac{f}{f_c} \sqrt{R_s + R_g}$$

Consequences: For improving noise figure

- R_s and R_g must be reduced

$$I_c \# \frac{\langle v \rangle}{2\pi L_g} \quad \text{must be as high as possible.}$$

Remarks:

- 1) The intrinsic noise figure F_{int} (for $R_s + R_g = 0$) remains always close to 1 !!!
- 2) For comparing devices of similar technologies (L_g, R_s, R_g), the quality factor can be the ratio: $r = \frac{I_{ds}}{f_c^2}$

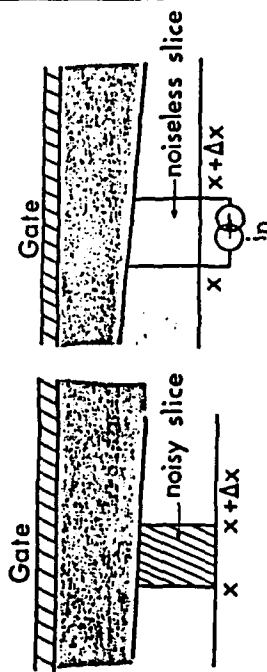
- When taking into account gate noise, more complicated formulae with F_{int} given by

$$F_{int} = 1 + 2 \frac{f}{f_c} \sqrt{PR(1 - C^2)}$$

C.H.S.

CALCULATIONS OF GATE AND DRAIN NOISE SOURCES

- 1) In a quasi 2D scheme, representation of a noisy slice by a noisy source in proportionnal to $n(x) D(x) \Delta f$



- 2) Use of the Impedance Field Method

(Vander Ziel, Shockley, Nougier, Cappy, Wang, Ghione)

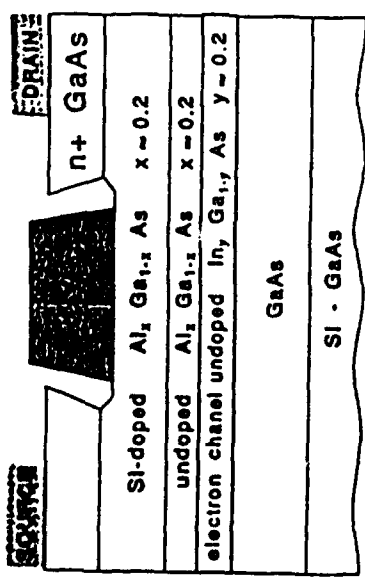
- Calculation of transfer small signal impedances $Z(\omega, x)$ between noise sources in the channel and drain and gate voltages.
- Summation over the whole length of the channel.

Remarks:

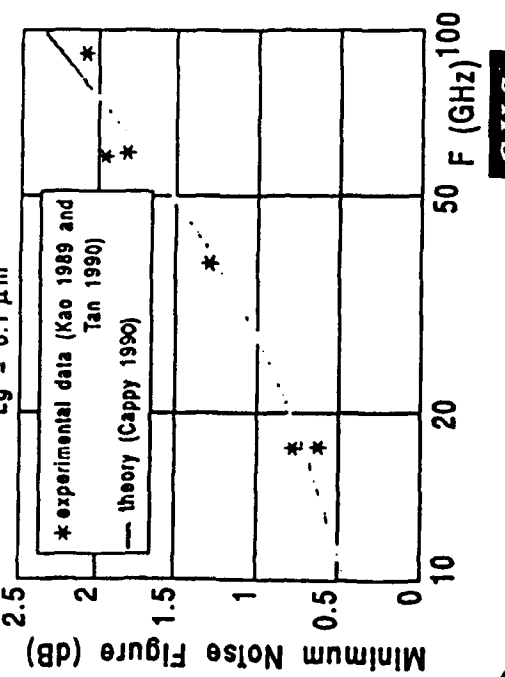
- Interest of taking into account the distributed character of the channel (Cappy et al, 1990)
- Possibility of using a complete two dimensional treatment (Ghione 1990).

C.H.S.

Noise Performance of High Electron Mobility Transistors (HEMT)



Pseudomorphic AlGaAs-InGaAs-GaAs HEMTs

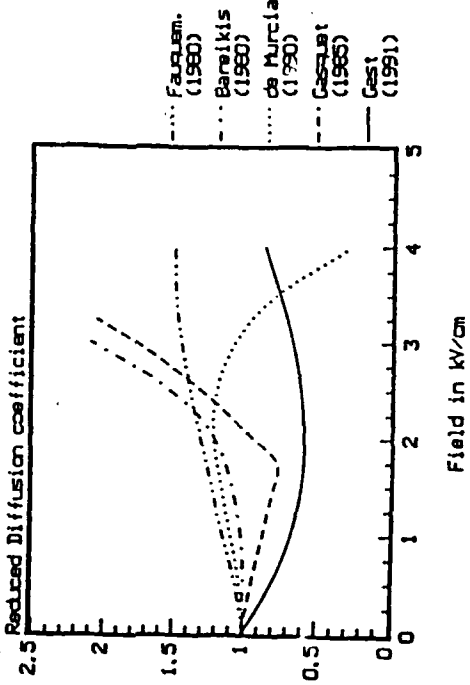


C.H.S.

SEM

NOISE CALCULATIONS : PROBLEMS

- Physical basis : uncorrelation between the noise sources in the channel ? Does it remain valid for very short gate length devices ($L_g \leq 500 \text{ \AA}$) ?
- Values of diffusion coefficient are not well known : for instance in AlGaAs/GaAs heterojunction.



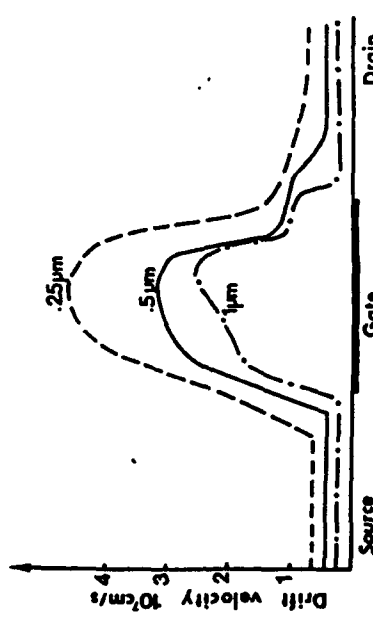
From Zimmerman et al, 1991

C.H.S.

LOW NOISE MESFET'S

Improvement of noise figure

- Intrinsic $f_t = \frac{g_m}{2\pi C_{gs}} \cdot \frac{1}{2\pi L_g}$ must be increased
- Main possibility. A decrease of gate length
- L_g that allows also an increase of $\langle v \rangle$



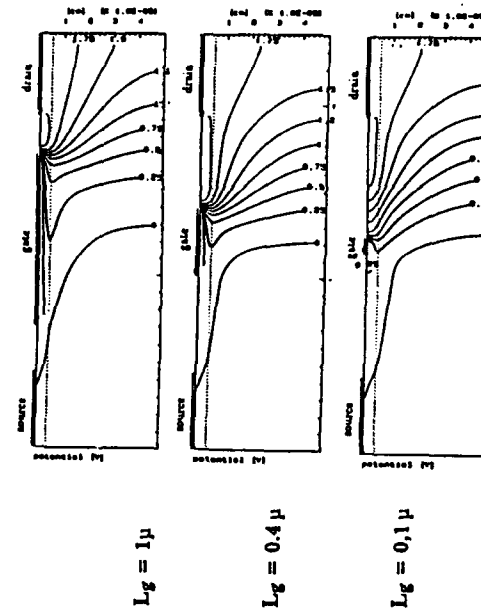
Typical variations of drift velocities in MESFET's for various gate lengths (Carnez et al)

But if the aspect ratio L_g/a is not high enough, short channel effects may cause a degradation of performances:

When L_g decreases g_m may decrease } Gain ↑
 g_d increases } f_t is not improved

C.H.S.

GaAs MESFET INFLUENCE OF THE ASPECT RATIO



Equipotential contours

| L_g μm | L_g/a | g_m mS/mm | g_d mS/mm |
|-------------|---------|----------------|----------------|
| 1 | 19 | 320 | 25 |
| 0.4 | 7.6 | 420 | 45 |
| 0.1 | 1.9 | 380 | 60 |

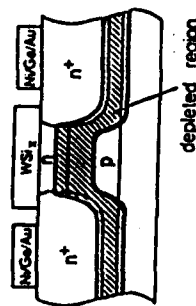
Simulations performed by Makowicz
and Brockerhoff.
(Europ. Trans. on Tel.N° 4 19 90).

C.H.S.

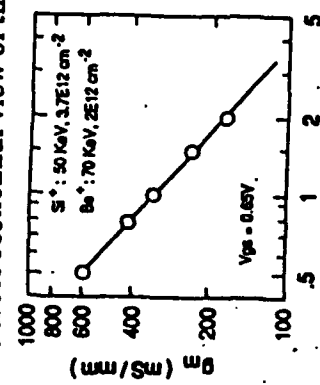
iemm

SUPPRESSION OF SHORT CHANNEL EFFECTS

- Use of a partially depleted layer:



Schematic cross sectionnal view of the MESFET.



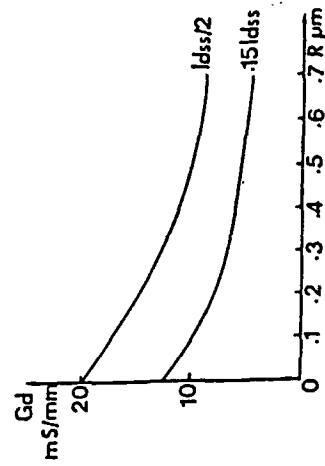
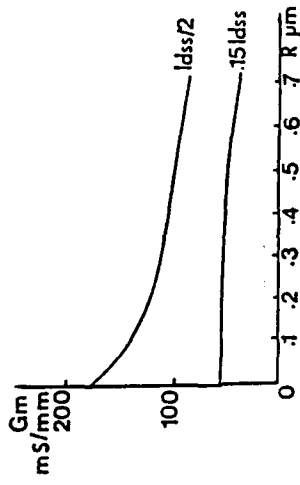
Gate length dependance of g_m .

From Noda et al (IEEE Trans. 1991).

C.H.S.

C.H.S.

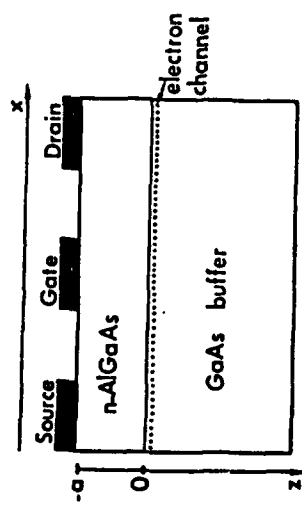
RECESSED GATE GaAs MESFET



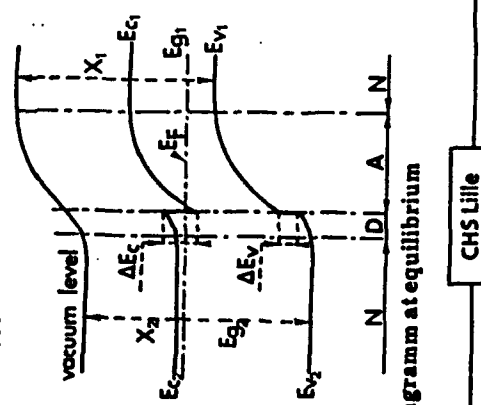
Transconductance and output conductance dependances upon the distance R for a 0,3 μm gate MESFET at $Idss/2$ and $0,15 Idss$

Heliodore et al IEEE Trans. 1988.

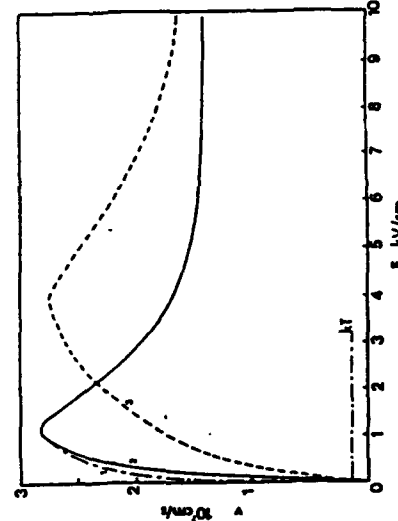
CONVENTIONAL AlGaAs/GaAs MODFETs



• Device Structure



• Band diagram at equilibrium



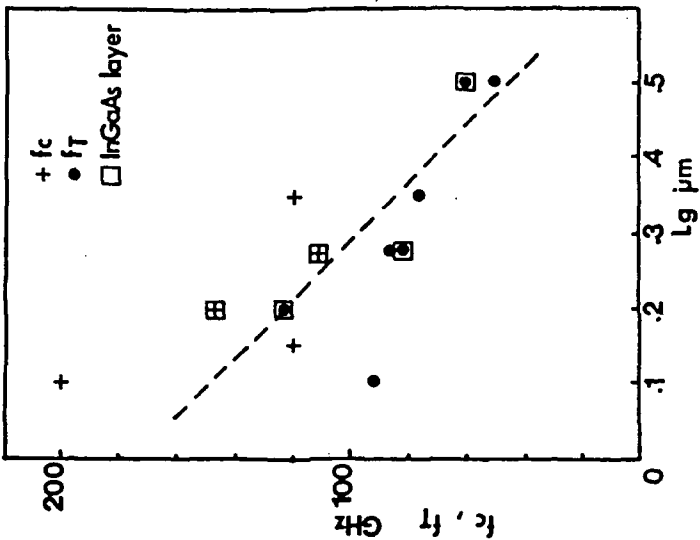
Theoretical velocity field characteristics at 77°K

VERY SHORT GATE LENGTHS MESFET'S

Other possibilities for improving the performance:

- Unsymmetrical recessed gate structures $\frac{g_m}{g_d}$ can be improved by a factor of two
- Use of highly doped (ion implanted) InGaAs unmatched layers (Feng et al)
- Use of very highly doped ($4 \cdot 10^{18}$) thin GaAs layers (150 \AA) in order to maintain a good aspect ratio even for small gate length.
but carriers mobility decreases strongly down to $1000 \text{ cm}^2/\text{Vsec.}$

MESFET's CAPABILITIES: Recent results

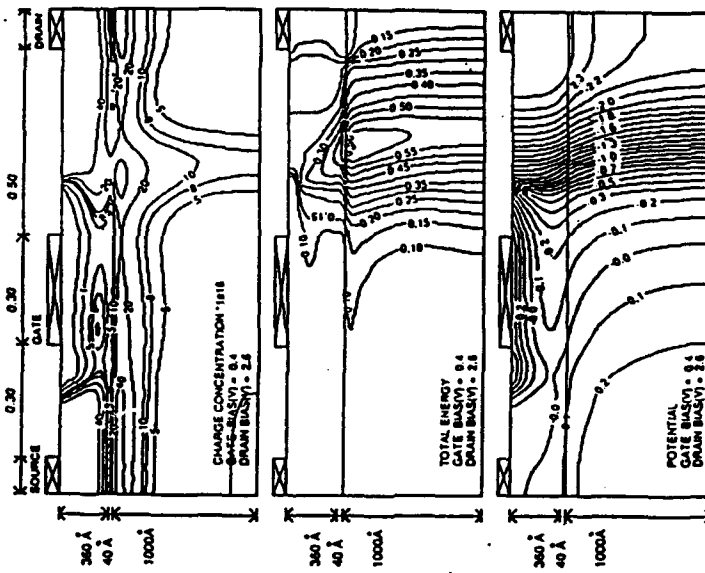


Current gain cut-off frequency
versus gate length.
- 1991 -

C.H.S.

C.H.S.

PHYSICAL BEHAVIOUR OF CONVENTIONAL MODFET's

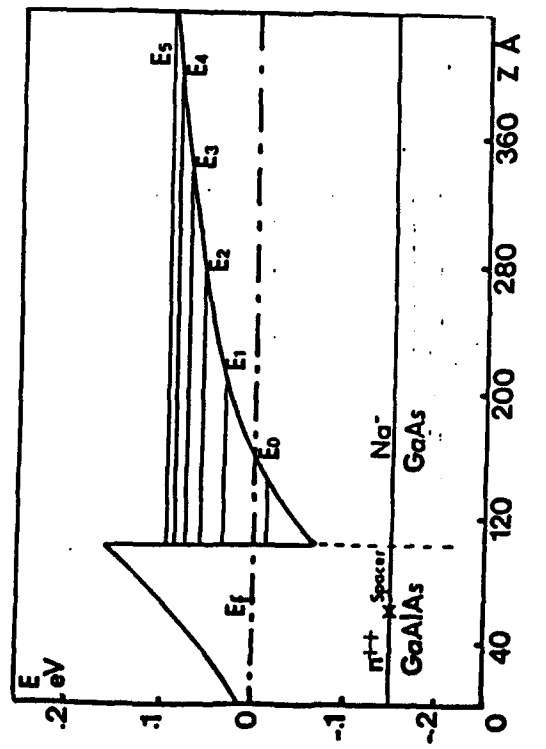


- Equiconcentration. Equipotential contours for a 0.3 μm gate MODFET by taking into account surface effects

(from Shawki and Salmer)

CHS Lille

SUBBAND STRUCTURE IN THE QUANTUM WELL OF A CONVENTIONAL MODFET



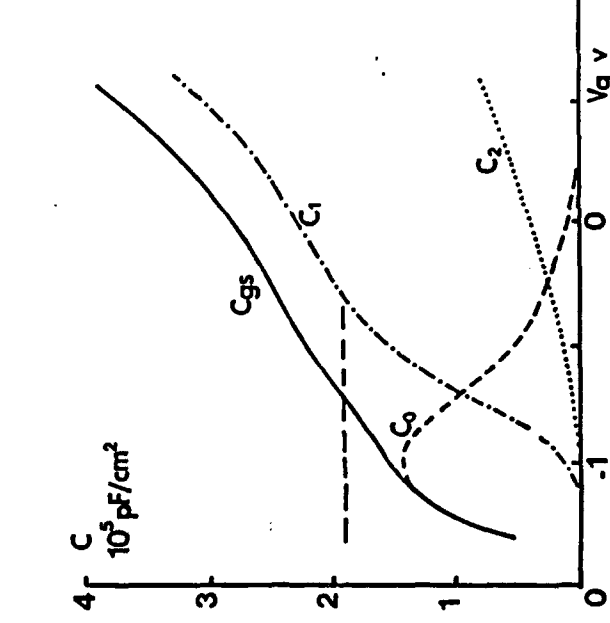
- If space charge reaction is neglected, and well triangular shape is assumed:

$$E_{n\alpha} = \left(\frac{\hbar}{2m} \right)^2 \left(\frac{3}{2} \pi q E_s \right)^{2/3} \left(n + \frac{3}{4} \right)^{2/3}$$

Note that E_s is proportionnal to n_s .

CHS Lille

PARTICULARITIES OF CHARGE CONTROL LAW IN CONVENTIONAL MODFET's

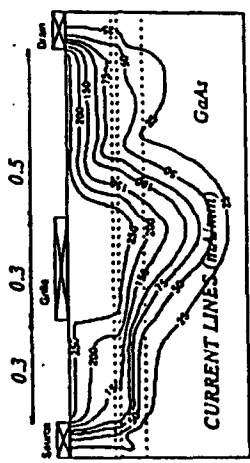


Variations of total capacitance C_g as function of V_g

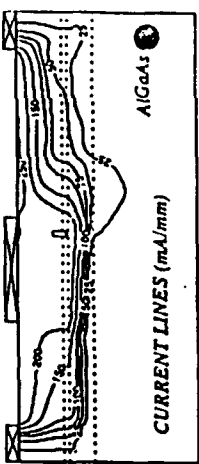
Contributions of electrons C_0 in the well
 C_1 free in AlGaAs
 C_2 trapped in AlGaAs

CHS Lille

USE OF AN AlGaAs BUFFER LAYER



Conventional MODFET



AlGaAs Buffer Layer

Current lines in submicron gate MODFET's

Following Shawki and Salmer (1990)

heim

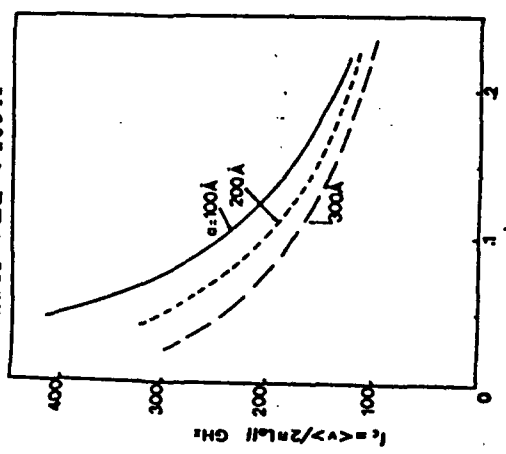
SHORT CHANNEL EFFECTS IN CONVENTIONNAL HEMTS

Following Han and Ferry (1990), it is possible to define an effective gate length

$$L_{eff} = L_g + 2(a + \Delta d)$$

a AlGaAs layer thickness
 Δd equivalent distance of the 2D EG.

$$50 \text{ \AA} < \Delta d < 100 \text{ \AA}$$



First order evaluation of the influence of aspect ratio on intrinsic current gain frequency.

C.H.S.

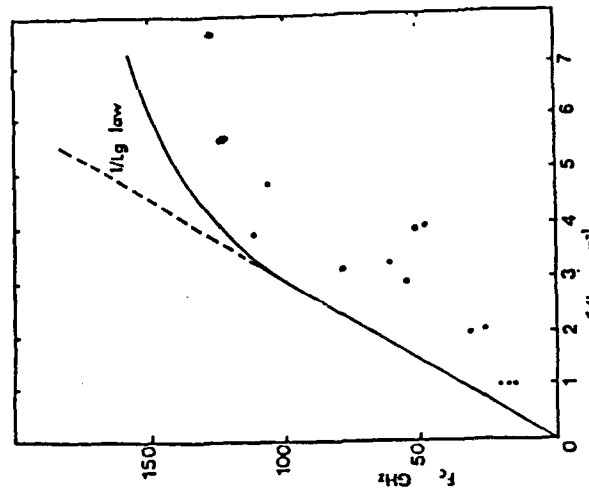
CONVENTIONAL MODFET'S

Main limitations

- Total carrier concentration in the channel:
 $n_s < 1.2 \text{ } 10^{12}/\text{cm}^2$
 $I_{dss} < 250 \text{ mA/mm}$
- Quantum well height: $\Delta E_c < 0.25 \text{ eV}$
- Carrier injection into the buffer layer
→ High values of g_d .
- Threshold voltage variations.
- Parasitic effects under low temperature conditions.

CHS Lille

IMPORTANCE OF THE ASPECT RATIO: L_g/a

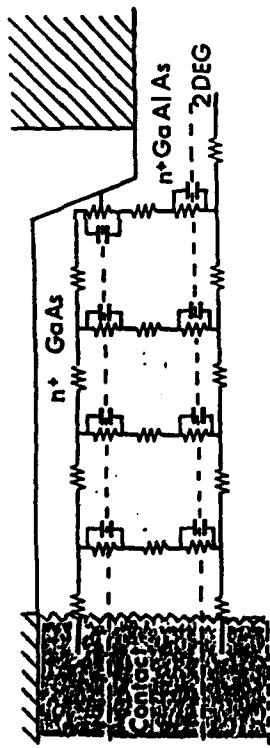


Theoretical intrinsic current gain cut-off frequencies ($f_c = g_m/2\pi C_{gs}$) dependence upon gate length L_g , for a conventional MODFET, the AlGaAs layer thickness a remaining constant ($a = 400 \text{ \AA}$)

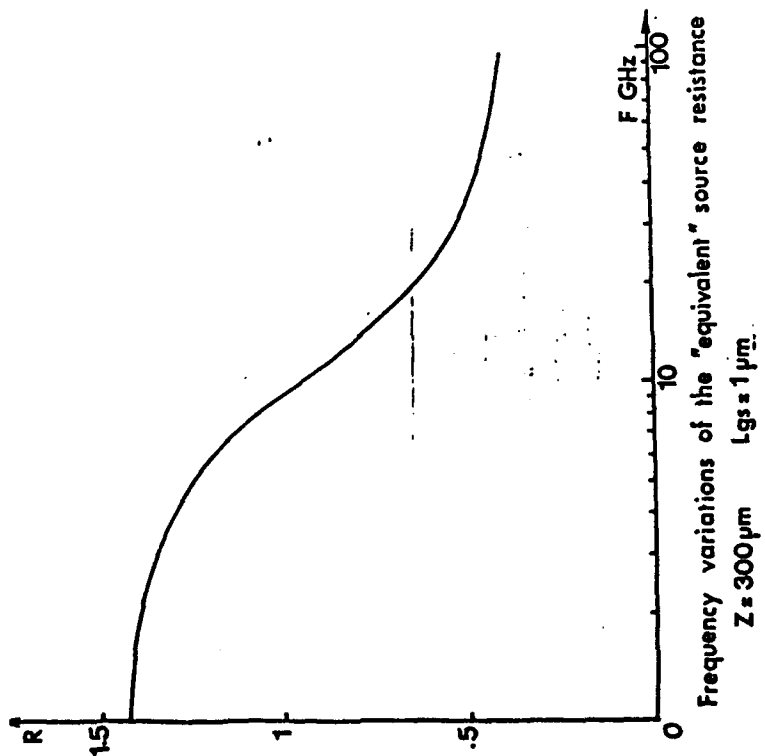
Following Fauquemergue calculations.

- Experimental extrinsic current gain cut-off frequencies.

CHS Lille

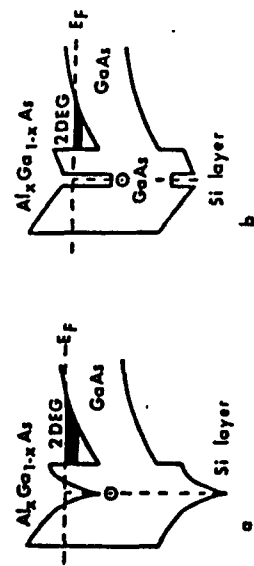


Equivalent scheme of the source access zone.



Frequency variations of the "equivalent" source resistance
 $Z = 3000 \mu\text{m}$ $L_g = 1 \mu\text{m}$

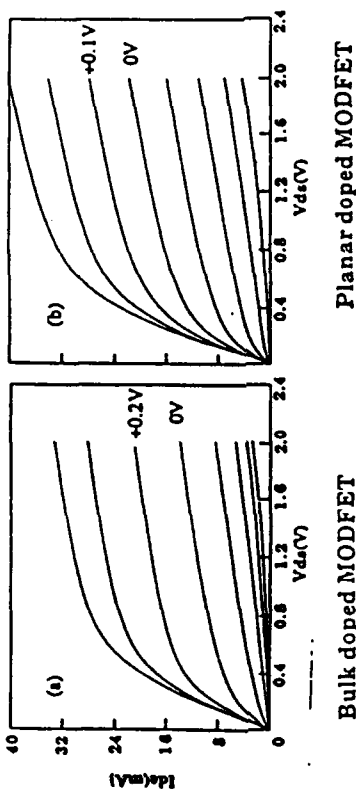
PLANAR DOPED HETEROSTRUCTURES



- Higher carrier concentration: $n_s \approx 1.5 \times 10^{12}$
- Improvement of the ratio L_g/a and then g_m/g_d (gain).
- Improvement of the breakdown voltage.
- Suppression of parasitic effects due to DX Center.
- But: Parasitic access resistances may increase.

iemn

PLANAR DOPED MODFET: Improvement of the transconductance



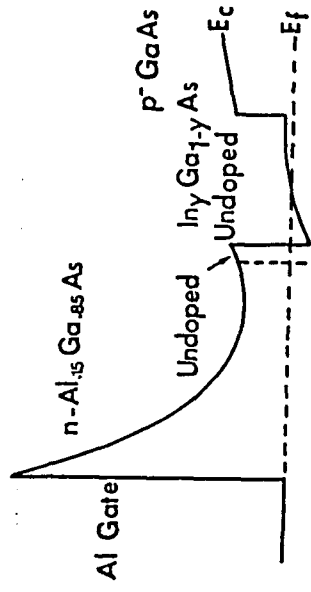
Bulk doped MODFET

Planar doped MODFET

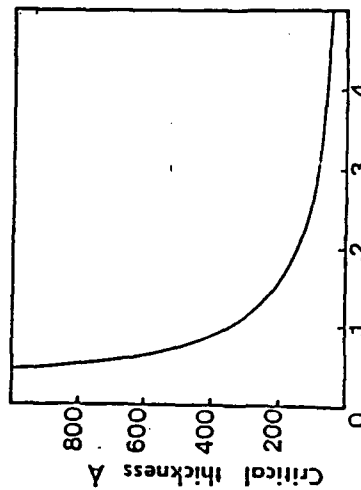
Jin et al (1991)

C.H.S.

PSEUDOMORPHIC AlGaAs/InGaAs MODFET's

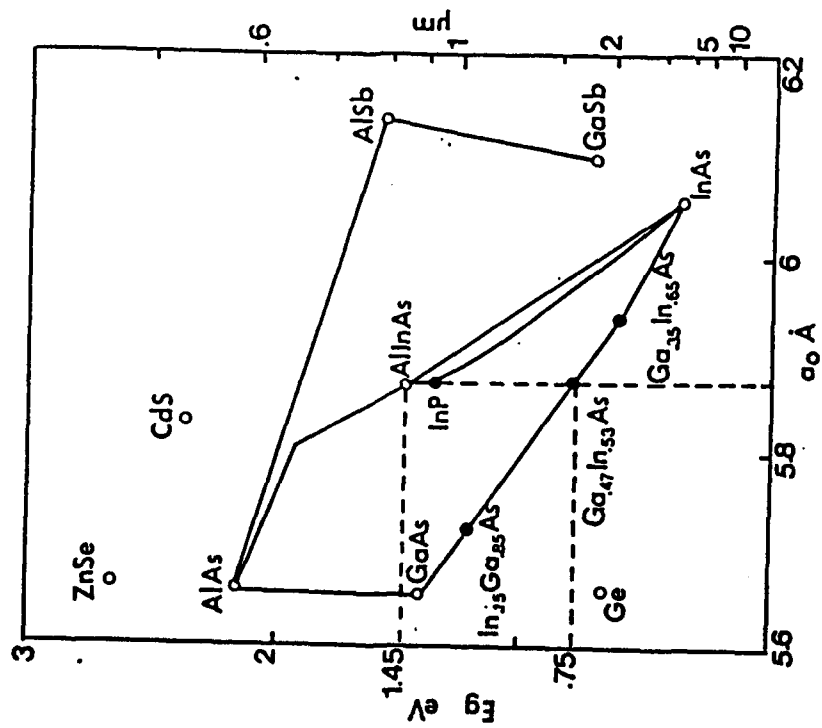


• Energy band diagram



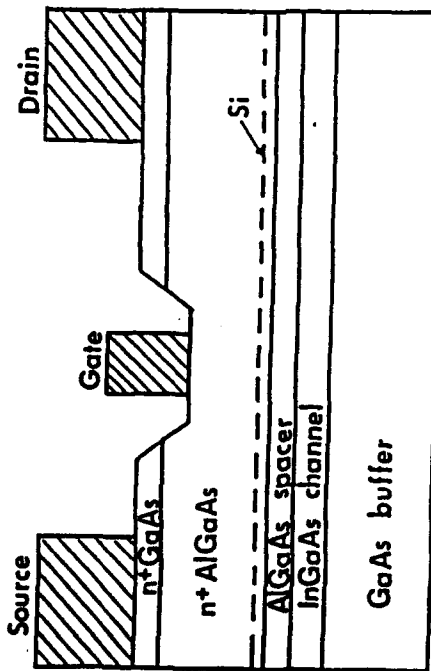
- Critical thickness of the well as function of In mole fraction

CHS Lille



Energy band gap versus lattice constant.

PSEUDOMORPHIC AlGaAs/InGaAs MODFET'S

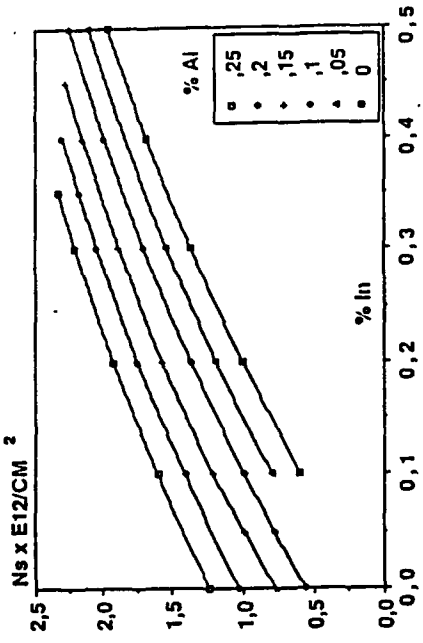


Advantages:

- More favourable transport properties?
- Better confinement.
- Higher carrier concentration values :

$n_s = 2.5 \cdot 10^{12}/\text{cm}^2$.
CHS Lille

PSEUDOMORPHIC AlGaAs/InGaAs MODFET's

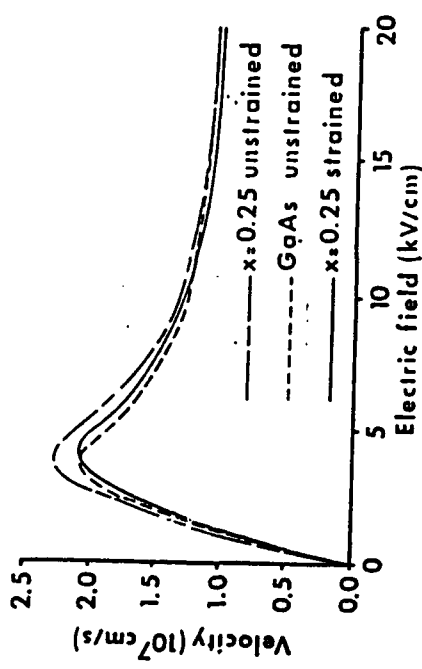


Carrier concentration dependence upon Al and In contents:
Self consistent solution of Schrödinger equation

From Cappy et al (1989)

PSEUDOMORPHIC MATERIALS

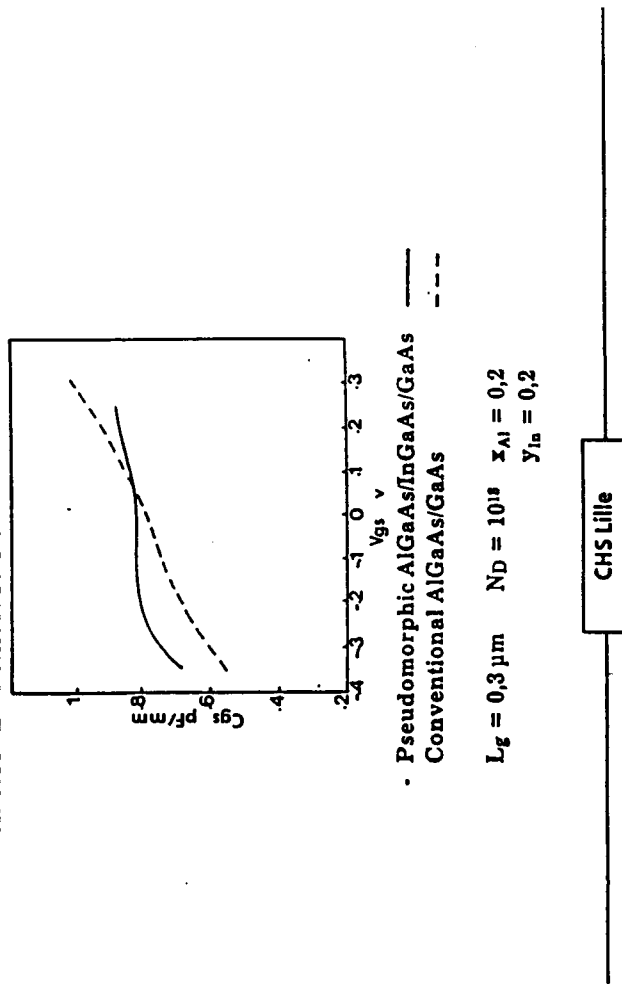
Influence of strain



Velocity field characteristics
in $In_xGa_{1-x}As$ layers

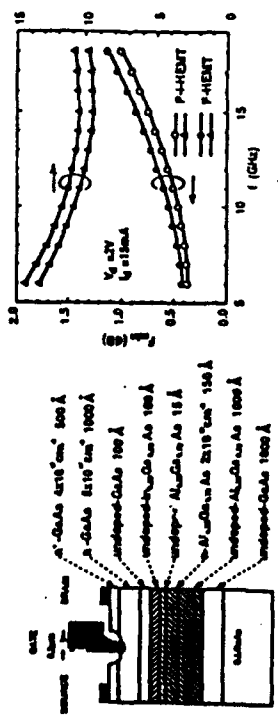
From Thobel et al (1989)

COMPARATIVE VARIATIONS OF INTRINSIC CAPACITANCE CGS

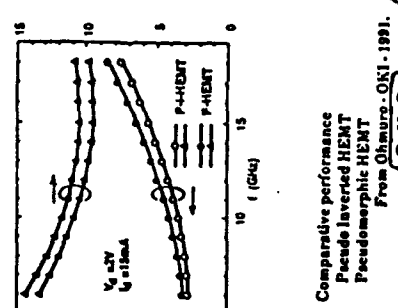


iemn

PSEUDOMORPHIC INVERTED MODFET



Schematic cross-section of the device

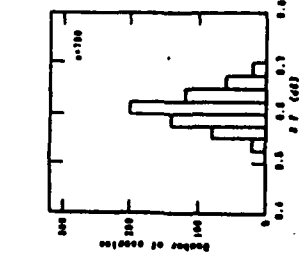


Comparative performance
Pseudolayered HEMT
Pseudomorphic HEMT
From Ohura - OKI - 1991.

C.H.S.

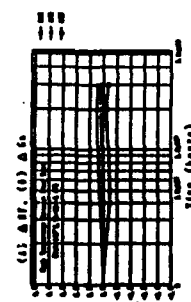
iemn

LOW NOISE PSEUDOMORPHIC MODFET'S EXAMPLE OF REPRODUCIBILITY AND FIABILITY



Distribution of noise figure at 12 GHz

From Tokuji - JEDM 01
C.H.S.



NF as function of test time.
From Tokuji - JEDM 01
C.H.S.

C.H.S.

PSEUDOMORPHIC ALGaAs/InGaAs MODFET'S

• Various structures :

- n channel - uniform doping
- n channel - planar doped
- n multiple channel
- n short period superlattice channel
- n channel with variable In content
- inverted device
- MIS Like FET
- p channel

• Among the best performance:

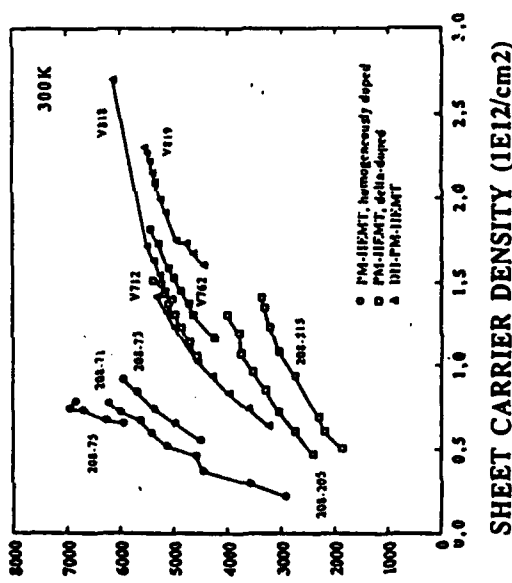
- Tan et al (TRW)

$L_g = 0.1 \mu m$ $f_T = 135$ GHz
 $N_F = 2.1$ dB $G_a = 6.3$ dB at 94 GHz.

C.H.S.

iemm

CARRIER MOBILITY VARIATIONS
IN AlGaAs/InGaAs
PSEUDOMORPHIC STRUCTURES

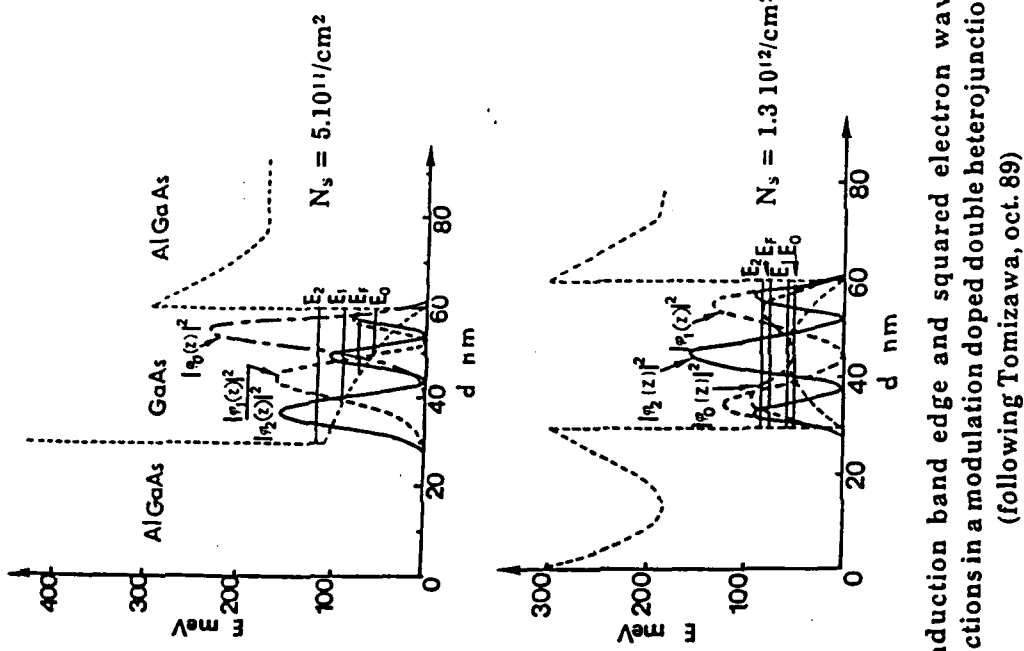


Gated Van der Pauw Hall Effect Measurements

From Pons - Thomson CSF.

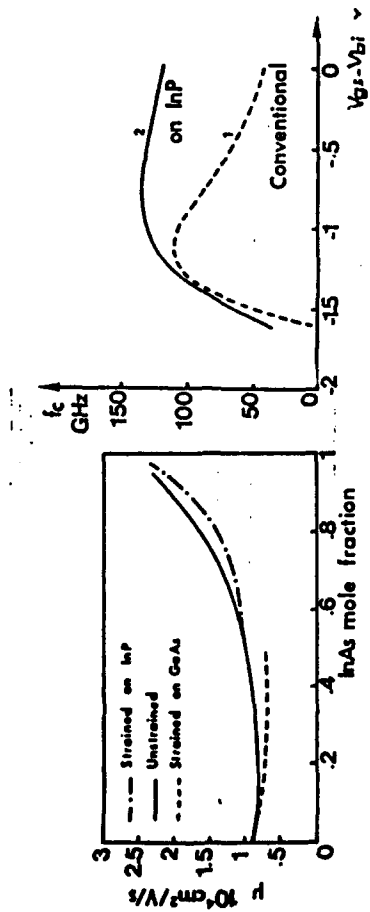
C.H.S.

INFLUENCE OF QUANTUM EFFECTS



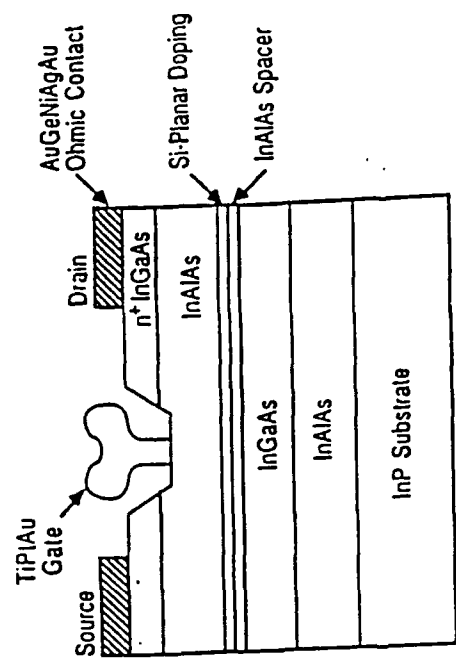
Conduction band edge and squared electron wave functions in a modulation doped double heterojunction
(following Tomizawa, oct. 89)

ADVANTAGES OF InAlAs/InGaAs on InP MODFETS



Improvements of carrier mobility and cut-off frequency

MODFET on InP SUBSTRATE

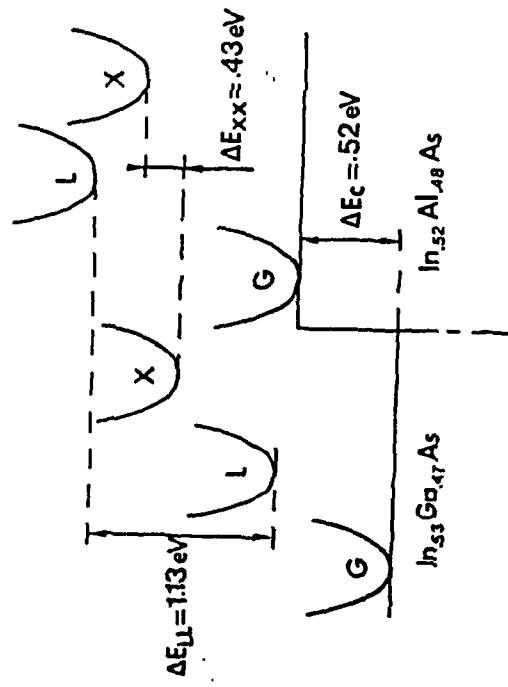


Schematic cross section of a
In_{0.52}Al_{0.48}As/In_{0.53}Ga_{0.47}As MODFET

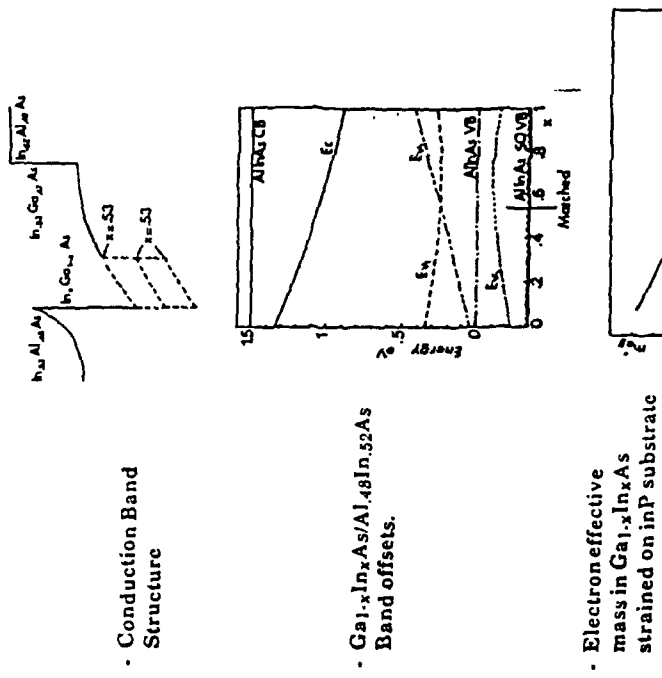
Potential interest

- Better velocity field characteristics
- Higher conduction based discontinuity and then better confinement
- Higher carrier concentration in the channel.

MULTIVALLEY TRANSFER ACROSS THE HETEROJUNCTION



INTEREST OF InGaAs ON InP PSEUDOMORPHIC STRUCTURES

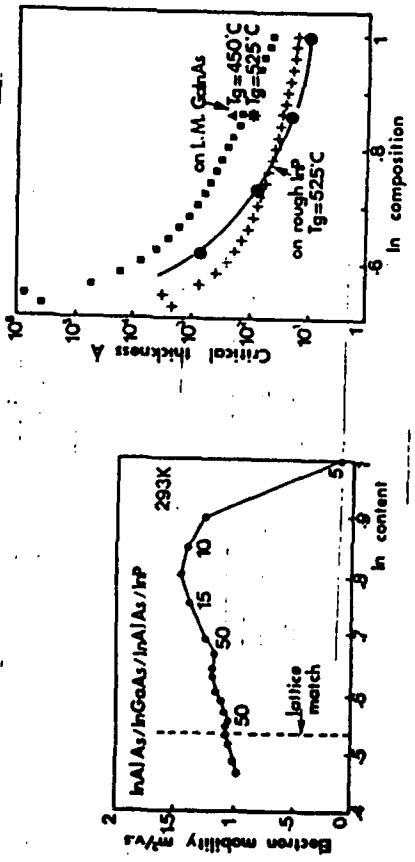


Following Priester (1990).

C.H.S.

lemon

In_xAl_{1-x}As/In_xGa_{1-x}As on InP PSEUDOMORPHIC STRUCTURES



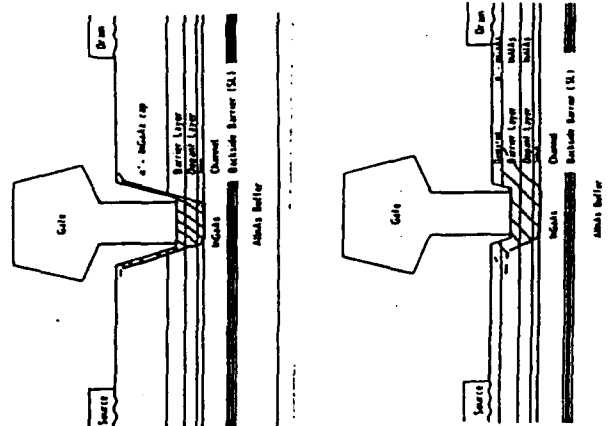
Electron mobility
Tacon et al (1991)

Critical layer thickness
Victorovitch et al (1991)

C.H.S.

lemon

INFLUENCE OF CAP LAYER CHARACTERISTICS



Trade-off between :

- Improvement of parasitic resistance : Thick-Doped.
- Improvement of output conductance : Thin and depleted cap layer

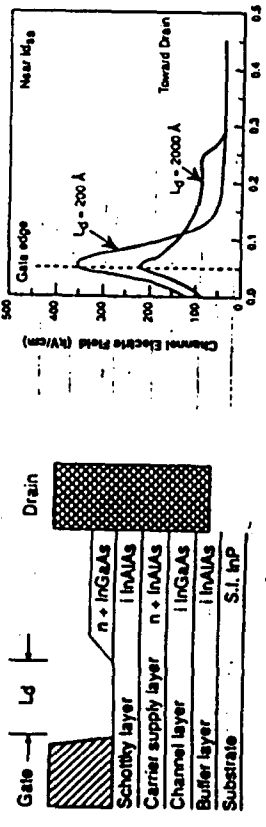
From Dickman (1991).

C.H.S.

10m
10m
10m

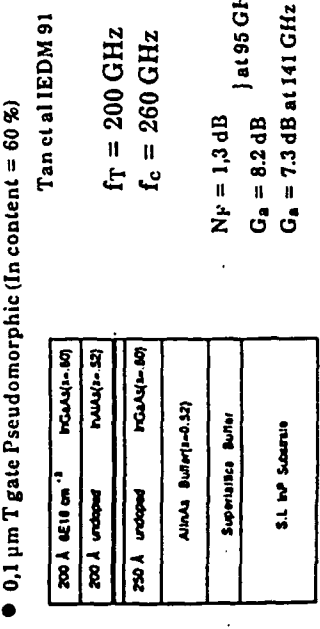
IMPROVEMENT OF THE OUTPUT CONDUCTANCE AND DECREASE OF KINK EFFECT IN InGaAs/InAlAs MODFET (Zhan et al) 1991.

Main cause: Ionization in the channel



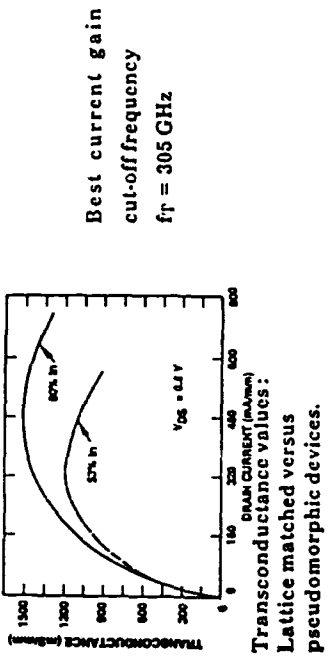
Schematic cross-section
of the device

Electric field in the
channel deduced from simulation
[C.H.S.]



Device cross section

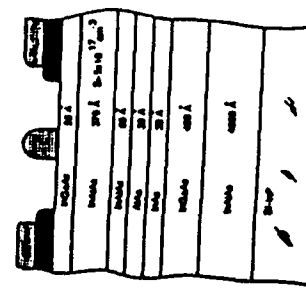
• 0.1 μ m T gate Pseudomorphic (In content = 60 %)
Tan et al IEDM 91



C.H.S.

MODFET's ON InP SUBSTRATE:
NOVEL STRUCTURES

- InAlAs/InAs: Eugster et al - Dec. 91



Remarks: Very thin InAs layer
for avoiding dislocations.

Small mobility: $5400 \text{ cm}^2/\text{V}\cdot\text{sec}$

Reasons are not clear:

- Strongly quantized channel?
- Dislocations?
- Roughness of interfaces.

$$L_g = 2 \mu\text{m} \quad g_m = 170 \text{ mS/mm}$$

- InAs/AlSb - Werking et al (1992) - Yo et al (1991)

• Very promising properties

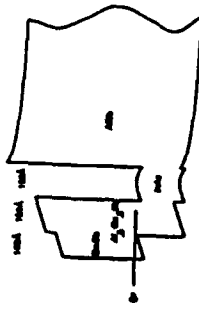
$$n_s = 3.8 \cdot 10^{15} \text{ cm}^{-3}$$

$$\mu = 21000 \text{ cm}^2/\text{V}\cdot\text{sec}$$

$$\text{For } L_g = 2 \mu\text{m}$$

$$g_m = 473 \text{ mS/mm}$$

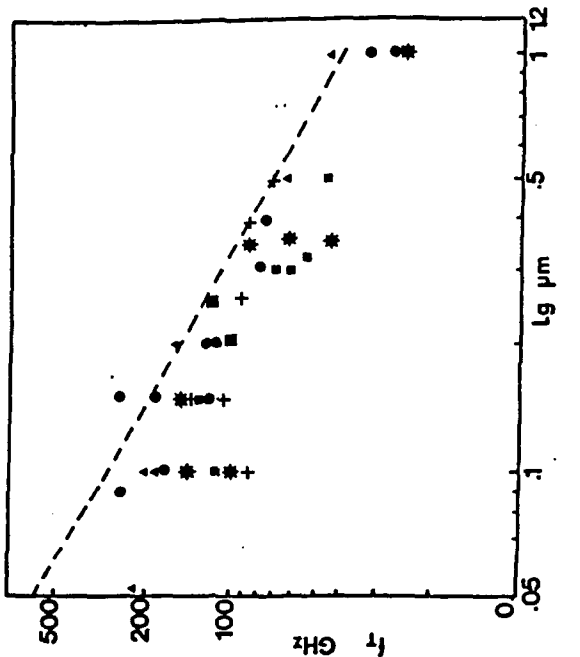
• Very difficult technologies



Energy band diagram

FIELD EFFECT TRANSISTORS

State of the art (March 1992)

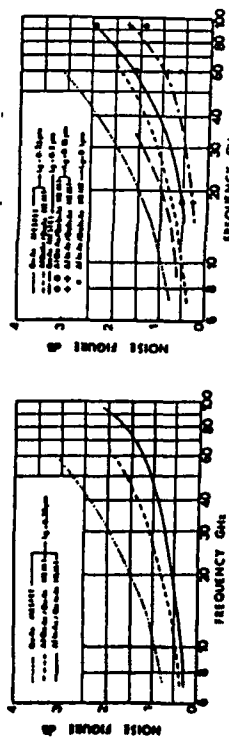


- + GaAs and InGaAs MESFET
- ▲ Strained InAlAs/InGaAs MODFET
- Lattice Matched InGaAs on InP MODFET
- * Pseudomorphic AlGaAs/InGaAs MODFET
- AlGaAs/GaAs MODFET

C.H.S.

C.H.S.

iemm
LOW NOISE FIELD EFFECTS TRANSISTORS

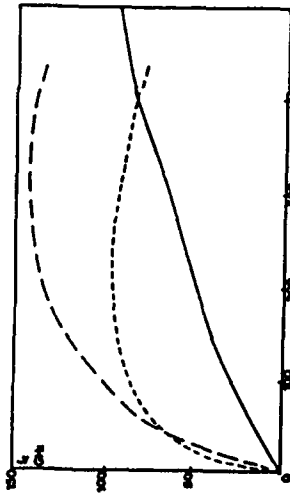


iemm
Comparison between FET's
for the same gate length (0.25 μ m)
from DUN (IMTT 81)

Noise figure versus frequency
Among the best results
published (16 March 82).

C.I.I.S.

iemm
COMPARATIVE BEHAVIOUR OF 0.2 μ m GATE FET'S



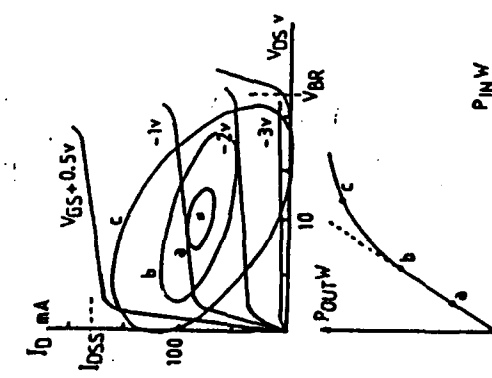
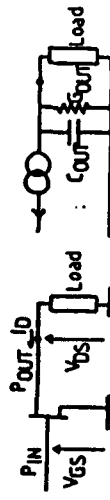
Comparison of noise figure (dB) versus frequency (GHz) for 0.2 μ m gate length FET's

Legend:
— GaAs MESFET, very well optimised (from PONS)
- - - GaAs MODFET, well optimised
- - - - - pseudomorphic AlGaAs/GaAlAs MODFET

C.H.S.

C.H.S.

POWER FET LIMITATIONS



$$P_{out} \# 1/8 I_{DS} V_{BR} \cos \Phi$$

Requirements:

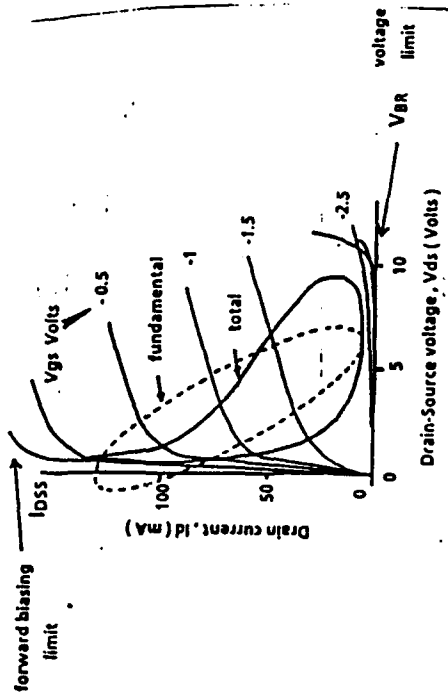
- I_{DS} } as high as possible.
- V_{BR}
- Output impedance less reactive as possible
- Gain linearity : variation of MAG with VGS.

C.H.S.

LARGE SIGNAL SIMULATIONS OF POWER FETs

It is necessary but very difficult to take into account at the same time :

- Physical device behaviour (hot electron effects, surface effects) and physical limitations (breakdown)
- Harmonic components of drain voltages and currents



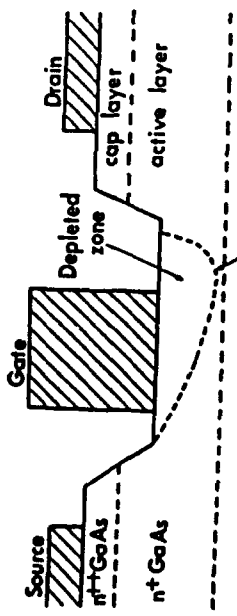
from Halkias (1988).

- Parasitic elements
- Device configuration : association of a large number of gates (100 at 100 GHz?)
- Thermal considerations (dc and pulse).

C.H.S.

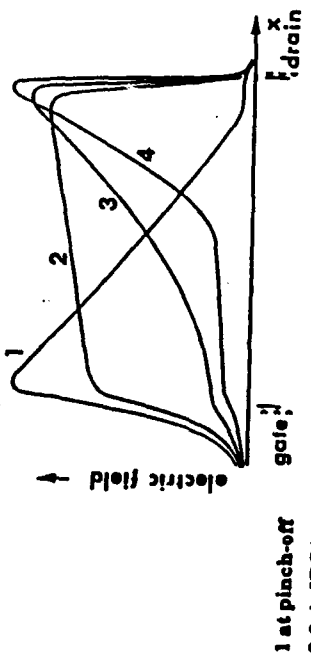
BREAKDOWN PHENOMENA: PHYSICAL KNOWLEDGE

Example of MESFET



Physical causes

Impact ionization in the channel:



1 at pinch-off 2-3-4 : IDS increasing From Wroblewski et al (1983)

- In the gate depletion region
 - impact ionization (at pinch-off)
 - gate current (thermionic or tunneling)

C.H.S.

SIMULATIONS OF BREAKDOWN PHENOMENA

Simplified models

- Quasi 2D models : (Wroblewski 1983)
 - Channel breakdown : good estimation
 - Optimization of MESFET (recess structure)
 - Problems of gate breakdown, calculation.
- 2D Solution of Poisson equation (Wroblewski - Zaitlin, Fellon).
- Calculation of multiplication factor.
- Evaluation of electric field at the gate edges
 - Tunneling currents.
- Problems :

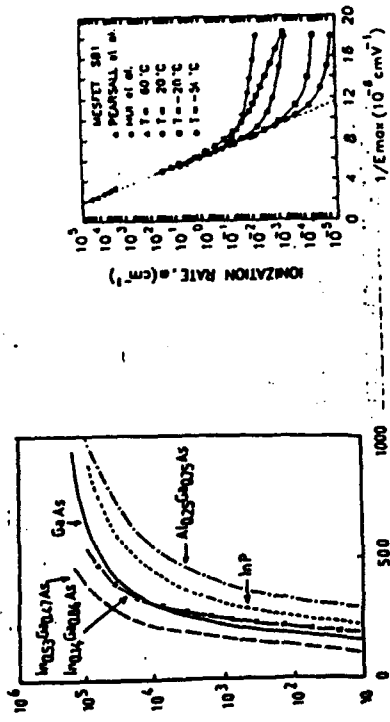
- knowledge of ionization rates and accurate predictions of tunneling currents.
- space charge reaction is not included : valid only for small I_{ds} .
- 2D models (Mizuta, Wada, Lefebvre, Chan, Barton, Ashworth, ...)
- Introduction of ionization effects or tunneling currents.
- Problems :

- drift diffusion models
- Ionization effects and tunneling currents are not introduced together.
-
-

C.H.S.

iemn

IONIZATION RATES IN BINARY AND TERNARY III-V MATERIALS



Ionization coefficients data for InGaAs
Accurate determination of α in GaAs by Canali et al (1991)

C.H.S.

Material properties:

- Ionization rates in bulk material
- Problems: Ionization rates in very thin channels ??
- Strained materials : Improvement of the breakdown voltage due to strained : $\downarrow \alpha$ (Eisenbeiser - 1991)

Epilayer characteristics :

- Doping level of the last layer under the gate is the most important.

- Trade off with high Id_{ss}
- Use of Low-High doping profile
- Very thin top layer (100 to 200 Å). Influence of tunneling currents.

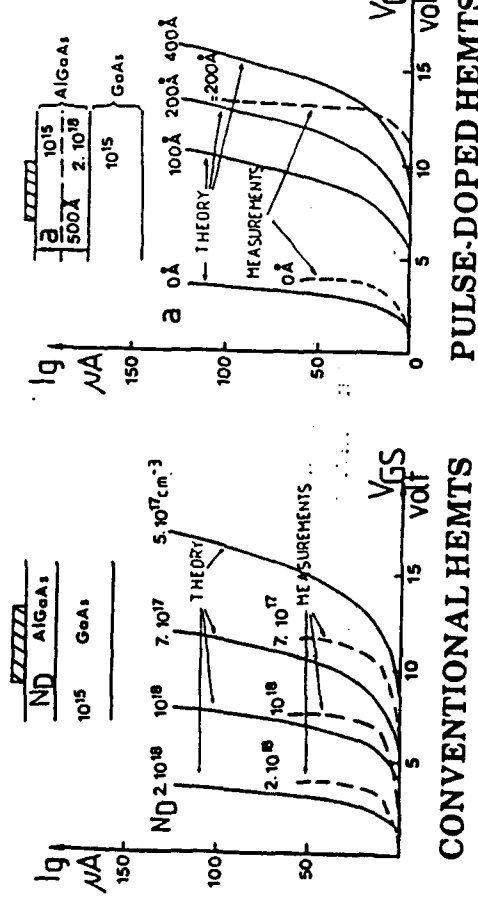
Semiinsulated substrate : Hole capture.

Recess zone configuration :

- Double recess gate process allow to improve breakdown voltage : from 8 to 16 V in InAlAs/InGaAs/InP HEMT (Boss - 1991).
- Problems of surface states under dynamic conditions (Huang - 1991).

C.H.S.

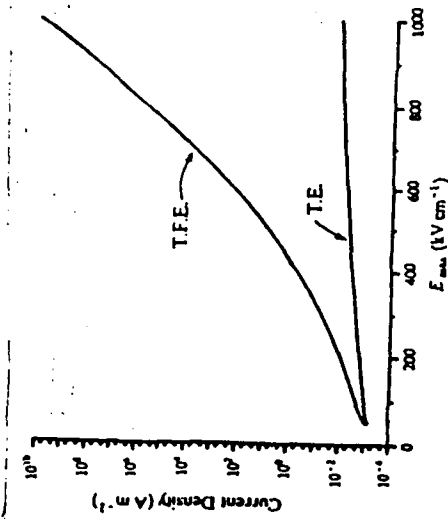
BREAKDOWN IN HEMT: TUNNEL CURRENTS



Following CROSNIER et al

CALCULATIONS OF GATE CURRENT

- Main origins :
 - Thermoionic emission process (T.E.)
 - Field effect tunneling (F.E.)
 - Thermionic field effect tunneling (T.F.E.)
 - Surface effects.
- Example of comparative values
Current density versus electric field for a Schottky (following Barton).



C.H.S.

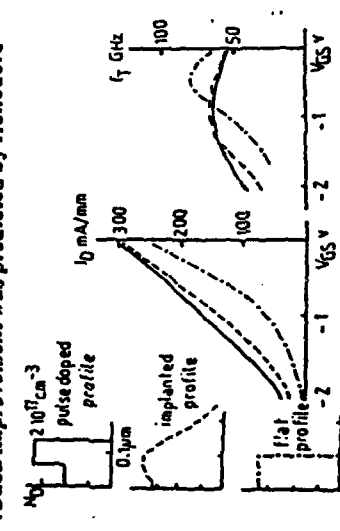
iemm

IMPROVEMENTS OF GaAs MESFET

Pulse doped active layer:

.It allows to improve breakdown voltage and linearity : for instance Chu obtained 23 dB between IP3 and $P_{0.1}$ dB

.Such improvement was predicted by Hcliodore



.Example of result: 220 mW output power at 35 GHz (RCA)
 $0.5 \mu\text{m} \times 600 \mu\text{m}$ gate.

Highly doped InGaAs channels (Feng and Wang)

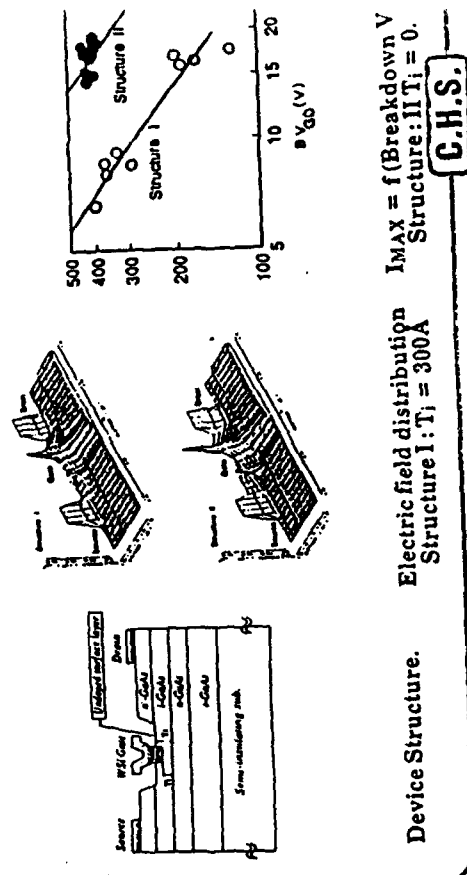
$L_g = 0.25 \mu\text{m}$
 $96 \text{ mW at } 44 \text{ GHz}$ 1 W/mm in
 $121 \text{ mW at } 60 \text{ GHz}$ 1 both cases

Pulse doped InGaAs channel: Kim
 $L_g = 0.25 \mu\text{m}$ $I_{DS} = 700 \text{ mA/mm}$
 $P_0 = 50 \text{ mW} \cdot 0.6 \text{ W/mm at } 60 \text{ GHz}$

Other improvements: AlGaAs buffer - via holes.

iemm

IMPROVEMENTS OF BREAKDOWN VOLTAGE AND PERFORMANCE BY USING A LOW-HIGH DOPING PROFILE (Takahashi - 1991).



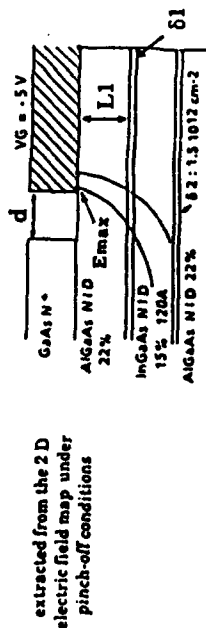
Device Structure. $V_{BD} = f(V_{GD})$
 Structure I: $T_i = 300 \text{ K}$

C.H.S.

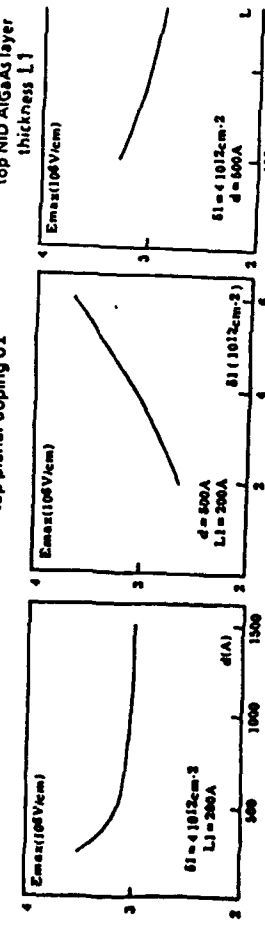
lemn

IEAN - CHS UNIVERSITE DE LILLE

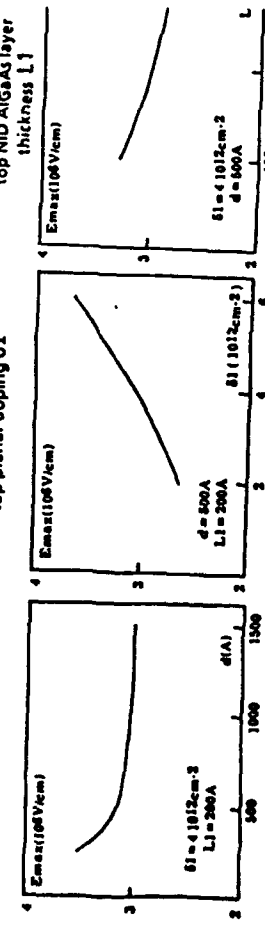
SENSITIVITY OF THE MAXIMUM ELECTRIC FIELD AT THE GATE CORNER
OF A PLANAR DOPED PM HFET TO THE STRUCTURE PARAMETERS.



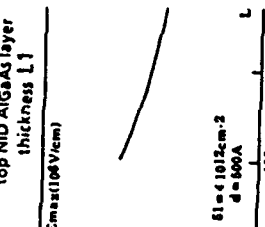
Influence of the recess spacing d



Influence of the top planar doping d_1



Influence of the top N/D AlGaAs layer thickness L_1



POWER FIELD EFFECT TRANSISTORS

• MESFET:

- GaAs
- InGaAs on GaAs substrate.

• MODFET:

- Conventional AlGaAs/GaAs
- Multichannel AlGaAs/GaAs
- Single channel AlGaAs/InGaAs
- Multichannel AlGaAs/InGaAs/GaAs
- InAlAs/InGaAs on InP substrate..

• HFET or D.M.T.:

- AlGaAs/InGaAs (n^+ doped) strained or not on GaAs.
- InAlAs/InGaAs (n^+ doped) on InP.
- InAlAs/InP (n^+) on InP substrate.

• MISFET:

- InGaAs n^+ doped) on InP
- InP n^+ doped)
- LT GaAs insulating layer.

C.H.S.

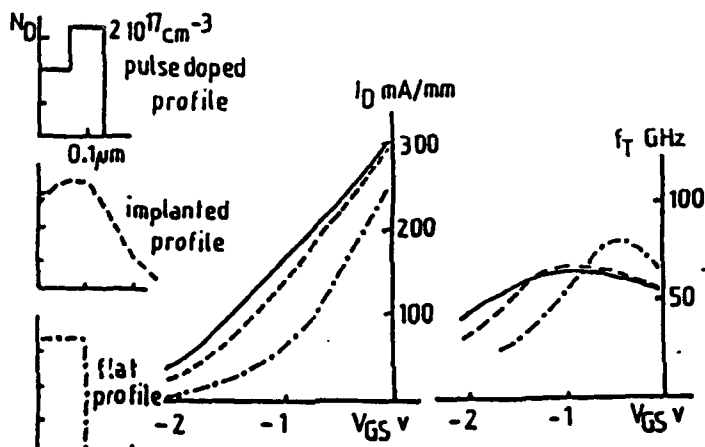
iemn

IMPROVEMENTS OF GaAs MESFET

- Pulse doped active layer:

. It allows to improve breakdown voltage and linearity : for instance Chu obtained 23 dB between IP3 and P0.1 dB

. Such improvement was predicted by Heliodore



- Example of result : 220 mW output power at 35 GHz (RCA)
0.5 μ m x 600 μ m gate.

- Highly doped InGaAs channels (Feng and Wang)

$$L_g = 0.25 \mu\text{m}$$

$$96 \text{ mW at 44 GHz} \quad \quad \quad 0.6 \text{ W/mm in}$$

$$121 \text{ mW at 60 GHz} \quad \quad \quad \text{both cases}$$

- Pulse doped InGaAs channel : Kim

$$L_g = 0.25 \mu\text{m} \quad I_{DSS} = 700 \text{ mA/mm}$$

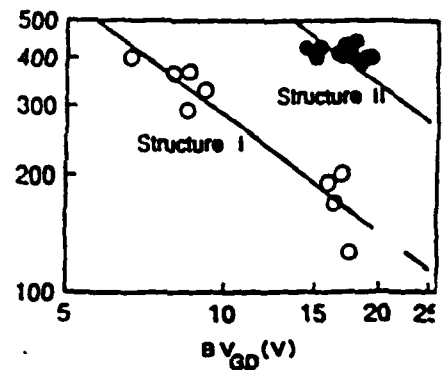
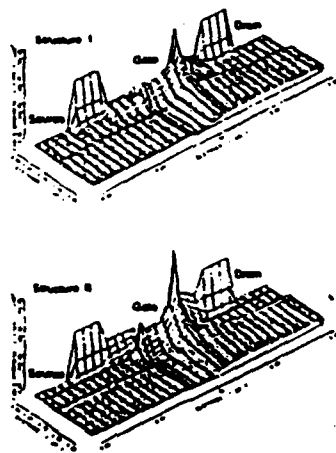
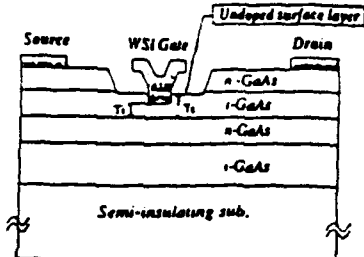
$$P_0 = 50 \text{ mW} \sim 0.6 \text{ W/mm at 60 GHz.}$$

- Other improvements : AlGaAs buffer - via holes.

C.H.S.

iemn

IMPROVEMENTS OF BREAKDOWN VOLTAGE AND PERFORMANCE BY USING A LOW-HIGH DOPING PROFILE (Takahashi - 1991).



Device Structure.

Electric field distribution
Structure I : $T_i = 300A$

$I_{max} = f(\text{Breakdown V})$
Structure : II $T_i = 0$.

C.H.S.

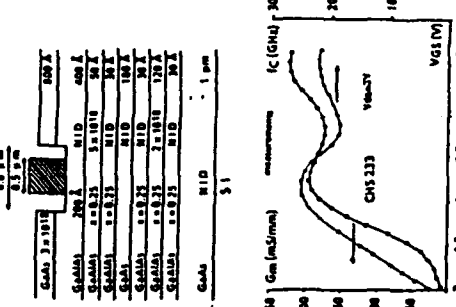
CONVENTIONAL AlGaAs/GaAs HEMT

Single channel

- Sheet carrier density smaller than $1.2 \times 10^{12} \text{ cm}^{-2}$: influence of DX centers for $x > 0.2$
- IDS is too small: $< 300 \text{ mA/mm}$.

Multichannel devices

- n_s and I_{DS} may be higher
 $n_s = 5.3 \times 10^{12} \text{ cm}^{-2}$
 $I_{DS} = 1.100 \text{ mA/mm}$ for a 3 channels.
- Improvement of linearity
- Problem of R_s



From Temcamani

- Example of performance: Fujitsu
 $0.5 \times 2400 \mu\text{m} \quad ID_{SS} = 530 \text{ mA/mm}$
 $P_0 = 1.2 \text{ W at 30 GHz.}$

C.H.S.

PSEUDOMORPHIC HFET LAYER STRUCTURES

| HEMT | | DCHFET | |
|---|--|---|--|
| $4 \times 10^{18} \text{ GaAs}$ | | $4 \times 10^{18} \text{ GaAs}$ | |
| $1 \times 10^{17} \text{ Al}_{20} \text{Ga}_{70} \text{As}$ | | $1 \times 10^{17} \text{ Al}_{25} \text{Ga}_{75} \text{As}$ | |
| $5 \times 10^{12} \text{ Si planar doping}$ | | $2.6 \times 10^{10} \text{ In}_{22} \text{Ga}_{78} \text{As well } 125 \text{ \AA}$ | |
| undoped $\text{Al}_{20} \text{Ga}_{70} \text{As}$ spacer | | $\text{Al}_{25} \text{Ga}_{75} \text{As/GaAs superlattice}$ | |
| undoped $\text{In}_{22} \text{Ga}_{78} \text{As well } 125 \text{ \AA}$ | | GaAs buffer | |
| $\text{Al}_{20} \text{Ga}_{70} \text{As/GaAs superlattice}$ | | Semi-insulating GaAs | |
| GaAs buffer | | $n_s = 4.9 \times 10^{12}$ | |
| Semi-insulating GaAs | | $\mu = 1900$ | |
| DCH MODFET | | DH HEMT | |
| $4 \times 10^{18} \text{ GaAs}$ | | $4 \times 10^{18} \text{ GaAs}$ | |
| $1 \times 10^{17} \text{ Al}_{25} \text{Ga}_{75} \text{As}$ | | $1 \times 10^{17} \text{ Al}_{25} \text{Ga}_{75} \text{As}$ | |
| $5 \times 10^{12} \text{ Si planar doping}$ | | $4 \times 10^{12} \text{ Si planar doping}$ | |
| undoped $\text{Al}_{25} \text{Ga}_{75} \text{As}$ spacer | | undoped $\text{Al}_{25} \text{Ga}_{75} \text{As}$ spacer | |
| undoped $\text{In}_{22} \text{Ga}_{78} \text{As well } 63 \text{ \AA}$ | | undoped $\text{In}_{22} \text{Ga}_{78} \text{As well } 63 \text{ \AA}$ | |
| $1.1 \times 10^{12} \text{ Si planar doping}$ | | undoped $\text{Al}_{25} \text{Ga}_{75} \text{As}$ spacer | |
| undoped $\text{In}_{22} \text{Ga}_{78} \text{As well } 63 \text{ \AA}$ | | $1 \times 10^{18} \text{ Al}_{25} \text{Ga}_{75} \text{As } 50 \text{ \AA}$ | |
| $\text{Al}_{25} \text{Ga}_{75} \text{As/GaAs superlattice}$ | | $\text{Al}_{25} \text{Ga}_{75} \text{As/GaAs superlattice}$ | |
| GaAs buffer | | GaAs buffer | |
| Semi-insulating GaAs | | Semi-insulating GaAs | |
| $n_s = 4 \times 10^{12}$ | | $n_s = 3.4 \times 10^{12}$ | |
| $\mu = 3100$ | | $\mu = 5200$ | |

From Lester et al (1989)

PSEUDOMORPHIC HFET STRUCTURES

Summary of D.C. characteristics and
35 GHz Power Performance

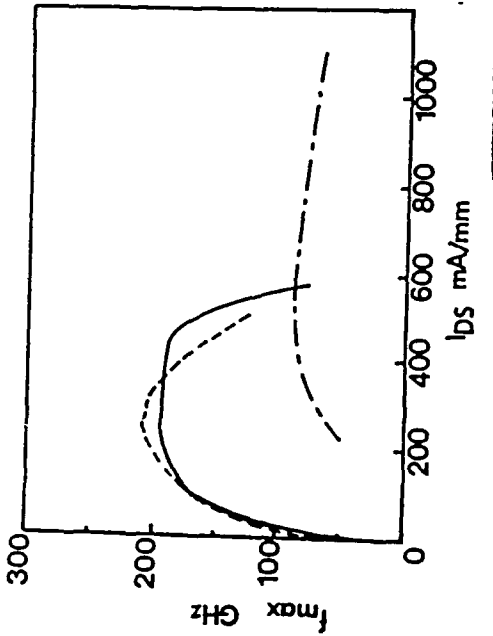
| DEVICE | HEMT | DCHFET | DHEMT | DCH MODFET |
|---------------------------|------|--------|-------|------------|
| Current Density mA/mm | 455 | 470 | 630 | 600 |
| Transconductance mS/mm | 625 | 745 | 790 | 747 |
| Breakdown Voltage v | 9.5 | 7.2 | 9.5 | 9.5 |
| Efficiency % | 40 | 35.5 | 43 | 47 |
| Maximum Power W/mm | 0.75 | 0.77 | 0.97 | 0.94 |

Following Lester et al - DRC 1989

AlGaAs/InGaAs PSEUDOMORPHIC HFET

DOPED CHANNEL OR NOT ?

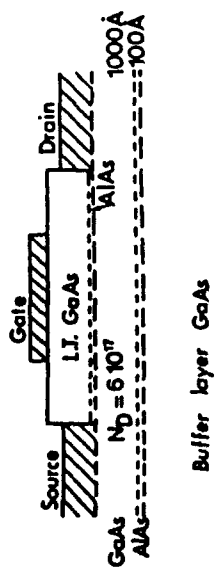
- Best result at 60 GHz : 1 W/mm · $L_g = 0.25 \mu m$
Homogeneously doped channel $f_M = 150$ GHz.
- Work of Dickmann et al (1991)
 - * Comparison
 - Conventional HEMT
 - Centrally pulse doped channel HFET
 - Backside pulse doped channel HFET
- * Experimental results : $f_M = f(IDs)$.



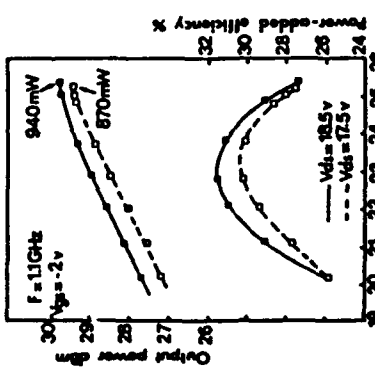
C.H.S.

C.H.S.

HIGH POWER DENSITY GaAs MISFET WITH A LT GROWN AS THE INSULATOR



Device Structure.



Power performance at 1.1 GHz from Chen (1991).

HEMTON InP SUBSTRATE FOR POWER APPLICATIONS

AlInAs/InGaAs/InAlAs HEMT

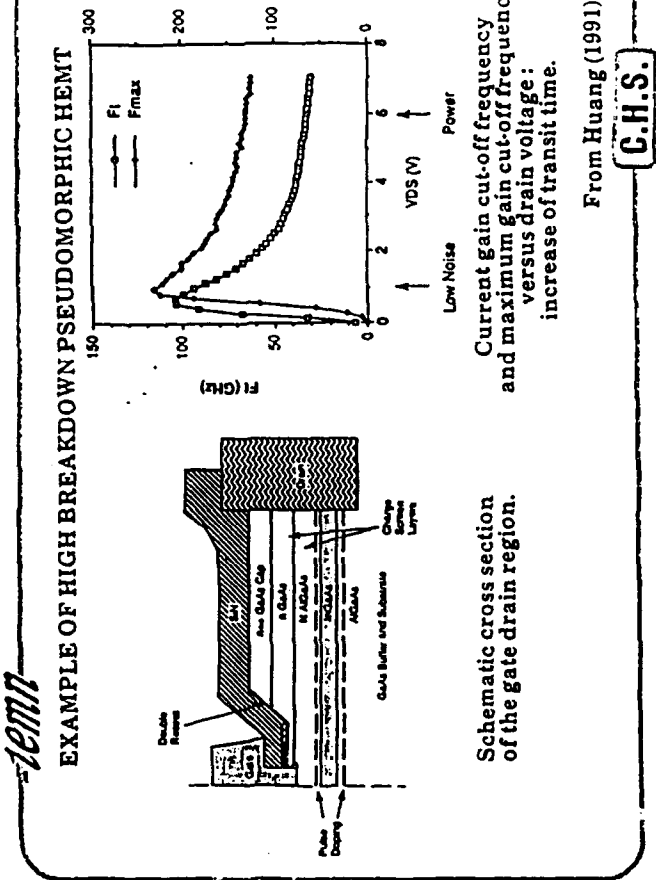
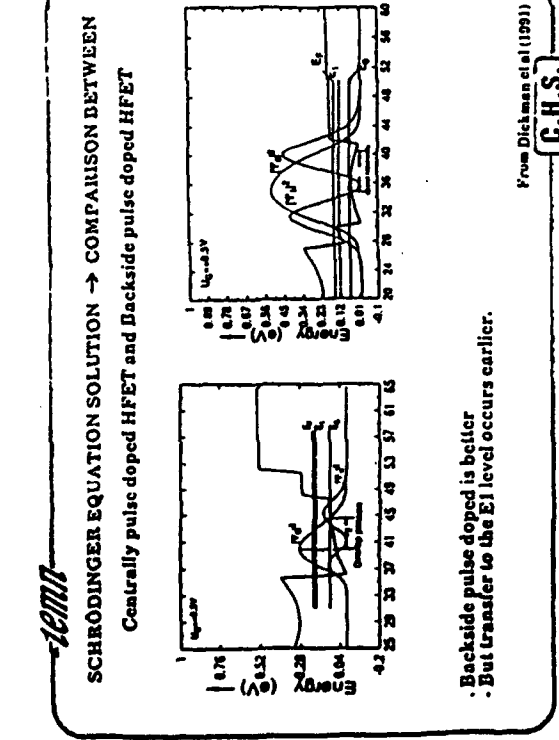
- Typical device structure (Matloubian)

Promising results

- Matloubian et al: $L_g = 0.22 \mu\text{m}$
 $V_B = 9 \text{ V}$ $I_{DS} = 770 \text{ mA/m}$
 $P_0 = 0.96 \text{ W/mm at 12 GHz}$ $\eta = 40 \%$.
- Kao et al: $L_g = 0.12 \mu\text{m}$. Pseudomorphic
 $V_H = 4.8 \text{ V}$ $I_{DS} = 600 \text{ mA/mm}$
 $P_0 = 0.35 \text{ W/mm at 60 GHz}$
 $P_0 = 0.2 \text{ W/mm at 94 GHz}$ 100 mW
 (as compared to 67 mW for InGaAs/GaAs HEMT)
- Kuang et al: D HEMT
 $I_{DS} = 1.5 \text{ A/mm}.$

But problems of reliability.

C.H.S.



OTHER POWER FET DEVICES ON InP SUBSTRATE FOR MILLIMETER WAVE RANGE

- HFET :

- InAlAs/n + InGaAs

Del Alamo

- Interesting results but trade-off between V_B (max 19 V) and $IDSS$ (max 450 mA/mm)
- No power results available.

- InAlAs/n + InP

Del Alamo - Aina

- Promising results in term of gm and $IDSS$ for long devices.
- No power results.

- MISFET :

- InP :

- Very high breakdown voltage
- High drain current density
- Small gain
- Problems of stability.

Very promising results :

- 1.6 W/mm at 18 GHz. Bredenbender
- 1.8 W/mm at 30 GHz. Saunier et al.

- InGaAs :

- High drain current density
- Small gain.

Encouraging results : Johnson - 1991.
 $L_g = 1 \mu m P_0 = 1.07 \text{ W/mm at 12 GHz}$

CONCLUSION

- PHYSICAL MODELS

- They are able to furnish very interesting informations on device behaviour;
- They can be used systematically for device optimization;
- They cannot give always accurate predictions due to the lack of knowledge in basic physics.

- LOW NOISE DEVICES :

- Pseudomorphic AlGaAs/InGaAs MODFET can now constitute the basis of a mature technology;
- InGaAs on InP MODFET is the most promising but problems of reliability must be solved;
- Noise figure smaller than 1 dB at 94 GHz can be hoped in near future;
- Temperature dependence must be studied.

- POWER DEVICES

- The situation is not clear, but for next future, MODFETs on GaAs remain preferable;
- Studies must be done on several kinds of devices. New device configurations must be envisaged for adding properly output powers of devices.

C.H.S.

C.H.S.

TWO - TERMINAL MILLIMETER - WAVE DEVICES

J. Freyer

University of München • Germany

Two terminal millimetre-wave devices

J. Freyer, Technical University of Munich

$$\begin{aligned}
 Z_D + Z_L &= 0 && \text{Kirchhoff's law} \\
 R_D + R_L &= 0 \\
 X_D + X_L &= 0
 \end{aligned}$$

$$P_{rf} = 1/2 |V_{rf}|^2 R_L = 1/2 |V_{rf}|^2 (R_D +$$

(available output power)

series resistance R_s

$$P_{rf} = 1/2 |V_{rf}|^2 (R_D + R_s)$$

Basic equations

$$\frac{\partial n}{\partial t} = \frac{1}{q} \frac{\partial J_n}{\partial x} + G$$

continuity equations

$$\frac{\partial p}{\partial t} = -\frac{1}{q} \frac{\partial J_p}{\partial x} + G$$

$$\begin{aligned}
 J_n &= q v_n n \\
 J_p &= q v_p p
 \end{aligned}$$

current density equations

$$\frac{\partial E}{\partial x} = q(N_D - N_A + p - n)$$

Poisson equation

| | |
|----------------------------------|------------------------------------|
| n : electron density | x : space coordinate |
| p : hole density | v_n : electron drift velocity |
| J_n : electron current density | v_p : hole drift velocity |
| J_p : hole current density | ϵ_p : dielectric constant |
| G : generation | E : electric field |
| q : electronic charge | N_D : donor density |
| t : time | N_A : acceptor density |

- Basic principles of power generation
- Gunn element (transferred electron device)
- IMPATT diode
- MITATT and TUNNETT diode
- PIN-avalanche diode
- BARITT diode
- Double-barrier and QWTT diode
- Device fabrication and packaging
- Resonators
- Application and state-of-the-art performance

n-type semiconductor

$$\frac{\partial E}{\partial x} = -\frac{q}{\epsilon} (n - N_D)$$

Poisson equation

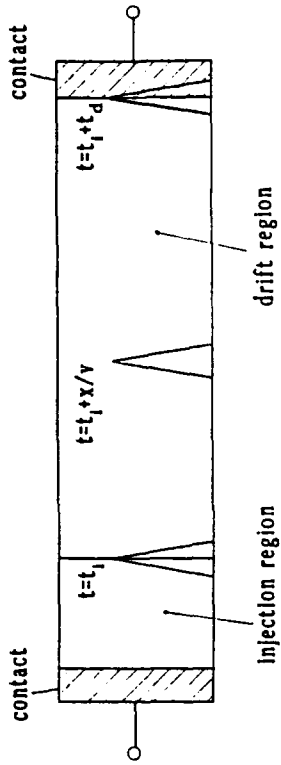
$$I_c = A q n v(E)$$

convection current

$$I_{tot} = I_c + A \epsilon \frac{\partial E}{\partial t}$$

total current

$$I_{tot} = A \left\{ \epsilon \frac{\partial E}{\partial t} + q (N_D \frac{d}{dx} \frac{\partial E}{\partial x}) v(E) \right\}$$



Schematical presentation of a transit-time device

small signal assumption

$$E = E_0 + E_1 \exp(i\omega t)$$

$$I_{tot} = I_{tot0} + I_{tot1} \exp(i\omega t)$$

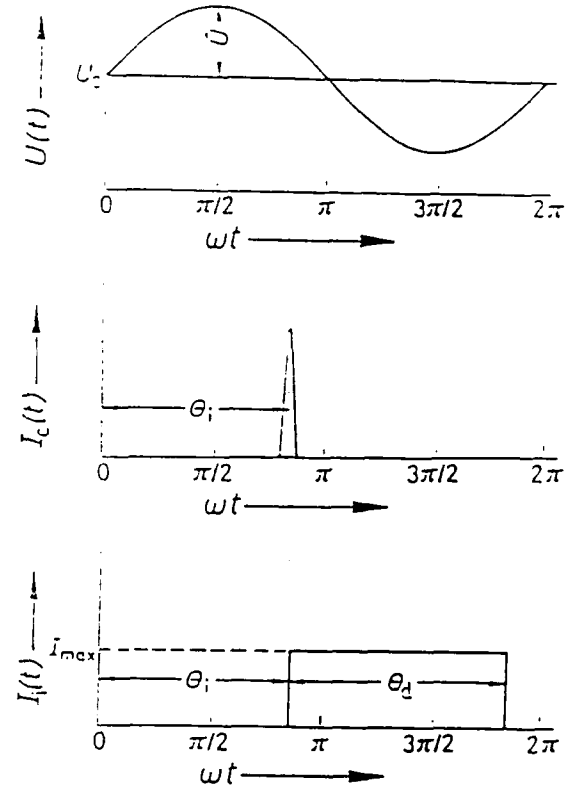
$$E_1(x) = \frac{I_{tot1}}{j\epsilon A v_0 (\omega/v_0 - j q N_D / \epsilon v_0 \partial^2 E / \partial x^2)}$$

$$\left\{ 1 - \exp(-j\omega x/v_0) \exp(-q N_D / \epsilon v_0 \partial v / \partial E) \right\}$$

$\frac{dv}{dE} > 0$ damping

$\frac{dv}{dE} = 0$ no attenuation

$\frac{dv}{dE} < 0$ growing up



Voltage, injected convection current and induced current of a transit-time device

Transit-time device

- injection region
- drift region

$$I_{rf} = 2 I_0 \sin(\theta_d/2) / (\theta_d/2)$$

Fourier component

$$I_0 = I_{max} \theta_d / (2\pi)$$

dc-current

$$P_{rf} = U_{rf} I_0 \frac{\sin(\theta_d/2)}{\theta_d/2} \sin(\theta_1 + \theta_d/2)$$

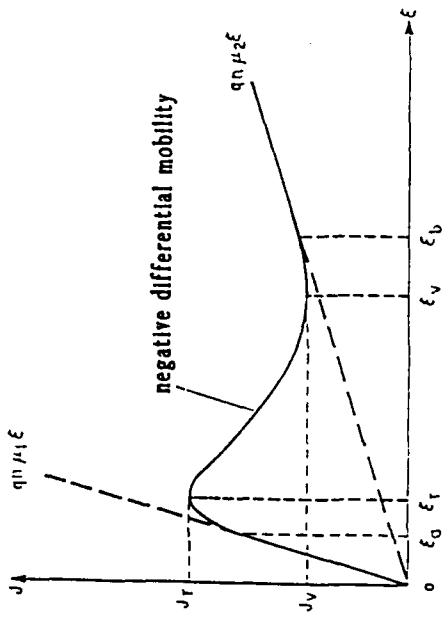
$$\theta_1 = \omega t_1$$

Injection angle

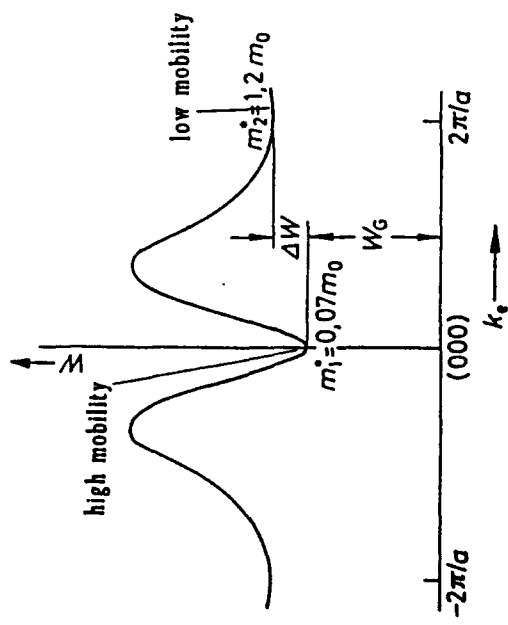
$$\theta_d = \omega t_d$$

drift angle

Generation of output power : $\pi < \theta_1 + \theta_d/2 < 2\pi$

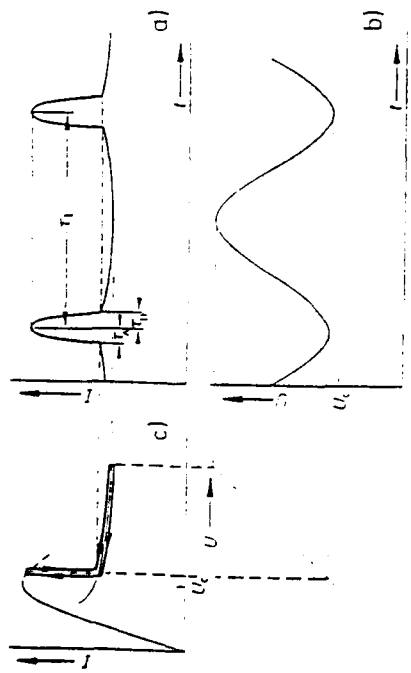


Current density versus electric field
of a two-valley semiconductor



Schematical structure of a Gunn element

Energy band structure of GaAs



Current and voltage of a Gunn element in transit-time mode

Noise of Gunn elements

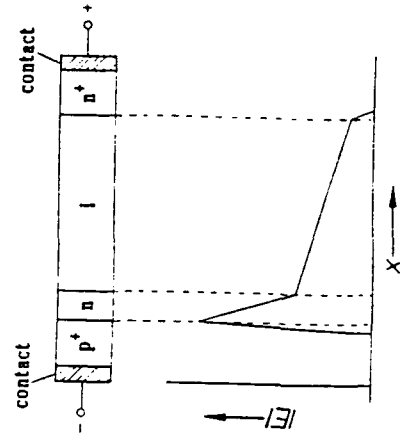
- primary noise
- diffusion (statistical velocity fluctuations of drifting carriers)
- modulation (low frequency fluctuations of dc-current, temperature)
- up-conversion via the device impedance

Limitation of output power of Gunn elements

- The negative mobility vanishes if the oscillation period reaches the scattering time
- The "n" cathode injects "cold" electrons which must gain energy before they can transfer. A "dead" zone results which occupies a large fraction of the total n-zone

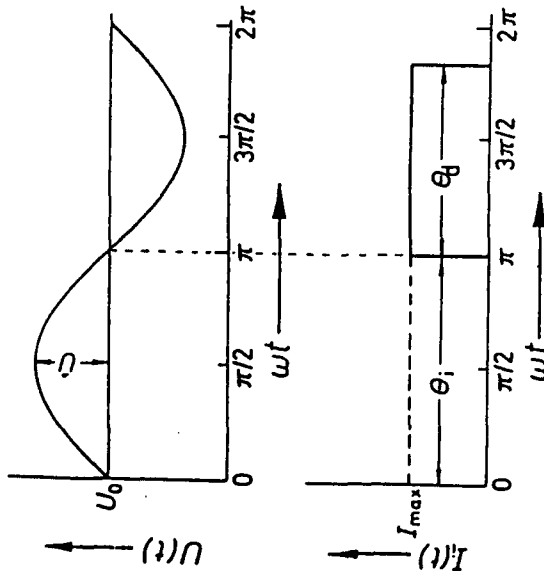
Improvement

- Injection of "hot" electrons
- GaAlAs/GaAs launcher
- planar doped barriers
- camel dikes
- tunnel injection
- reverse biased Schottky barriers



Structure and field distribution of a Gunn diode

Negative resistance of IMPATT diode



Rf-voltage and induced current of a
Read IMPATT diode

$$\begin{aligned}
 C &= \alpha v_a (J_n + J_p) \\
 \frac{dJ_n}{dt} &= -v_a \frac{\partial J_n}{\partial t} + \alpha v_a (J_n + J_p) \\
 \frac{dJ_p}{dt} &= v_a \frac{\partial J_p}{\partial t} + \alpha v_a (J_n + J_p) \\
 J_c &= J_n + J_p \\
 \boxed{\frac{v_a}{2} \frac{dJ_c}{dt} = J_c \left(\int_0^{l_a} \alpha dx - 1 \right) + J_s \quad \text{Read equation}}
 \end{aligned}$$

$$\begin{aligned}
 v_a &= l_a / v_s \\
 J_s &: \text{saturation current density} \\
 R_D &= \frac{1}{\omega C_d} \frac{(1 - \cos \theta_d) / \theta_d}{(1 - \omega^2 / \omega_a^2)} \\
 \omega_a &= \sqrt{2\alpha v_a J_0 / e} \quad J_0 : \text{dc current density}, \quad \alpha' = d\alpha / dE
 \end{aligned}$$

Limitation of output power of IMPATT diodes

- l_a/w increases with increasing doping concentration
- The fraction of the "dead" space increases with decreasing avalanche zone width
- For high frequencies the generation of carriers is reduced because of the finite intrinsic avalanche response time
- With increasing electric field more carriers are generated by tunnel effect
- The saturation drift velocity reduces with increasing electric field (v_a is reduced)
- The ionization rates saturate with increasing electric field (ω_a is reduced)
- The thermal conductivity limits the maximum input power

Si : 1.45 W/cmK, InP : 0.68 W/cmK, GaAs : 0.44 W/cmK

IMPATT diode

$$\theta_i = \pi$$

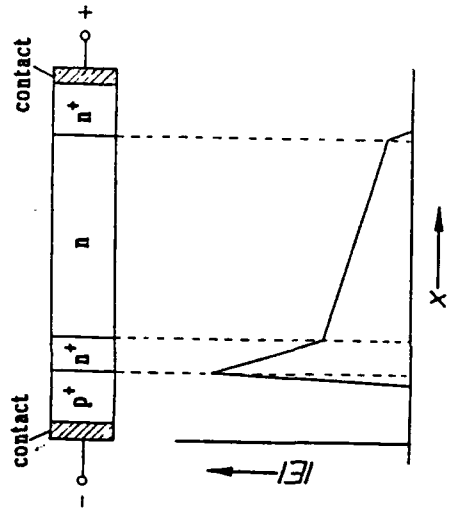
$$\begin{aligned}
 P_{rf} &= U_{rf} I_0 \frac{(1 - \cos \theta_d)}{\theta_d} (1 - l_a/w) \\
 l_a &: \text{length of the avalanche zone} \\
 w &: \text{total width}
 \end{aligned}$$

$$\theta_{dopt} = 3\pi/4$$

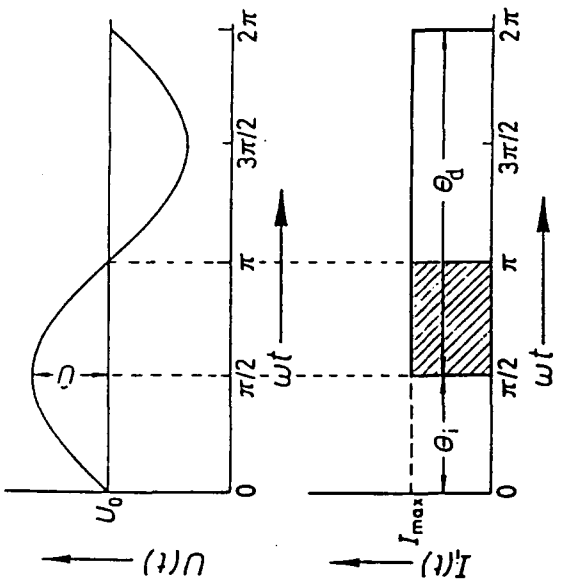
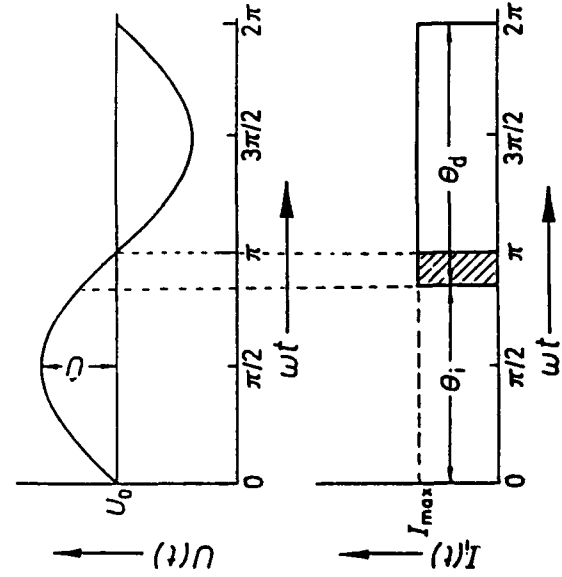
$$\begin{aligned}
 \text{optimum drift length} : l_d &= \frac{\theta_d v_a}{2 \pi f} = \frac{3}{8} \frac{v_a}{f}
 \end{aligned}$$

Noise of IMPATT diodes

- The IMPATT mode exhibits an intrinsically high noise level
- The noise power is mainly generated by the statistical nature of the avalanche process
- The noise behaviour is dependent on
 - semiconductor material
 - diode doping profile
 - bias conditions
 - rf-signal levels
 - parametric interactions
- Generally GaAs IMPATT diode are less noisy than Si devices

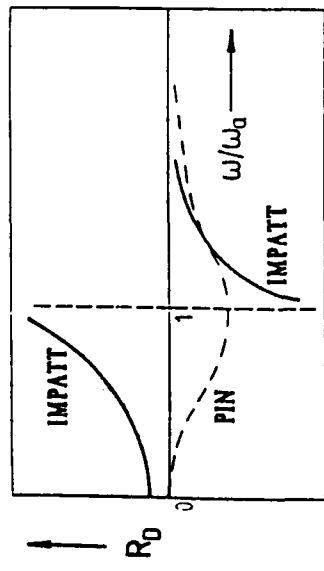


Structure and field distribution of a TUNNELL diode

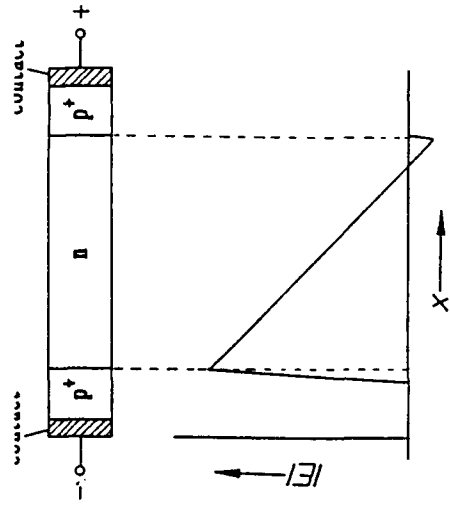


Rf-voltage and induced current of a TUNNELL diode

Rf-voltage and induced current of a TUNNELL diode



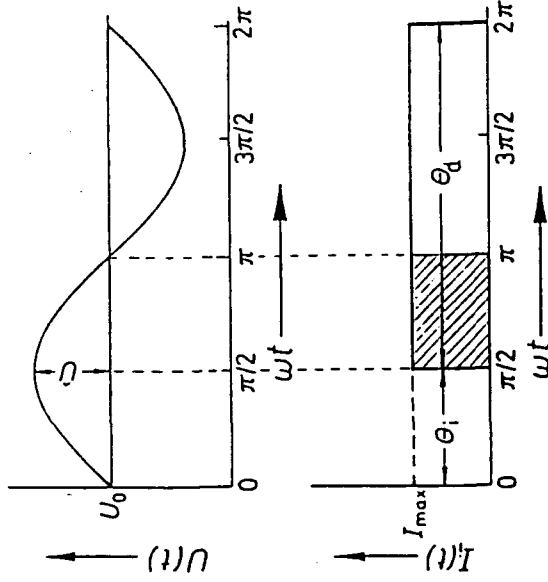
Real part of IMPATT and PIN-avalanche diode impedance versus frequency



Structure and field distribution of a BARITT diode

PIN-avalanche diode

- Negative resistance not only above avalanche frequency but also below
- Broadband negative resistance
- Advantage for pulsed diodes : relatively large negative resistance at $\omega = \omega_a$
- The resistance is zero at $\omega = \omega_a$. No large capacitive currents which limit output power



RF-voltage and induced current of a BARITT diode

TUNNETT diode

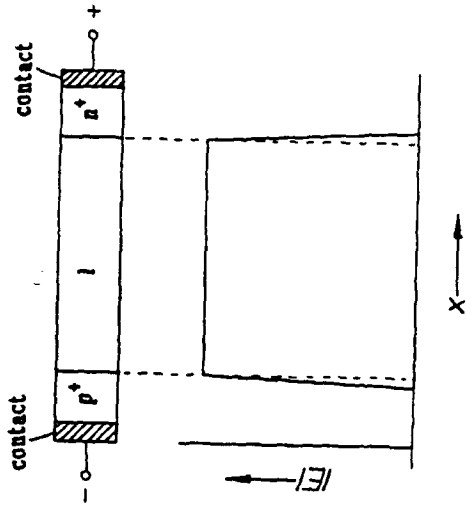
$$\theta_t = \pi/2$$

$$P_{rf} = U_{rf} I_0 \frac{\sin \theta_d}{\theta_d} (1 - I_d/w)$$

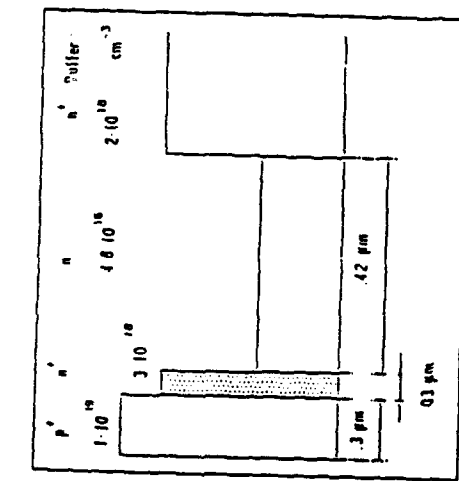
l_a : length of the generation zone
 w : total width

$$\theta_{d, \text{opt}} = 3\pi/2$$

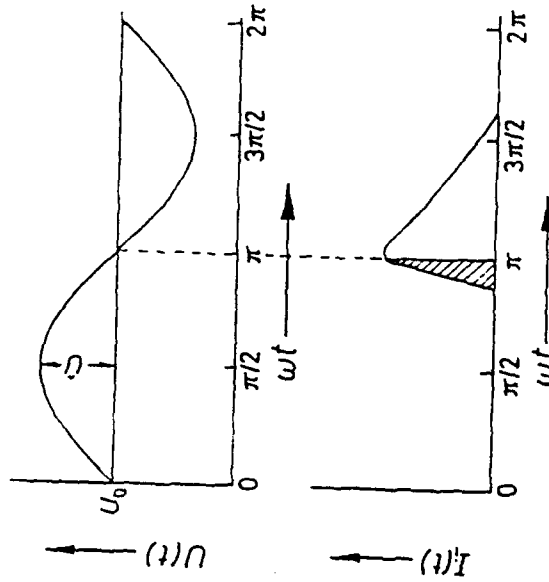
$$\text{optimum drift length} : l_d = \frac{\theta_d v_s}{2\pi f} = \frac{3}{4} \frac{v_s}{f}$$



Structure and field distribution of a PIN-avalanche diode



Doping profile of a W-band TUNNETT diode



RF-voltage and induced current of a PIN-avalanche diode

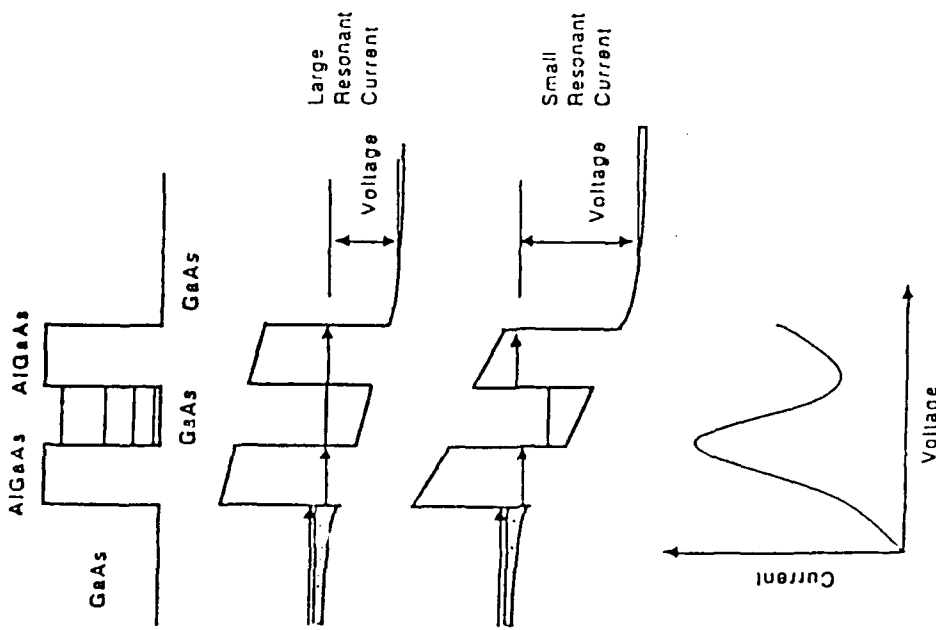
BARITT diode

$$\theta_1 = \pi/2$$

$$P_{rf} = U_{rf} I_0 \frac{\sin \theta_d}{\theta_d}$$

$$\theta_{d, \text{opt}} = 3\pi/2$$

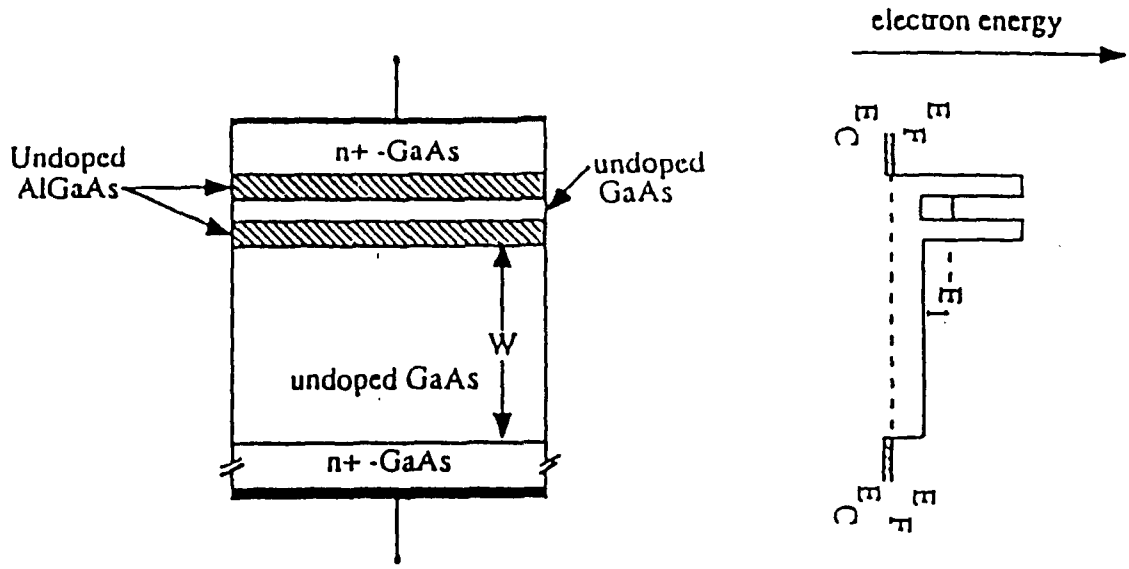
$$\text{optimum length: } l_d = \frac{\theta_d v_A}{2\pi f} = \frac{3}{4} \frac{v_A}{f}$$



Noise of BARITT diodes

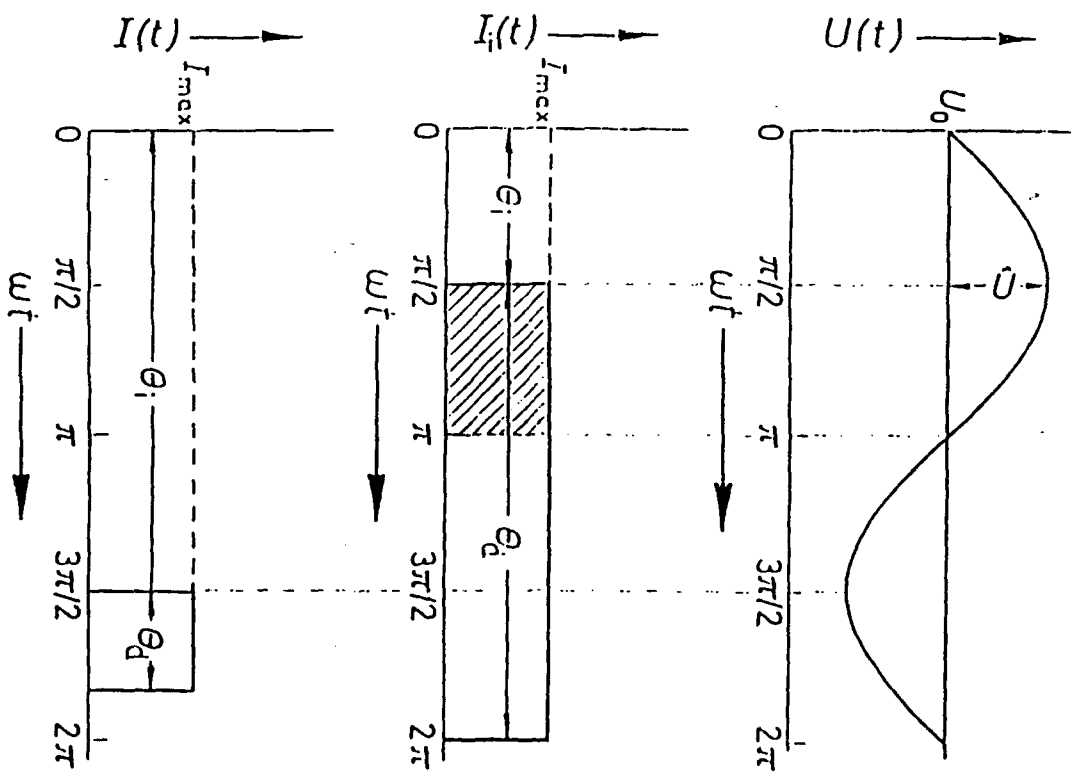
- diffusion noise of drifting carriers
- shot noise due to the injection mechanism
- low frequency noise (up-conversion)
- Phase noise as low as for Gunn elements
- Application as self-oscillating mixer
 - 60 GHz : minimum detectable signal $\sim 160 \text{ dBm}$
 - conversion gain $\sim 30 \text{ dB}$
 - (15 to 20 dB better than for Gunn elements)

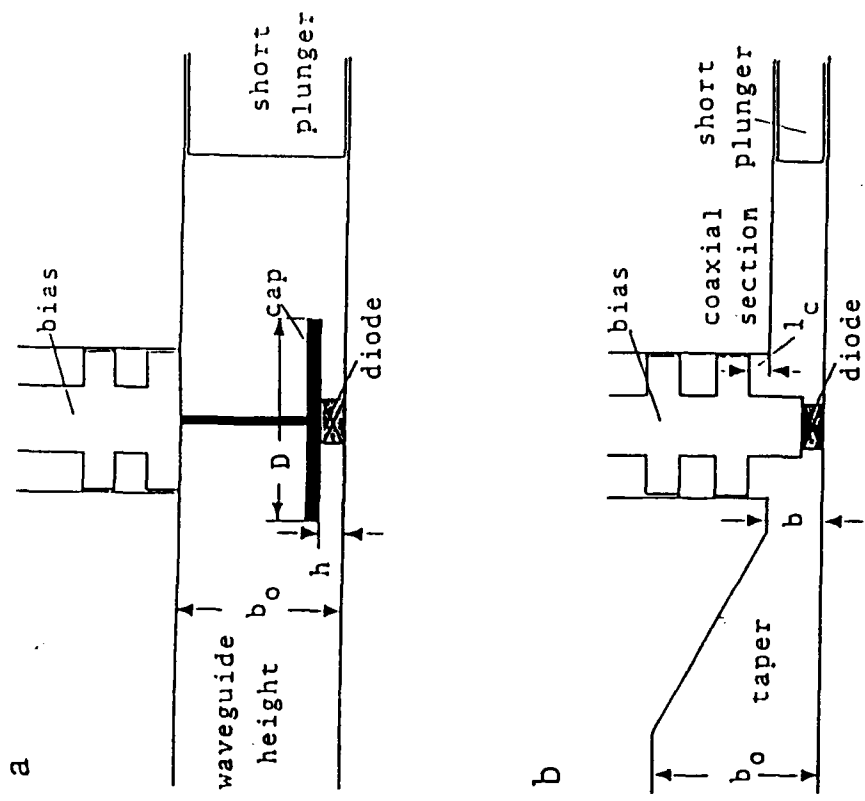
Energy band structure of a quantum-well resonant tunneling device



Structure and energy band diagram of a GaAs/GaAlAs QWITT diode

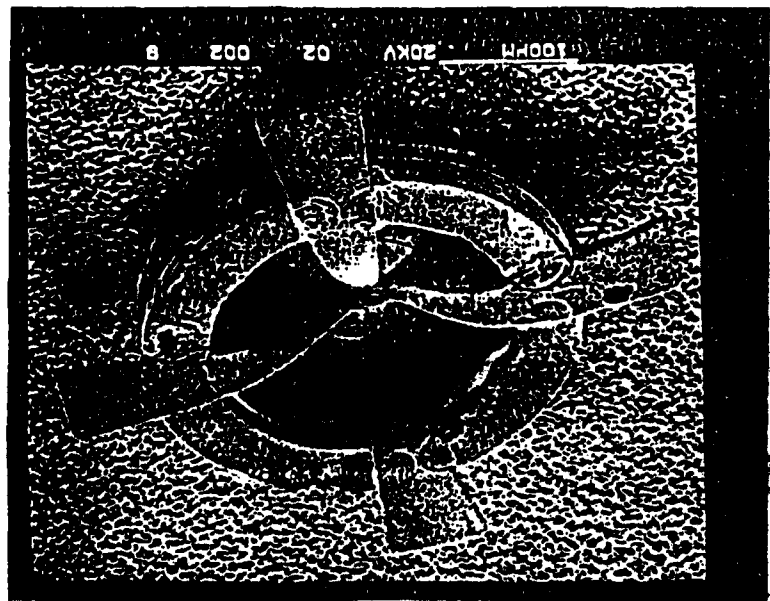
Rf-voltage and induced current of a QWITT diode
 $(\Theta_1 = \pi/2$ and $\Theta_1 = 3\pi/2)$





Full and reduced waveguide height resonator

Encapsulated W-band GaAs IMPATT diode



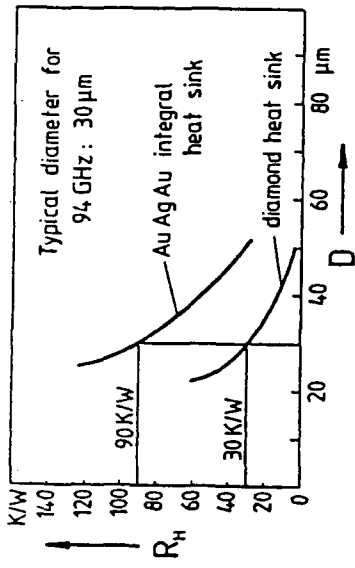
Device fabrication

Si, GaAs, InP for mm-wave devices

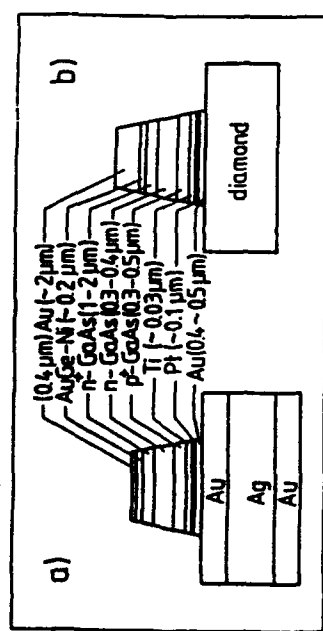
- Molecular beam epitaxy
(important for elevated frequencies)
- Photorealist technology
- Etching processes (wet, dry)
- Metallization (evaporation, sputtering, plating)

Reduction of losses

- low ohmic contacts
- substrate thickness : 1 - 3 μm
- low heat flow resistance
(diamond)
- reduction of parasitic capacitance
and inductance
- matching to the resonator impedance
- 94 GHz : $C < 0.07 \text{ pF}$, $L < 15 \text{ pH}$
quartz ring height < 75 μm

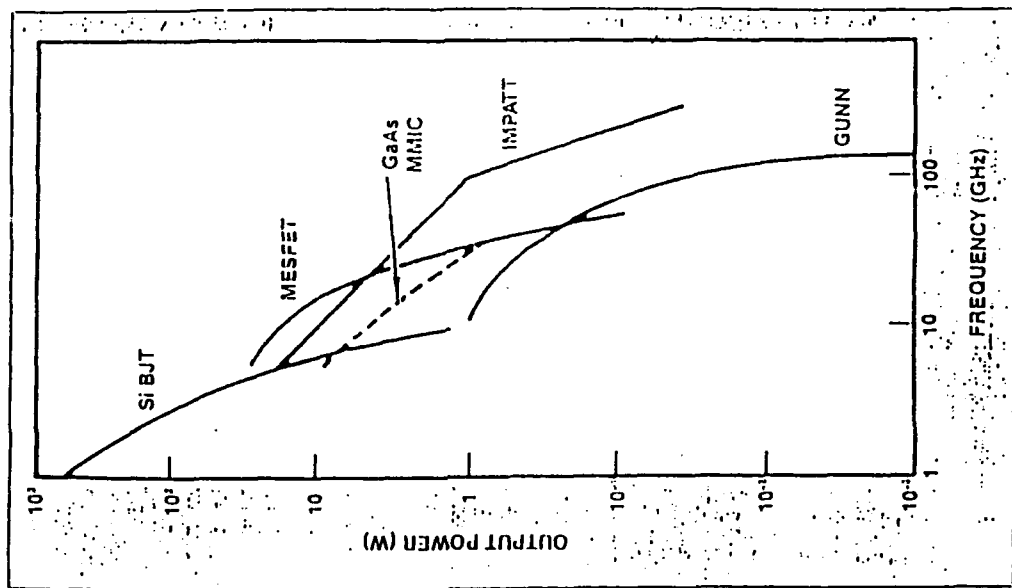


Heat flow resistance of 94 GHz IMPATT diodes versus device diameter

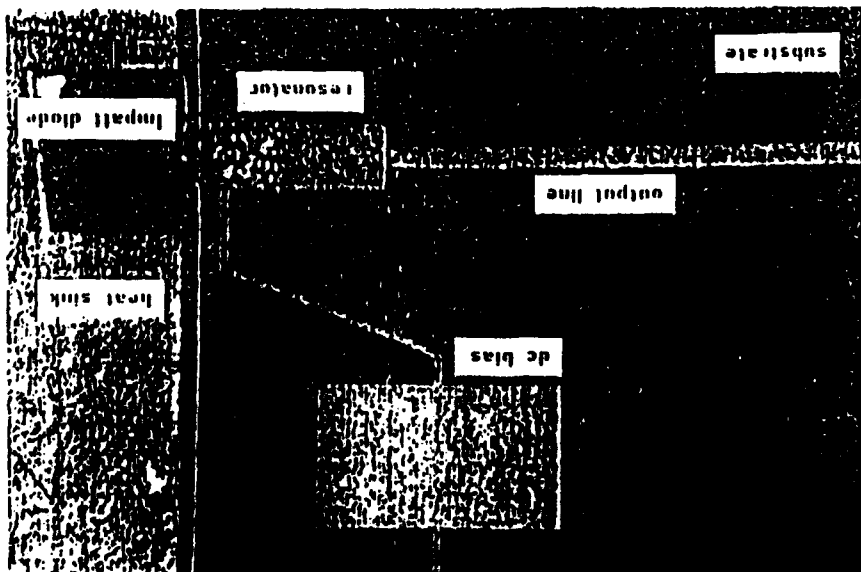


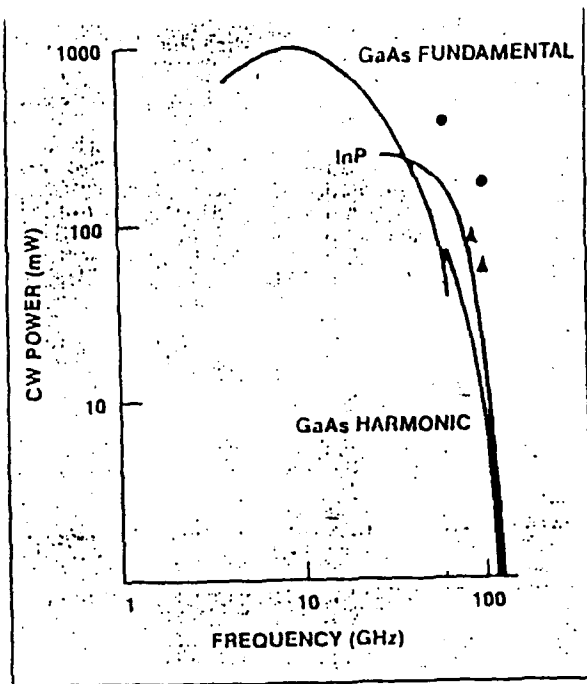
GaAs IMPATT diode with Au/Ag/Au and diamond heat sink

State-of-the-art performance
of solid-state power devices
(after Shih and Kung)

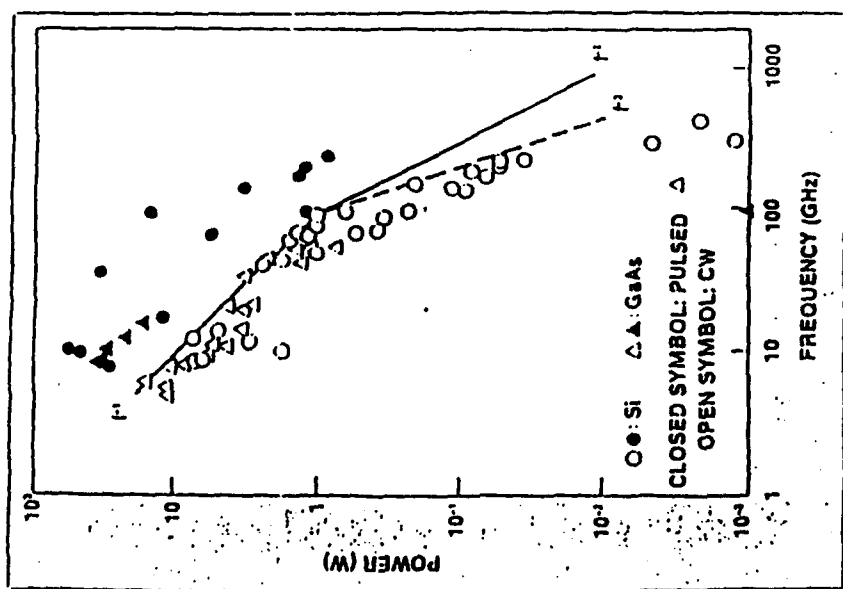


Photograph of a $\lambda/4$ strip-line resonator
on seminsulating GaAs substrate





Cw-output power of Gunn elements
 (▲ GaAlAs/GaAs launcher
 ● InP current limiting cathode)



State-of-the-art performance
 of Si and GaAs IMPATT diodes
 After Shin and Kuno

Maximum efficiency

Impatt 20 % $f < 40$ GHz for GaAs devices
 10 % $f > 40$ GHz

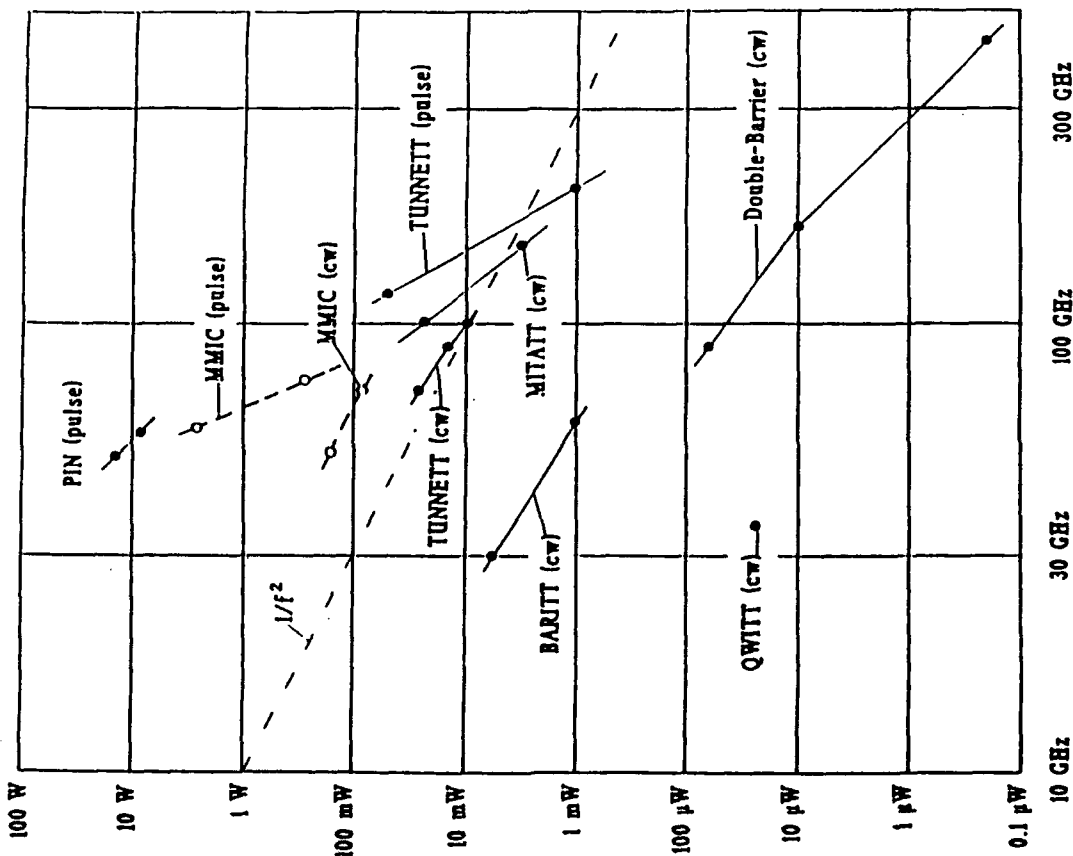
 10 - 12 % for silicon devices

Gunn 2 - 5 % for GaAs devices
 5.7 % at 94 GHz for InP devices
 (12 % at 60 GHz, pulsed, for InP)

TUNNETT 2 % at 94 GHz

BARRITT 0.4 % at 60 GHz

MITATT 0.5 % at 150 GHz



Cw and pulsed output power
of different mm-wave devices

Noise measure

$$M = \frac{F - 1}{1 - 1/G} = \frac{\overline{u_n^2}/B}{4kT_0|R_D|}$$

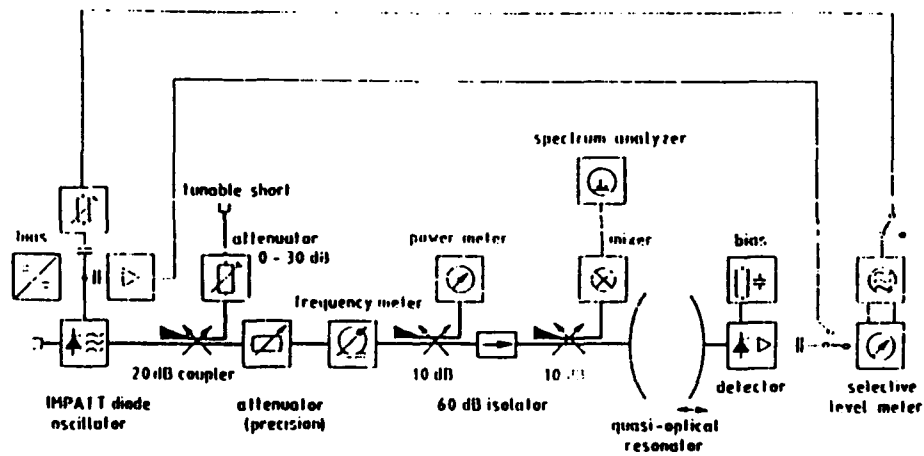
F : Noise figure
 G : amplification
 $\overline{u_n^2}$: primary noise voltage source
 B : bandwidth
 k : Boltzmann constant
 T_0 : room temperature
 R_D : negative diode resistance

$$M = \frac{P}{kT_0 B} \frac{\Delta f_{rms}^2 Q_{ex}^2}{f_0^2}$$

94 GHz : $M_{TUNNETT} \approx 18$ dB

$M_{IMPATT} \approx 21$ dB

P : rf power
 Δf_{rms} : rms frequency deviation
 f_0 : oscillation frequency
 Q_{ex} : external quality factor



Noise measurement set-up

**TECHNOLOGY DEVELOPMENTS TOWARDS NANOMETRIC
STRUCTURES**

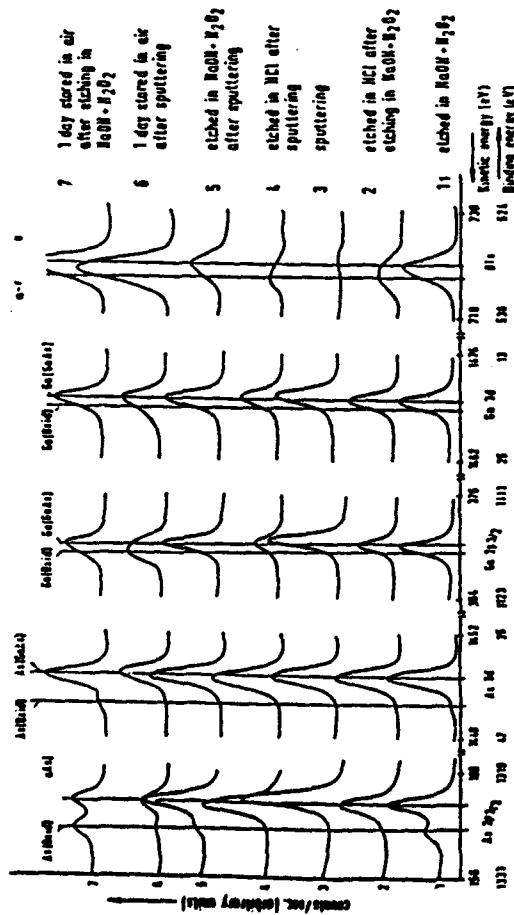
H. L. Hartnagel

University of Darmstadt • Germany

Technology Developments towards Nanometric Structures

H. L. Hartnagel
Techn. University Darmstadt
Inst. f. Hochfrequenztechnik
Merckstr. 25
61 Darmstadt
Germany

-) Basic Considerations towards Nanometric Devices
-) Selective Epitaxy
- i) E-beam Lithography and soft Electrolytic Processes:
Anodic, Etching and Cathodic metal deposition.
- Local-Structure Deposition by point-like Electrode Current scanned by Piezo-Actuators.
-) Evaluation of Nanometric Surfaces
-) Outlook



XPS-spectra of GaAs(100) surfaces after different surface treatments
The As 2p_{3/2}, As 3d, Ga 2p_{3/2}, Ga 3d and O 1s core level peaks are shown

Basic Considerations towards Nanometric Devices

- Dimensional Reduction

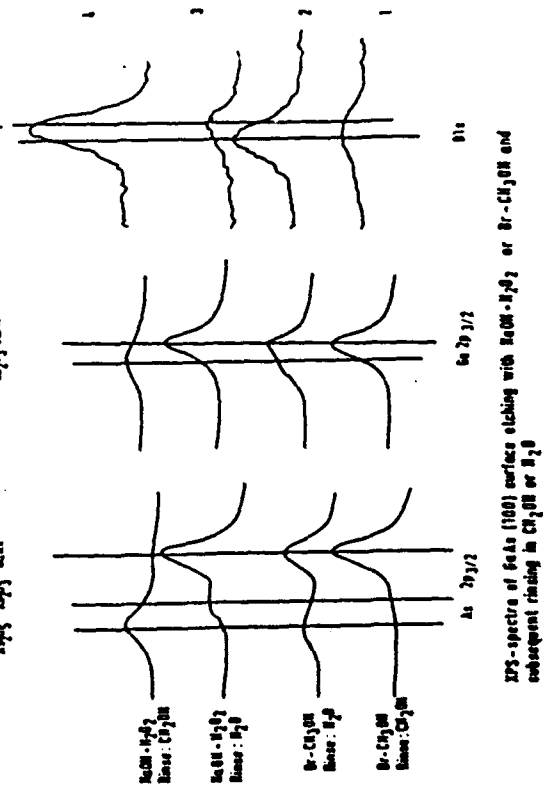
- a) hot-electron transport \longrightarrow High Speeds
- b) high packing densities for highly complex signal processing
- c) impedance optimization for capacitances based on optimal space-charge layers for mm waves:

$$|Z_c| = \frac{1}{\omega C_j}$$

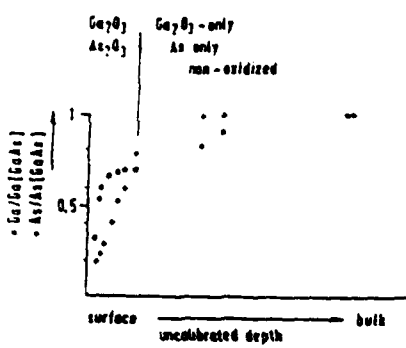
- d) minimization of heat loss for current crowding along emitter periphery of power transistors for mm waves

- Increase of Surface to Volume Ratio

- a) no damage acceptable leading to traps
- b) space-charge layer minimization to obtain carrier-density independent, controllable conditions

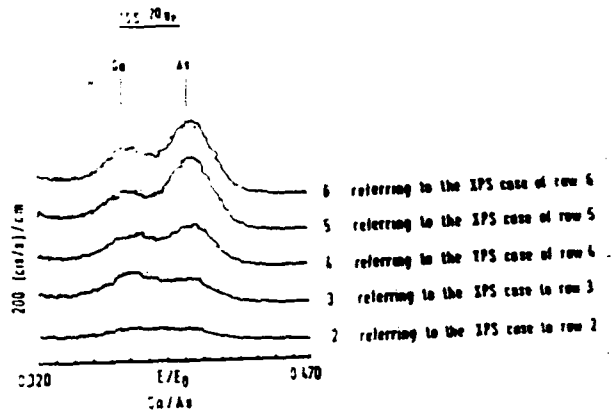


XPS-spectra of GaAs(100) surfaces etching with H2O2 + H₂O₂ or H₂O₂ and subsequent rinsing in CH₃OH or H₂O

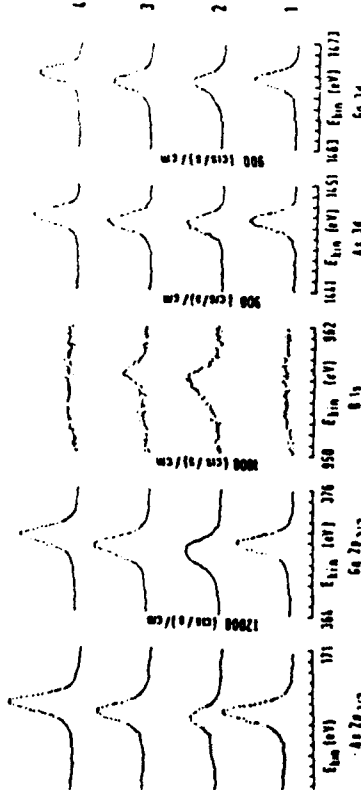


Depth profile of Ga and As by detailed ^{75}As -ISS analysis
Ge_xGeAs: concentration of Ga in GeAs-compound
As_xGeAs: concentration of As in GeAs-compound
Ge: concentration of As after the given etch step
As: concentration of As after the given etch step

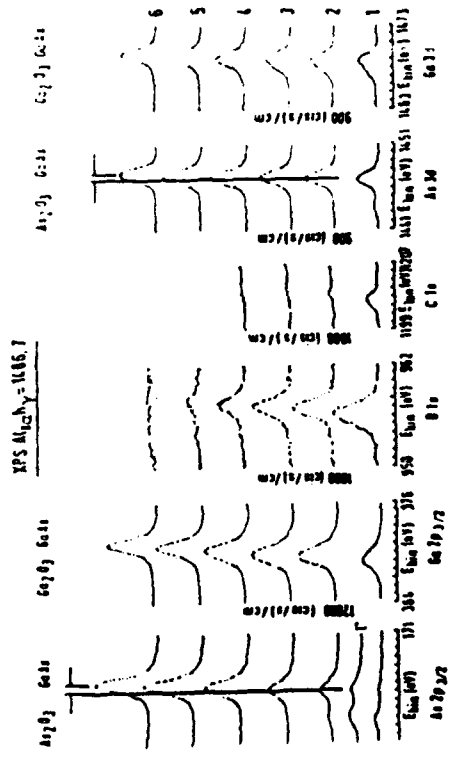
ISS spectra of GaAs



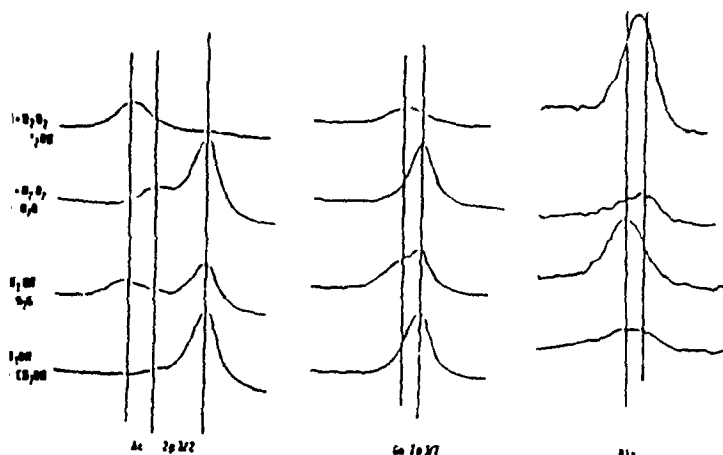
3 Ge - ISS spectra



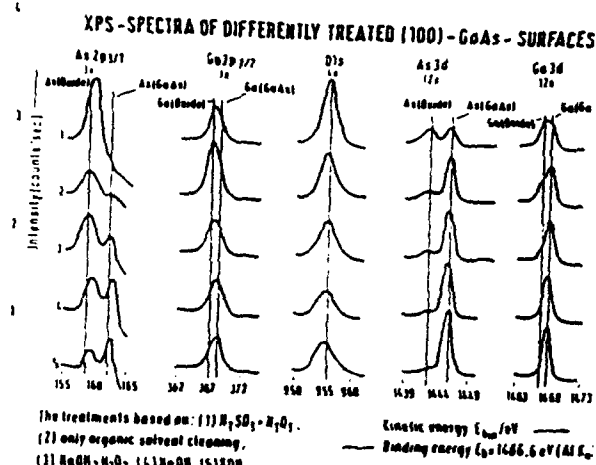
row 1 identical with Fig. 3 row 6
row 2 after recrystallization in air for 30 min
row 3 after short heating
row 4 after heavy Ar etching similar to that before spectrum given by Fig 3 row 6



2.2.2. *Specular* original bats-sample as inserted into the vacuum system (row 2 to 5 subsequent etching with Ar^+ of different intensities and duration times last each step when Ar^+ was used 1 hr is much heavier than He^+)



XPS-spectra of GaAs(100) surface etching with $\text{NaOH} + \text{H}_2\text{O}_2$ or $\text{Br}-\text{CH}_2\text{OH}$ and subsequent rinsing in CH_2OH or H_2O

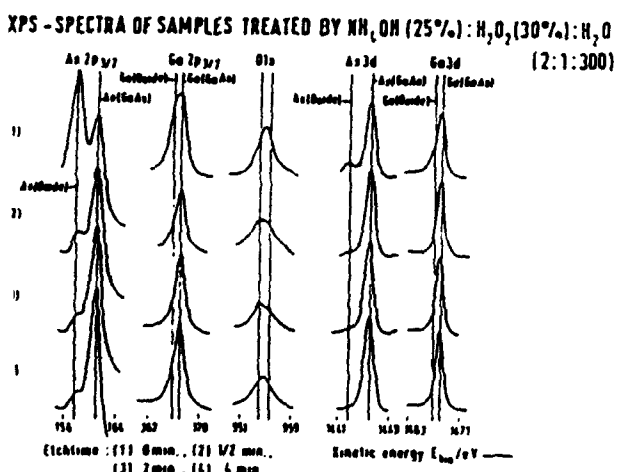


The treatments based on: (1) $\text{H}_2\text{SO}_4 + \text{H}_2\text{O}_2$,

(2) only organic solvent cleaning,

(3) $\text{NaOH} + \text{H}_2\text{O}_2$, (4) NaOH , (5) ION

— Kinetic energy E_{kin}/eV
— Binding energy $E_b = 1686.6 \text{ eV} (\text{Al K}\alpha)$



Etchtime: (1) 0 min., (2) 1/2 min.,

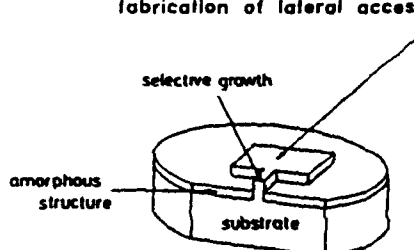
(3) 2 min., (4) 4 min.

Selective Epitaxy

Starting with high-temperature capable amorphous mask

Growth required with good quality on side walls

Same growth rate as with volume case to allow fabrication of lateral access structures



: E-beam Lithography and Soft Electrolytic Processes:

Anodic Etching and Cathodic Metal Deposition

- 1) nanometric structurization by electron-beam illumination
- 2) gas-plasma etching through E-beam resist pattern
 - a) steep structures possible
 - b) but ion bombardment minimized only by protective grids or plasma potential control
- 3) anodic wet etching through resist pattern
 - a) side-steepness by combined adjustment of bias and opt. illumination
 - b) passage through various epitaxial and doping layers by optical hole generation as required for anodic process

Ion-Beam Lithography

H^+ , 60 KeV into PMMA
spread: $0.1 \mu m$
no proximity effect
no backscattering on Si

-15.

E-Beam Lithography

pos. resist

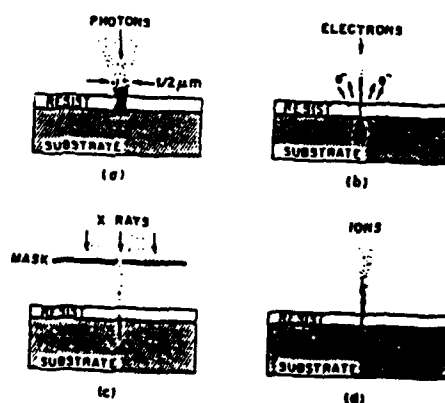
PMMA polymethyl metacrylate
PBS polybutane -1 sulfone
resolution: $1 \mu m$

neg. resist:

COP Polyglycidyl methacrylate -
co- ethyl acrylate
resolution due to swelling: $1 \mu m$

limitation:

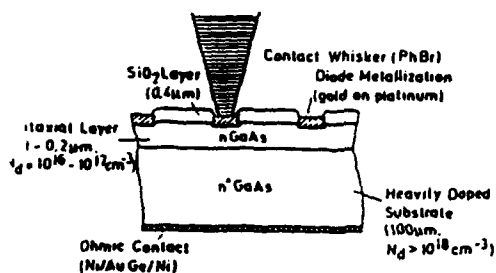
electron scattering, 20 keV
($\lambda \sim 1 \text{ \AA}$); proximity effect



Types of advanced lithographic methods. (a) Optical Lithography, (b) Photo-beam Lithography, (c) X-ray Lithography, (d) Ion-beam Lithography.

hottky-Barrier-Dioden für Sub-mm-Wellen-Mischung

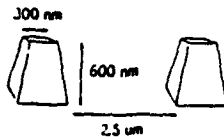
Continuation: Electrolytic Processes



Schematischer Diodenquerschnitt

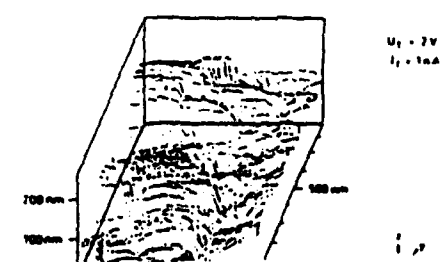
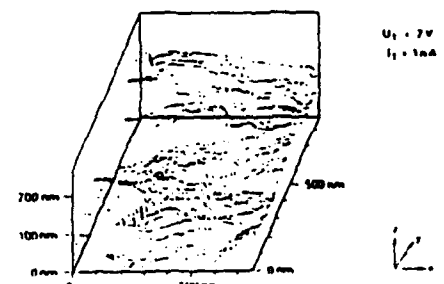
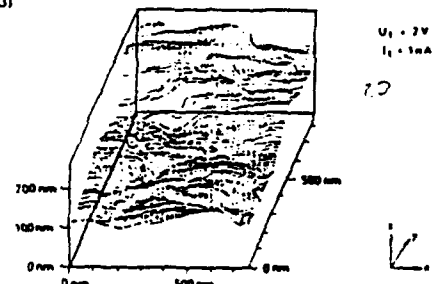
Selected structures (1): 19

of GaAs towers

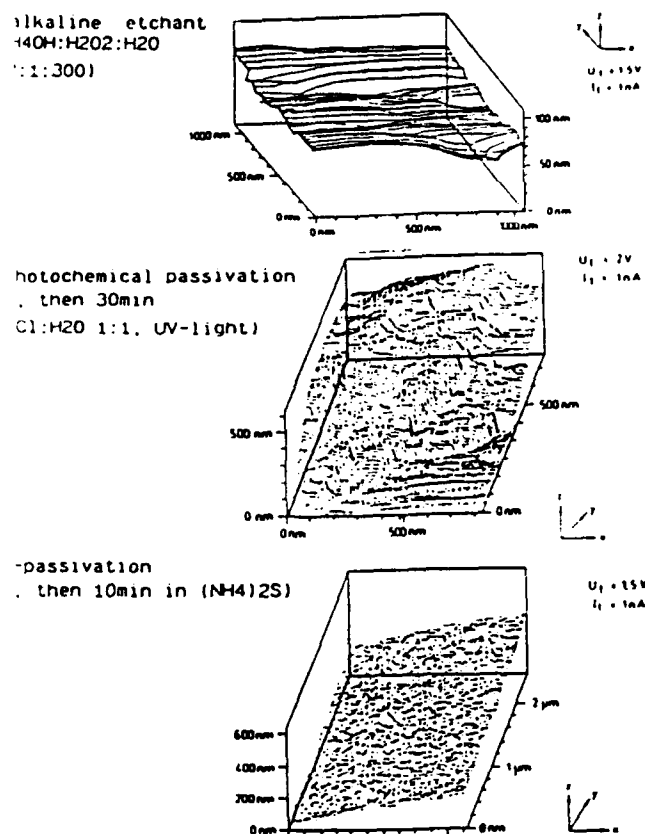


- 3)
 - c) Selection of electrolyte: reaction-limited solution instead of diffusion limited one
 - d) Equal solution rates for each of the components of the semiconductor
 - e) pulsed-bias
- 4) cathodic metal deposition through resist pattern
 - a) resulting metal thickness proportional to local current density
 - b) therefore illumination to increase current flow over layers of reduced conductivity
 - c) sometimes side-wall metallization avoided by intermediate insulating epi layer and deposition in darkness

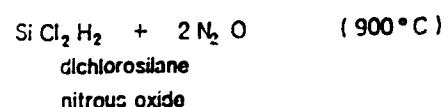
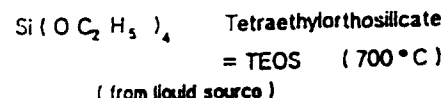
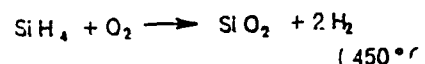
Changes of surface structure
in air after treatment b)
measured by STM
(15min between each
measurement)



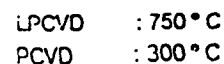
STM-Studies of GaAs(100) Surfaces after different etch treatments



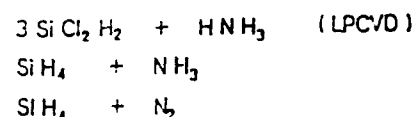
SiO_2



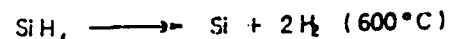
Si_3N_4



(final chip passivation against scratch protection, moisture barrier, sodium barrier)



Poly Si (larger stability than Al)



Chemical Vapour Deposition

(e.g. SiO_2 to insulate multilevel metalisation)

1) atmospheric-pressure CVD

2) low-pressure CVD

3) plasma-assisted CVD

- Hot-wall reactor

- Low-Temperature CVD for Si submicron techn.)

(reduced thermal broadening of dopants

by diffusion)

energy-enhanced CVD

(possible: SiO_2 at 150 Å/min for 50°C

by UV light; in

* Chemical Vapour Deposition *

1984, ed.: M.D. Robinson et al

Electrochem. Soc., Pennington, USA)

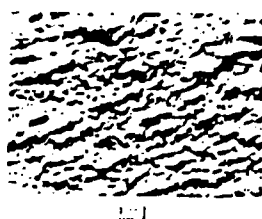
Cont.: Electrolytic Processes

d) metal sequences by several cathodic steps as required for

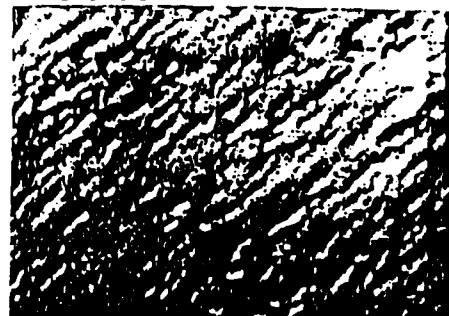
- ohmic contacts
- Schottky contacts
- good adhesion
- high stability (diffusion barrier)

e) selective deposition on semiconducting islands in semiconducting surface in darkness

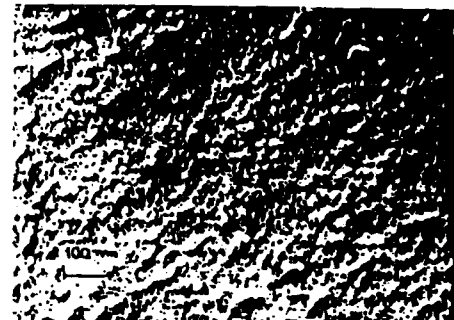
f) pulsed bias



DOUBLE-REPLICA TEM PHOTOGRAPH OF
 H_2SO_4 ; H_2O_2 ETCHED GaAs SURFACE



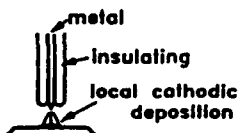
DOUBLE-REPLICA TEM PHOTOGRAPH OF Al-FILM SURFACE



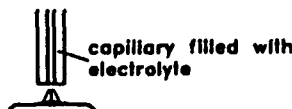
Local Structure Deposition by
Point-like Electrode Current
scanned by Piezo-Actuators

1) Point Current Source by

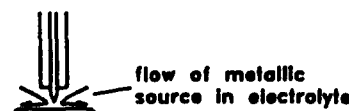
a) needle with insulation except on tip



b) fine capillary in conducting electrolyte

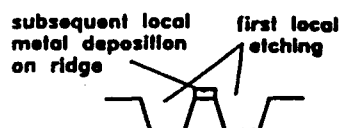


2) Pulsed Bias for optimization of results



3) Position control by piezo actuators similar to
Scanning Tunnelling Microscope.

4) Combination with local etching under point
current source

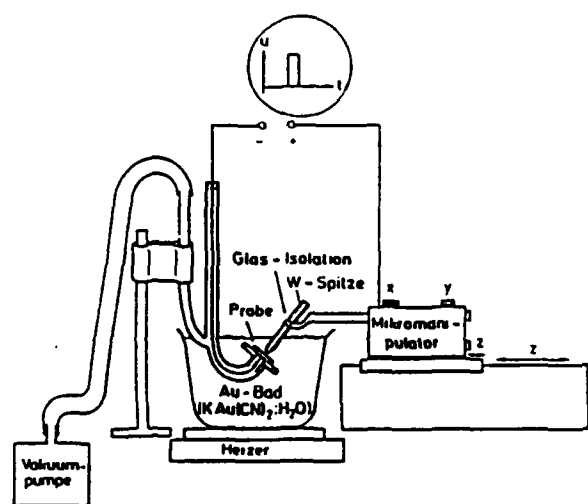


5) Surface preparation by focussed-electron
(SEM) or focussed-ion illumination for
local etching with point or line
metallizations.

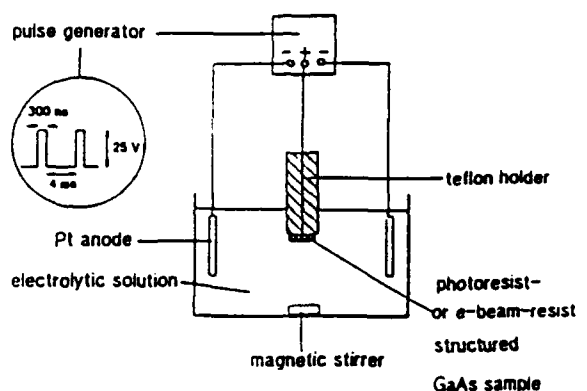
Direct writing of submicron metallisation patterns on GaAs

Development of a new process for writing submicron metallisation patterns with a tungsten-tip on n-GaAs in an electrolytic Au-bath

Experimental set-up

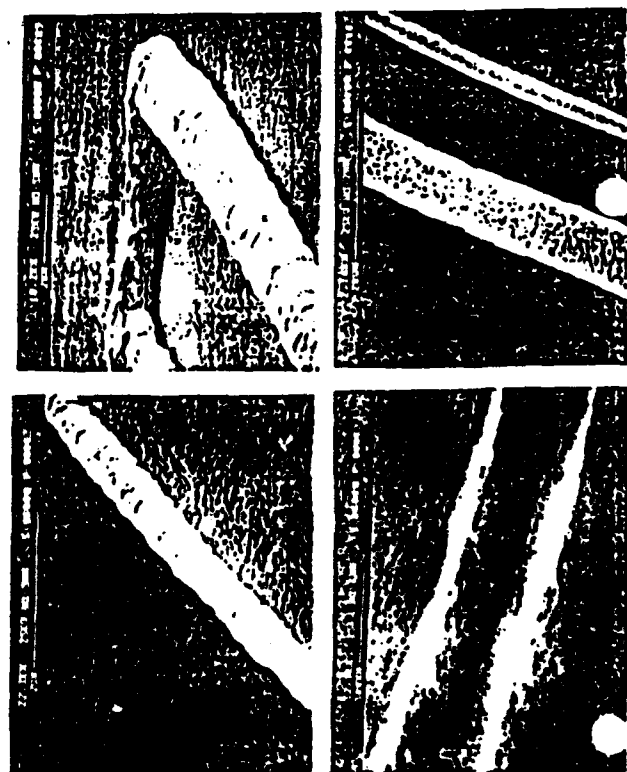
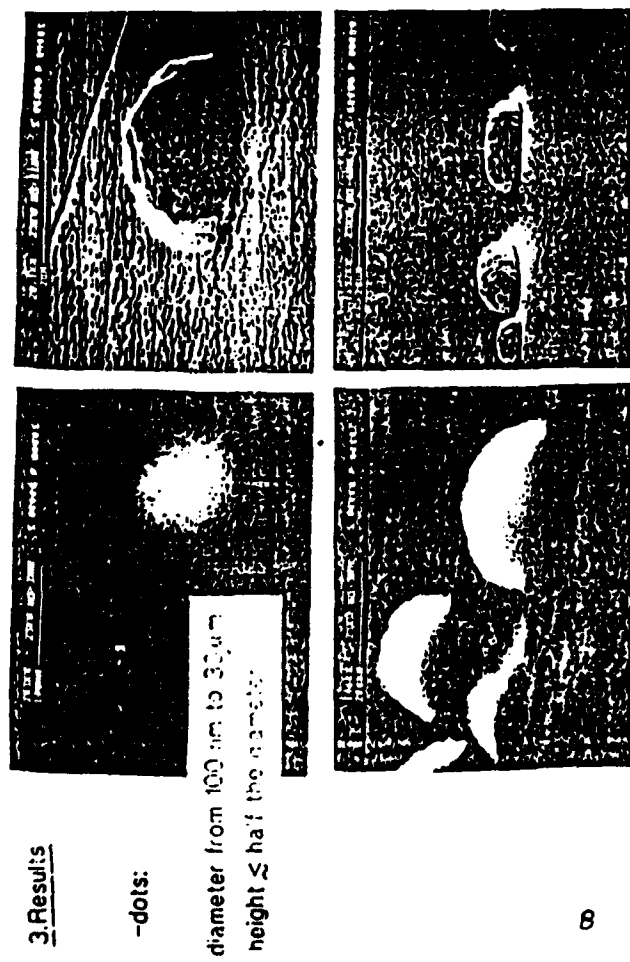


experimental setup:



Pt-solution temperature: 40°C

etch rate: 4 nm/pulse



Evaluation of Nanometric Surfaces

- 1) STM and its derivatives in particular scanning tunnelling luminescence
- 2) Electron-beam evaluation
 - a) SEM
 - b) Scanning beam cathodoluminescence
 - c) TEM, particularly at angle or transverse; possibly with double replica techniques.
- 3) Focussed-ion techniques
incl. Ion Scattering Spectroscopy

- Soft structurization
- Local epitaxy
- relevant structure characterization
 - will give
- mm-wave devices and IC's
- high packing densities for complex signal processing with short interconnection delays
- extension to μ m waves
- broad-band approach

OPTICAL CONTROL OF MILLIMETER - WAVE CIRCUITS

T. Itoh

UCLA • USA

PROGRESS OF A TUNABLE ACTIVE BANDPASS FILTER

Introduction

- Filter in MMIC form is difficult to realize because of the low Q value for MMIC element.
→ **Active Filter**
- Direct optical control of microwave devices has been an area of growing interest.
→ **Tunable Active Bandpass Filter Using MESFETs**
- Use of both negative resistance and reactance of an active device has design potential in microwave active circuit.
→ **Tunable Active Bandpass Filter Using one MESFET**

Professor Tatsuo Itoh

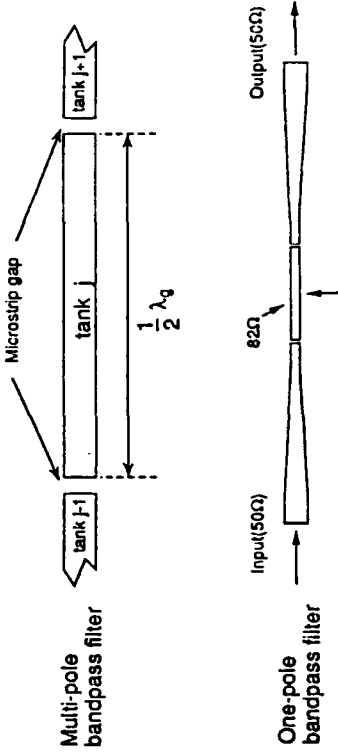
Electrical Engineering Department
University of California, Los Angeles
U.S.A.

AGENDA

- Introduction
- Passive Bandpass Filter
- Active Bandpass Filter
 - coupled negative resistance method
- Tunable Active Bandpass Filter Using Varactor Diode
- Tunable Active Bandpass Filter Using MESFET as Varactor
 - optical tuning as well as electrical tuning
- Tunable Active Bandpass Filter Using Three-terminal MESFET Varactor
 - different ways of using MESFETs as varactors
 - passive mode, active mode
- Conclusion

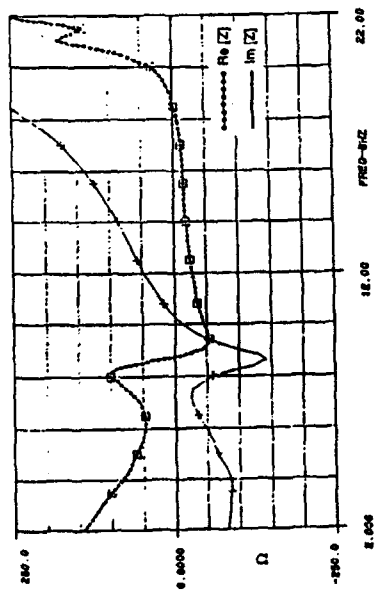
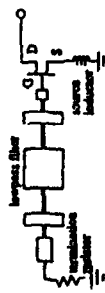
Microstrip-line Bandpass Filter

- Passive circuit
 - loss is large, Q value is low
 - Half-wavelength resonator
 - determine the frequency of each pole
- End-coupled bandpass filter
 - Chebyshev response if lossless



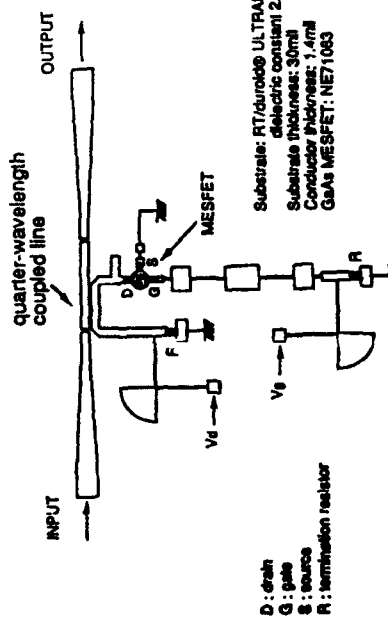
Active Bandpass Filter

Simulation Result of Negative Resistance Using NE71083

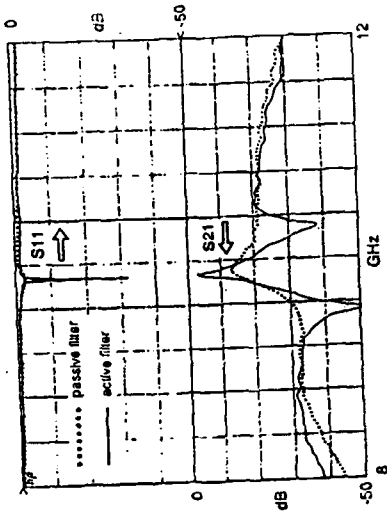


Active Bandpass Filter

- Coupled negative resistance –
compensate the loss of resonant tank, increase the Q value
- Fixed center frequency of passband

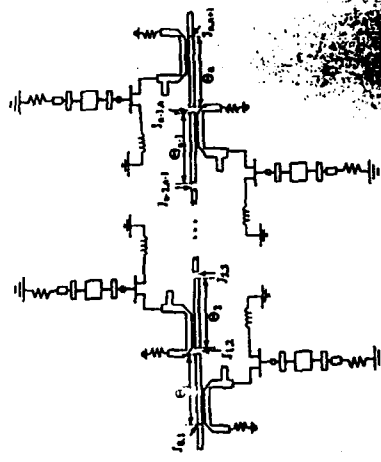


- Comparison of passive filter and active filter
- The Q value is increased by coupled negative resistance method



Active Bandpass Filter

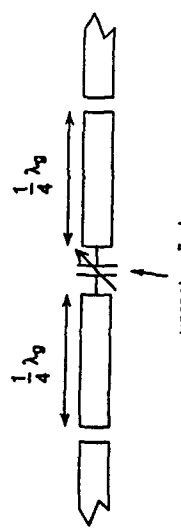
- Multi-pole configuration
- Coupled negative resistance in each tank circuit
- Chebyshev response



Tunable Active Bandpass Filter Using Varactor Diode

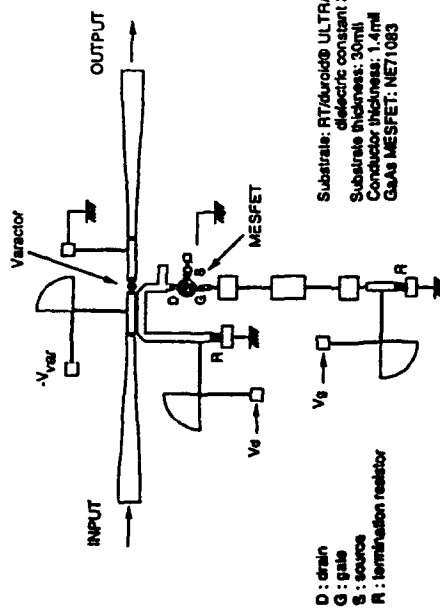
The function of varactor diode:
change the effective electrical length of half-wavelength resonant tank, thus change the center frequency of the passband

Two quarter-wavelength sections are connected by the varactor diode



$C=C(V)$, variable capacitance

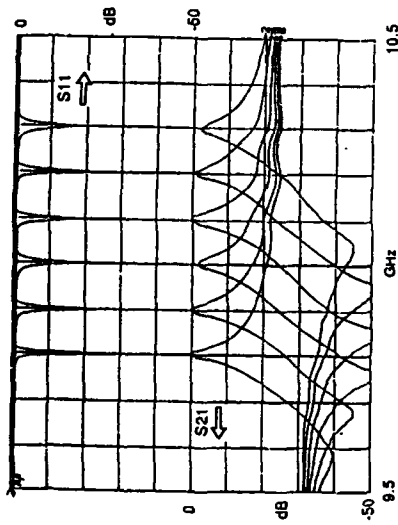
Tunable Active Bandpass Filter Using Varactor Diode



Substrate: RT/Varicell ULTRALAM
dielectric constant 2.35
Substrate thickness: 30 mil
Conductor thickness: 1.4 mil
GaAs MESFET: NE71083

Tunable Active Bandpass Filter Using Varactor Diode

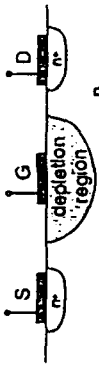
- 500 MHz tuning range
- MESFET bias voltage changes to compensate the different Q value of the tank



IEEE Trans. on MTT, MTT-38, December 1990

Tunable Active Bandpass Filter Using

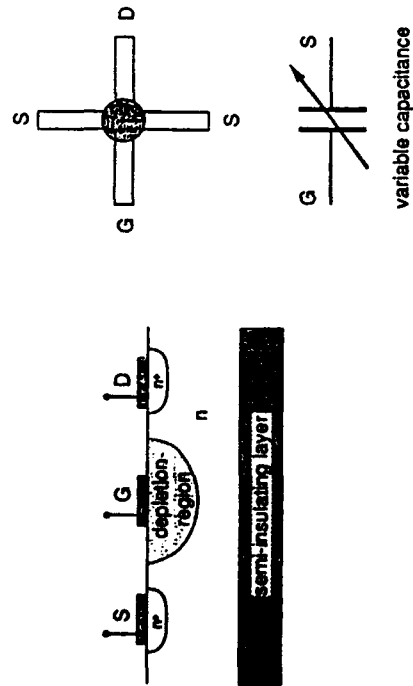
- Gate-to-source capacitance is a function of bias V
- used to replace the varactor diode



Semi-insulating layer

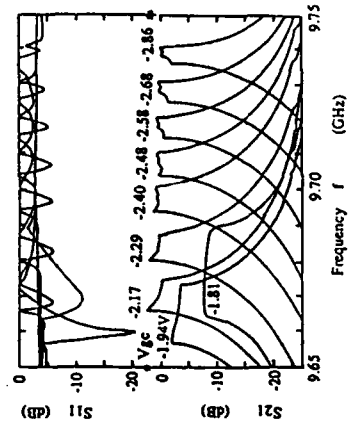
Tunable Active Bandpass Filter Using MESFET as Varactor

- Gate-to-source capacitance is a function of bias voltage
 - used to replace the varactor diode



Tunable Active Bandpass Filter Using MESFET as Varactor

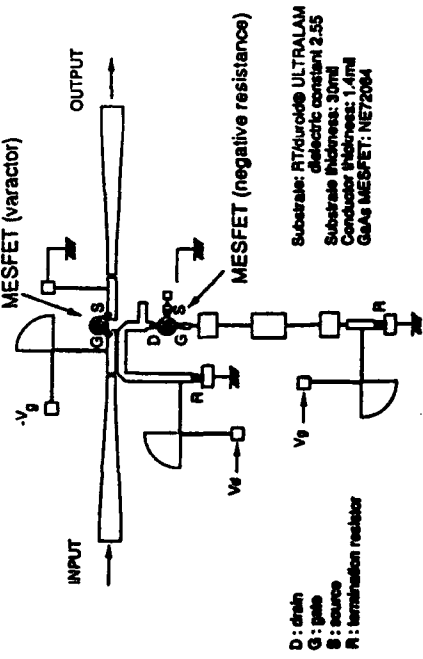
- electrical-tuning result
 - 75 MHz tuning range without compensation of Q value



IEEE Microwave and Guided Wave Letters, May 1991

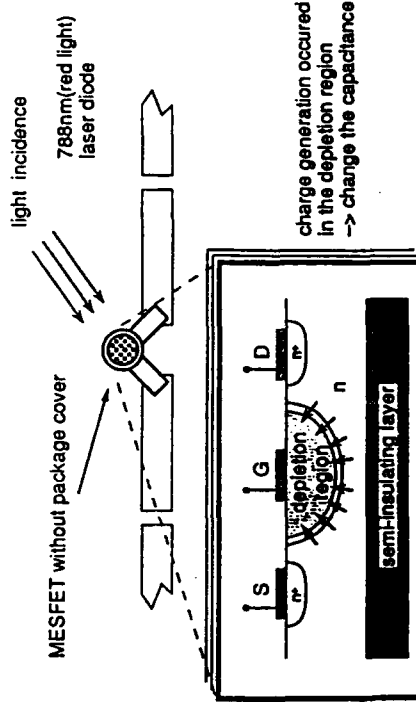
Tunable Active Bandpass Filter Using MESFET as Varactor

- Both devices in this circuit are MESFETs - advantage



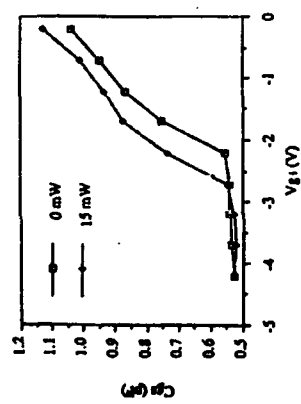
Tunable Active Bandpass Filter Using MESFET as Varactor

- Optical control of solid state device



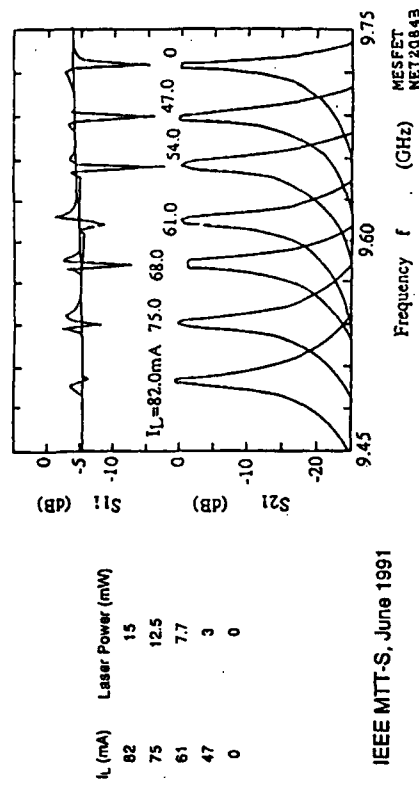
Tunable Active Bandpass Filter Using MESFET as Varactor

C_{GS} of the MESFET as a function of V_{GS} at two different levels of light
Illumination: $P_L = 0$ mW and $P_L = 15$ mW (P_L is the output power of
a semiconductor laser diode, Sharp LT021MC0)



Tunable Active Bandpass Filter Using MESFET as Varactor

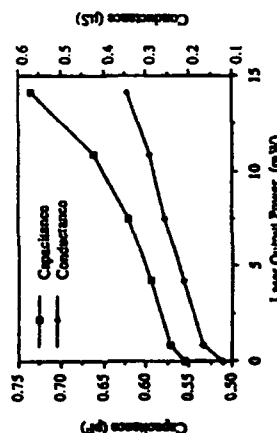
- optical-tuning result
- 225 MHz tuning range
- MESFET (negative resistance) bias voltage changes to compensate the different Q value of the tank



IEEE MTT-S, June 1991

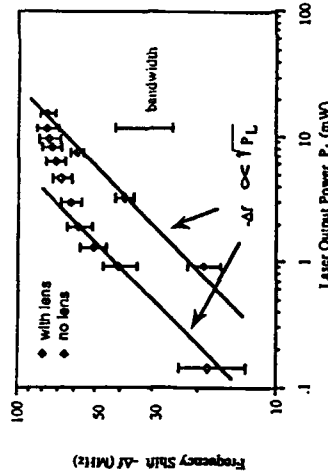
Tunable Active Bandpass Filter Using MESFET as Varactor

C_{GS} and G_{GS} as a function of the output power from a
semiconductor laser diode (Sharp LT021MC0).
Bias voltage (V_{GS}) = -2.21V



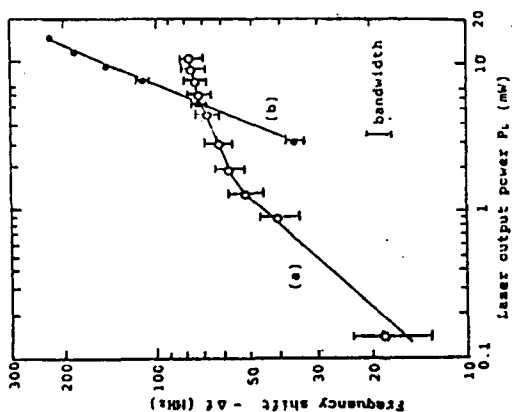
Tunable Active Bandpass Filter Using MESFET as Varactor

- Optical Tuning
– frequency shift v.s. laser power



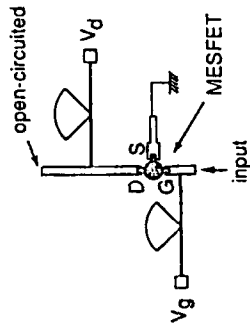
Tunable Active Bandpass Filter Using MESFET as Varactor

- Optical Tuning - frequency shift v.s. laser power
 - (a) constant bias voltages
 - (b) compensation case (varying bias voltages)



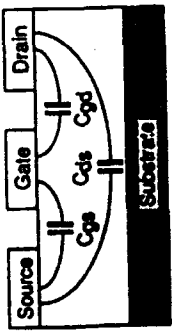
Using Three-terminal MESFET Varactor in the Passive Mode

- Reactance-tuning circuit
- The MESFET is biased in the passive mode
 - The impedance at the input port is nearly reactance
 - If resistance presents at the input port - Q value is affected



Tunable Active Bandpass Filter Using Three-terminal MESFET Varactor

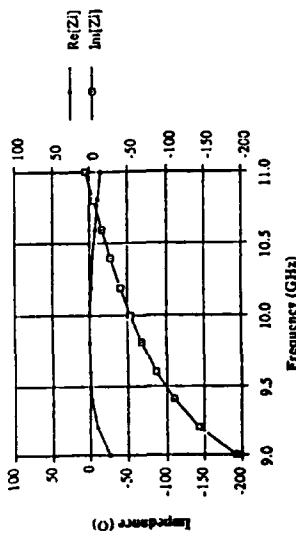
- MESFET in three-terminal application



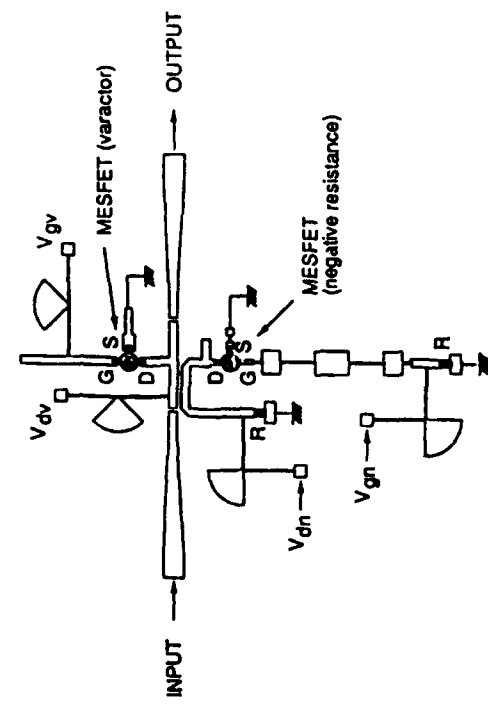
- Three capacitances are involved

Tunable Active Bandpass Filter Using Three-terminal MESFET Varactor in the Passive Mode

- Simulation result of reactance-tuning circuit

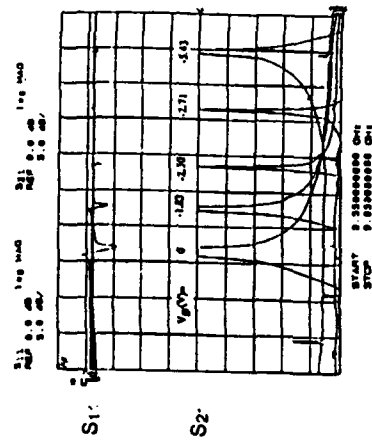


Tunable Active Bandpass Filter Using Three-terminal MESFET Varactor in the Passive Mode



Tunable Active Bandpass Filter Using Three-terminal MESFET Varactor in the Passive Mode

- electrical-tuning result
- no degradation occurs at $V_{gr}=0$
- 170 MHz tuning range

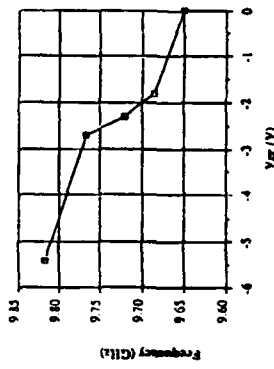


Tunable Active Bandpass Filter Using Three-terminal MESFET Varactor in the Passive Mode



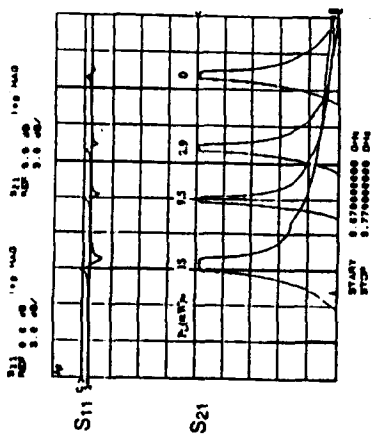
Tunable Active Bandpass Filter Using Three-terminal MESFET Varactor in the Passive Mode

- electrical-tuning result
- V_{gr} increases
 - C_{gs} and C_{gd} increase
 - electrical length increases
 - frequency decreases



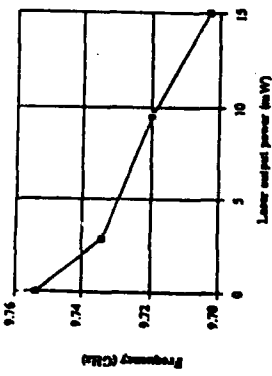
- The position to add the reactance – (b) is chosen

- optical-tuning result
 - no degradation occurs
 - 50 MHz tuning range



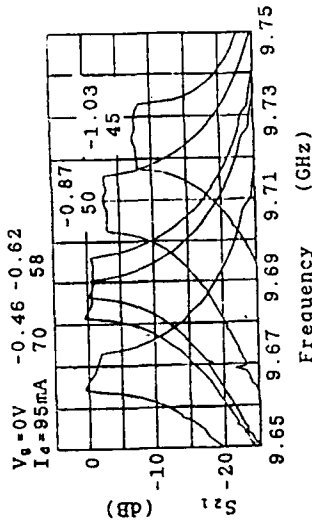
Tunable Active Bandpass Filter Using Three-terminal MESFET Varactor in the Passive Mode

- optical-tuning result
 - Laser output power increases
 - C_{GS} and C_{DS} increase
 - electrical length increases
 - frequency decreases



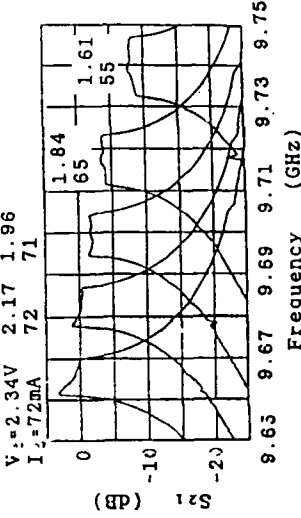
III.C. Frequency Tuning

- Preliminary result from the filter using two-terminal MESFET varactor
 - no degradation occurs
 - Passband shifts when V_g of the negative resistance MESFET varies from -1.03V to 0V
 - V_d of the negative resistance MESFET is kept constant (-2.19V)
 - V_g of the MESFET varactor is kept constant (-2.19V)



Tunable Active Bandpass Filter Using Three-terminal MESFET Varactor in the Active Mode

- Preliminary result from the filter using two-terminal MESFET varactor
 - Passband shifts when V_d of the negative resistance MESFET varies from 1.61V to 2.34V
 - V_g of the negative resistance MESFET is kept constant (-0.46V)
 - V_g of the MESFET varactor is kept constant (-2.20V)



Tunable Active Bandpass Filter Using Three-terminal MESFET Varactor in the Active Mode

Some observations from the preliminary result

1. Tuning range of V_d -tuning is larger than tuning range of V_g tuning.
2. The tuning direction of V_g -tuning can be explained by the depletion-layer capacitance.
 - V_g increases \rightarrow capacitance increases \rightarrow electrical length increases
 \rightarrow frequency decreases
 - 3. The tuning direction of V_d -tuning cannot be explained by the depletion-layer capacitance.
 - V_d increases \rightarrow capacitance decreases \rightarrow electrical length decreases
 \rightarrow frequency increases \rightarrow not agree with experimental result?

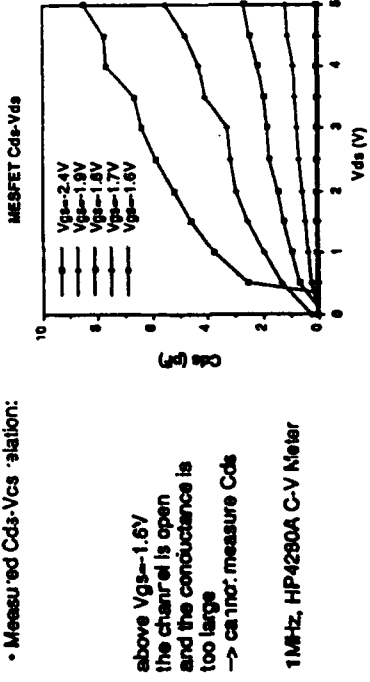
Tunable Active Bandpass Filter Using Three-terminal MESFET Varactor in the Active Mode

Try to design a tunable active bandpass filter using only one MESFET

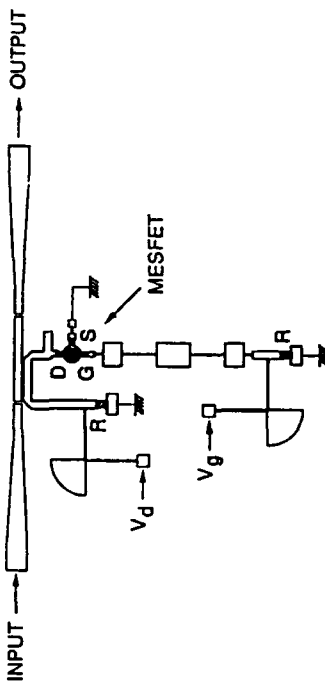
- Capacitance variation is larger \rightarrow Tuning range is wider
- If $V_{gs} = -1.6V$ is selected, capacitance variation is optimum
- To keep the insertion loss of active filter at 0dB, the separation of quarter-wavelength coupled line is adjusted from 18 mil to 8 mil
- Then, the gate voltage of the negative resistance needed to keep the insertion loss at 0dB is changed from -0.46V to -1.6V

Tunable Active Bandpass Filter Using Three-terminal MESFET Varactor in the Active Mode

- Active-channel capacitance is important when the MESFET varactor is operated in the active mode.
- C_{ds} is dominant in V_d -tuning
- Measured $C_{ds} \cdot V_{gs}$ -station:

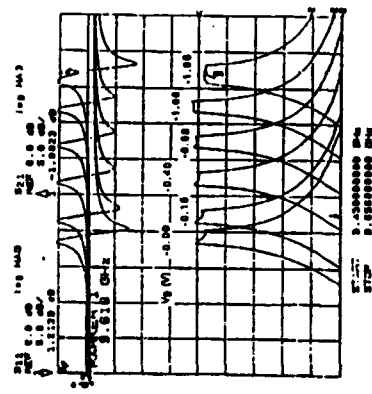


Tunable Active Bandpass Filter Using Three-terminal MESFET Varactor in the Active Mode



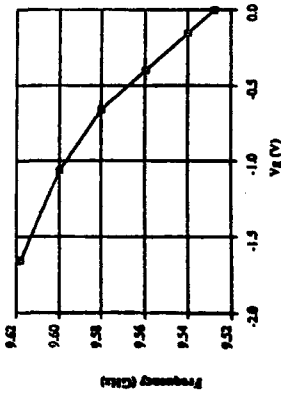
Tunable Active Bandpass Filter
Using Three-terminal MESFET Varactor
in the Active Mode

- electrical-tuning result of V_g -tuning
• 90 MHz tuning range – smaller than V_d tuning



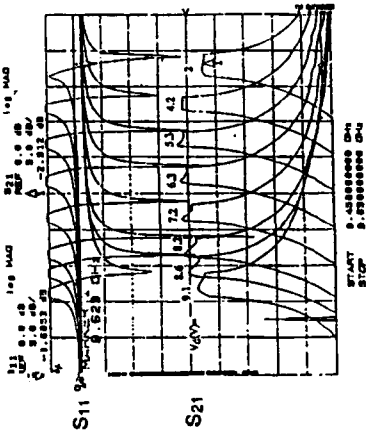
Tunable Active Bandpass Filter
Using Three-terminal MESFET Varactor
in the Active Mode

- electrical-tuning result of V_g -tuning
 - V_g increases
 - C_{gs} and C_{gd} increase
 - electrical length increases
 - frequency decreases



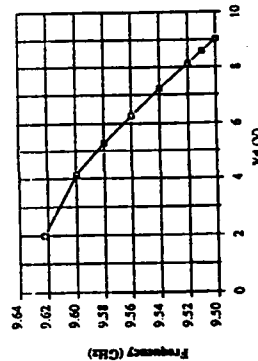
Tunable Active Bandpass Filter
Using Three-terminal MESFET Varactor
in the Active Mode

- electrical-tuning result of V_d -tuning
• 120 MHz tuning range



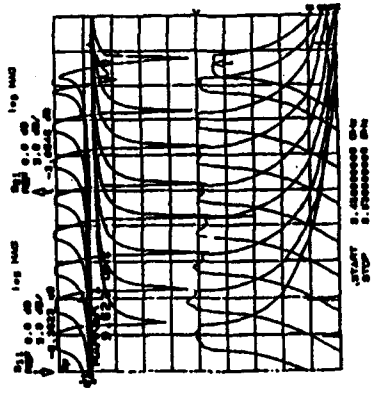
Tunable Active Bandpass Filter
Using Three-terminal MESFET Varactor
in the Active Mode

- electrical-tuning result of V_d -tuning
 - V_d increases
 - C_{gd} decreases, but C_{ds} increases and dominates
 - electrical length increases
 - frequency decreases



Tunable Active Bandpass Filter
Using Three-terminal MESFET Varactor
in the Active Mode

- electrical-tuning by both V_d and V_g
- 150 MHz tuning range



Tunable Active Bandpass Filter
Using Three-terminal MESFET Varactor
in the Active Mode

- Optical tuning range is very small (<10MHz)

- The optimum gate bias for optical tuning is above -2V e.g. -2.35V for the three-terminal MESFET varactor in passive mode

- To keep the insertion loss of the filter at 0dB, a much higher gate bias is needed.

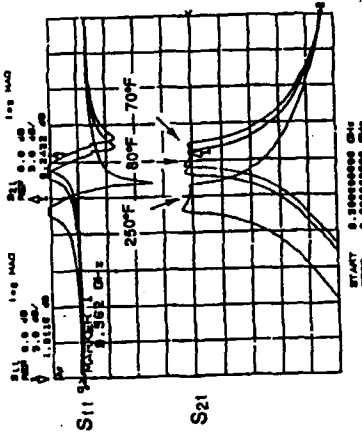
- e.g. -1.6V in V_d -tuning
-1.8V to 0V in V_g tuning

- If the optimum bias condition for the optical tuning is the same as the bias condition needed for negative resistance, optical tuning becomes practical.

Tunable Active Bandpass Filter
Using Three-terminal MESFET Varactor
in the Active Mode

- electrical-tuning by both V_d and V_g

| Resonant Cycles | V_d (V) | V_g (V) |
|-----------------|-----------|-----------|
| 0.623 | 1.83 | -1.31 |
| 0.610 | 2.17 | -1.31 |
| 0.598 | 4.59 | -1.62 |
| 0.570 | 5.48 | -1.67 |
| 0.550 | 4.64 | -1.64 |
| 0.530 | 2.54 | -1.64 |
| 0.510 | 1.21 | -1.55 |
| 0.490 | 1.21 | 0 |
| 0.470 | 3.49 | 0 |



Tunable Active Bandpass Filter
Using Three-terminal MESFET Varactor

- Temperature Stability
• 2 MHz shift from 70°F to 80°F

Conclusion

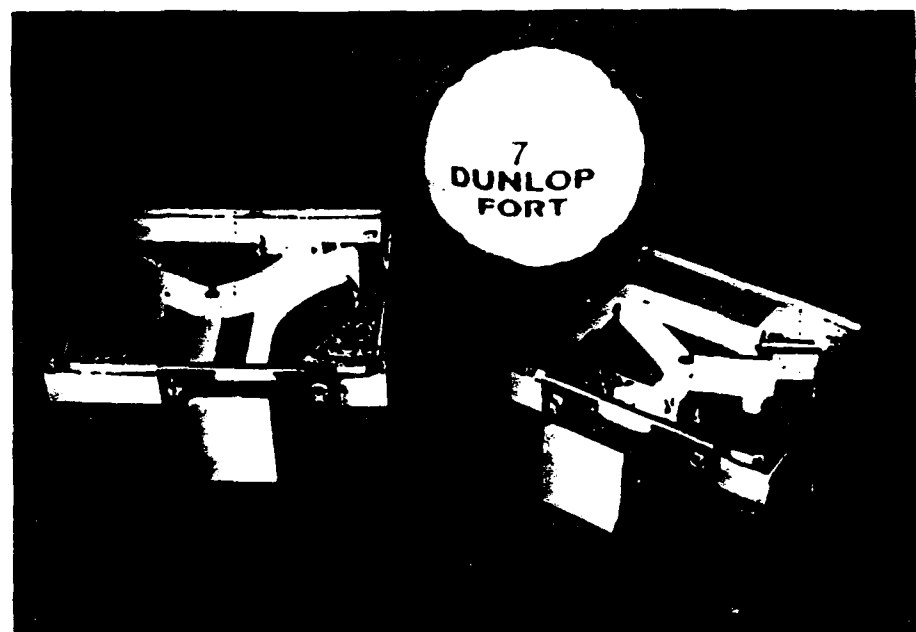
- Coupled Negative Resistance –
increase the Q value for MMIC application
- Varactor Diode –
tune the center frequency of the passband
- MESFET Varactor
 - 1. In addition to the electronic tuning, optical tuning is realized.
 - 2. Same type of device as the active device generating negative resistance.
 - 3. Operation in three-terminal mode is investigated.
 - 4. Show the possibility of using one active device to generate negative resistance and tune the frequency.

RECENT DEVELOPMENTS OF NRD - GUIDE TECHNOLOGY

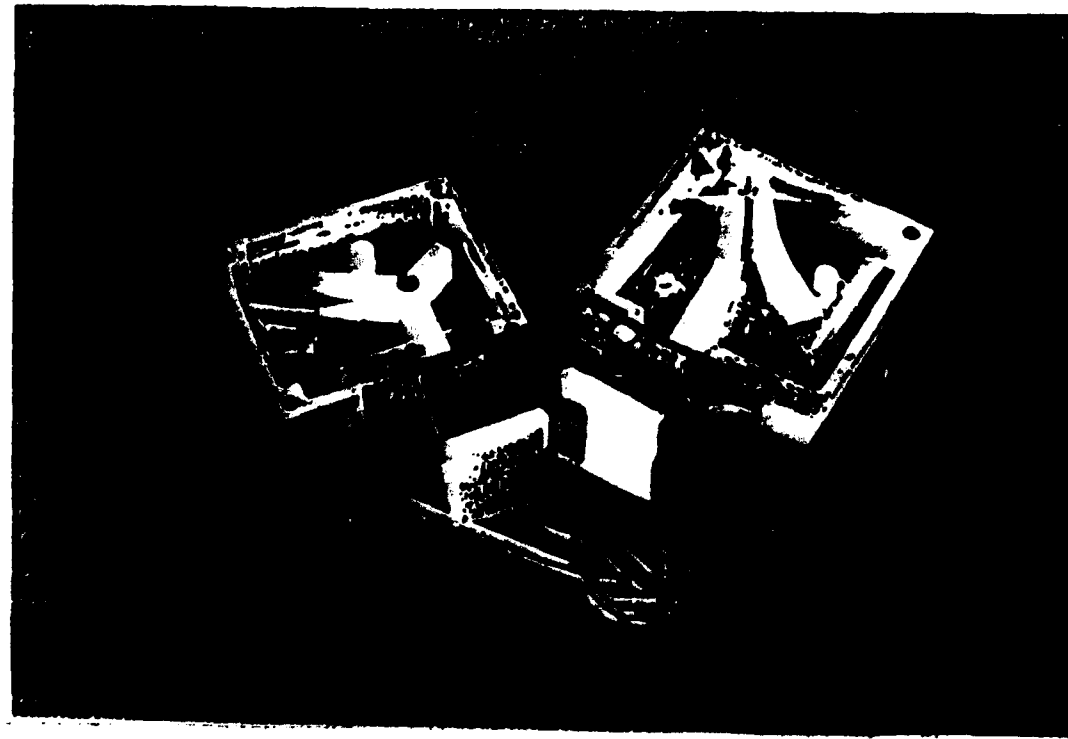
T. Yoneyama

Tohoku University • Japan

3



4



CONTENTS

Recent Developement in NRD-Guide Technology

Tsukasa Yoneyama

Research Institute of Electrical Communication
Tohoku University
Katahira 2-1-1, Aoba-ku
Sendai, 980 Japan

I. Introduction

II. NRD-Guide Integrated Circuits

2.1 RF Front Ends at 35 GHz

2.2 Gunn Oscillator at 60 GHz

III. Proposal of Planar Antennas Fed by Leaky NRD-Guides

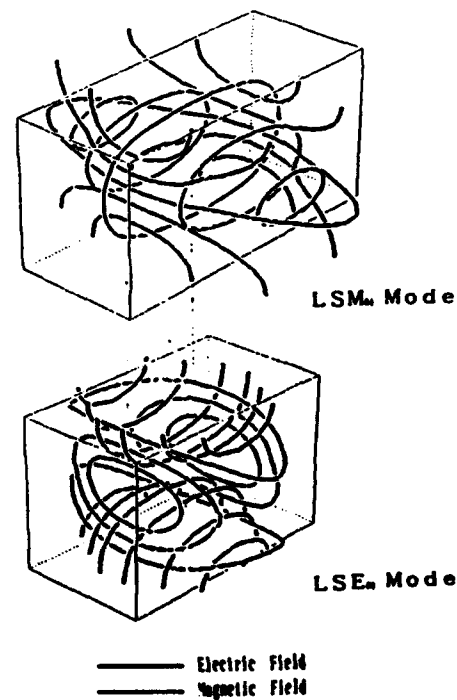
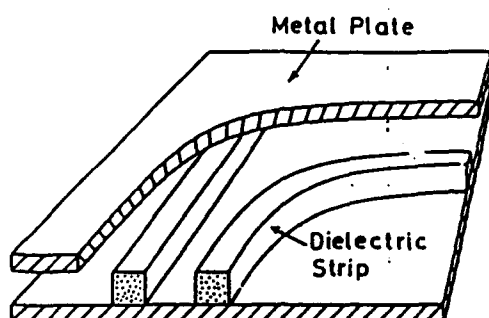
3.1 Review of Uniform Leaky NRD-Guides

3.2 Periodic Leaky NRD-Guides

3.3 Planar Antennas Fed by Leaky NRD-Guides

3.4 Applications

IV. Conclusions



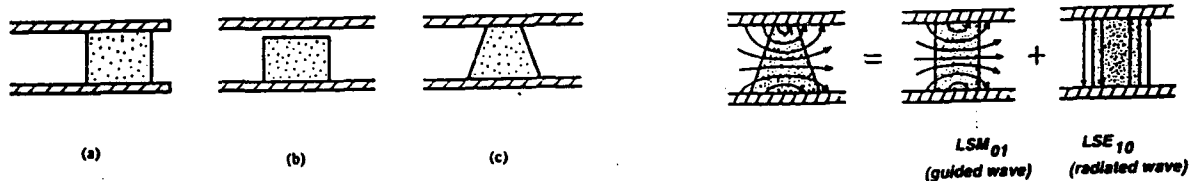


Fig.1 Classical types of leaky wave NRD-guides

Fig.2 Operation principle of leaky wave NRD-guide

5

6

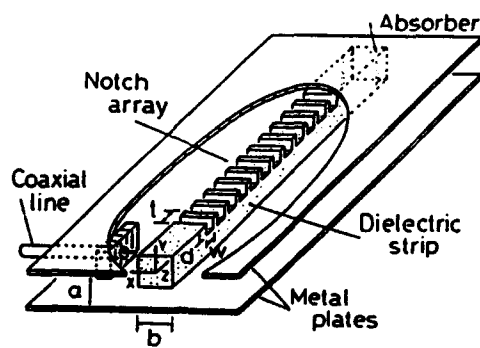


Fig.4 Leaky wave NRD-guide having notches

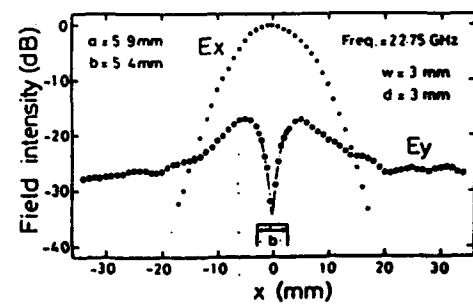


Fig.5 Field distributions in the cross sectional plane of leaky wave NRD-guide having notches

7

8

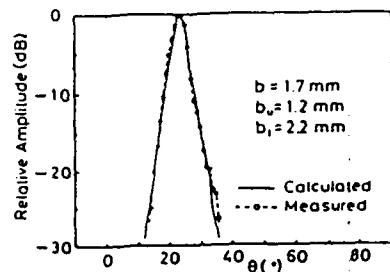
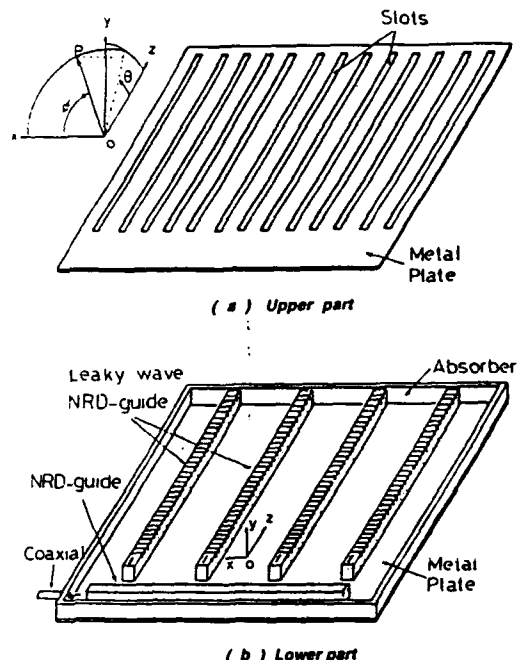


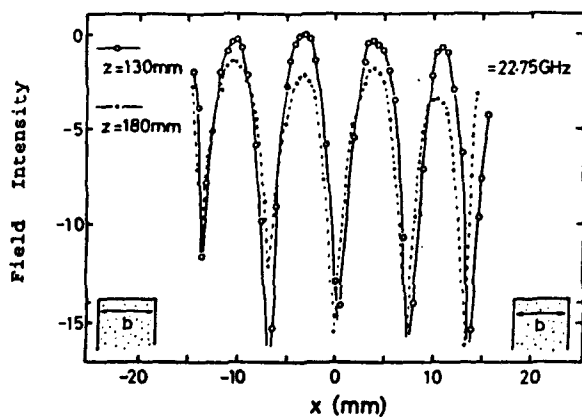
Fig.3 Radiation pattern of leaky wave NRD-guide having trapezoid dielectric strip



Structure of leaky wave NRD-guide fed planar antenna

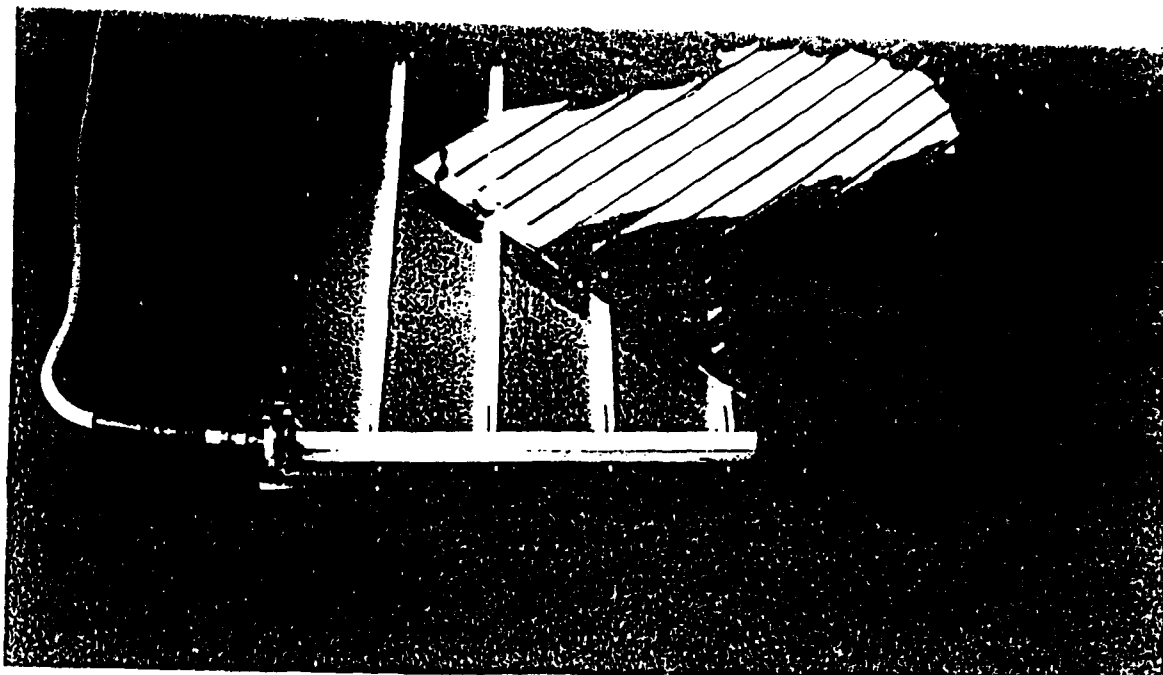
9

10

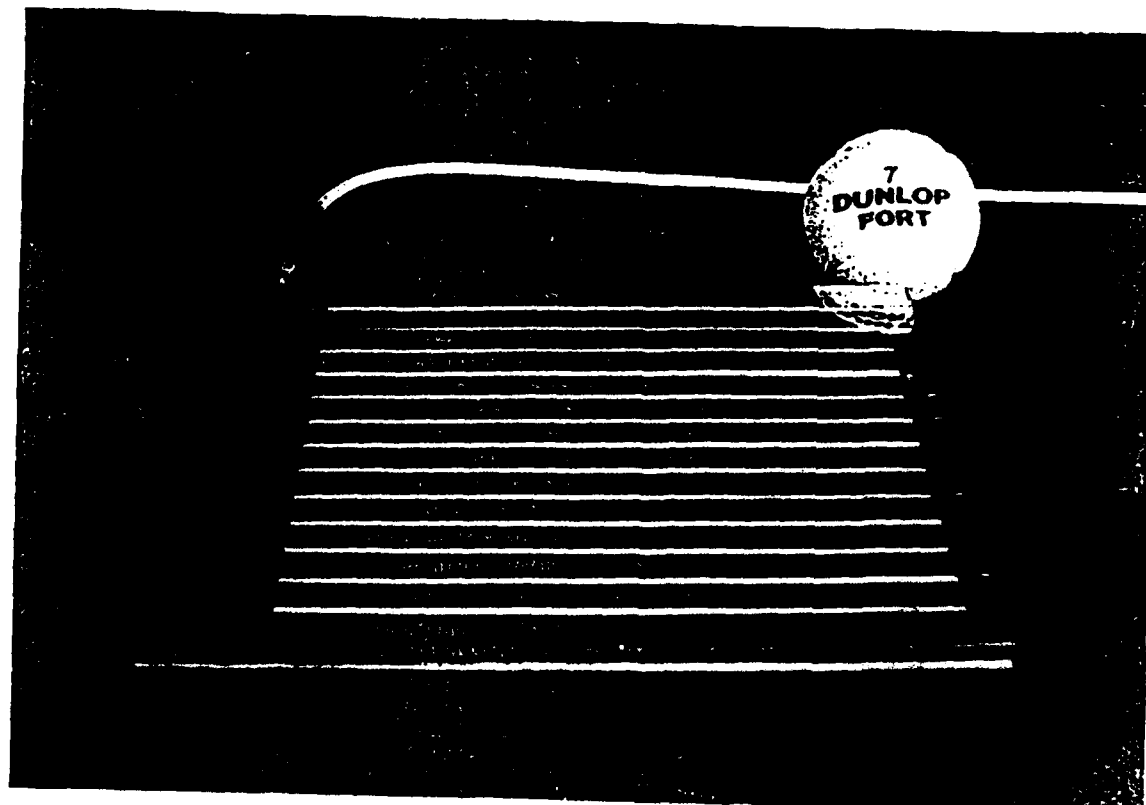


Distribution of vertical component of E-field in the planar antenna

12



13



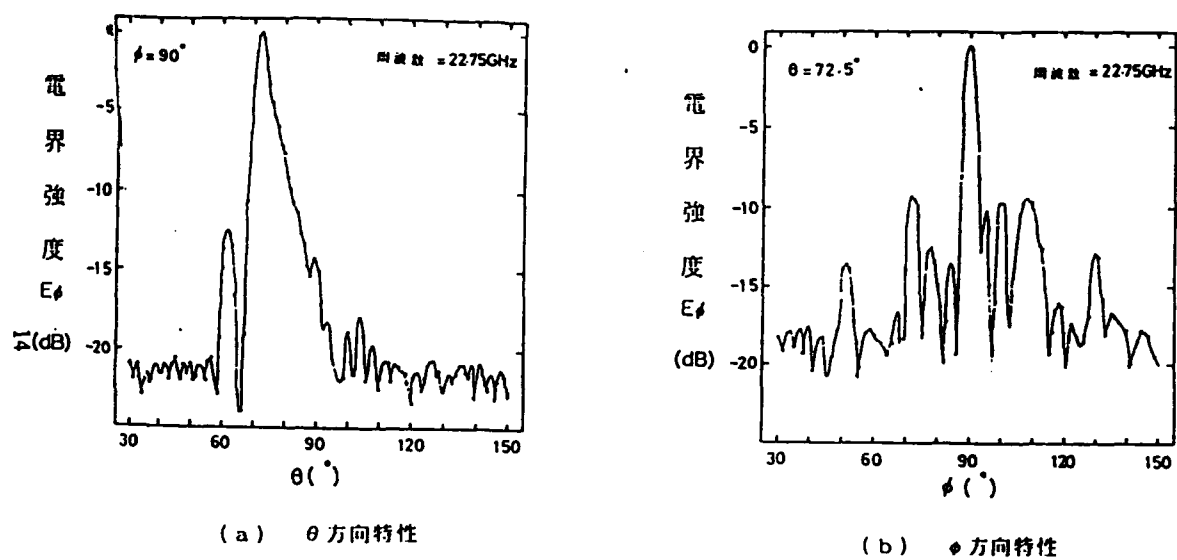


図7 縫れ波N RDガイド給電平面アンテナの放射指向性

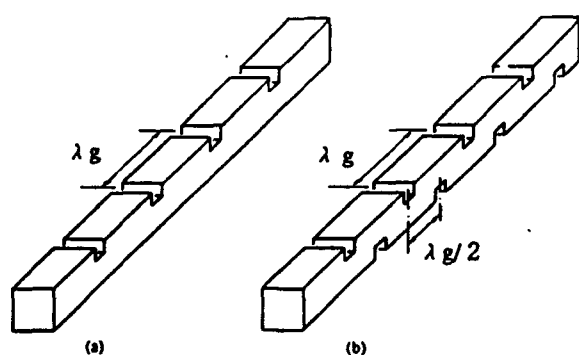


Fig.6 Structure of broadside leaky wave NRD-guide

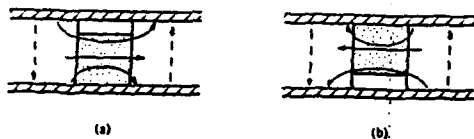
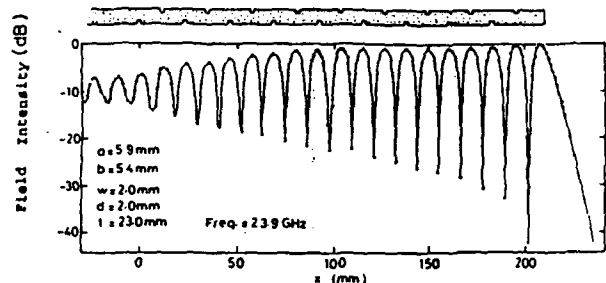


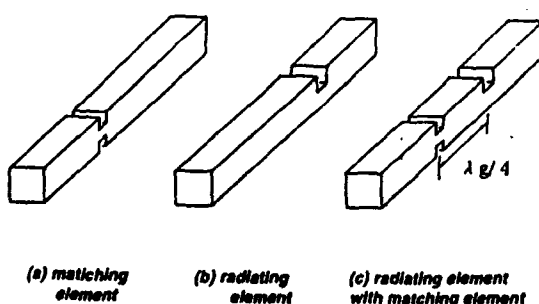
Fig.7 Field distributions of broadside leaky wave NRD-guide
at notches separated by half a wavelength
(solid line : guided wave, dotted line : radiated wave)



Standing wave pattern along broadside leaky wave NRD-guide

16

17



(a) matching element (b) radiating element (c) radiating element with matching element

Fig.8 Matching element and radiating element

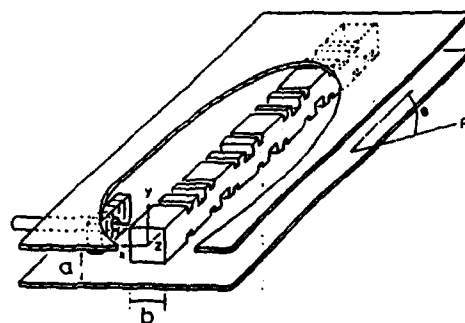


Fig.9 Structure of broadside leaky wave NRD-guide

18

19

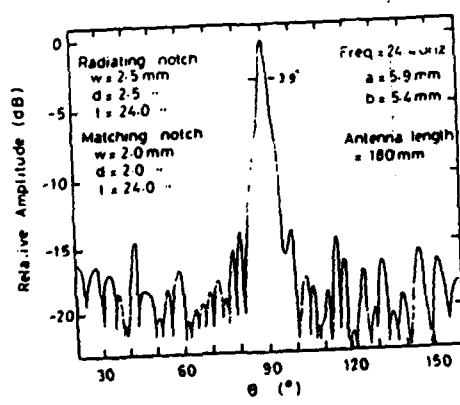
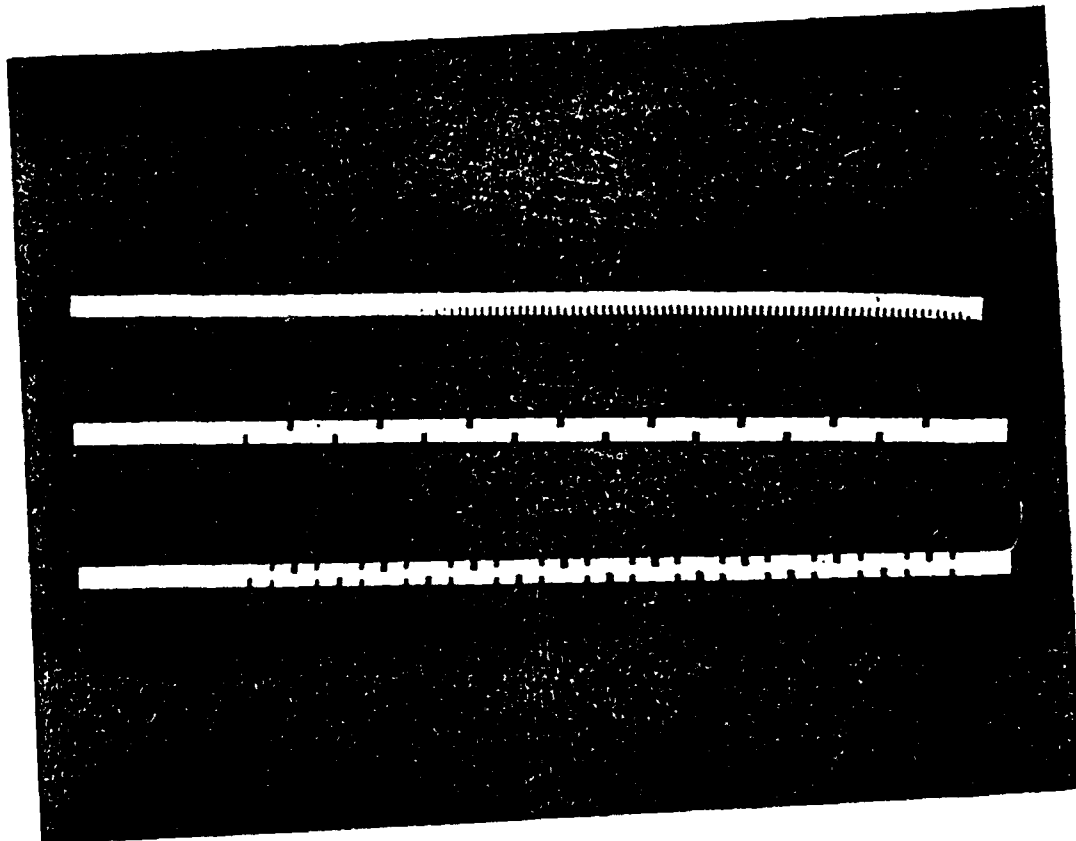


Fig.10 Radiation pattern of broadside leaky wave NRD-guide

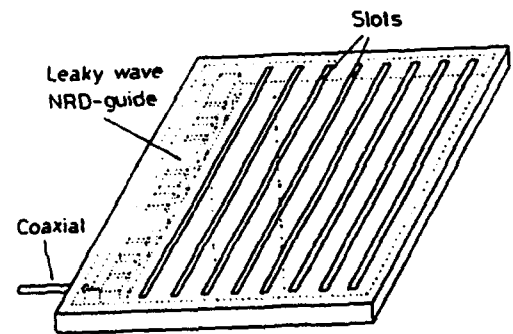
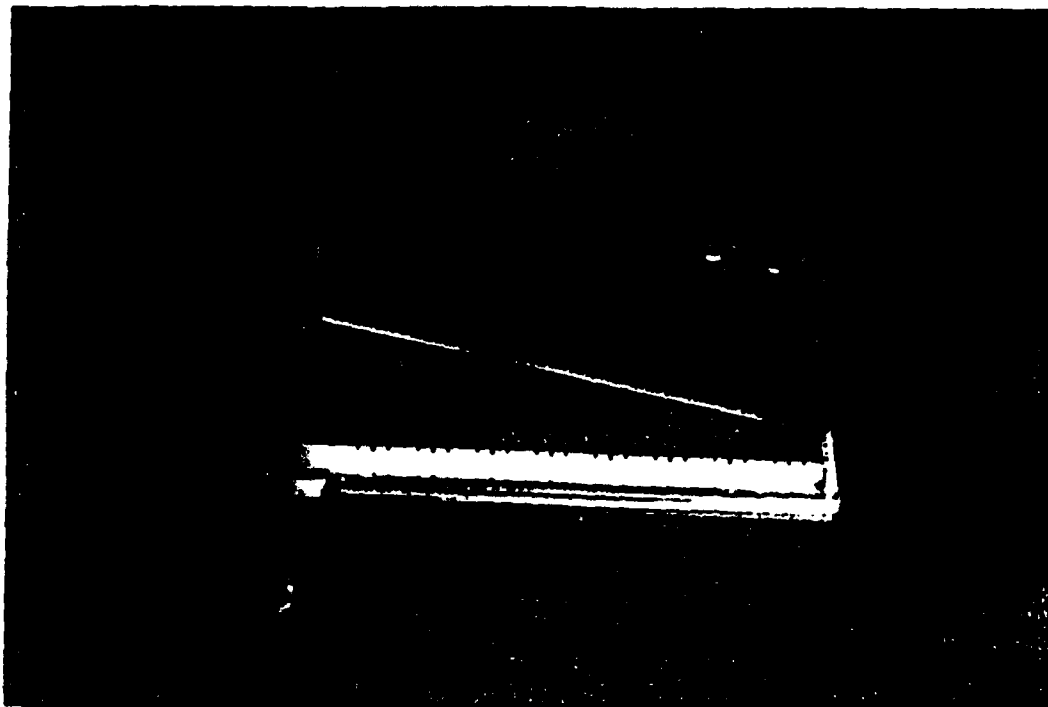
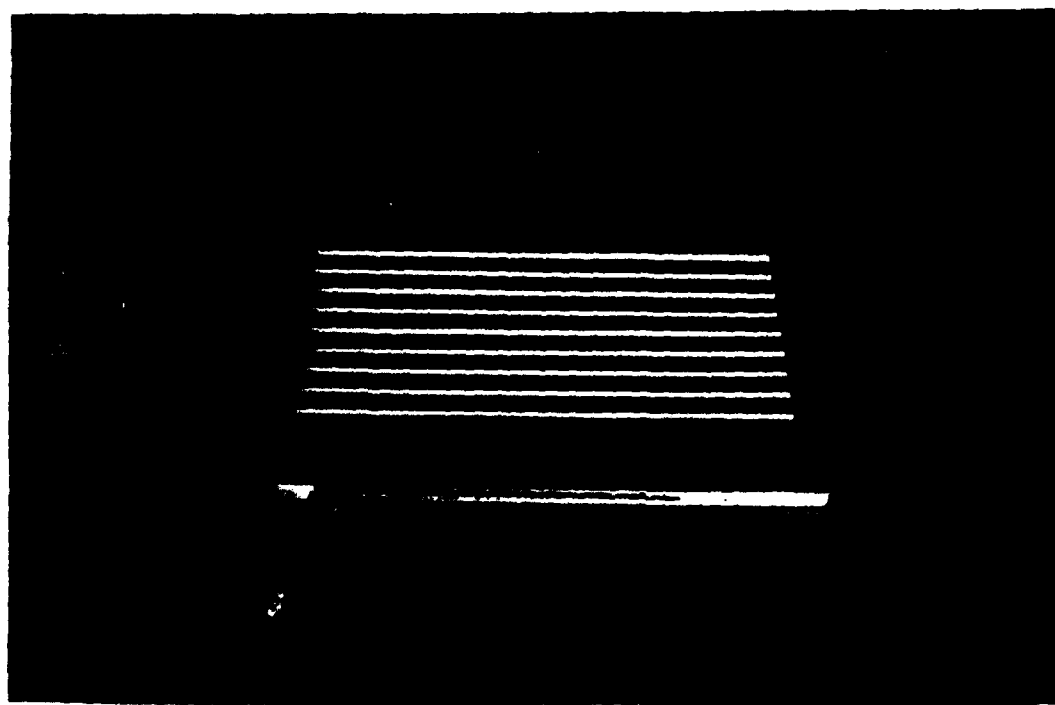


Fig. 11 Planar antenna fed by leaky wave NRD-guide

23



24



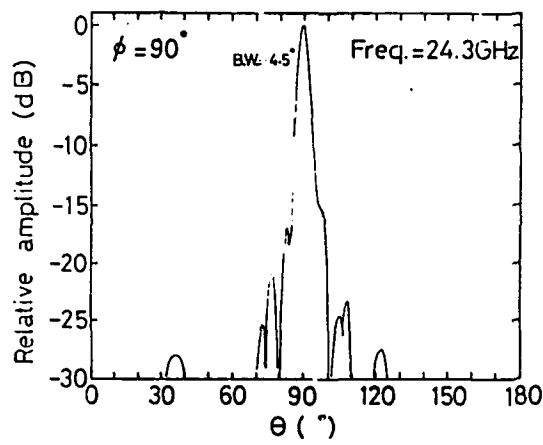


Fig.12-(a) **Radiation pattern of broadside leaky wave NRD-guide fed planar antenna (230x150x7 in mm) (in the vertical plane parallel to the slot)**

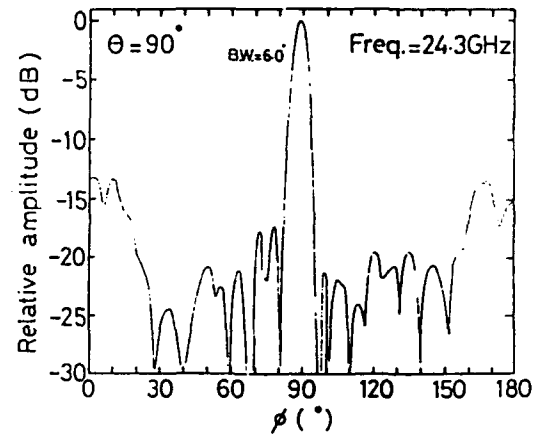
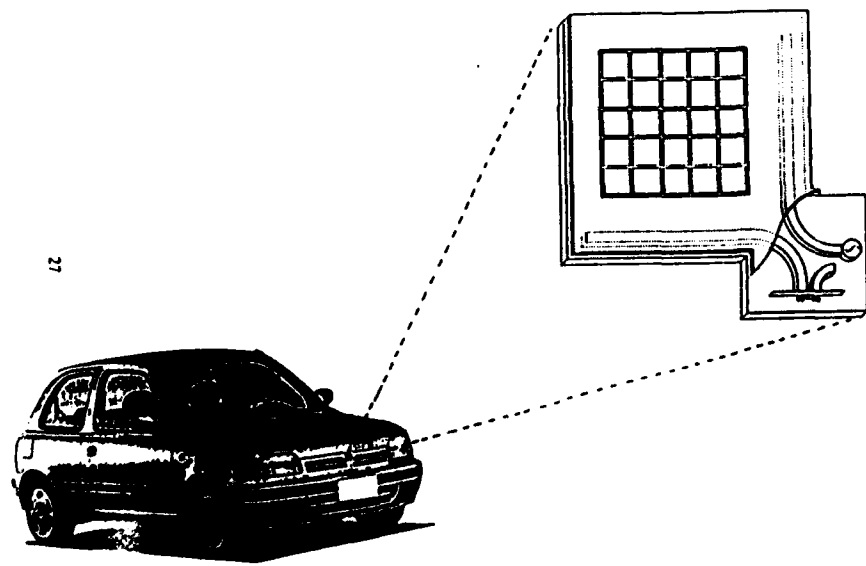


Fig.12-(b) **Radiation pattern of broadside leaky wave NRD-guide fed planar antenna (230x150x7 in mm) (in the vertical plane perpendicular to the slot)**



**ADVANCED DESIGN TECHNIQUES
FOR LINEAR AND NON LINEAR MMIC'S INTO THE
MILLIMETER - WAVE REGION**

R. H. Jansen

Jansen Microwave • Germany

ADVANCED DESIGN TECHNIQUES FOR LINEAR AND NONLINEAR MMICS

INTO THE MM-WAVE REGION

Rolf H. Jansen, Jansen Microwave, Ratingen, Germany

SUMMARY

In the past few years, the field of high-speed and microwave monolithic integrated circuits (MMICs) has seen an increasing range of nonmilitary applications. Particularly large growth rates and competitive development prevails in the emerging markets of mobile and satellite communications as well as of automotive electronic equipment up to high mm-wave frequencies. Commercial pressure is now driving the demand for faster development and lower cost manufacturing of GaAs MESFET-based and HEMT-based MMICs. From a design point of view, this is reflected in the following trends:

- The requirement for high packing density circuits, i.e. MMICs with minimized chip size, and for multifunction circuits integrating several functional blocks on a single chip while maintaining reasonably small size and thus acceptable yield. This is paralleled by the creation of miniaturized lumped components working well into the mm-wave region.
- The tendency towards lower noise figures and higher frequencies through the gradual transition from MESFET to HEMT technologies and in view of mm-wave applications like collision-avoidance radars. Several MMIC foundry services are now in the stage of moving to higher frequency limits, i.e. from about 20 GHz presently to 40...60 GHz in the near future.
- The demand for better CAD capable of addressing the problems associated with high packing density design and with high mm-wave frequencies in process-related form. The goal here is the reduction of development time and the full exploitation of the degrees of freedom offered by the MMIC medium for linear and nonlinear circuit design.

Under contract with GEC-Marconi Materials Technology, UK, formerly Plessey Research Caswell, the author and his group have worked over a number of years on such as the above outlined issues. Progress achieved is visualized by representative examples. A brief overview is given over advances in CAD techniques directly related to the MMIC process technology. This includes third generation look-up table concepts for single and dual metallization structures as well as 3D electromagnetic full-wave simulation with high speed and for high geometrical complexity. A unified approach

has been made available here for microstrip type MMICs and for coplanar waveguide type (CPW) circuits. For specific, repeatedly used structures like via holes, approximate field-theory based models have been developed for fast interactive CAD. Further, linear and nonlinear distributed FET/HEMT modelling in terms of device layout geometry is described, including automated parameter extraction. CAD based on this approach has near interactive speed and has primarily been developed for frequency domain design involving larger devices and for analogue MMICs operating at high mm-wave frequencies.

REFERENCES related to this workshop contribution

- /1/ Hente, D. and Jansen, R.H.: A frequency-domain continuation method for the analysis and stability investigation of nonlinear microwave circuits, *IEE Proc.*, Vol. 133, Pt.H., Oct. 1986, 351-362.
- /2/ Jansen, R.H.: Recent advances in the full-wave analysis of transmission lines for application in MIC and MMIC design, Invited Paper, *Proc. SBMO Intern. Microwave Symposium*, Rio de Janeiro, July 1987, 467-475.
- /3/ Jansen, R.H. and Wertgen, W.: A 3D field-theoretical simulation tool for the CAD of mm-wave MMICs, *Alta Frequenza, Italy*, vol. LVII, 1987, 203-216.
- /4/ Jansen, R.H. et al: A comprehensive CAD approach to the design of monolithic microwave integrated circuits, *Invited Paper, IEEE Trans.*, MTT-36, (1988), 206-219.
- /5/ Wiemer, L. and Jansen, R.H.: Reciprocity-related definition of strip characteristic impedances for multiconductor hybrid-mode transmission lines, *Microwave and Optical Technology Letters*, Wiley Interscience, vol. 1, (1988), 22-25.
- /6/ Jansen, R.H., Eddison, I.G., Arnold, R.G.: Recent developments in the CAD of high packing density MMICs, *Microwave and Optronics Conf (MIOP)*, 1989, Sindelfingen, Germany, paper 1/3.
- /7/ Jansen, R.H. and Wiemer, L.: Full-wave theory based development of mm-wave circuit models for microstrip open end, gap, step, bend and tee, *IEEE MTT-S Digest, Long Beach, USA*, 1989, 779-782.
- /8/ Jansen, R.H.: Full-wave analysis and modeling for CAD of mm-wave MMICs, *Proc. Intern. Workshop on Millimeter Waves*, April 1989, Perugia, Italy, Paper No. 2, also in *Alta Frequenza*, vol. LVIII, 1989, 551-558.

/9/ Wertgen, W. and Jansen, R.H.: Efficient direct and iterative electrodynamic analysis of geometrically complex MIC and MMIC structures, Intern. Journal of Numerical Modelling, Wiley, vol. 2, 1989, 153-186.

/10/ Jansen, R.H.: Advanced CAD/CAM software for process-related MMIC design, Proc. ESA Workshop on MMICs for Space Applic., Noordwijk, March 1990, paper 7/2.

/11/ Jansen, R.H.: LINMIC+, A European family of CAD tools for MIC and MMIC design, Microwave Engineering Europe, March/April 1991, 21-24.

/12/ Brömme, R. and Jansen, R.H.: Systematic investigation of coplanar waveguide MIC/MMIC structures using a unified strip/slot 3D electromagnetic simulator, IEEE MTT-S Digest, Boston, USA, 1991, 1081-1084.

/13/ Jansen, R.H. and Sauer, J.: High-speed 3D electromagnetic simulation for MIC/MMIC CAD using the spectral operator expansion (SOE) technique, IEEE MTT-S Digest, Boston, USA, 1991, 1087-1091.

/14/ Jansen, R.H. and Pogatzki, P.: Nonlinear distributed modelling of multifinger FETs/HEMTs in terms of layout geometry and process data, Proc. 21st Europ. Microwave Conf., Stuttgart, Germany, Sept. 1991, 609-614.

/15/ Jansen, R.H.: CAD oriented spectral domain modelling of MIC/MMIC structures, Intern. Workshop IEEE MTT/AP Germany Digest, Stuttgart, Sept. 1991, 19-31.

/16/ Jansen, R.H.: Novel, process-related design techniques for linear and nonlinear MMICs, 1991 Asia-Pacific Microwave Technology and Education Workshop, Taiwan, Sept. 1991, paper TA3, 65 pages.

/17/ Jansen, R.H.: A full-wave electromagnetic model of cylindrical and conical via hole grounds for use in interactive MIC/MMIC design, IEEE MTT-S Int. Microwave Symposium, Albuquerque, USA, 1992, accepted for publication.

**CAD OF MILLIMETER - WAVE PASSIVE COMPONENTS
IN SUSPENDED MICROSTRIP TECHNOLOGY**

V. Fouad Hanna

CNET • France

| WHY? | |
|---------------------------|---|
| Stripline (microstrip) | Suspended Stripline (suspended microstrip) |
| Attenuation losses | High 75% Less than microstrip |
| Dispersion | Moderate Little |
| CAD Facilities | Rich Poor |

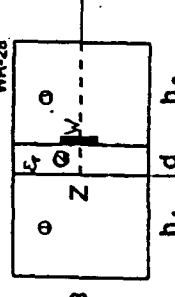
enet

FRANCE
TELECOM

enet
Groupe national d'études des télécommunications

- PLA N
- * INTRODUCTION.
- * EVALUATION OF EIGENMODES IN SUSPENDED STRIPLINE (SSL) TECHNOLOGY.
- * CHARACTERISATION OF UNIAXIAL SSL DISCONTINUITIES.
- * REALISATION OF PASSIVE MICROVEE COMPONENTS IN SSL TECHNOLOGY : Directional Coupler-Resonator-Filter.
- * CHARACTERISATION OF MULTIAXIAL SSL DISCONTINUITIES : Bend , Stub , Bent-Stub.

SPECTRAL DOMAIN APPROACH
for a SSL
WR-28



$$E_z(x, y, z, t) = \sum_n E_z(\alpha_n, y) \cdot e^{j\alpha_n x} \cdot e^{j(\omega t - \mu z)} \quad (1)$$

where

$$\alpha_n = n \frac{\pi}{B} \quad (2)$$

$$\begin{bmatrix} E_z(\alpha_n, d) \\ E_z(\alpha_n, d') \end{bmatrix} = \begin{bmatrix} C_{11}(\alpha_n, \beta, \omega) & C_{12}(\alpha_n, \beta, \omega) \\ C_{21}(\alpha_n, \beta, \omega) & C_{22}(\alpha_n, \beta, \omega) \end{bmatrix} \begin{bmatrix} J_x(\alpha_n, d) \\ J_z(\alpha_n, d) \end{bmatrix}$$

Fig. 3

enet
Groupe national d'études des télécommunications

enet

FRANCE
TELECOM

CAD OF MILLIMETER-WAVE PASSIVE COMPONENTS
IN SUSPENDED MICROSTRIP TECHNOLOGY

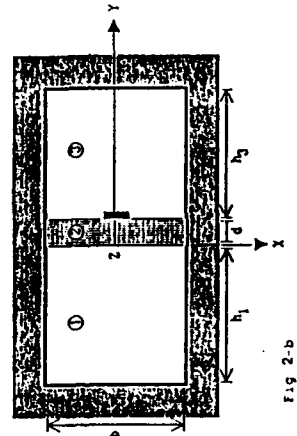
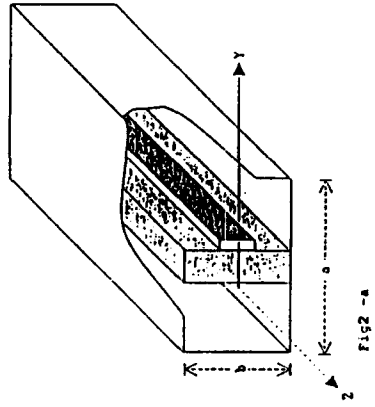
Victor FOUAD HANNA, Joseph ACHKAR,^{*} Odile PICON, Jacques CITERNE^{**}

**DIVISION
SYSTEMES DE TELECOMMUNICATIONS PAR SATELLITE**

CENTRE NATIONAL D'ETUDES DES TELECOMMUNICATIONS

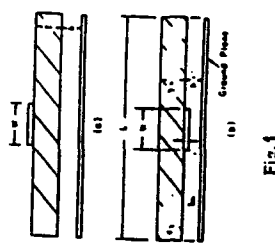
PARIS, FRANCE

^{*}^{**}InSA Rennes, France



Longitudinal (1-a) and cross-sectional (1-b) view of suspended stripline.

SUSPENDED AND INVERTED MICROSTRIP LINES



- Reduced attenuation (detached ground plane)
- Microwave applications
- Shielding
- Field configurations TEM (closer than microstrip)
- Circuit layout on both sides of the substrate.

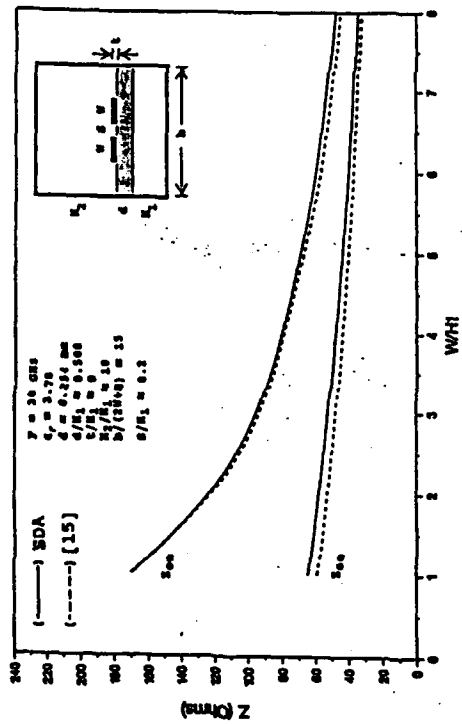


Fig 6 Variation of the characteristic impedance for the even and odd modes as a function of W/H for coupled SSL's: (—) our analysis, (--) reference [15].

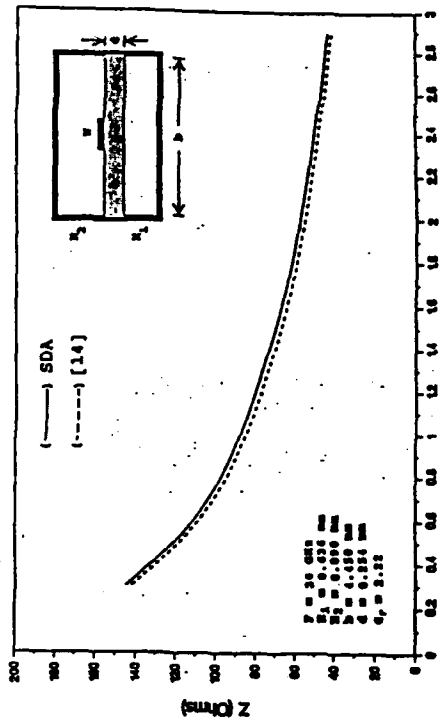


Fig. 7 Variation of the characteristic impedance as a function of W for an SSL: (—) our analysis, (---) reference [14].

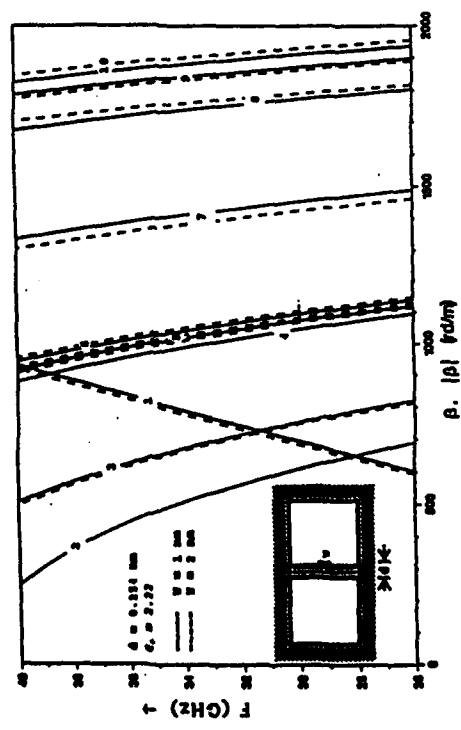


Fig 4 Dispersion characteristics of symmetric SSL's ($\epsilon = 2.22$).

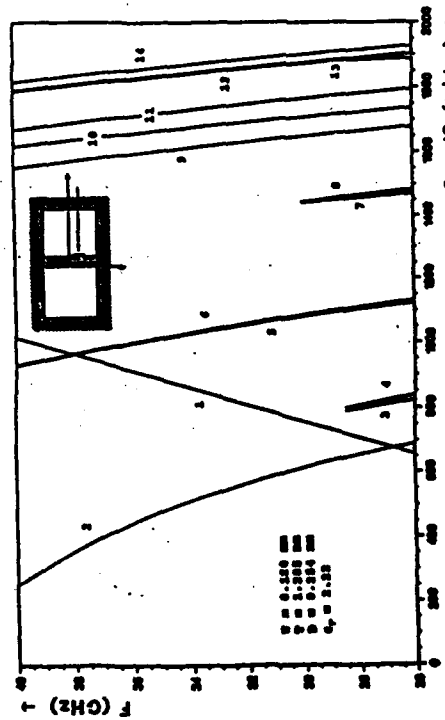


Fig. 5 Dispersion characteristics of asymmetric SSL ($\epsilon = 2.22$).

Method of GALERKIN

$$\begin{aligned}
 J_s(x, d) &= \sum_{i=1}^k a_i \cdot J_{s,i}(x, d) \quad \Rightarrow \quad J_s(a_0, d) = \sum_{i=1}^k a_i \cdot J_{s,i}(a_0, d) \quad (3) \\
 J_i(x, d) &= \sum_{i=1}^k b_i \cdot J_{s,i}(x, d) \quad \Rightarrow \quad J_i(a_0, d) = \sum_{i=1}^k b_i \cdot J_{s,i}(a_0, d)
 \end{aligned}$$

Relationship of Complementarity

$$\begin{aligned}
 (4) \quad \int_{-a}^a E_s(x, d) \cdot J_i(x, d) \cdot dx = 0 &\quad \Rightarrow \quad (R+S) \text{ homogeneous linear equations} \\
 \int_{-a}^a E_s(x, d) \cdot J_i(x, d) \cdot dx = 0 &\quad \Downarrow \\
 \text{Det } (\beta, i, \text{geometry}) = 0 &\quad \rightarrow \quad \beta^2 < 0 \quad (5) \\
 \beta^2 > 0 &\quad \leftarrow \quad \text{propagating modes} \\
 &\quad \text{evanescent modes}
 \end{aligned}$$

| | $R(x)$ | $J(a_0)$ |
|----------|---|--|
| J_{x1} | 1 | $\frac{2}{a_0} \sin \frac{a_0}{2}$ |
| | $ x \leq \frac{a_0}{2}$ | |
| | $0 < x \leq \frac{3a_0}{2}$ | |
| J_{x2} | $\frac{1}{\sqrt{1 - \left(\frac{2x}{a_0}\right)^2}}$ | $\frac{a_0}{2} J_0\left(\frac{a_0}{2}\right)$ |
| | | |
| J_{x1} | $\frac{2x}{a_0} \sqrt{1 - \left(\frac{2x}{a_0}\right)^2}$ | $-J_0\left(\frac{a_0}{2}\right)$ |
| | | |
| J_{x2} | $\frac{\sin\left(a_0 \frac{x}{2}\right)}{\sqrt{1 - \left(\frac{2x}{a_0}\right)^2}}$ | $\left[J_0\left(\frac{a_0}{2}\right) \cdot J_0\left(\frac{(2n-1)a_0}{2}\right)\right]$ |
| | | |
| | | $a_0 \cdot e^{-(2n-1)a_0/2}$ |
| | | $n=1, 2, \dots$ |

$$\left| \begin{array}{l}
 \left\{ \begin{array}{l} \vec{E}'_T = \sum_{p=1}^P (A'_p + B'_p) \cdot \vec{e}_{p,T} \\ \vec{H}'_T = \sum_{p=1}^P (A'_p - B'_p) \cdot \vec{h}_{p,T} \end{array} \right\} \quad (6) \\
 \left\{ \begin{array}{l} \vec{E}''_T = \sum_{q=1}^Q (A''_q + B''_q) \cdot \vec{e}_{q,T} \\ \vec{H}''_T = \sum_{q=1}^Q (B''_q - A''_q) \cdot \vec{h}_{q,T} \end{array} \right\} \quad (7) \\
 \text{at } \vec{u} \quad \text{TELECOM} \quad \text{at } \vec{u} \quad \text{TELECOM}
 \end{array} \right.$$

$$\left| \begin{array}{l}
 \text{Discontinuity Boundary Conditions} \\
 \text{on } S_1: \left\{ \begin{array}{l} \vec{E}'_T = 0 \\ \vec{H}''_T + \vec{J}'_T \times \vec{u} = 0 \end{array} \right\} \quad (8) \\
 \text{on } S_{12} - S_1: \left\{ \begin{array}{l} \vec{E}'_T = \vec{E}''_T \\ \vec{H}'_T = \vec{H}''_T \end{array} \right\} \quad (9) \\
 \vec{u} \quad \vec{u} \quad \text{TELECOM} \quad \text{TELECOM}
 \end{array} \right.$$

⇒ set of $2(P+Q)$ linear equations $\Rightarrow 2(P+Q)$ Model Amplitudes

$$\begin{aligned}
 [\mathcal{B}] &= [\mathcal{S}] \cdot [\mathcal{A}] \quad (10) \\
 [\mathcal{B}] &= \begin{bmatrix} [B'_P] \\ [B''_Q] \end{bmatrix} \\
 [\mathcal{A}] &= \begin{bmatrix} [A'_P] \\ [A''_Q] \end{bmatrix}
 \end{aligned}$$

$$[\mathcal{S}] = \begin{bmatrix} [S_{11}] & [S_{12}] \\ [S_{21}] & [S_{22}] \end{bmatrix}$$

a step discontinuity in an SSL

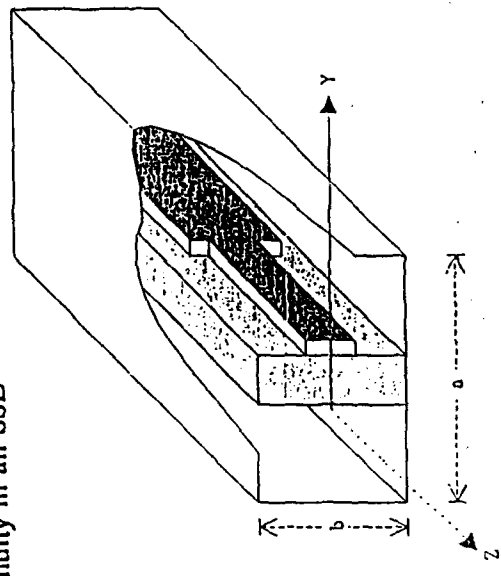


Fig 8 Variation of the x component of the electric field as a function of y (mm) in an SSL.

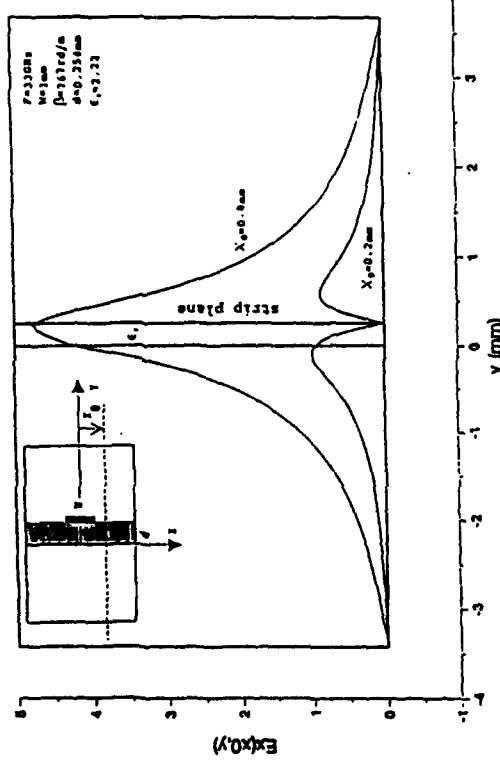


Fig 8

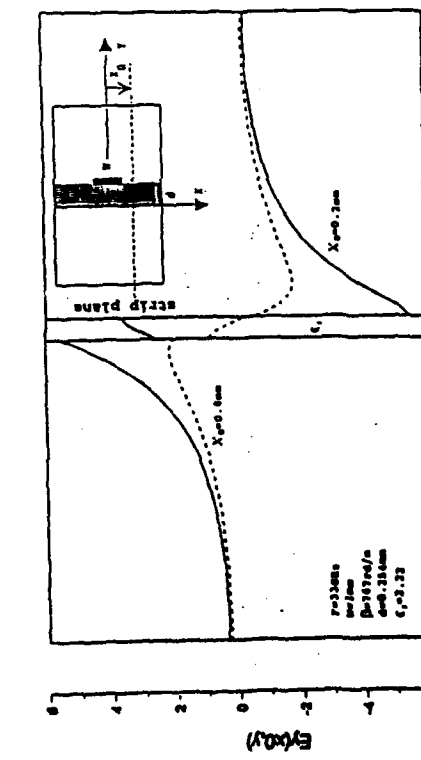


Fig 9 Variation of the y component of the electric field as a function of y (mm) in an SSL.

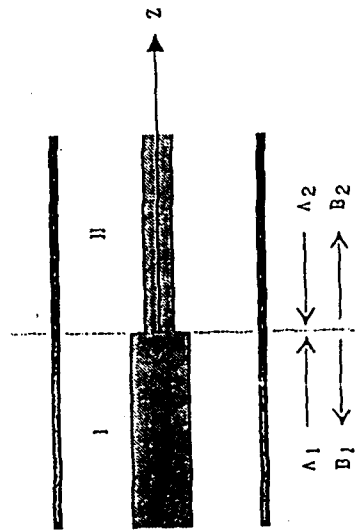


Fig 10

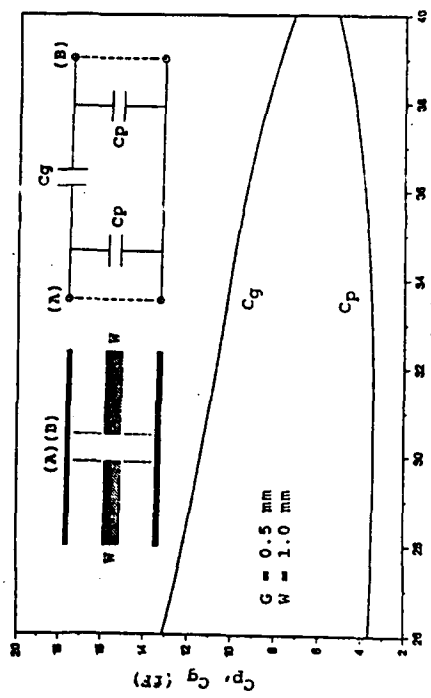


Fig 13 Variation of the equivalent end-effect length as a function of frequency in the Ka band for an open end asymmetric SSI.

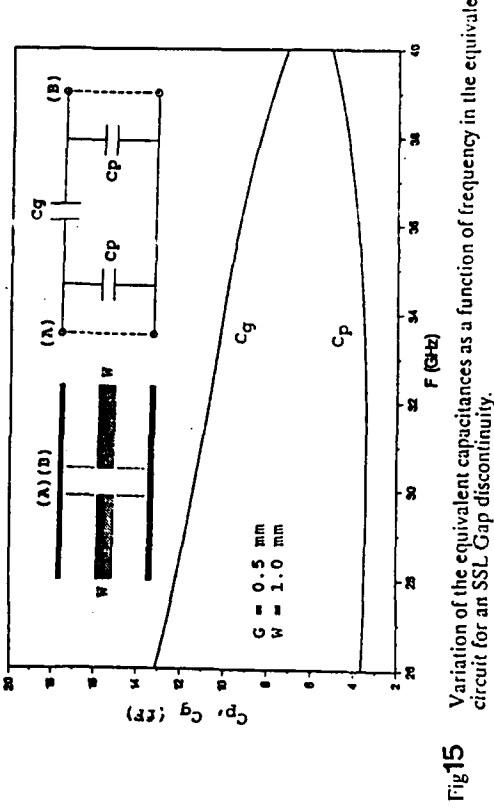


Fig 15 Variation of the equivalent capacitances as a function of frequency in the equivalent circuit for an SSI Gap discontinuity.

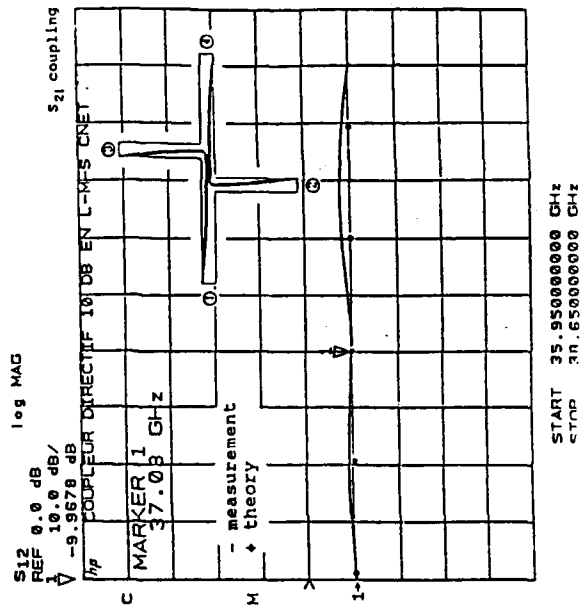


Fig 16 Theoretical and experimental variation of the coupling coefficient of the directional coupler as a function of frequency in the Ka band.

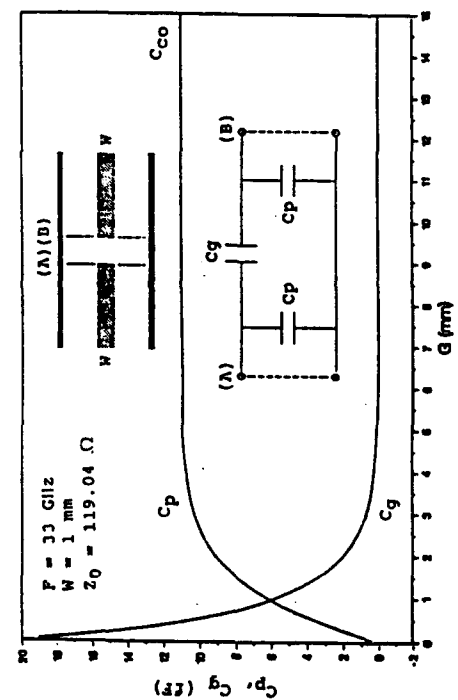


Fig 14 Variation of the equivalent capacitances as a function of the Gap's width in the equivalent circuit for an SSI Gap discontinuity.

Role of the Spectral Domain Approach

amplitudes of eigenmode field components.
 coupling coefficients } directly in the
 spectral domain
 er flow }

$$P_{p,q} = \frac{1}{2} \oint_S (\vec{E}' \wedge \vec{H}''') \cdot d\vec{S} \quad (11)$$

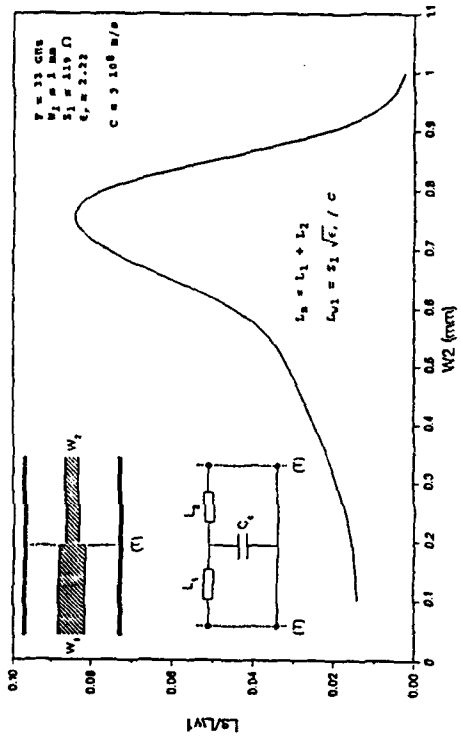
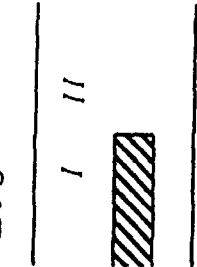


Fig 11 Variation of the equivalent normalized inductance as a function of the strip width in the equivalent circuit for an SSL step discontinuity.

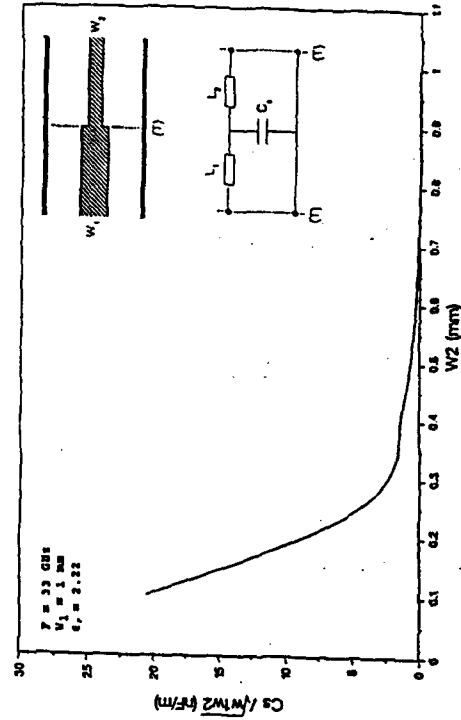


Fig 12 Variation of the equivalent normalized capacitance as a function of the strip width in the equivalent circuit for an SSL step discontinuity.

- INTEGRAL EQUATIONS TECHNIQUES
- METHOD OF MOMENTS
- MATCHED LOAD SIMULATION

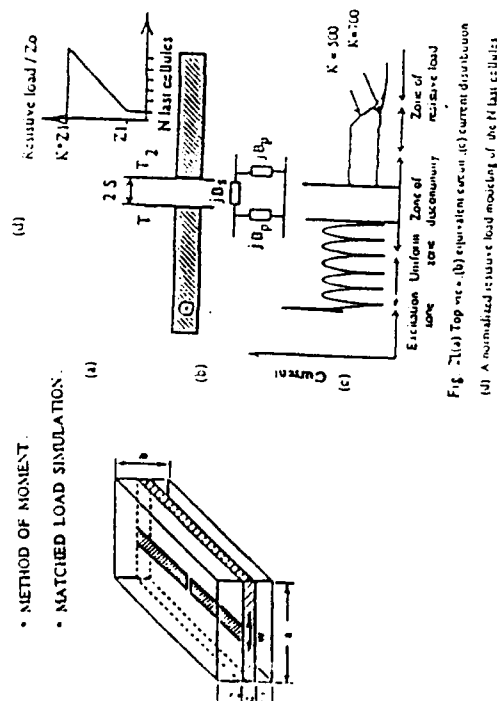


Fig. 21(a) Top view of a finite-difference cell showing a current distribution with nodes T_1, T_2, T_3, T_4
 (b) A normalized current load modeling of the finite cell
 (d) A 3D diagram of a conductor with a rectangular cell and a charge cell
 (e) A 3D diagram of a conductor with overlapping rectangular cells

INTEGRAL EQUATIONS → MATRIX EQUATION

- * CONDUCTOR RECTANGULAR CELLS
- * CURRENT → OVERLAPPING

$$J_s(r) = \frac{1}{W_{N+1}} \sum_{n=1}^{N-1} I(r) \cdot \epsilon_x \quad (7)$$

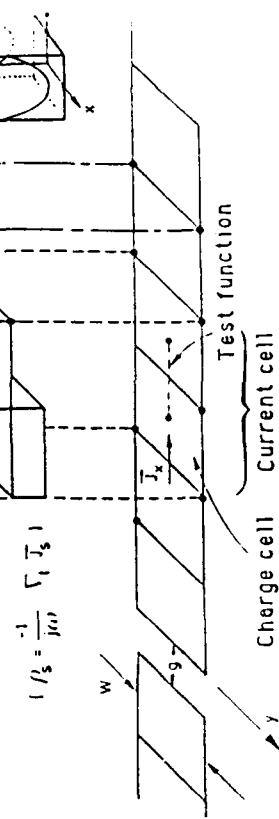


Fig. 22

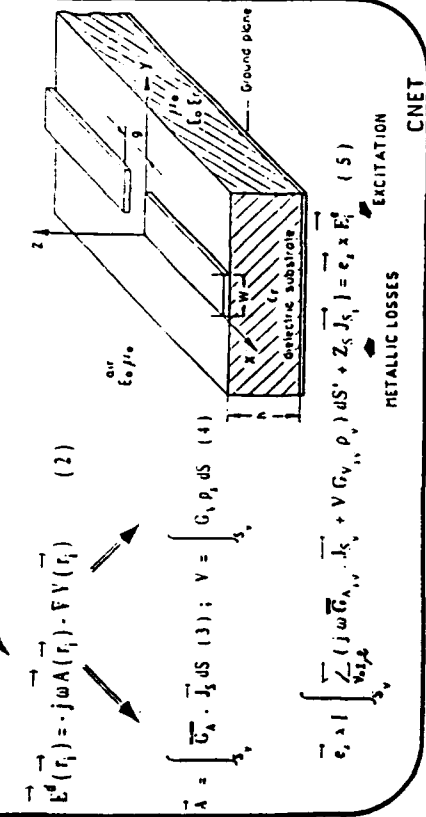
SIMULATION OF A VIRTUAL MATCHED LOAD
 The obtained new matrix equation for the loaded structure can be written in the form:

$$[Z] + [\Delta Z][I] = [V]$$

 where $[Z]$ is the generalized impedance matrix of the unloaded structure, $[I]$ is the unknown current vector, $[V]$ is the feeding voltage vector and $[\Delta Z]$ is a square diagonal impedance matrix.

ANALYSIS

$$\epsilon_x \times [\vec{E}(r_i) + \vec{E}^*(r_i)] = \epsilon_i \lambda [Z_s J_s(r_i)] \quad (1)$$



$$\vec{E}(r_i) \times \vec{A} \cdot \vec{J}_s \, ds \quad (3) ; \quad V = \int_S C_s \rho_s \, ds \quad (4)$$

$$\vec{A} = \int_{J_s} \vec{C}_A \cdot \vec{J}_s \, ds \quad (2) ; \quad \vec{V} = \int_S C_s \rho_s \, ds \quad (4)$$

$$\epsilon_s \times \int_{J_s} \frac{1}{\epsilon_s \mu_s} (j\omega \vec{G}_{s,s} \cdot \vec{J}_s + V G_{s,s} \rho_s) \, ds + 2 \epsilon_s \vec{J}_s = \epsilon_s \times \vec{E}_s^* \quad (5)$$

EXCITATION

CNET

Fig 17 Variation of the resonator reflection coefficient as a function of frequency in the K_u band ($L_0 = 4.45$ mm).

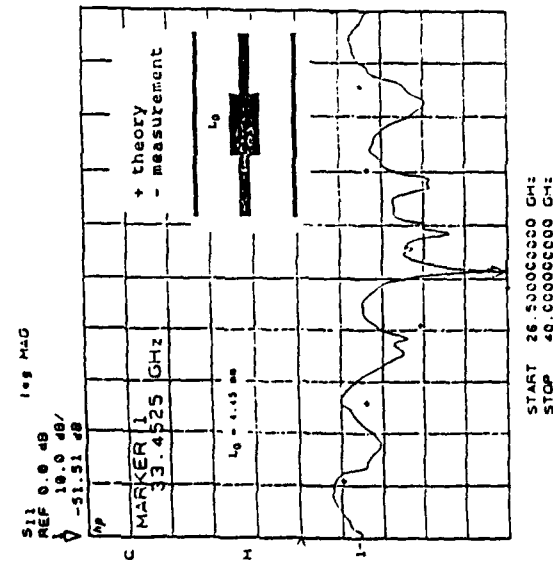


Fig 18 Variation of S11 (dB) and S21 (dB) as a function of the resonator length at $F = 33.425$ GHz.

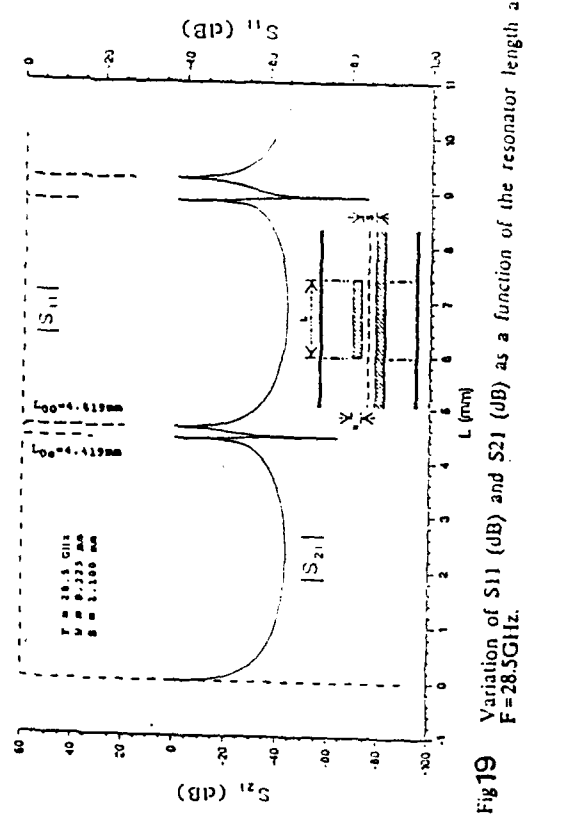


Fig 19 Variation of S11 (dB) and S21 (dB) as a function of the resonator length at $F = 28.5$ GHz.

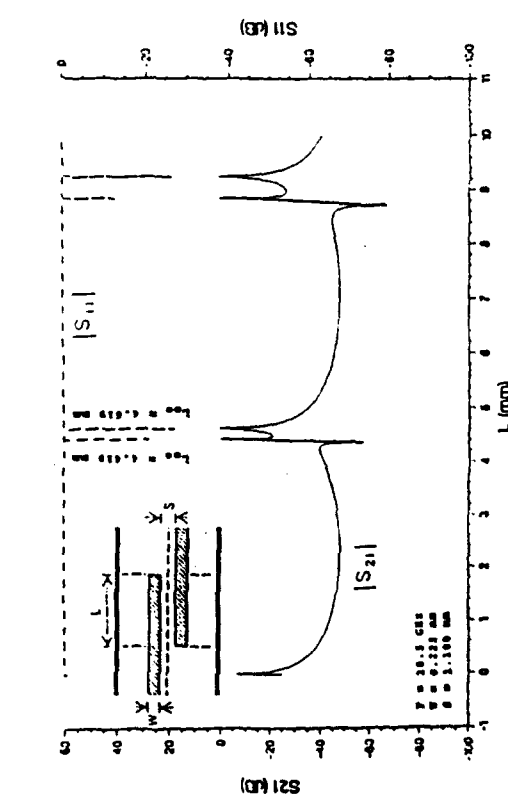


Fig 20 Theory, simulation and measure performances of the low-pass filter realized in SSI technology using RT/Duroid as substrate.

Fig 20 Theory, simulation and measure performances of the low-pass filter realized in SSI technology using RT/Duroid as substrate.

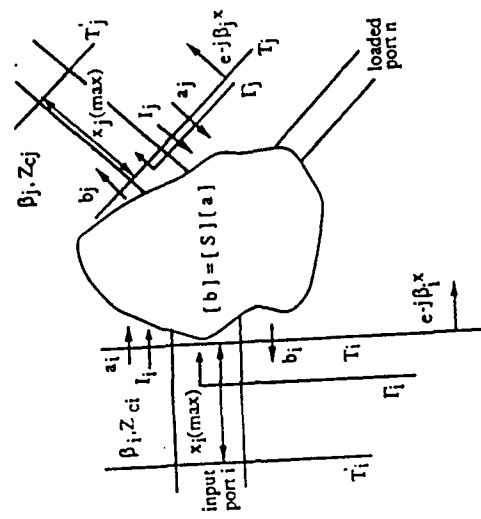


Fig. 25: General N-port discontinuity configuration

Fig. 23 Current distribution along a loaded microstrip line

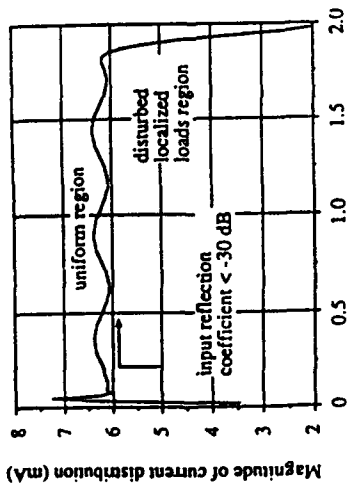
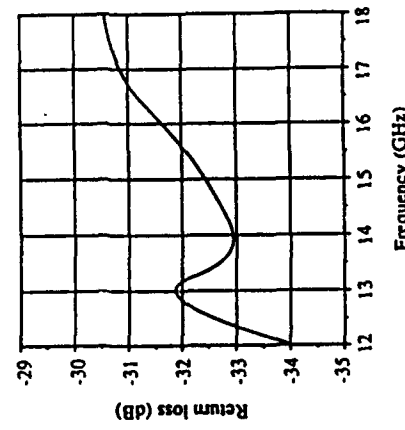


Fig. 24 Variation of the return loss as a function of frequency in the Ku-band for a matched load on a microstrip line ($a=80$ mm, $b=7.112$ mm, $c=3.56$ mm, $w=0.75$ mm, $h=254$ μ m, $\epsilon_r=2.22$)



$$|S_{ii}| = \frac{\alpha_{ii}}{1 + \alpha_{ii}} + \frac{1}{2} \sqrt{\left(\frac{2\alpha_{ii}}{\alpha_{ii} + 1} \right)^2 + 4 \left(\frac{\alpha_{ii} - 1}{\alpha_{ii} + 1} \right)}$$

$$\alpha_{ji} = \sum_{j=1}^N k_{ji}$$

where

$$k_{ji} = \frac{|I_j(\max)|^2 Z_{ei}}{|I_i(\max)|^2 Z_{ei}} \frac{1}{(1 + |T_j|)^2}$$

$$\angle T_i - 2\beta_i x_i(\max) = (2m + 1)\pi, \quad \angle T_j + 2\beta_j x_j(\max) = (2m + 1)\pi, \quad m = 0, 1, \dots, \infty$$

$$S_{ji} = \frac{|I_j(\max)|}{|I_i(\max)|} \frac{\sqrt{Z_{ei}} e^{j\beta_i x_i(\max)}}{\sqrt{Z_{ei}} e^{j\beta_j x_j(\max)}} \frac{(1 + |S_{ii}|)}{(1 + |T_j|)}$$

$$\angle S_{ji} = \angle T_j(\max) - \angle I_i(\max) + \beta_j x_j(\max) + \beta_i x_i(\max)$$

Fig. 24 Variation of the return loss as a function of frequency in the Ku-band for a matched load on a microstrip line ($a=80$ mm, $b=7.112$ mm, $c=3.56$ mm, $w=0.75$ mm, $h=254$ μ m, $\epsilon_r=2.22$)

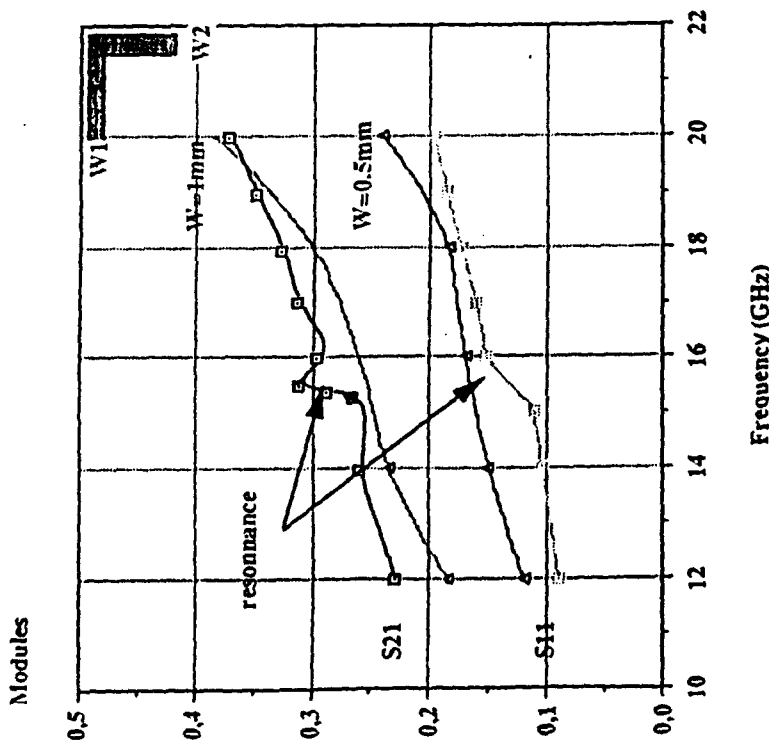


Fig.26 : Variation of S_{11} and S_{21} for a SSL bend discontinuity as a function of frequency ($W_1=W_2=W$, $a=b=12.7\text{mm}$, $c=3.81\text{mm}$, $\epsilon_r=9.8$, $h=0.635\text{mm}$, \square theory, \circ analysis, Δ our analysis, \blacktriangle resonance) reference (28)

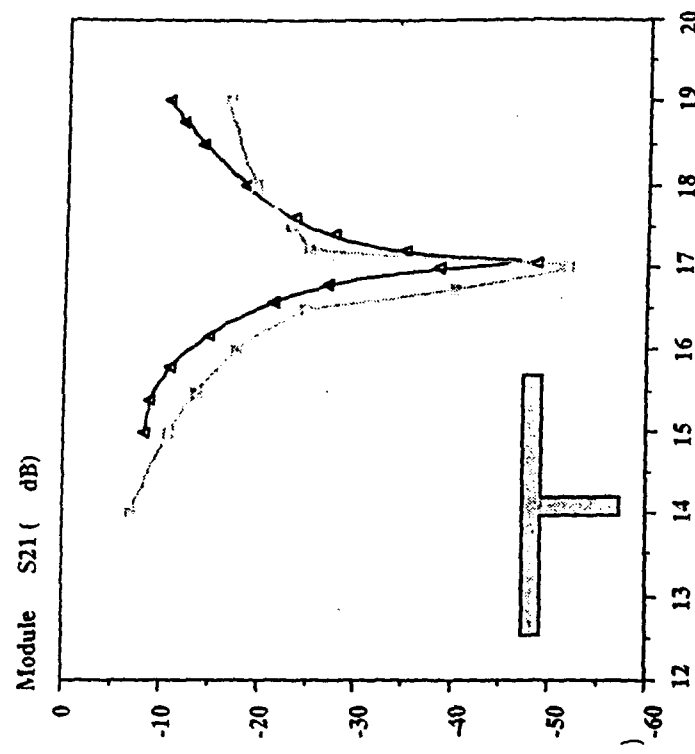


Fig. 27 : Variation of $|S_{21}|$ (\square Theory and Δ measurements) for a SSL stub discontinuity.

[9] PICON O, "Traitements électromagnétiques 3-D applicables aux composants passifs micro-électroniques en ondes millimétriques", Thèse de Docteur ès-sciences, Rennes, 1988.

[10] ACHKAR J, PICON O, FOUAD HANNA V, CITERNE J, "Etude des modes d'une ligne asymétrique et de lignes couplées en technologie ligne microuban suspendu par la méthode d'approche spectrale", 10^{me} Colloque Optique Hertzienne et Diélectrique, Rennes, pp 247-250, 1989.

[11] ACHKAR J, PICON O, FOUAD HANNA V, CITERNE J, "Analysis of symmetric and asymmetric coupled striplines and some associated discontinuities", 20th European Microwave Conference, Budapest, pp 537-542, 1990.

[12] OMAR A S, SCHUNEMANN K F, "Formulation of the singular integral equation technique for planar transmission lines", IEEE Trans on Microwave Theory and Techniques, Vol MTT-33, pp 1313-1322, 1985.

[13] GARDIOL F, "Hypérfréquences", Traité d'électricité, Vol 13, Dunod, Paris, 1987.

[14] YUNYI W, KAIJUN G, YONGHUI S, "Synthesis equations for shielded suspended substrate microstrip line and broadside coupled stripline", IEEE MTT-S, USA, pp 331-334, 1988.

[15] KOUL S K, BHATT B, "Propagation parameters of coupled microstrip like transmission lines for millimeter wave applications", IEEE Trans on Microwave Theory and Techniques, Vol MTT-29, pp 1364-1369, 1971.

[16] COLLIN R E, "Field theory of guided waves", Mc Graw-Hill, New York, 1960.

[17] ACHKAR J, "Etude et caractérisation de lignes microuban suspendu en vue de la réalisation de composants hyperfréquences passifs", Thèse de Doctorat, Paris, 1991.

[18] HARLAN HOWE Jr, "Stripline circuit design", Artech house, Massachusetts, 1974.

[19] HAMMERSTAD E, JANSEN R H, "Accurate models for microstrip computer aided design", IEEE International Microwave Symposium, pp 407-409, 1980.

[20] PICON O, ACHKAR J, "Logiciels de calcul de caractéristiques de lignes planaires fermées et de discontinuités uniaxiales associées", Journées d'Etudes sur la CAO Hypérfréquences, Chapitre IEEE MTT-S, Poigny-La-Forêt, 1989.

[21] COHN S B, "Shielded coupled-stripline transmission line", IEEE Trans on Microwave Theory and Techniques, Vol MTT-3, pp 29-38, 1955.

[22] ACHKAR J, PICON O, FOUAD HANNA V, CITERNE J, "Coupleur directif en technologie ligne microuban suspendu dans le domaine millimétrique", Annales des Télécommunications, Vol 45, N° 5-6, pp 296-299, 1990.

[23] ACHKAR J, PICON O, FOUAD HANNA V, CITERNE J, "Theoretical and experimental investigation of some different resonators in suspended stripline technology", 21st European Microwave Conference, Stuttgart, pp 1041-1046, 1991.

[24] MATTHAEL G L, YOUNG L, JONES E M T, "Microwave filters, impedance matching networks and coupling structures", Mc Graw-Hill, New York, 1964.

[25] TEMES G C, MITRA S K, "Modern filter theory and design", John Wiley & Sons Ltd, USA, 1973.

[26] EDWARDS T C, "Foundations for microstrip circuit design", John Wiley & Sons Ltd, USA, 1981.

[27] EESOF Inc, "Touchstone & Libra applications", USA, 1990.

[28] A. Hill and V.K. tripathi, "An efficient algorithm for the three-dimensional analysis of passive microstrip components and discontinuities for microwave and millimeter-wave integrated circuits", IEEE trans Microwave theory Tech., vol MTT-39, pp. 83-91, Jan. 1991.

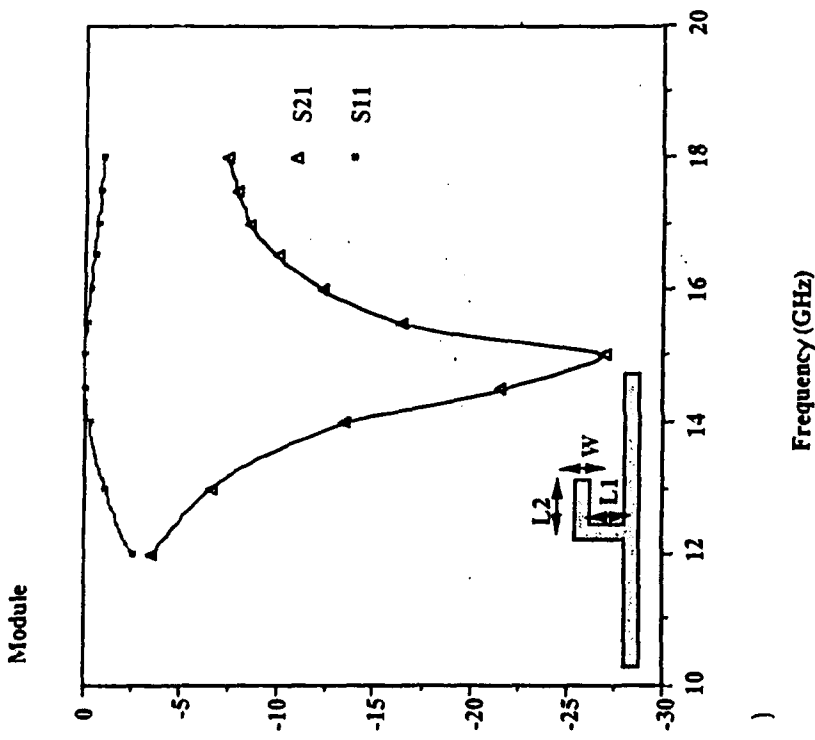


Fig. 28: Variation of S21,S11 (dB) for a bent-stub discontinuity as a function of frequency ($L_1=2.358\text{mm}$, $L_2=1.572\text{mm}$, $W=0.786\text{mm}$).

REFERENCES

- [1] SPELMAN B E, "Dissipation loss effects in isolated and coupled transmission lines", IEEE Trans on Microwave Theory and Techniques, Vol MTT-16, pp 648-656, 1977.
- [2] PICON O, ACHKAR J, FOUAD HANNA V, CITERNE J, "Scattering parameters of a step discontinuity in a suspended microstrip line", Microwave and Optical Technology Letters, USA, Vol 1, N° 7, pp 240-243, 1988.
- [3] ACHKAR J, PICON O, FOUAD HANNA V, CITERNE J, "Frequency dependent characteristics of an asymmetric suspended stripline and its open end discontinuity for millimeter wave applications", 19th European Microwave Conference, London, pp 767-772, 1989.
- [4] ITOH T, "An overview on numerical techniques for modelling 3-dimensional passive components", 15th European Microwave Conference, Paris, pp 1059-1063, 1985.
- [5] ITOH T, "Overview of quasi-planar transmission lines", IEEE Trans on Microwave Theory and Techniques, Vol MTT-37, pp 275-280, 1989.
- [6] WEIXELER A, "Solution of waveguide discontinuities by modal analysis", IEEE Trans on Microwave Theory and Techniques, Vol MTT-15, pp 508-517, 1967.
- [7] MITTRA R, ITOH T, "A new technique for the analysis of dispersion characteristics of microstrip lines", IEEE Trans on Microwave Theory and Techniques, Vol MTT-19, pp 47-56, 1971.
- [8] GUPTA K C, GARG R, BAHL I J, "Microstrip lines and slotlines", Artech house, Massachusetts, 1979.

**LEAKAGE AND CROSSTALK EFFECTS IN MILLIMETER -
WAVE INTEGRATED CIRCUITS**

A. A. Oliner

Polytechnic University • USA

LEAKAGE AND CROSSTALK EFFECTS IN MILLIMETER-WAVE INTEGRATED CIRCUITS

Arthur A. Oliner

Professor Emeritus
Polytechnic University
Brooklyn, New York, USA

New Address: 11 Daves Road
Lexington, MA 02173
USA

Telephone: 617-863-5900
Fax: (same)

3rd International Workshop on Millimeter Waves
Orvieto, Italy
April 22-24, 1992

become leaky, then describe the physical properties of the leakage, and finally present several examples of such leakage. After that, we examine the effects of crosstalk due to such leakage and also to transmission-line discontinuities, along the lines indicated earlier. Finally we look at package effects, and examine how discontinuities and leakage may each influence package guided modes and participate in resonances of the package as a whole.

The stress in the presentation will be on the physical principles and the performance consequences.

INTRODUCTION

It is evident that crosstalk in microwave and millimeter-wave integrated circuits can seriously disturb and even ruin circuit performance. It is therefore important to understand how crosstalk can be produced and what circuit effects can result from it.

Unwanted coupling between two different portions of a circuit can occur when two lines, for example, are too closely spaced to each other, so that one is in the near field of the other. This type of crosstalk has been well understood for a long time, and it will not be discussed here. We will examine, instead, the crosstalk that results from the excitation of surface waves within the circuit. These surface waves can travel throughout the circuit, bounce around, and cause various effects, ranging from direct interaction to package resonances.

Surface waves can be excited by two principal mechanisms:

- (a) circuit discontinuities, and
- (b) power leakage from the transmission-line dominant mode.

The fact that surface waves are excited at transmission-line discontinuities is of course well known, but what effects these surface waves produce have been examined only infrequently. We will discuss here the conditions under which discontinuities can interact with other portions of an integrated circuit, and how discontinuities can excite package guided modes and package cavity resonances.

The fact that transmission-line dominant modes can leak became known only a few years ago, principally as a result of work by Shigeawa, Tsuchi and Oliner. The leakage occurs in the form of a surface wave that propagates away at an angle from the axis of the transmission line. For most printed-circuit transmission lines, the dominant mode becomes leaky only at the higher frequencies, so that leakage effects become significant principally at millimeter wavelengths. The talk will discuss precisely when a dominant mode can become leaky, how the transmission line, when it leaks, can interact with other lines and with discontinuities, and how such leakage can excite package guided modes (whereas the dominant mode cannot interact with package guided modes when it is purely bound).

The present talk will begin with some necessary background material involving various constituent modes and their dispersion properties. The three printed-circuit lines that we consider are microstrip line, slot line and coplanar waveguide. We next discuss the way power can leak from the dominant mode on printed-circuit lines. In that connection, we first establish when a mode can

OUTLINE OF TALK

I. BACKGROUND AND REVIEW

- A. Constituent Basic Modes on Printed-Circuit Lines
- B. Dispersion Properties
 - 1. Modes on printed-circuit lines
 - 2. Surface waves

II. POWER LEAKAGE FROM PRINTED-CIRCUIT LINES

- A. When Can a Mode Become Leaky?
- B. Physical Properties of the Leakage
- C. Examples of Leakage

III. SOURCES OF CROSSTALK

- A. Waveguide Discontinuities
- B. Leakage Effects

IV. PACKAGE EFFECTS

- A. Guided Modes and Cavity Modes
- B. Coupling Between Leaky Modes and Guided Modes
- C. Excitation by Discontinuities

DISPERSION PROPERTIES

CONSTITUENT BASIC MODES

1. MODES ON PRINTED - CIRCUIT LINES

Microstrip Line

Slot Line

Coplanar Waveguide (CPW)

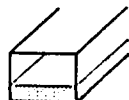
2. SURFACE WAVES ON THE SURROUNDING SUBSTRATE

(They are different when the line does or does not have a ground plane.)

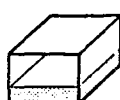


3. MODES OF THE PACKAGE

Guided Modes and Cavity Modes



waveguide



resonant cavity

$$\text{wavenumber} = \beta - j\alpha$$

β = phase constant

α = attenuation constant

α is due to material losses, and to leakage losses, where appropriate.

If only leakage is included, then α is called the leakage constant.

Dispersion means the variation of wavenumber with frequency.

Customary to plot as β/k_0 vs. frequency (or in normalized form, such as h/λ_0).

$$k_0 = 2\pi/\lambda_0 = \text{free-space wavenumber}$$

$$\frac{\beta}{k_0} = \frac{\lambda_0}{\lambda_z} = \frac{c}{v_p}$$

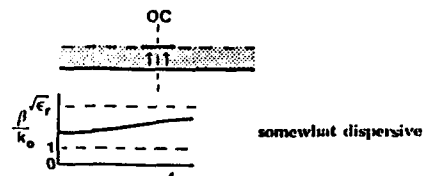
c = velocity of light in free space
 v_p = phase velocity of the mode

$$\epsilon_{\text{eff}} = \left(\frac{\beta}{k_0} \right)^2; \quad n_{\text{eff}} = \frac{\beta}{k_0}$$

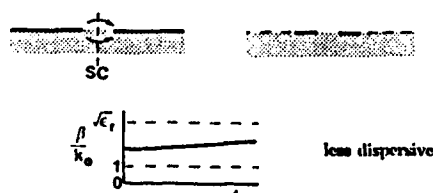
5

DISPERSION BEHAVIOR OF MODES ON PRINTED - CIRCUIT LINES

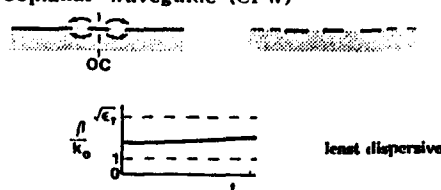
1. Microstrip Line



2. Slot Line

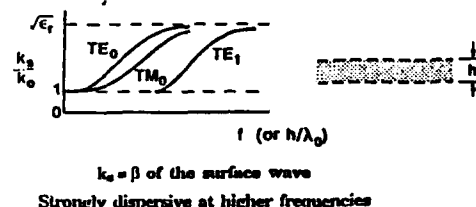


3. Coplanar Waveguide (CPW)

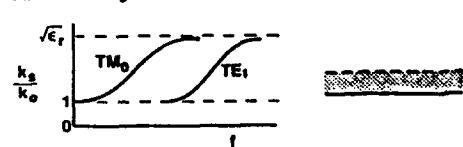


DISPERSION BEHAVIOR OF SURFACE WAVES

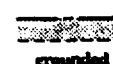
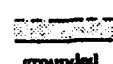
1. Ungrounded Layer



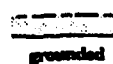
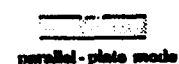
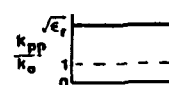
2. Grounded Layer



EXAMPLES

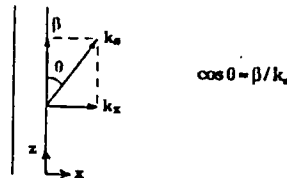


If conductor-backed:



WHEN CAN A DOMINANT MODE BECOME LEAKY?

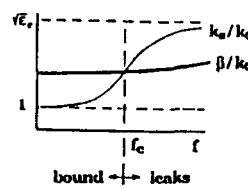
Suppose there is leakage:



Therefore, for real power to leak away we must have

$$\begin{aligned} \beta &< k_z \\ \text{or} \\ \beta/k_0 &< k_z/k_0 \end{aligned}$$

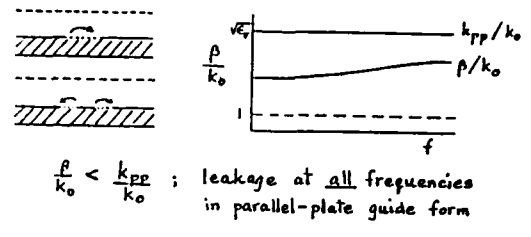
Example: CPW of finite width



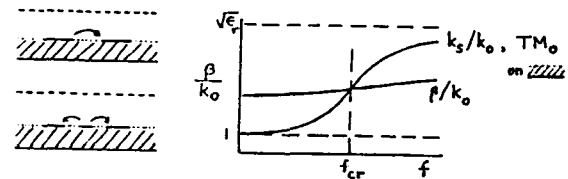
For $f > f_c$, the dominant mode on the CPW leaks.

DISPERSION PLOTS FOR VARIOUS CASES

1. Conductor-backed slot line or CPW of infinite width



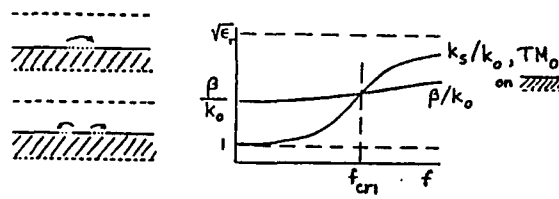
2. Conductor-backed slot line or CPW of finite width



At low frequencies, $\frac{\beta}{k_0} > \frac{k_z}{k_0}$; bound mode

Above f_{cr} , $\frac{\beta}{k_0} < \frac{k_z}{k_0}$; leakage in surface wave form, TM_0 on slot

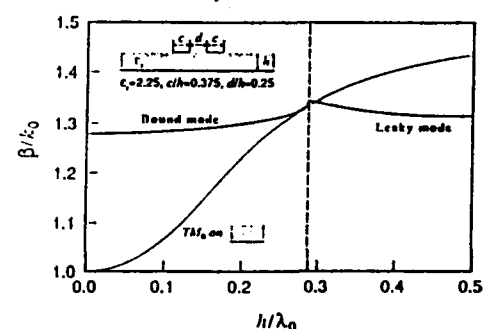
3. Conventional slot line or CPW of infinite width



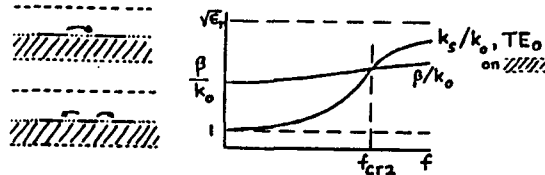
At low frequencies, $\frac{\beta}{k_0} > \frac{k_z}{k_0}$; bound wave

Above f_{cr1} , $\frac{\beta}{k_0} < \frac{k_z}{k_0}$; leakage in surface wave form, TM_0 on slot

NORMALIZED PHASE AND LEAKAGE CONSTANTS OF CONDUCTOR-BACKED SLOT LINE

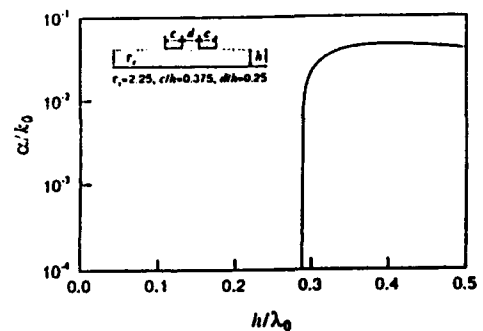


4. Conventional slot line or CPW of finite width

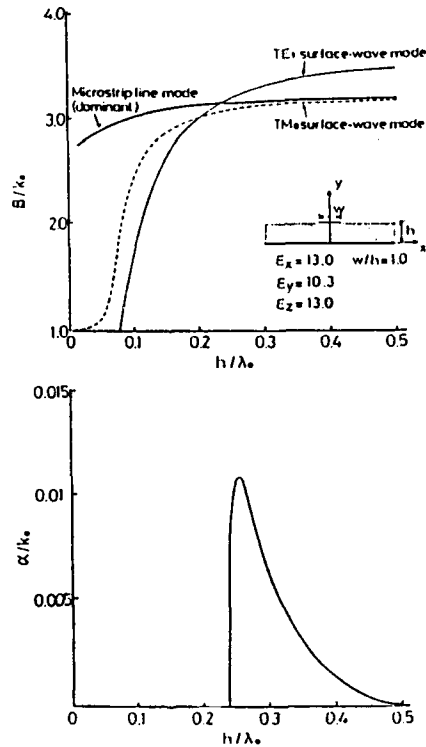


At low frequencies, $\frac{\beta}{k_0} > \frac{k_z}{k_0}$; bound wave

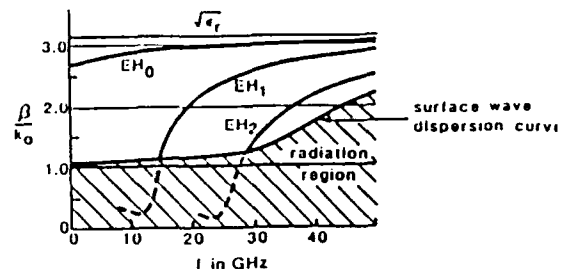
Above f_{cr2} , $\frac{\beta}{k_0} < \frac{k_z}{k_0}$; leakage in surface wave form, TE_0 on slot



NORMALIZED PHASE AND LEAKAGE CONSTANTS
FOR MICROSTRIP LINE ON AN
EPSILAM 10 SUBSTRATE



LEAKAGE FROM HIGHER MODES ON
MICROSTRIP LINE



The solutions are leaky where the curves are shown dashed. In that region just above cutoff, the surface wave leaks over a wide range of angles, from endfire to almost broadside as the frequency decreases toward cutoff.

If there is no top cover, leakage also occurs into space waves when $\beta/k_0 < 1$.

13

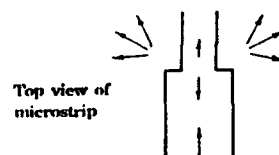
WAVEGUIDE DISCONTINUITIES

What occurs physically?

SOURCES OF CROSSTALK

1. Waveguide Discontinuities

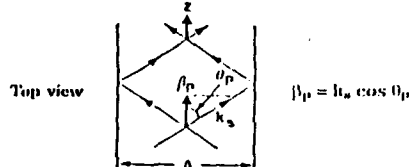
2. Leakage Effects



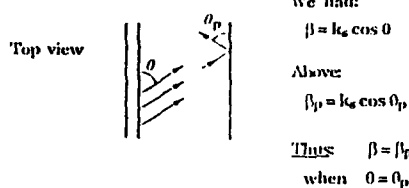
1. Higher modes on the line are excited, but decay away from it, and their power is essentially stored in the neighborhood of the discontinuity. They provide resistance to the equivalent network of the discontinuity.
2. The lowest surface wave (or waves) on the surrounding substrate is excited. It radiates power in surface-wave form over a wide range of angles, and it provides resistance to the equivalent network of the discontinuity.
3. If there are additional dominant modes, there will be some mode conversion into them. This effect contributes to resistance.

COUPLING BETWEEN 'LEAKY' MODES AND PACKAGE GUIDED MODES

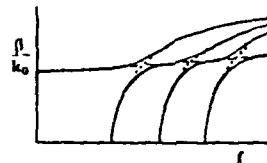
1. We can view the package guided mode in terms of a pair of surface waves at an angle.



2. The package guided mode can be excited by the "leaky" mode when the leakage angle θ becomes the same as the package guided mode angle θ_p . The two modes then couple to each other.



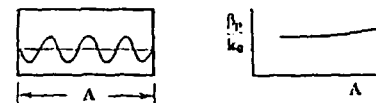
COUPLING BETWEEN 'LEAKY' MODES AND PACKAGE GUIDED MODES



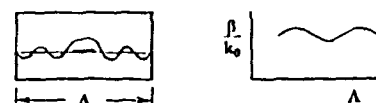
The dashed and dotted lines represent the original (unperturbed) transmission line mode and package guided modes, respectively. The solid lines represent the coupled mode result.

FURTHER INFORMATION

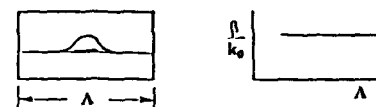
Package guided mode



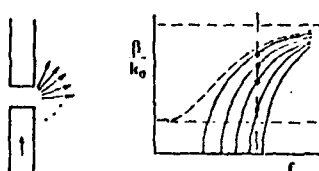
"Leaky" mode



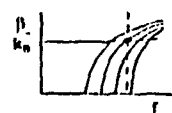
Bound mode



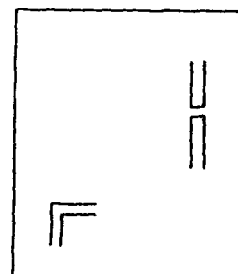
EXCITATION OF PACKAGE GUIDED MODES BY DISCONTINUITIES



1. The discontinuity excites surface waves at all angles, so that their β values range from 0 to k_s .
2. Therefore, at a particular frequency, they can couple to all package guided modes with β values in that range, usually a large number of them.
3. In the above example, 4 package guided modes are excited.
4. By contrast, a transmission line mode, with a given β at frequency f , could at most excite (couple to) a single package guided mode, and perhaps none unless the frequency were shifted.



EXCITATION OF PACKAGE CAVITY RESONANCES BY DISCONTINUITIES

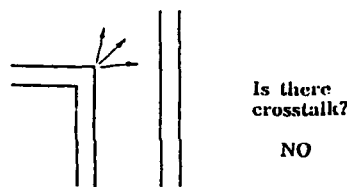


These two discontinuities can interact via the surface wave supported by the substrate. The coupling is ordinarily quite small, but gets large at frequencies corresponding to package cavity resonances. For a large package, the resonances become closely spaced in frequency.

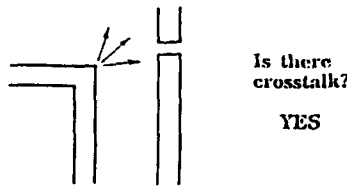
The cavity Q_s and therefore the undesired coupling or crosstalk, can be reduced by introducing loss, but the resonances broaden and can form almost a continuum in frequency in large packages.

CROSSTALK DUE TO LEAKAGE

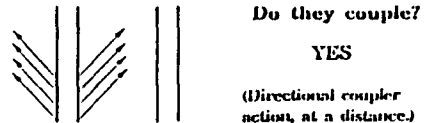
CROSSTALK BETWEEN LINES AND DISCONTINUITIES



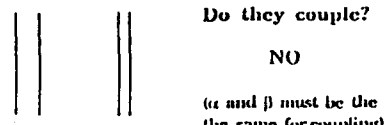
(The surface waves have wavenumbers that vary from k_x to 0 (or negative) in the component along the line length. They will couple only if the k_x component is β . Here $\beta > k_x$)



1. Two Identical Lines



2. Two Different Lines



3. If There Is a Discontinuity on the Second Line

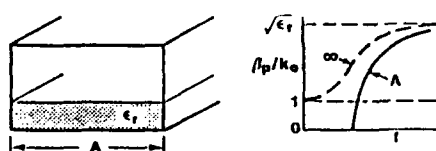


17

PACKAGE MODES

Two types: Guided modes
Cavity modes

EXAMPLE OF GUIDED MODES



If metal bounding walls

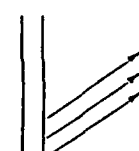
$$\beta_p^2 = k_z^2 - (n\pi/\Lambda)^2$$

$$\beta_z = k_z$$

Thus, there is a simple relation between the package guided modes and surface waves on an unbounded substrate. There are many package guided modes for each possible surface wave. If Λ is large, they are closely spaced in wavenumber.

WHAT HAPPENS TO LEAKAGE WHEN THE PACKAGE IS FINITE?

Infinite width Finite width



Complex wavenumber
 $\beta - ja$

Real wavenumber
 β

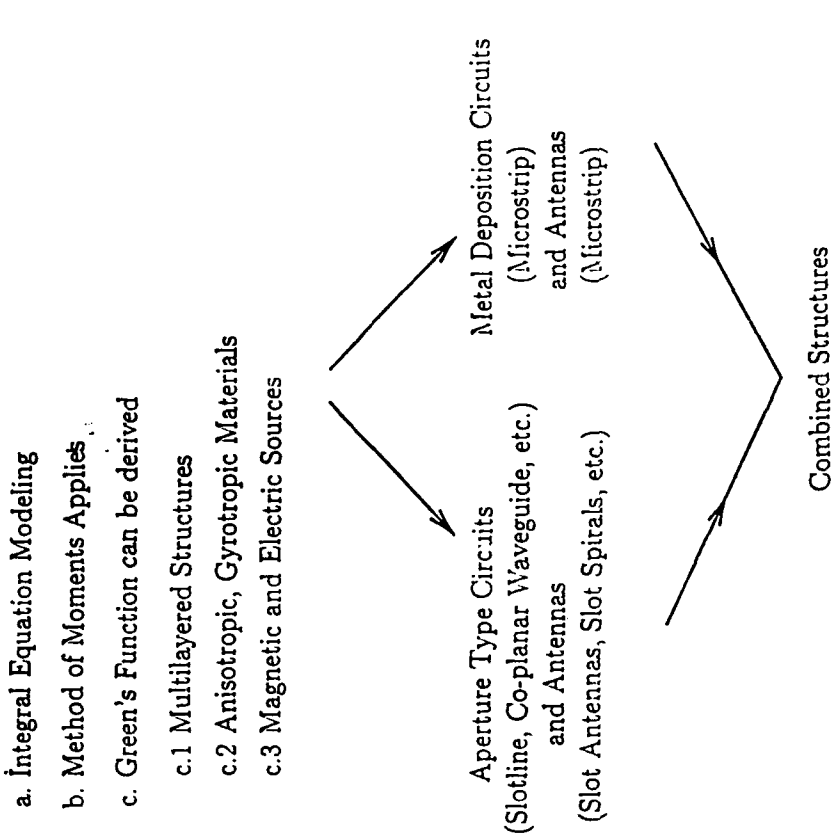
The "leakage" power is reflected from the boundaries, but it is still spread throughout the circuit, and still can cause crosstalk.

**3D MODELING OF MILLIMETER - WAVE CIRCUITS
AND ANTENNAS**

N. Alexopoulos

UCLA • USA

Unified Theory for
Printed Circuits, Antennas
and
Scatterers



N. G. Alexopoulos

Electrical Engineering Department

University of California

Los Angeles

C.A. 90024

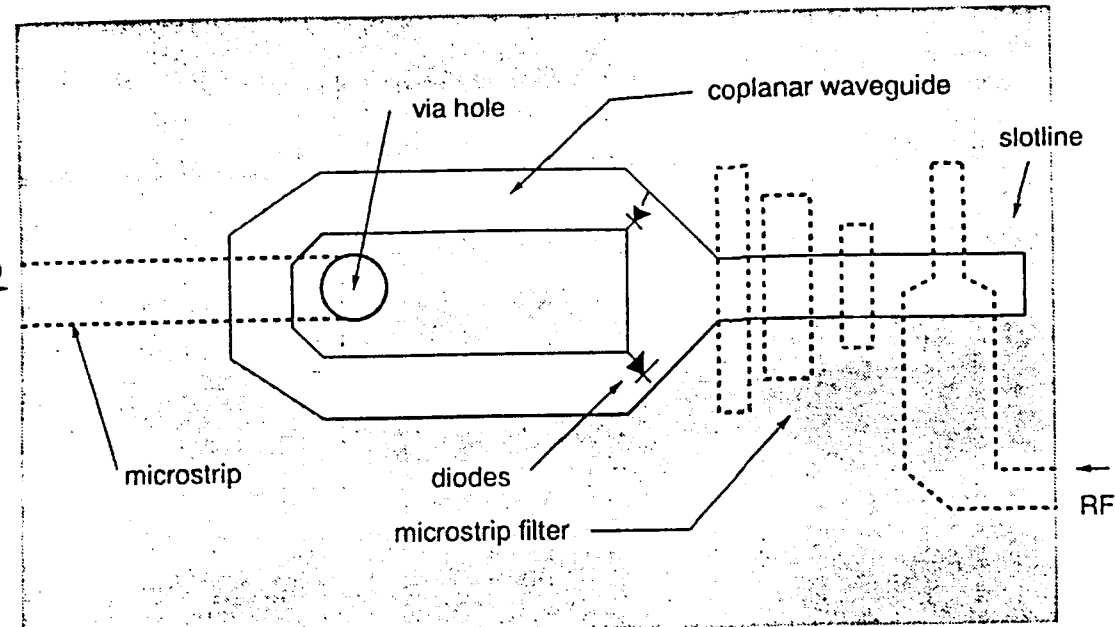
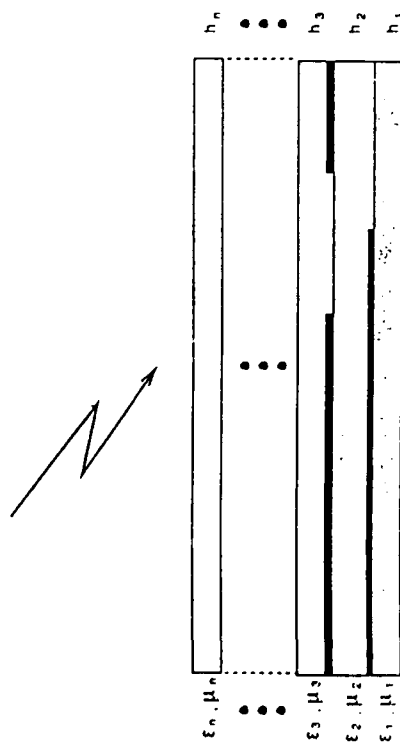


Fig. Balanced mixer

Microstrip Circuits - Aperture Antennas and Scatterers



Microstrip Circuits, Antennas and Scatterers

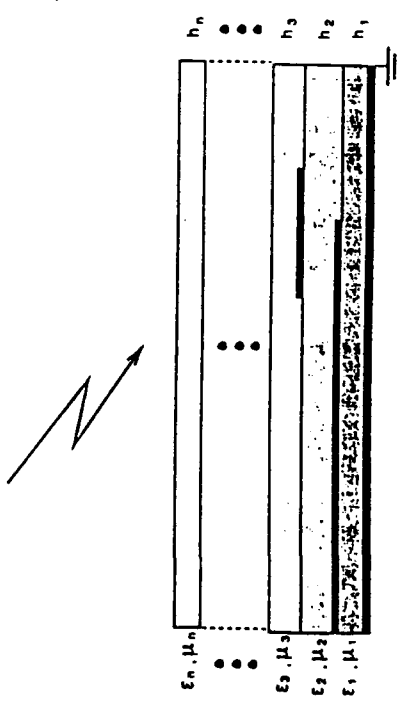




Fig. Linear array of microstrip dipoles

Microstrip Linear Array of EMC Dipoles with a Corporate Feed

Tzyy-Sheng Horng * and Nicolaos G. Alexopoulos
Electrical Engineering Department
University of California, Los Angeles
Los Angeles, CA90024

June, 1991

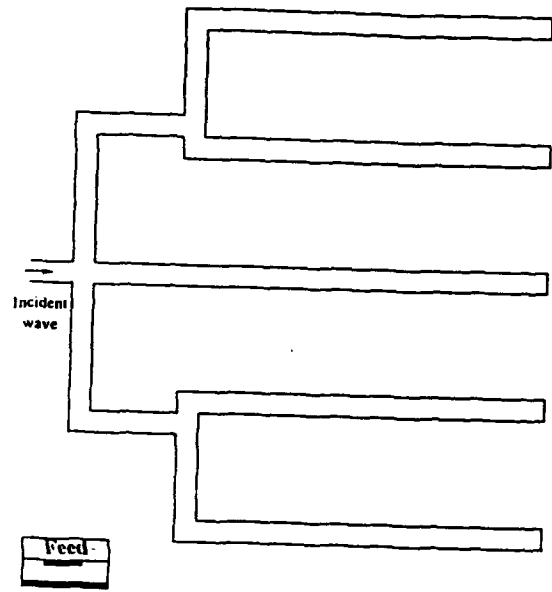


Fig Microstrip corporate feed

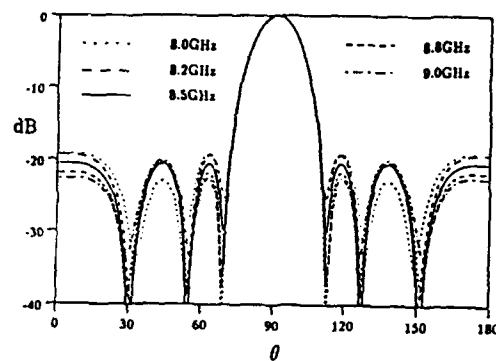


Fig. 7. Array pattern

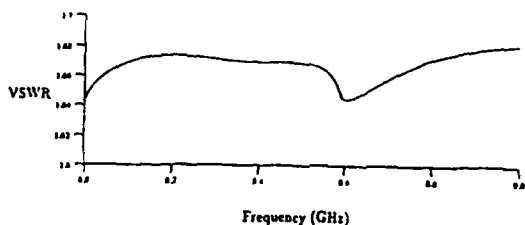


Fig. 8. VSWR versus Frequency

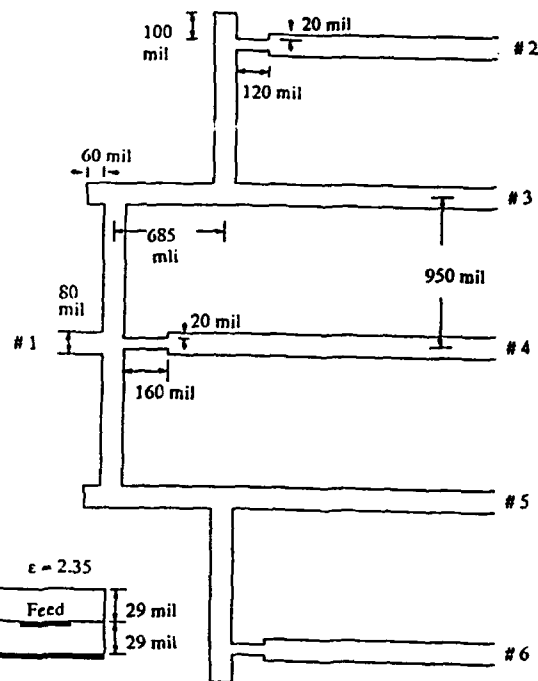
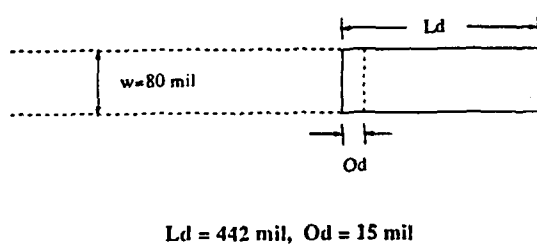


Fig. 6. An embedded microstrip corporate feed



$Ld = 442 \text{ mil}$, $Od = 15 \text{ mil}$

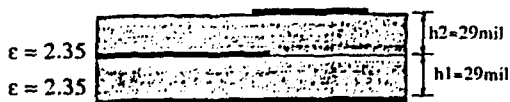


Fig. Electromagnetically coupled dipole fed by a microstripline

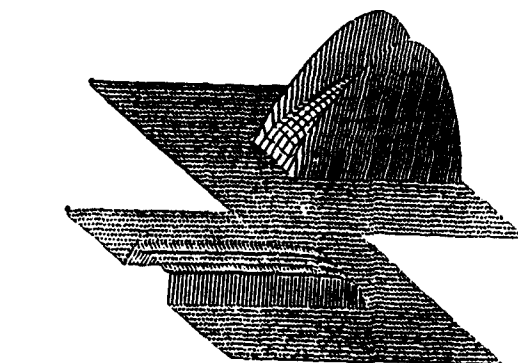
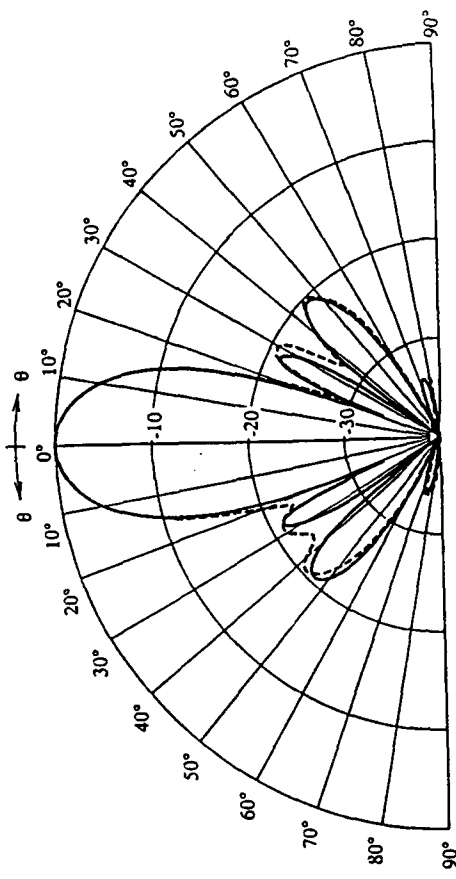
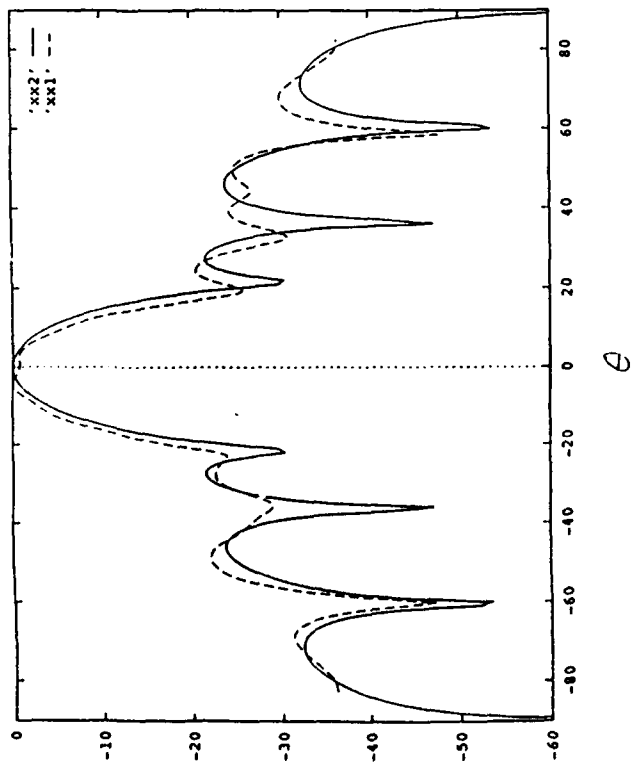


Fig. The magnitude of microstrip currents in an isolated EMC dipole

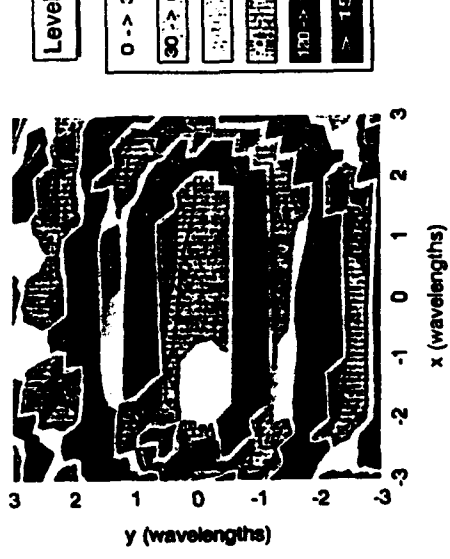


H Plane Pattern for a Linear 5 Element Array Microstrip Dipoles

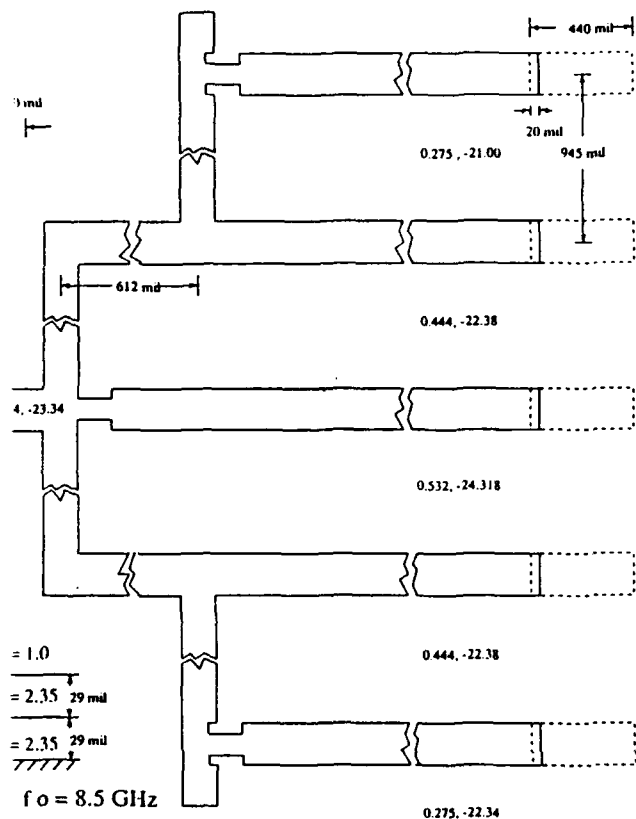


Phase Image of
5 Element Dipole Array

file = jason1.dat
freq = 8.5 GHz



Microstrip Linear Array of EMC Dipoles with a Corporate Feed



- Relative current distribution in the output ports

1/3.40° 2.42/1.22° 3.15/0° 2.42/1.22° 1/3.40°

- VSWR 1.67

- Directivity 5.77

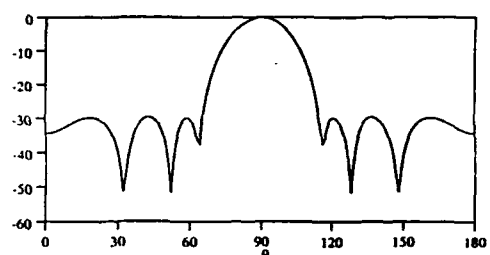
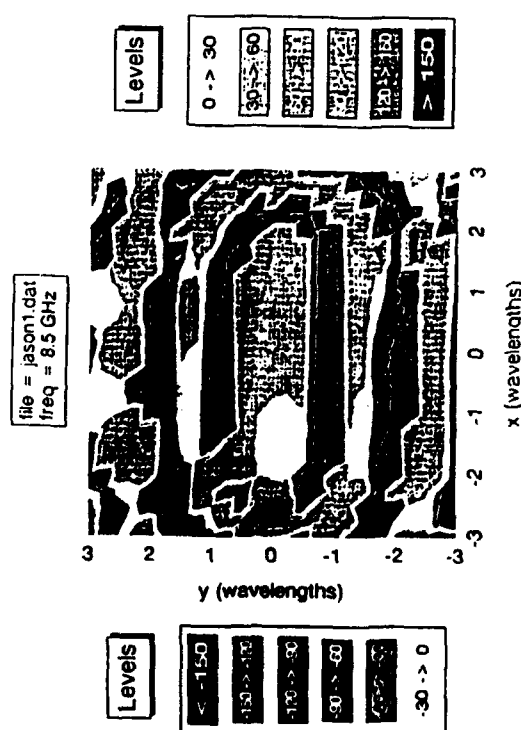
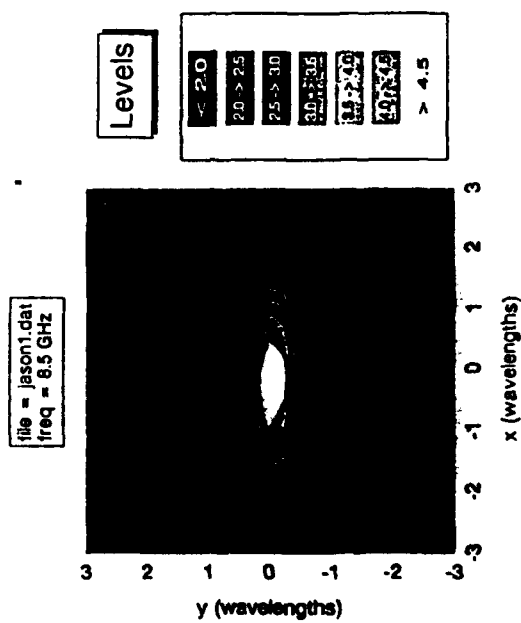


Fig. Array pattern

Phase Image of
5 Element Dipole Array



Magnitude Image of
5 Element Dipole Array



• Computation Time

GOAL: To calculate the matrix elements $Z_{ij}(m, n)$ between any two basis functions

where

i, j identify type of basis function

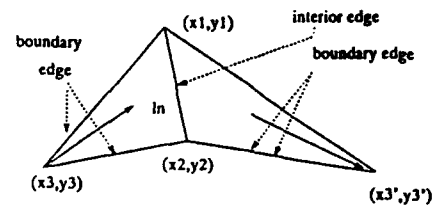
$$i, j = \begin{cases} 1, & \text{Rectangular subdomains} \\ 2, & \text{Triangular subdomains} \\ 3, & \text{Semi-infinite traveling wave modes} \end{cases}$$

m, n are relative distance indices, $m = [-50 : 50]$, $n = [-50 : 50]$

Computation time on IBM-3090 for matrix elements

- Z_{11} : 2100 sec 2 rect subdomains setting up database
- Z_{22} : 3900 sec 2 triang subdomains
- Z_{12} : 8500 sec

Triangular basis function



Ref : Rao, Wilton and Glisson, AP-30, pp.409-418, May 1982

For each interior edge l_n , the triangular basis function is defined as

$$\tilde{F}_n(x, y) = \begin{cases} \frac{l_n}{2A_n^+}(x - x_3, y - y_3), & x, y \text{ in } T_n^+ \\ \frac{l_n}{2A_n^-}(x_3' - x, y_3' - y), & x, y \text{ in } T_n^- \\ 0, & \text{otherwise} \end{cases}$$

• Method of Moments

Basis Functions

$$\vec{J}(x, y) = \sum_n C_n^e \vec{J}_n(x, y)$$

$$\vec{M}(x, y) = \sum_n C_n^m \vec{M}_n(x, y)$$

Integral Equations

$$\langle \vec{E}(x, y) \cdot \vec{J}_n(x, y) \rangle = 0, \quad n = 1, 2, \dots, N, \quad x, y \text{ on microstrips}$$

$$\langle \Delta \vec{H}(x, y) \cdot \vec{M}_n(x, y) \rangle = 0, \quad n = 1, 2, \dots, N, \quad x, y \text{ on slots}$$

Matrix Form

$$[Z]_{N \times N} [I]_N = [V]_N$$

max 5000 unknowns
~ 6000 bytes memory
~ 40 minutes
IBM 3090

Matrix Element

$$Z_{ij}(m, n) = \int_{-\infty}^{\infty} \int_{-\infty}^{\infty} \tilde{G}_{ij}(k_x, k_y) \tilde{J}_i^m(k_x, k_y) \tilde{J}_j^n(k_x, k_y) dk_x dk_y$$

• Expansion Functions

1. Rectangular subdomain modes

$$\vec{J}_n, \vec{M}_n = \begin{cases} PWS(x)P(y)\hat{x}, & x \text{-directed currents} \\ PWS(y)P(x)\hat{y}, & y \text{-directed currents} \end{cases}$$

2. Triangular subdomain modes

$$\vec{J}_n, \vec{M}_n = \begin{cases} \frac{l_n}{2A_n^+}(x - x_3, y - y_3), & x, y \text{ in } T_n^+ \\ \frac{l_n}{2A_n^-}(x_3' - x, y_3' - y), & x, y \text{ in } T_n^- \\ 0, & \text{otherwise} \end{cases}$$

3. Semi-infinite traveling wave modes (entire domain modes)

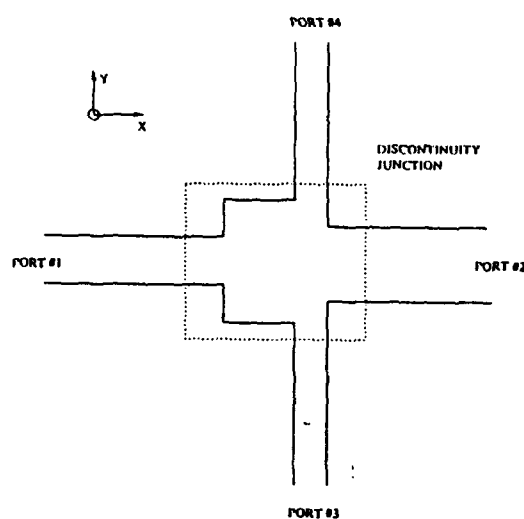
$$\vec{J}_n, \vec{M}_n = \begin{cases} U(x - x_r) e^{\pm j\beta(x - x_r)} P(y)\hat{x}, & x \text{-directed currents} \\ U(y - y_r) e^{\pm j\beta(y - y_r)} P(x)\hat{y}, & y \text{-directed currents} \end{cases}$$

• Testing Functions

Subdomain modes only

IMSL package

• Spectral-Domain Dyadic Green's Function

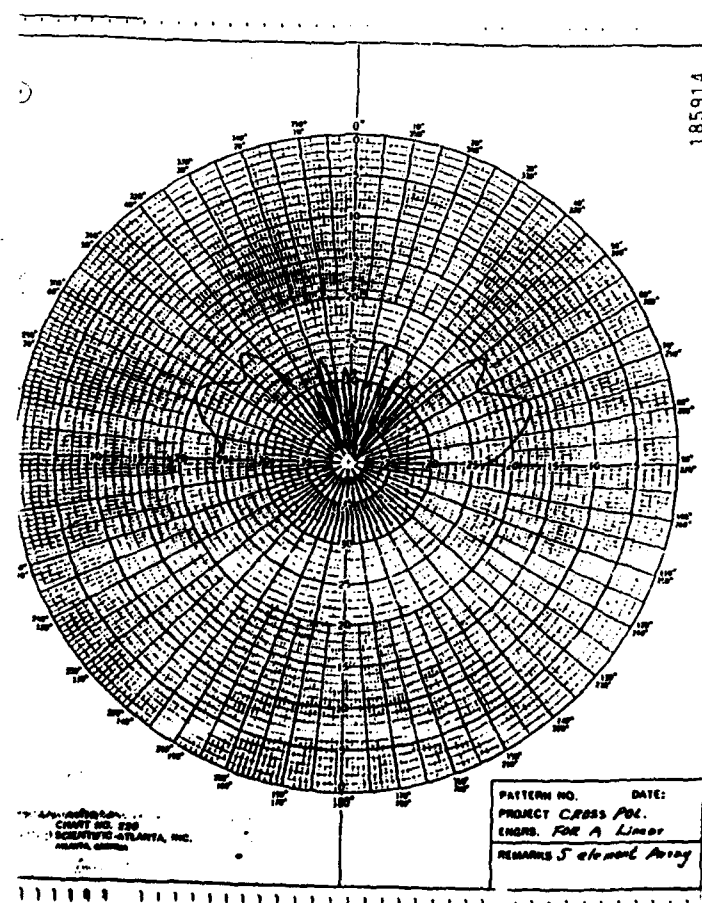


$$\begin{bmatrix} \vec{E}(x, y) \\ \Delta \vec{H}(x, y) \end{bmatrix} = \frac{1}{4\pi^2} \int_{-\infty}^{\infty} \int_{-\infty}^{\infty} \begin{bmatrix} \vec{G}_{ee}(k_x, k_y) & \vec{G}_{em}(k_x, k_y) \\ \vec{G}_{me}(k_x, k_y) & \vec{G}_{mm}(k_x, k_y) \end{bmatrix} \begin{bmatrix} \vec{j}(k_x, k_y) \\ \vec{M}(k_x, k_y) \end{bmatrix} e^{-jk_x x} e^{-jk_y y} dk_x dk_y$$

where

$$\vec{F}(k_x, k_y) = \int_{-\infty}^{\infty} \int_{-\infty}^{\infty} F(x, y) e^{jk_x x} e^{jk_y y} dx dy$$

Fig. 1 A generic structure of a four port microstrip discontinuity



DISCONTINUITIES
JUNCTIONS
AND
TRANSITIONS

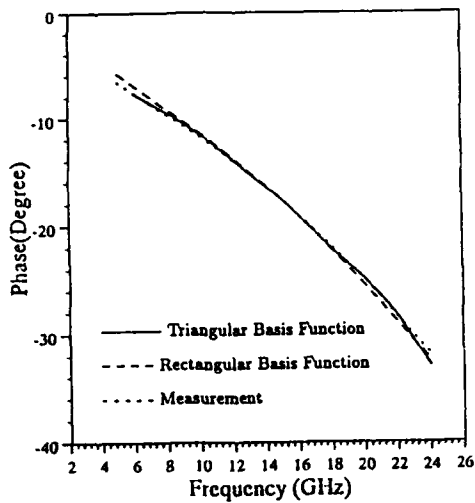


Fig. Phase of S parameters of an open-end
($\epsilon_r=9.9$, $w=24\text{mil}$, $h=25\text{mil}$)

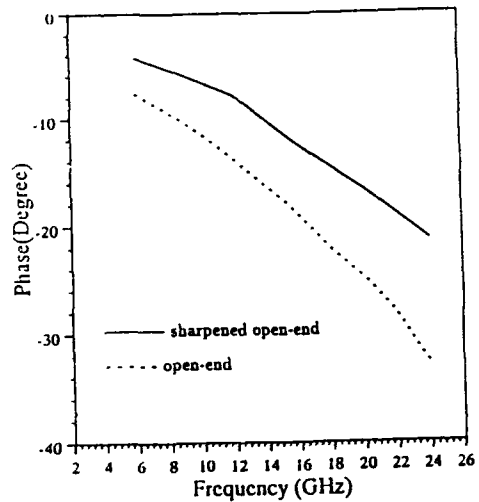


Fig. Phase of S parameters of a sharpened open-end and an open-end ($\epsilon_r=9.9$, $w=24\text{mil}$, $h=25\text{mil}$)

Basic Features Using Triangular Subdomains

1. Transmission lines have finite length.
2. Ideal current source is used for excitation.
3. The grid of subdomains is translated in the x,y plane to facilitate the computation of reaction elements.
4. Subdomains which are too distant from each other to be included in the grid have reactions which are set to zero.

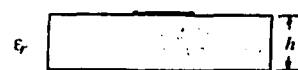
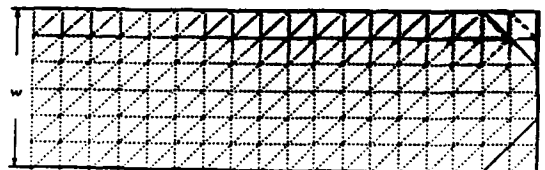


Fig. The geometry of an open-end and a sharpened open-end

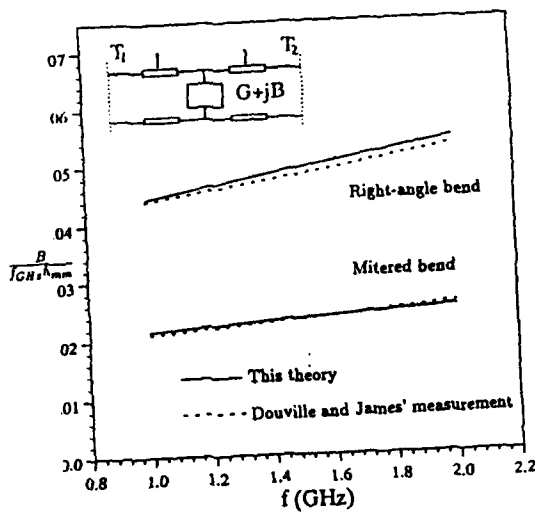


Fig. Frequency dependence of normalized susceptance for right-angle and mitered bend discontinuities ($\epsilon_r=10.8$, $w=4.572\text{mm}$, $h=5.08\text{mm}$)

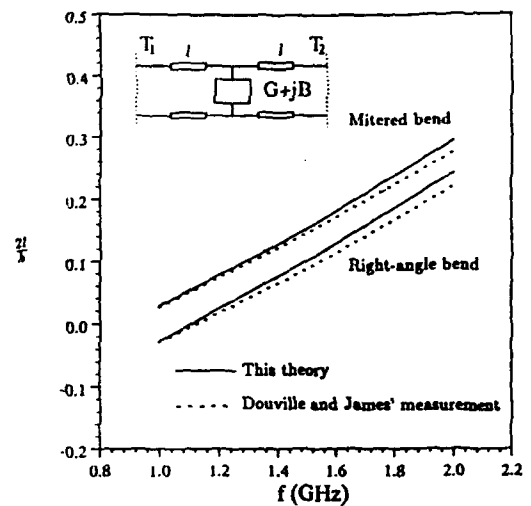


Fig. Frequency dependence of normalized electric length for right-angle bend and mitered bend discontinuities ($\epsilon_r=10.8$, $w=4.572\text{mm}$, $h=5.08\text{mm}$)

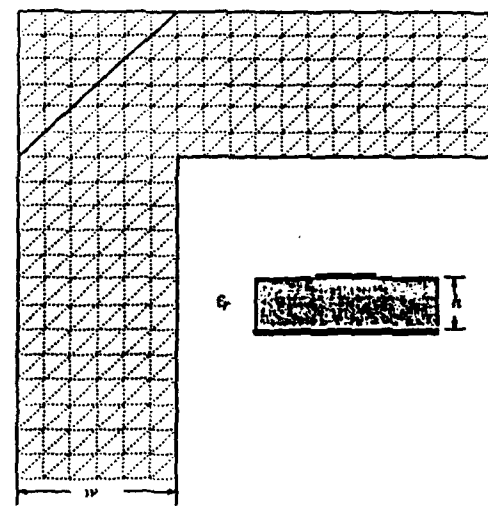
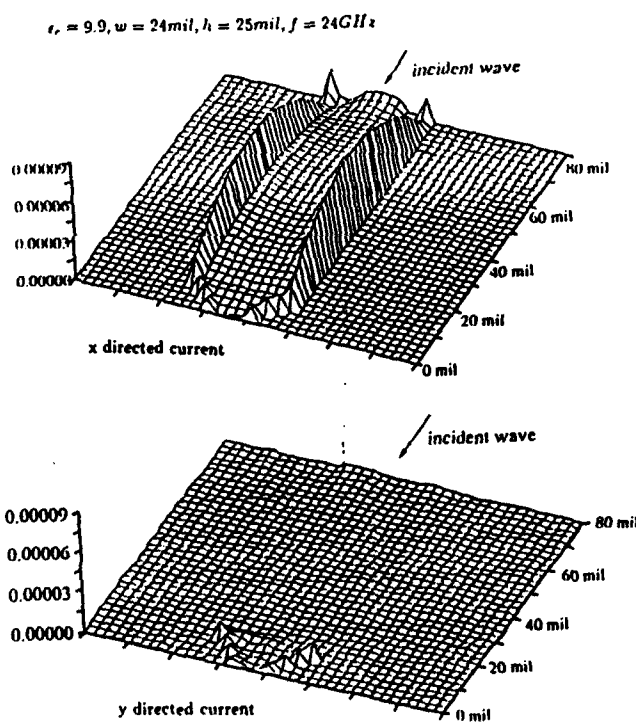


Fig. The geometry of right-angle bend and mitered bend discontinuities

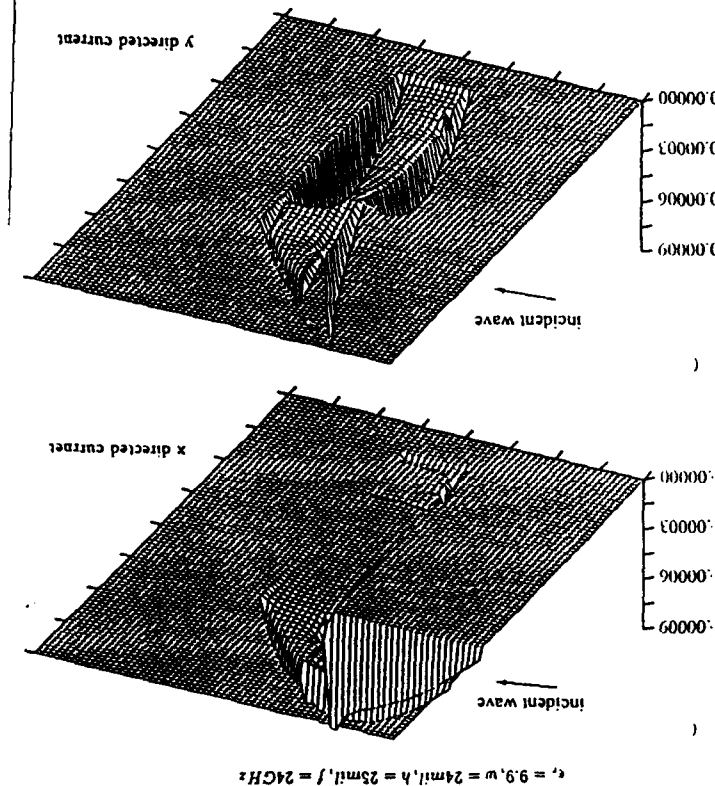
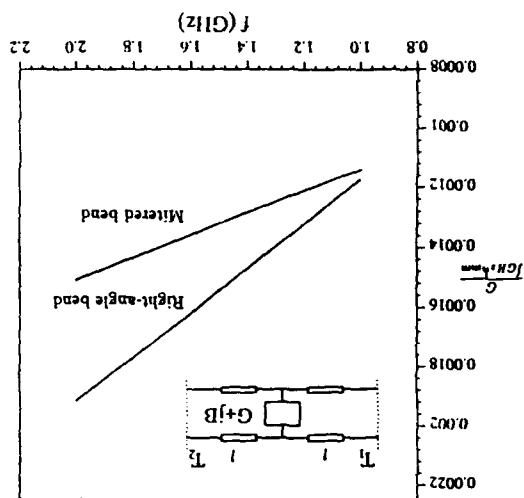


Fig. Frequency dependence of normalized conductance
($\epsilon_r=10.8$, $w=4.572\text{mm}$, $h=5.08\text{mm}$)
for right-angle bend and mitered bend discontinuities



$\epsilon_r=9.9$, $w=24\text{mm}$, $h=25\text{mm}$, $f=24\text{GHz}$

Fig. Magnitude of S parameters of a basic tee junction

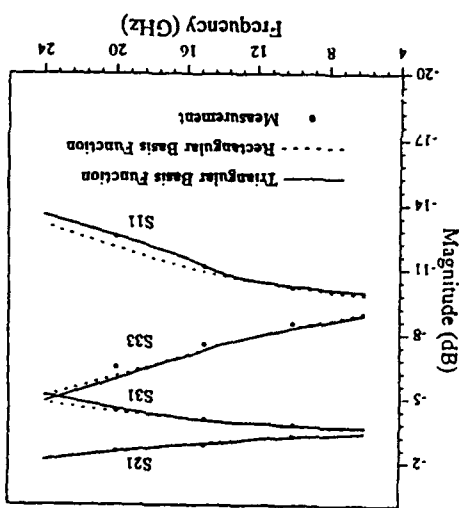
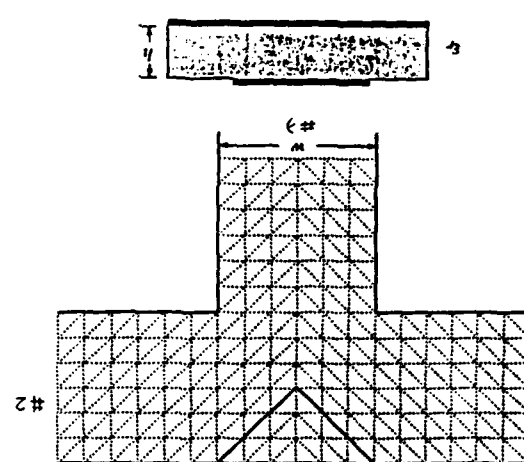


Fig. The geometry of tee and mitered tee junctions



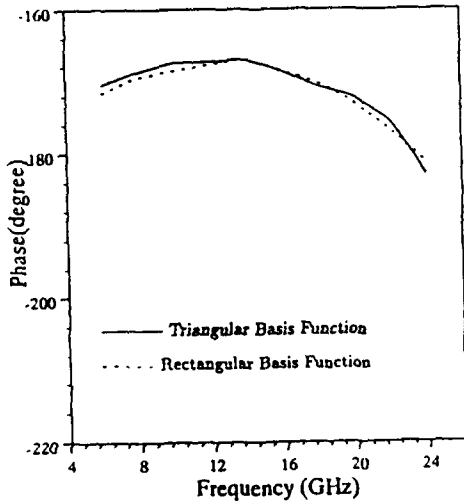


Fig. Phase of S33 of a basic tee junction
($\epsilon_r=9.9$, $w=24\text{mil}$, $h=25\text{mil}$)

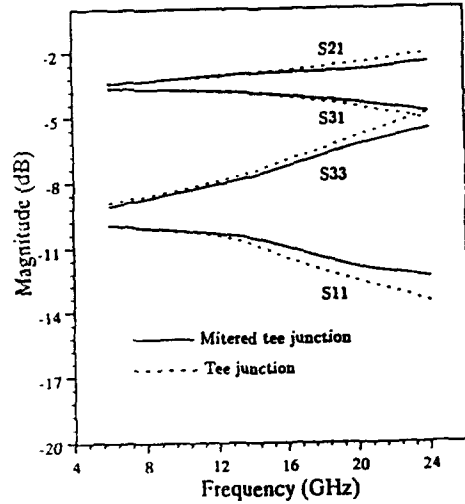


Fig. Magnitude of S parameters of tee and mitered tee junctions
($\epsilon_r=9.9$, $w=24\text{mil}$, $h=25\text{mil}$)

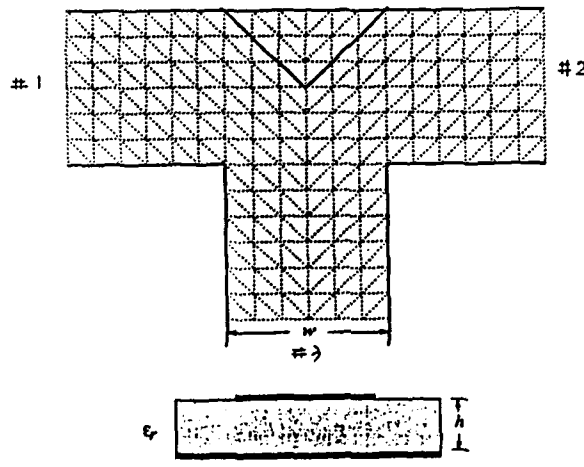


Fig. The geometry of tee and mitered tee junctions

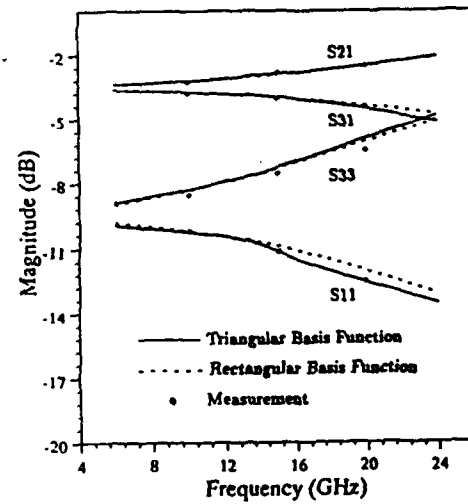


Fig. Magnitude of S parameters of a basic tee junction
($\epsilon_r=9.9$, $w=24\text{mil}$, $h=25\text{mil}$)

| Frequency (GHz) | Total Power | Reflected Power | Transmitted Power | Radiation Loss | Surface-wave Loss |
|-----------------|-------------|-----------------|-------------------|----------------|-------------------|
| 20 | 1.001 | 0.134 | 0.822 | 0.022 | 0.023 |
| 21 | 0.997 | 0.153 | 0.787 | 0.027 | 0.030 |
| 22 | 1.001 | 0.172 | 0.755 | 0.033 | 0.041 |
| 23 | 1.005 | 0.193 | 0.719 | 0.039 | 0.054 |
| 24 | 1.007 | 0.208 | 0.678 | 0.048 | 0.073 |

$$C_1 \cdot Z_0 = \frac{\lambda}{23} \left[-0.3154 + 1.1251 \tanh \left(1.3576 \frac{W}{\lambda} \right) \right] (pF \cdot \Omega) \quad (1)$$

$$C_2 \cdot Z_0 = \frac{\lambda}{23} \left[0.9102 + 6.8222 \tanh \left(0.0109 \frac{W}{\lambda} \right) \right] (pF \cdot \Omega) \quad (2)$$

$$L / Z_0 = \frac{\lambda}{23} \left[0.0103 + 0.0083 \tanh \left(0.5665 \frac{W}{\lambda} \right) \right] (\mu H / \Omega) \quad (3)$$

$$R / Z_0 = 1.1040 - 1.2385 \tanh \left(0.1036 \frac{W}{\lambda} \right) \quad (4)$$

Table 1. Power conservation check for right-angle bend discontinuity.
(Parameters are the same as those in Fig. 4.)

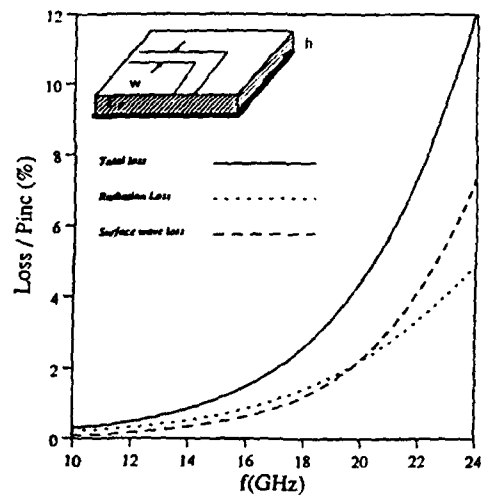


Fig. 4. Power losses versus frequency for right-angle bend discontinuity.
($\epsilon_r = 10.2$, $w = 24\text{mil}$, $h = 25\text{mil}$)

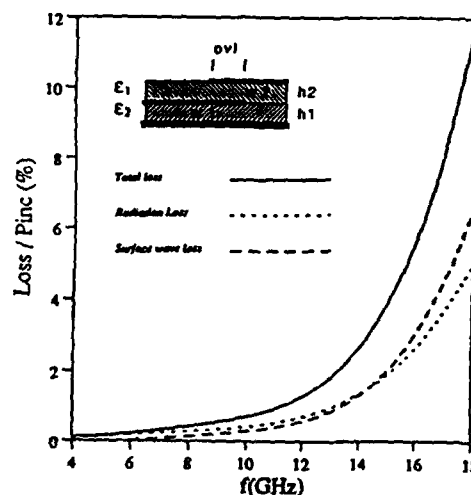
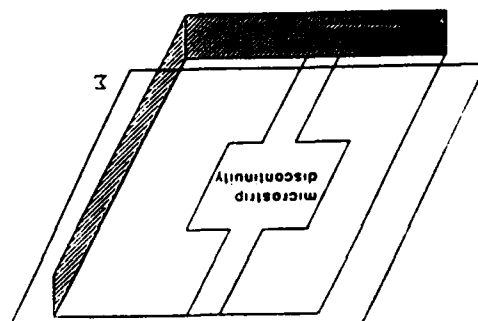
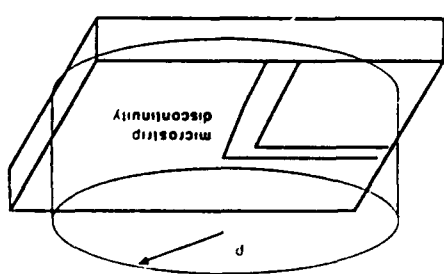
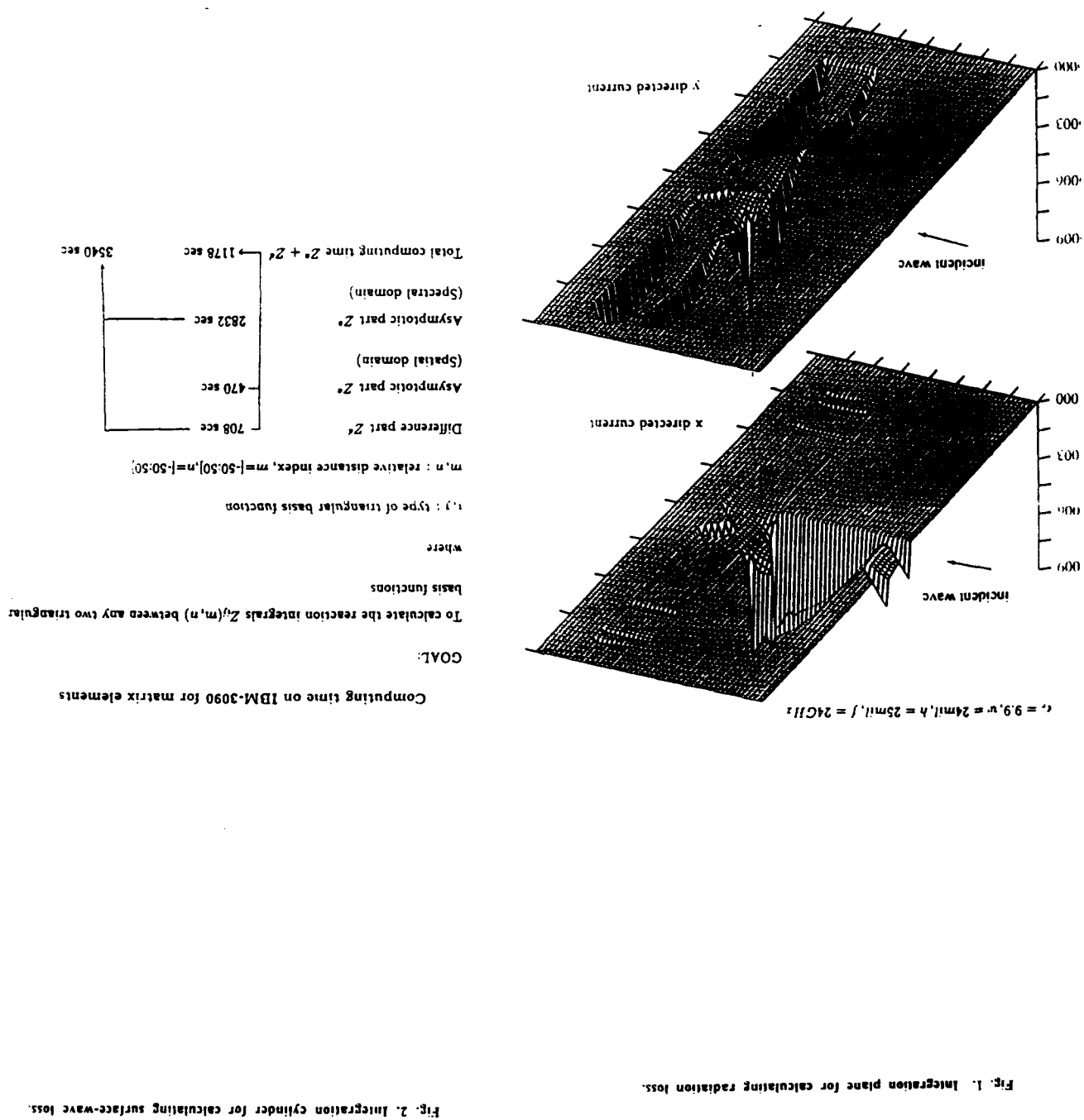


Fig. 5. Power losses versus frequency for overlay EMC lines.
($\epsilon_r = 2.2$, $\epsilon_r = 10.2$, $h_1 = 25\text{mil}$, $h_2 = 25\text{mil}$,
 $w_1 = 42\text{mil}$, $w_2 = 76\text{mil}$, $ovl = 83\text{mil}$)



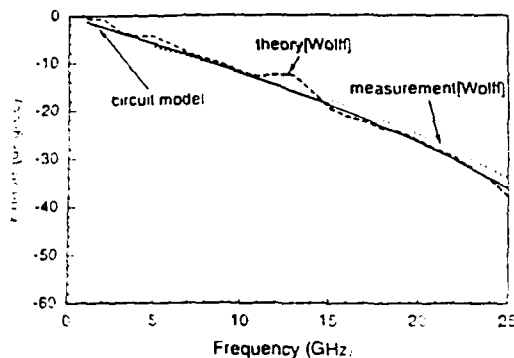
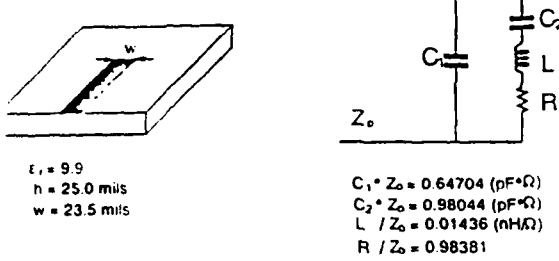
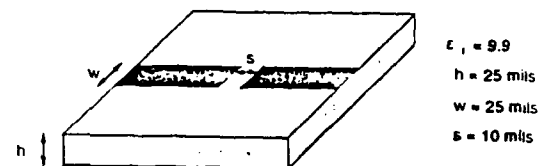


Fig. 3 Comparison of the Phase of the Open-End Discontinuity between the Proposed Circuit Model and the Measured Data

• Geometry of Microstrip Gap Discontinuity :



• Proposed Circuit Model :

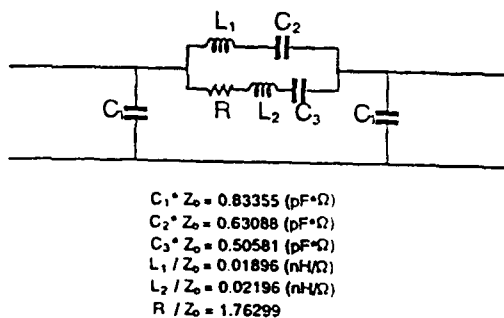
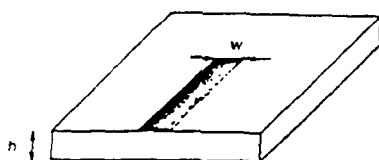


Fig. 4 Physical Dimension and the Equivalent Circuit Model of a Microstrip Gap Discontinuity

Microstrip Open-End Geometry :



Proposed Circuit Model :

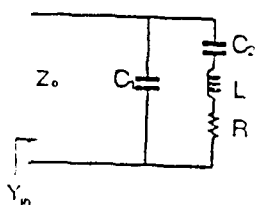


Fig. 1 Physical Dimension and the Equivalent Circuit Model of a Microstrip Open-End Discontinuity.

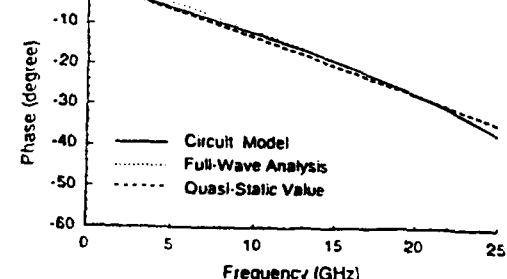
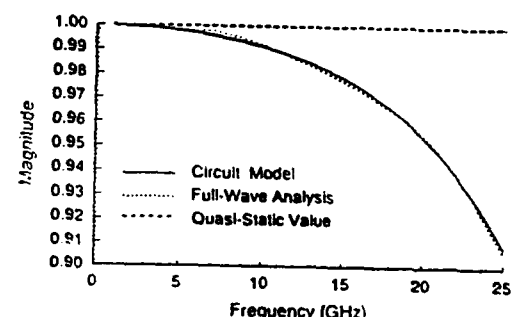
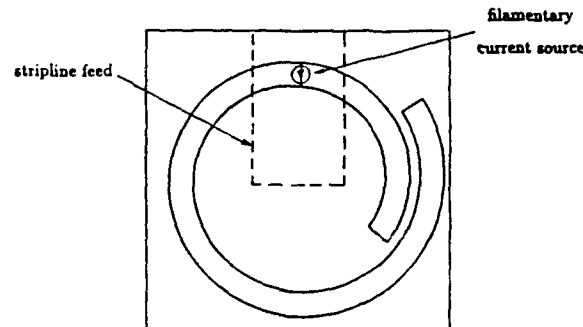
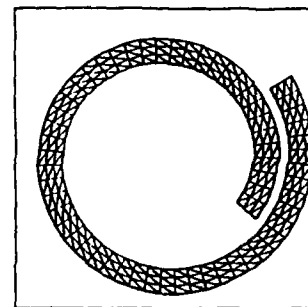
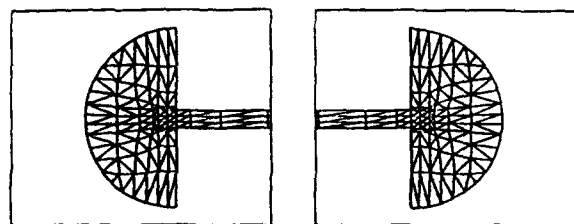
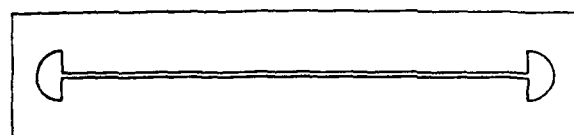


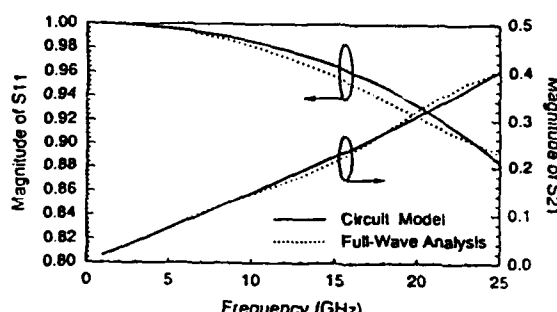
Fig. 2 Reflection Coefficient of a Microstrip Open-End ($\epsilon_r = 9.9$, $h = 25 \text{ mils}$, $W = 25 \text{ mils}$)

Slot with Radial Open Ends

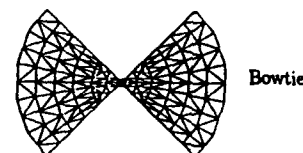


CC

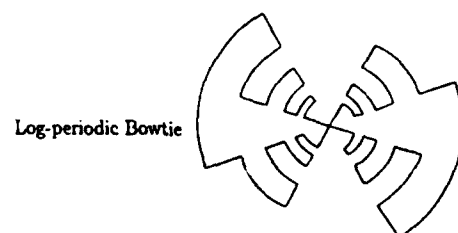
CS



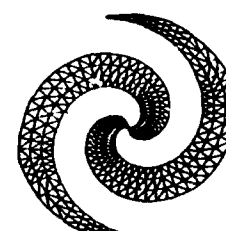
Potential Applications: Microwave and millimeterwave
aperture-type antennas whose geometries include



Bowtie



Log-periodic Bowtie



Archimedian Spiral

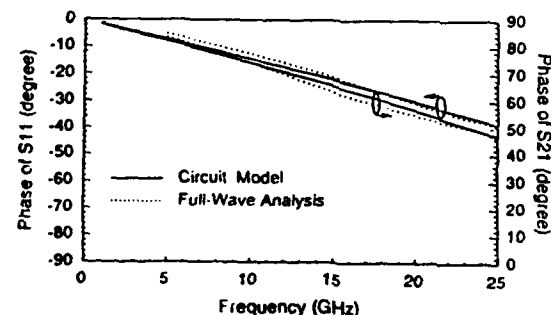
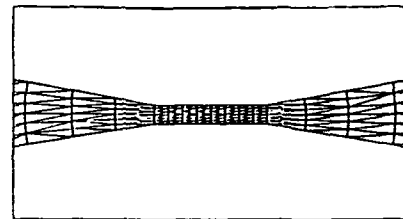
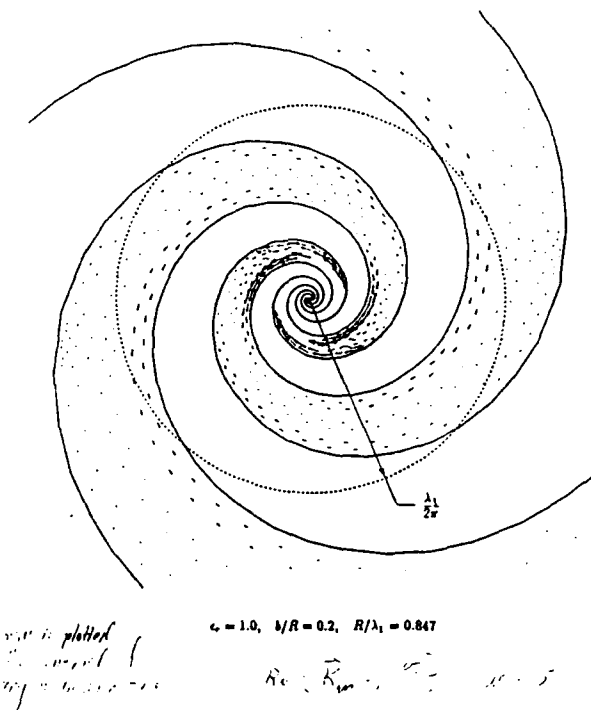


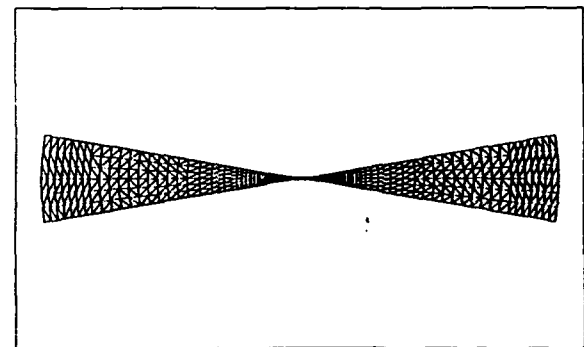
Fig. 5 S Parameters of a Microstrip Gap Discontinuity
($\epsilon_r = 9.9$, $h = 25$ mils, $W = 25$ mils, $s = 10$ mils)

Distribution of Magnetic Current



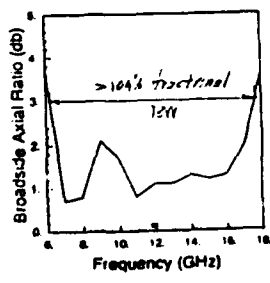
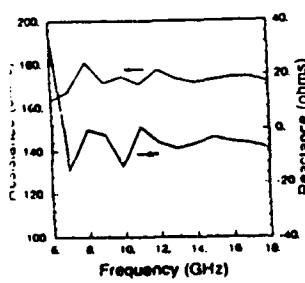
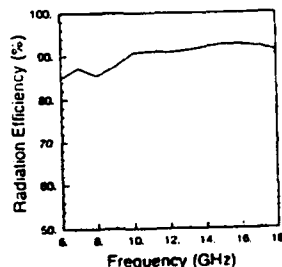
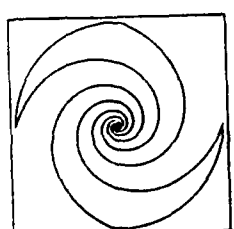
10° Bowtie Slot Antenna

(898 edges, 2000 mil radius, 40 mil gap)



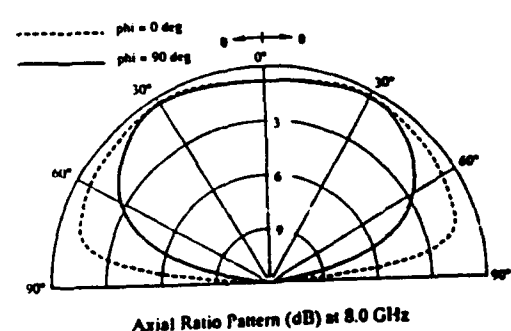
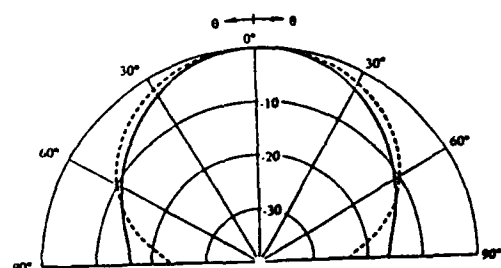
Equiangular Spiral Slot Antenna

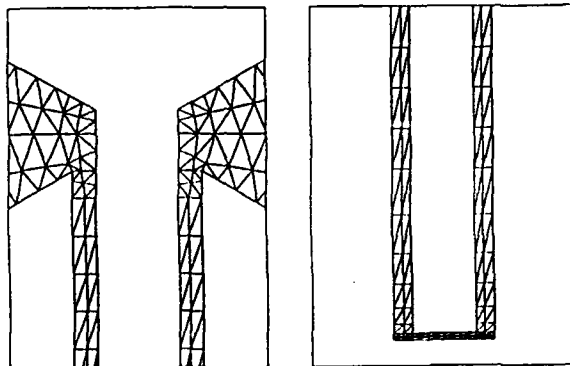
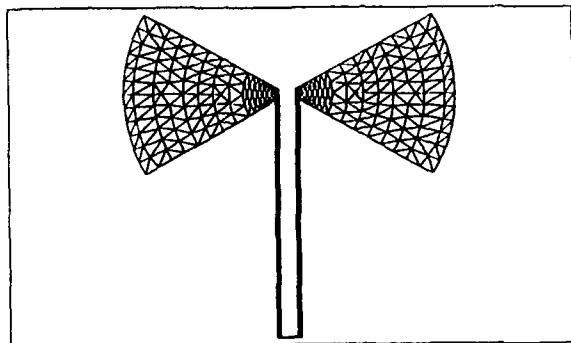
$(\epsilon_r = 1.0, b = 300 \text{ mils}, R = 1000 \text{ mils})$
 $(\rho = e^{a\theta+n\frac{2\pi}{3}}, a = 0.3063/\text{rad}, n \in \{0, 1, 2, 3\}, 5 < \rho < 1000 \text{ mils})$



Equiangular Spiral Slot Antenna

$(\epsilon_r = 1.0, b = 300 \text{ mils}, R = 1000 \text{ mils})$
 $(\rho = e^{a\theta+n\frac{2\pi}{3}}, a = 0.3063/\text{rad}, n \in \{0, 1, 2, 3\}, 5 < \rho < 1000 \text{ mils})$





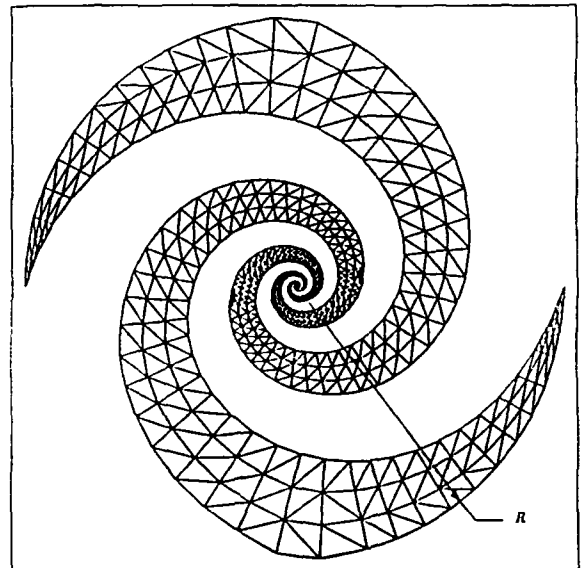
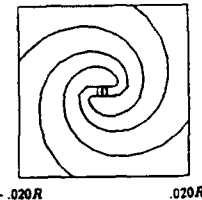
30° Bowtie Slot Antenna with 100Ω CPW Feed

(898 edges, 2000 mil radius)

Equiangular Spiral Slot Antenna

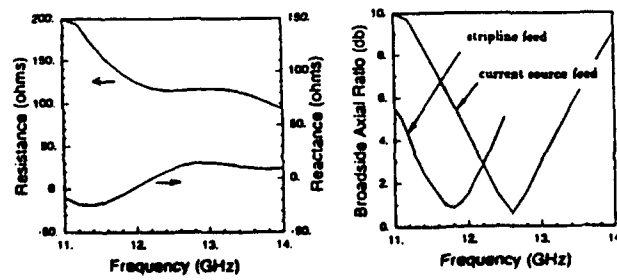
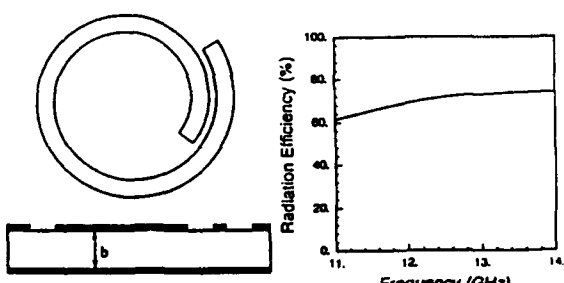
$$\rho = \exp \left[0.3063 \left(\theta - \frac{\pi}{2} \right) \right]$$

$n = 0, 1, 2, 3 \quad ; \quad 0.005R < \rho < R$



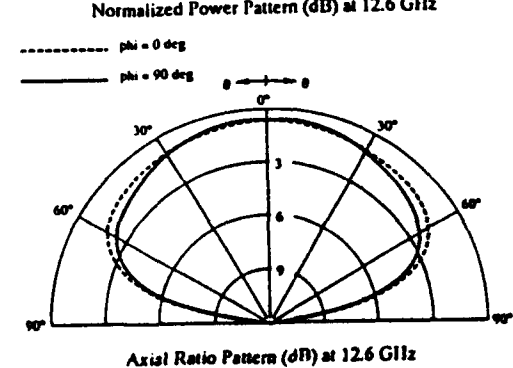
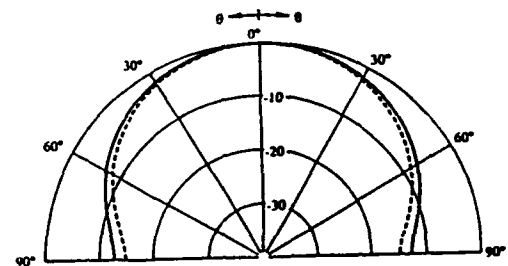
Monofilar Archimedean Spiral Slot Antenna

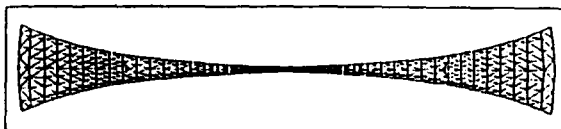
$(\epsilon_r = 2.2, b = 500 \text{ mils}, w = 40 \text{ mils}, \theta_{in} = 5.81\pi, \theta_{end} = 8.188\pi)$
 $(\rho = a\theta + \Delta, a = 9.055 \text{ mils/rad}, \Delta = 7.087 \text{ mils})$



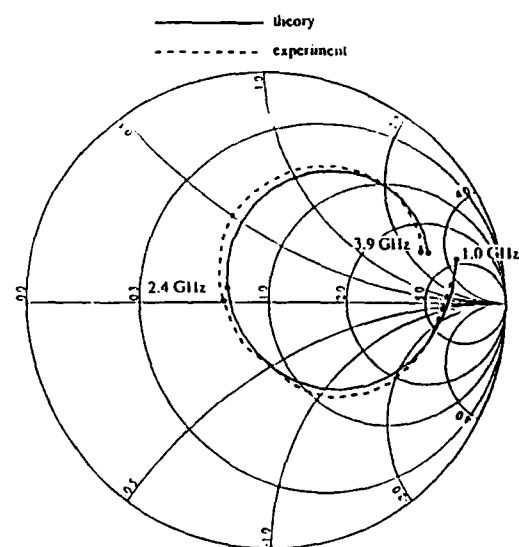
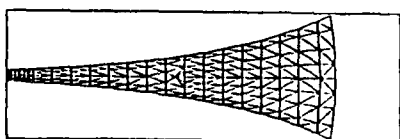
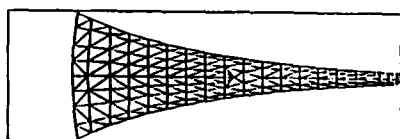
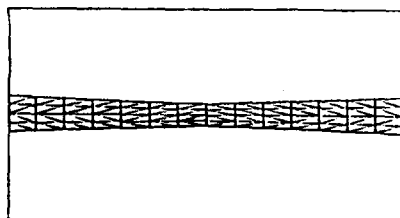
Monofilar Archimedean Spiral Slot Antenna

$(\epsilon_r = 2.2, b = 500 \text{ mils}, w = 40 \text{ mils}, \theta_{in} = 5.81\pi, \theta_{end} = 8.188\pi)$
 $(\rho = a\theta + \Delta, a = 9.055 \text{ mils/rad}, \Delta = 7.087 \text{ mils})$



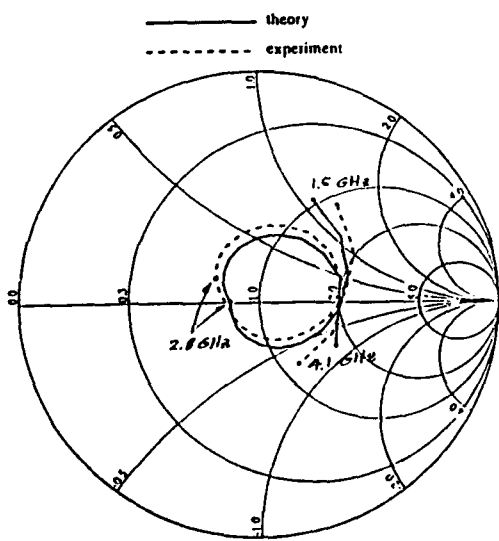


Exponentially-Tapered Slot Antenna
(736 edges, 2000 mil radius, $w = 40 \exp(z/700)$ mils)



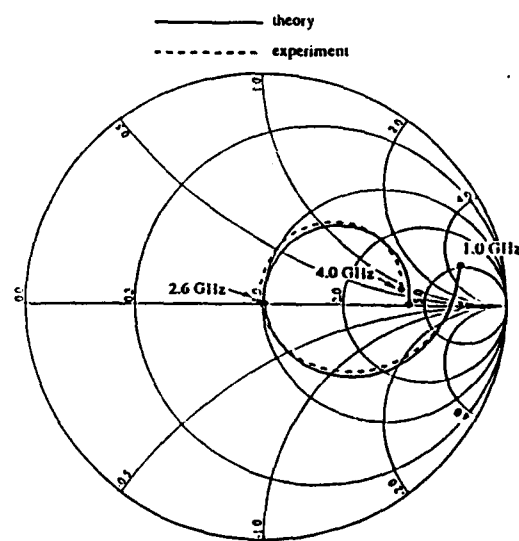
Reflection Coefficient for the Exponentially-Tapered Slot

$Z_o = 50\Omega$



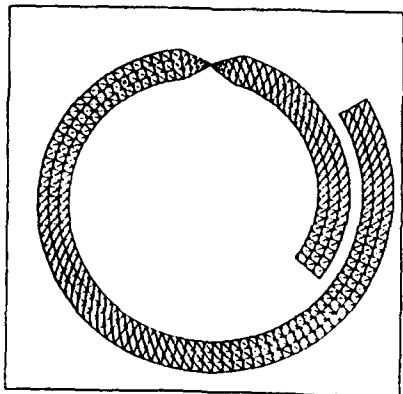
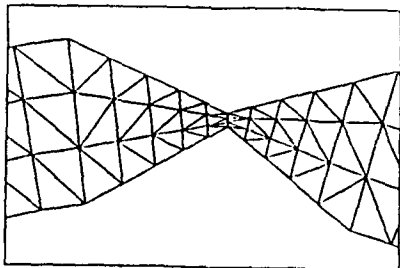
Reflection Coefficient, 30 Degree Bowtie w/ feed

$Z_o = 100\Omega$



Reflection Coefficient for the 10 Degree Bowtie

$Z_o = 50\Omega$

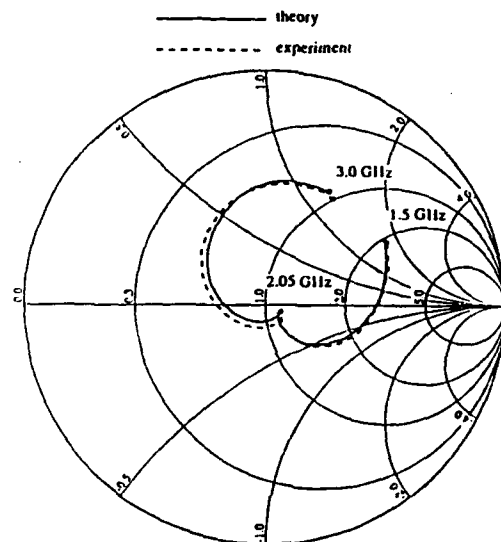


Geometry of the Monofilar Archimedean Spiral
(989 edges, $w=254$ mils, $r_{min} = 1004$ mils, $r_{max} = 1434$ mils)

Monofilar Archimedean Spiral Slot Antenna

$$(\epsilon_r = 1.08, b = 1000 \text{ mils}, w = 254 \text{ mils}, \theta_{sl} = 5.81\pi, \theta_{end} = 8.188\pi)$$

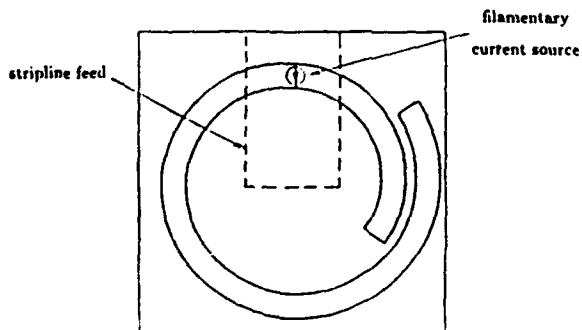
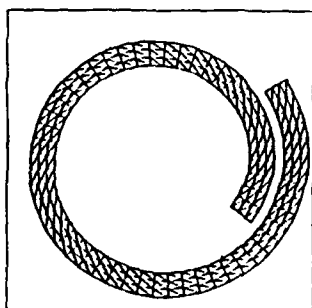
$$(\rho = a\theta + \Delta, a = 57.5 \text{ mils/rad}, \Delta = 45 \text{ mils})$$



Reflection Coefficient for the Monofilar Spiral Slot Antenna

$$Z_0 \approx 100 \text{ ohms}$$

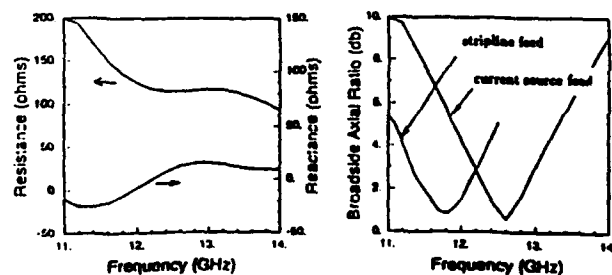
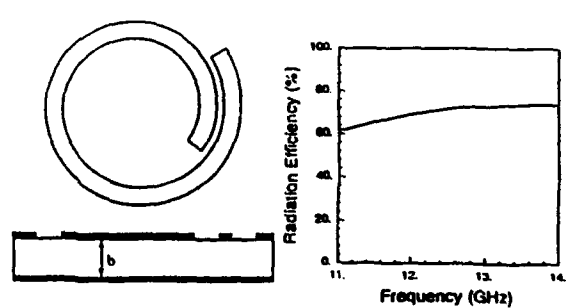
Monofilar Archimedean Spiral Slot Antenna
(Ref: Nakano, 1991 IEEE AP Symposium)



Monofilar Archimedean Spiral Slot Antenna

$$(\epsilon_r = 2.2, b = 500 \text{ mils}, w = 40 \text{ mils}, \theta_{sl} = 5.81\pi, \theta_{end} = 8.188\pi)$$

$$(\rho = a\theta + \Delta, a = 9.055 \text{ mils/rad}, \Delta = 7.087 \text{ mils})$$



- In each elementary waveguide the e.m. field can be considered as generated by equivalent current and charge sheets placed at the magnetic walls

$$J_s(x, y) = \pm u_x \times H(x, y) \quad p_s(x, y) = -\nabla \cdot J_s(x, y) / j\omega$$

$$\text{where } \nabla = u_x \frac{\partial}{\partial x} + u_y \frac{\partial}{\partial y} - j\beta u_z$$

- The electric field can be expressed as:

$$E(x, y) = -\nabla \int_{\text{magnetic walls}} F(x, y; y') \rho_s(x, y') dy' - j\omega \int_{\text{magnetic walls}} G(x, y; y', \omega, \beta) \cdot J_s(x', y') dy'$$

where the integrals represent the scalar and the vector potentials in the Coulomb gauge, and F and G are the pertinent Green's functions. They are the solution of the problem:

$$\nabla \cdot \epsilon \nabla F = -\delta(x-x') \delta(y-y')$$

$$\nabla \times \mu^{-1} \nabla \times G - \omega^2 \epsilon G = \mathbf{1} \delta(x-x') \delta(y-y') - \epsilon \nabla \nabla F$$

with appropriate boundary conditions.

- Functions F and G can be determined analytically in each region.

- Enforcing the continuity of $u_x \times E$ at the interfaces between the elementary waveguides a system of integral equations is obtained.

- The problem is put into algebraic form using the method of the moments, with base functions suitable to represent both the components of the unknown currents (J_s) and the related charges (ρ_s) and taking into account the singularities at the metallic and the dielectric edges.

Standard integral equation approach

- For a given β, ω is found by solving a non-linear eigenvalue problem

- The solution of this problem requires the search of the zeros of a ω -dependent matrix, which must be recalculated at each step in the search
- The search of the zeros is a time consuming procedure especially when:
 - the propagating frequencies of many modes are required
 - no estimate of the expected values is available
 - quasi-degenerate modes must be resolved
- The troubles of the integral equation approach derive from the fact that G is a transcendental function of ω

Departement of Electronics
University of Pavia
via Abbiategrasso 209, 27100 Pavia (Italy)

Microwave Group

G. Conciauro
(responsible)

P. Ardoni
M. Bressan
P. Gamba
L. Peruggini

Present activities on numerical modelling of passive structures:

- Quasi planar waveguides and transmission lines
- Quasi planar 3 D circuits
- Cavities resonators

Development of non conventional approaches aiming at

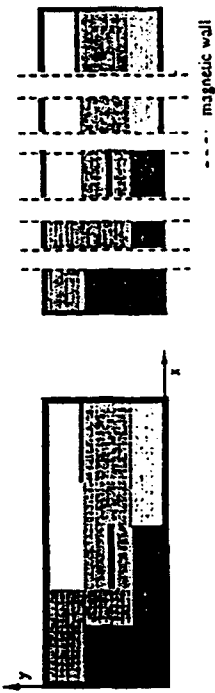
- flexibility
- accuracy
- efficiency

A new method for numerical modelling of general quasi-planar waveguides

M. Bressan, G. Conciauro, P. Gamba

(to be presented at U.R.S.I. Symposium on Electromagnetic Theory,
Sydney, 17-20 August 1992)

- Most of the quasi-planar millimeter wave and optical waveguides
can be segmented into side-coupled uniformly stratified
rectangular waveguides.



- For any propagating mode, the e.m. field in the structure can be
expressed as:

$$\mathbf{E} = \mathbf{E}(x,y) e^{j(\omega t - \beta z)}$$

- The algorithm permits one to calculate the dispersion ($\omega - \beta$)
diagram and the modal fields.

The following presentation aims at giving an idea of the approach
under investigation.

PARTECIPANTS' CONTRIBUTIONS

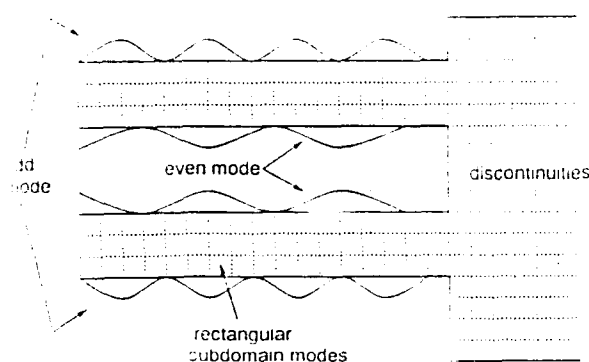


Fig. 2. Layout of expansion modes for magnetic currents on slots

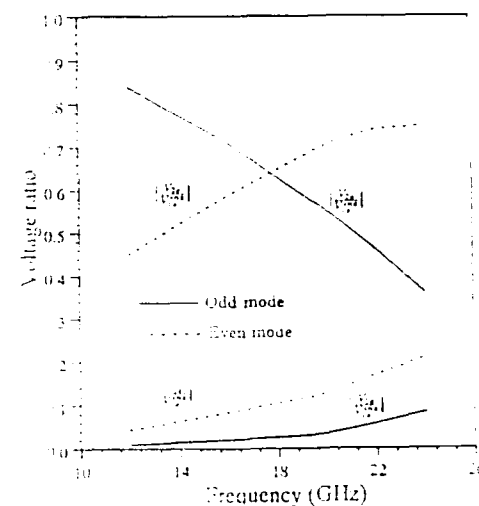
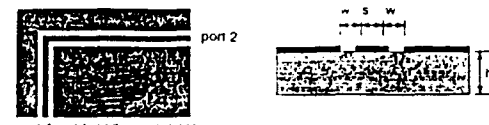


Fig. 3. The slot voltages of even modes and odd modes in a CPW right-angle bend ($\epsilon_r=9.9$, $w=24\text{ mil}$, $s=24\text{ mil}$, $h=25\text{ mil}$)

Computational Performance

of the Arbitrary-Geometry Modeling Software
on the IBM 3090

| antenna elements | no. of basis functions | execution time per frequency (seconds) | storage required (megabytes) |
|--------------------|------------------------|--|------------------------------|
| Slot Dipole | 200 - 500 | 50 - 300 | .05 - 4 |
| Bowtie Slot | 400 - 800 | 250 - 500 | 2.5 - 11 |
| Monofilar Spiral | 500 - 800 | 300 - 500 | 4 - 11 |
| Archimedean Spiral | 700 - 2000 | 450 - 2000 | 8 - 64 |
| Equiangular Spiral | 1000 - 3000 | 800 - 3500 | 16 - 150 |

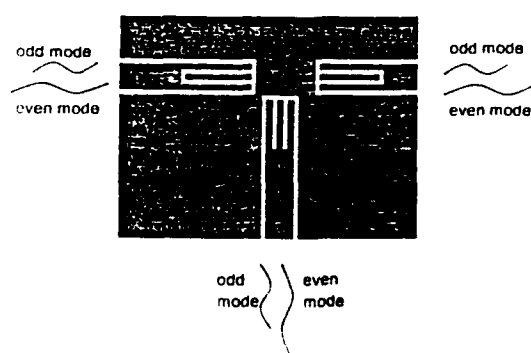
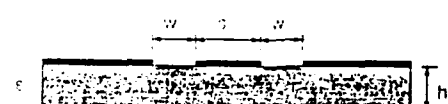


Fig. 1. Asymmetric coplanar waveguide discontinuities

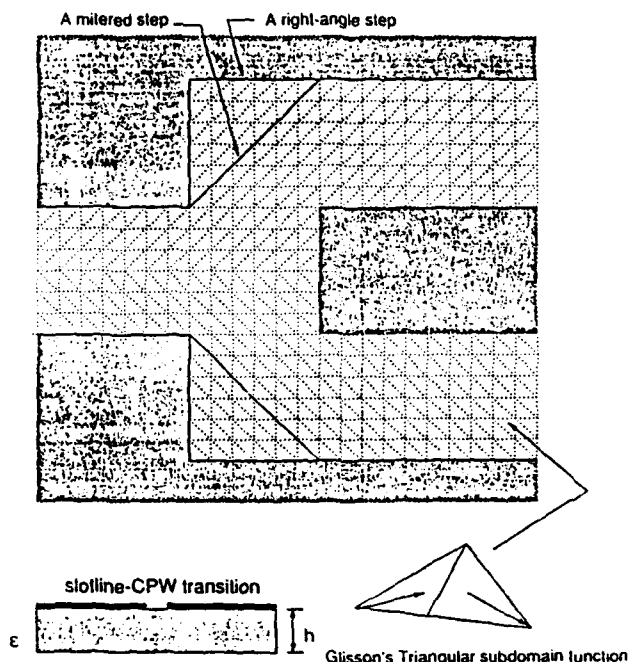


Fig. 1. Slot-to-CPW transition

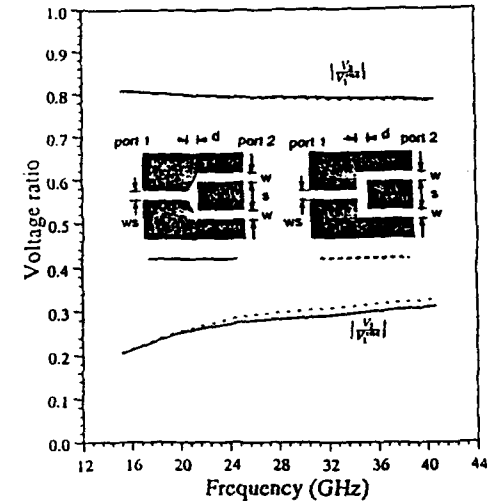


Fig. 2. The slot voltages in a slotline-CPW junction ($\epsilon_r=9.9$, $ws=0.24\text{mm}$, $w=0.24\text{mm}$, $s=0.24\text{mm}$, $h=0.25\text{mm}$, $d=0.24\text{mm}$)

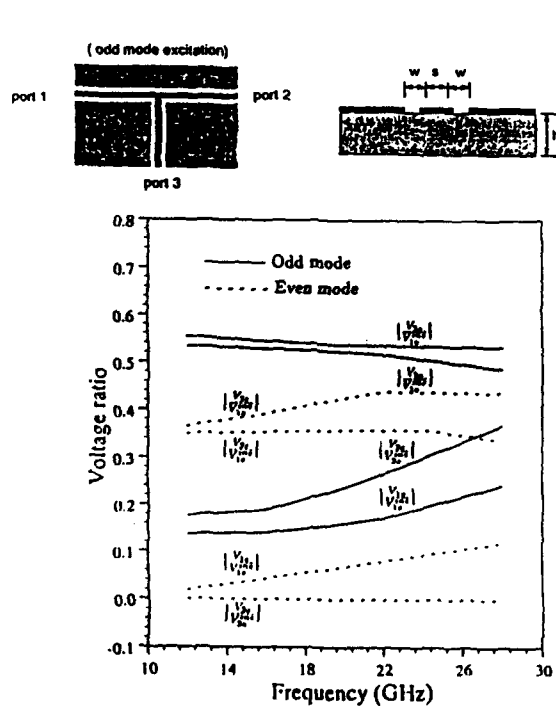


Fig. 4. The slot voltages of even modes and odd modes in a CPW tee junction ($\epsilon_r=9.9$, $w=24\text{mil}$, $s=24\text{mil}$, $h=25\text{mil}$)

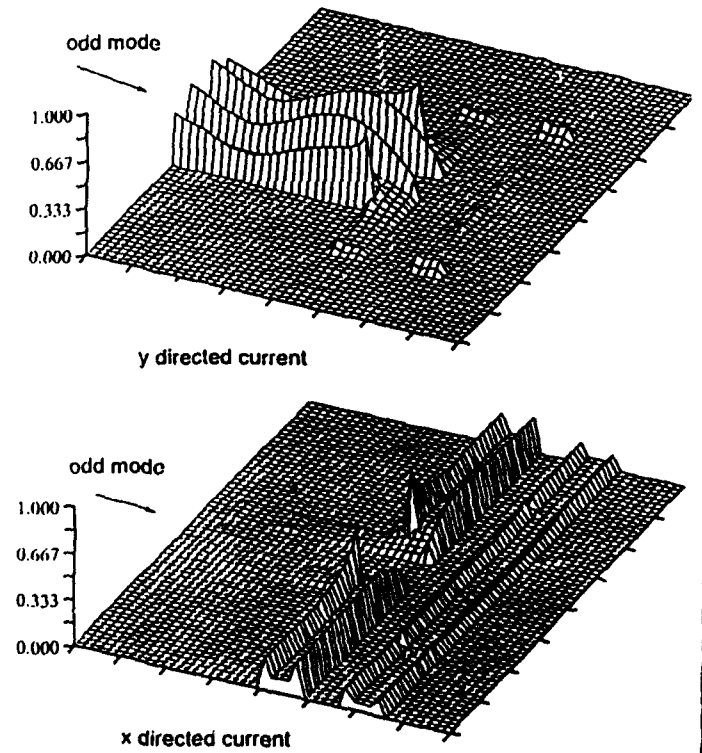
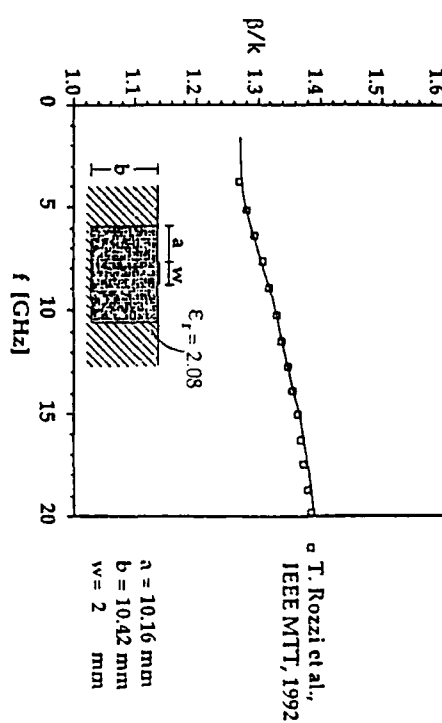


Fig. 5. Magnitude of equivalent magnetic current in a tee junction

Microstrip loaded Inset Guide



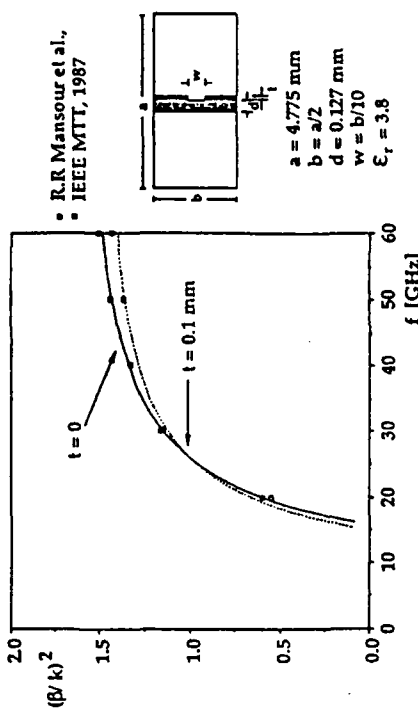
Abstract

This paper presents a six-port reflectometer in the W band using Schottky diodes as power detectors. A linearization procedure and AC detection technique are used to improve the measurement accuracy. Moreover, a calibration procedure requiring two standards is described.

A MILLIMETER WAVE SIX-PORT REFLECTOMETER
S. ABOUCHAHINE, B. HUYART, E. BERGEAULT,
L. JALLET
TELECOM PARIS, 46, RUE BARRAULT, 75634 PARIS
FRANCE

Hybrid integral equation/mode matching approach

Unilateral Finline



- \mathfrak{L} can be represented as:

$$\mathfrak{L}(x, y, x', y', \omega, \beta) = \mathfrak{L}(x, y, x', y', 0, \beta) - \omega^2 \sum_m \frac{B_m(x, y, \beta) B_m(x', y', \beta)}{[\omega_m^2 - \omega_m^2(\beta)] \omega_m^2(\beta)}$$

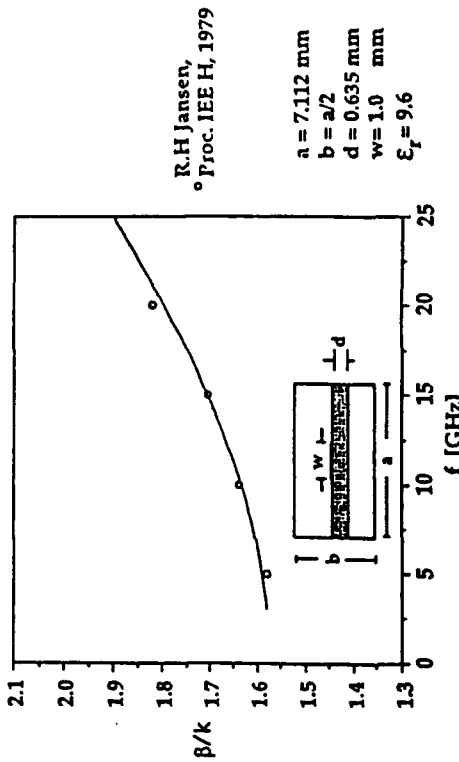
where ω_m and B_m represent the electric fields and the cutoff frequencies of the modes of the elementary waveguides. They are the eigenvalues and the eigenvectors of the problem:

$$\nabla \times \mu^{-1} \nabla \times g - \omega^2 \epsilon g = 0$$

with suitable boundary conditions and normalization.

- Due to its fast convergence (like ω_m^{-4}) the series can be truncated without relative convergence problems.
- After truncation \mathfrak{L} is represented by a rational function of ω .
- Introducing a set of auxiliary variables related to the mode amplitudes in the elementary waveguides, the problem arising from the method of the moments can be converted into a linear eigenvalue problem, involving frequency independent matrices.
- Since the variables involved represent both the fields at the interfaces and the amplitudes of some nodes, the described technique can be viewed as an hybrid between the boundary integral equation method and the mode matching technique.

Suspended Strip Line



FREQUENCY DEPENDENT ANALYSIS OF PACKAGING PROBLEMS
USING THE THREE-DIMENSIONAL INTEGRAL EQUATIONS TECHNIQUE

II. GHALI*, M. DRISSI*, J. CITERNE* and V. FOUAD HANNA**

*Laboratoire Composants et Systèmes pour Télécommunications
URA 834, INSA, 35043 RENNES, FRANCE

**CNET/PAB, 92131 ISSY LES MOULINEAUX, FRANCE

ABSTRACT

The main problems associated with packaging technique for microwave and millimeter integrated or monolithic circuits are the shielding effects, discontinuity and chip connections characterization. In this paper, a dynamic analysis, based on the three-dimensional integral equations technique associated with the method of moments is presented for the characterization of shielded discontinuity problems. It uses the three-dimensional Green's function for a general current distribution inside a shielded box. The theory of loaded scatterers is also used to take into account the effect of existing localized and distributed active devices or passive loads. Using this last theory, a virtual matched load is simulated, numerically, by introducing localized absorbing loads at circuit sections corresponding to output ports. Consequently, a scattering parameters extraction technique, based on the use of these matched terminations, is developed, and hence the [S] parameters of the studied discontinuity are determined from the knowledge of only current or electric field maxima which are often accurately determined under good matching conditions. The shielding effects on a wide range of planar and three-dimensional discontinuities are given. The behaviour of a typical chip connection as a strip air bridge is also studied and the frequency dependent characteristics of these discontinuities are presented.

Single Side Source Grounded Configuration

Guido Baumann
SEL ALCATEL
Mannheimerstr. 22b, 7330 Pforzheim, Germany

ABSTRACT

This paper presents an oscillator design using a new concept of a FET model, which allows to characterize the single side source grounded configuration of a FET, and therefore to predict the oscillator frequency in the mm-wave range very precisely. The freerunning oscillator was fabricated on a GaAs chip, Al:36 GHz, Al:36 GHz, an output power of 14 dBm, and an external quality factor of greater than 100 was achieved.

SUMMARY

For an accurate oscillator design in the mm-wave range the modeling of the active device is essential for a successful design. Especially oscillators are often layouted in a single side grounded source (SSG) configuration, that means only one source pad is grounded, while the second one is not connected. Depending on the gatewidth and the dimensions of the FET, distributed effects for low noise MESFETs have to be regarded above approximately 30 GHz [1], [2]. This assumption is only valid if both source pads are grounded. If the FET is used in a single side grounded source configuration, the FET should be regarded as distributed even above 15 GHz. To our knowledge the effect of SSG has not been regarded yet by any commercial CAD tool.

Especially for oscillator design the FET is often used in a SSG configuration [3] to reach the required instability, otherwise both source connections will have symmetrical networks which will increase the area on a chip. The difference in the measured S-parameters between single side source grounded (SSG) and double side source grounded (DSG) configuration is shown in Fig. 1. Above 15 GHz the S-parameters S12 and S11 show great differences. From the layout orientation of the 4-finger MESFET TEG4-50-25, Fig. 2, a modular distributed model was deduced, Fig. 3. A 4-finger MESFET with a 0.25 μm gate length and a total gatewidth of 200 μm from TEG is used. The geometrical dimensions of the chip and source configuration are directly implemented as microstrip elements. The source pad which is not grounded in the SSG configuration is described by a tapered open line. The distributed model provides 3-port S-parameters for SSG configuration. Fig. 4 indicates the excellent agreement of the modeled and measured S-parameters for SSG configuration.

The FET model is also able to describe the reverse channel operation. Measurements of the MESFET were performed using an inhouse developed testfixture with IRL calibration standards for microstrip measurements up to 40 GHz.

The basic concept of the oscillator is a reflection type oscillator with the output at the drain side [4, 5]. In Fig. 5 the layout of the 28 GHz oscillator is shown. The FET is positioned at the edge of the chip and only one sourcepad is extended with a microstrip transmission line to provide the required instability. The GaAs oscillator has a chip size of 3x3 mm and is fabricated on a 150 μm GaAs substrat. The performance of the 36 GHz freerunning Oscillator with $U_{ds}=5\text{V}$ and $I_{ds}=30\text{mA}$ has a power output $P_{out} = 14 \text{ dBm}$, an external quality factor $Q_{ext} = 100$.

• Telefunken Electronic, Heilbronn, Germany

shown in Fig. 6 and Fig. 7, respectively. Using a common FET model for this oscillator design, the simulated and measured resonance frequency had an offset of about ± 3 GHz. With the new distributed FET model the predicted resonance frequency of the freerunning oscillator was within a range of ± 200 MHz.

CONCLUSION

This paper shows that the FET has to be regarded as distributed above 15 GHz if the FET is used in a SSG configuration. The deduced model describes very accurately the SSG configuration and uses only lumped elements and microstrip lines which makes it practicable for online simulation. This leads to a higher accuracy in oscillator design. The predicted resonance frequency of the freerunning oscillator lies within a range of ± 200 MHz from the design frequency. Oscillators designed with common FET models had their resonance frequency within a range of ± 3 GHz. For nonlinear modeling the intrinsic FET will be changed to a large signal model to provide also the possibility of nonlinear circuit design in SSG-configuration.

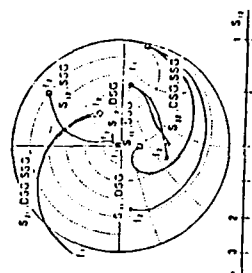


Fig. 1: Measured S-parameters in double side grounded (DSG) and single side grounded (SSG) configuration of a MESFET TEG4-50-25; $f_1 = 1 \text{ GHz}$, $f_2 = 40 \text{ GHz}$.

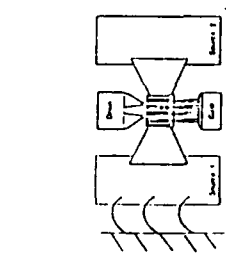
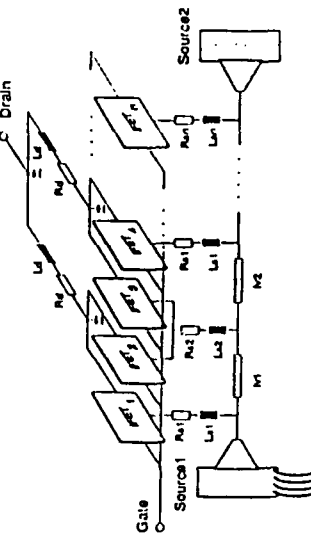


Fig. 2: Layout of the 4-finger MESFET TEG4-50-25;



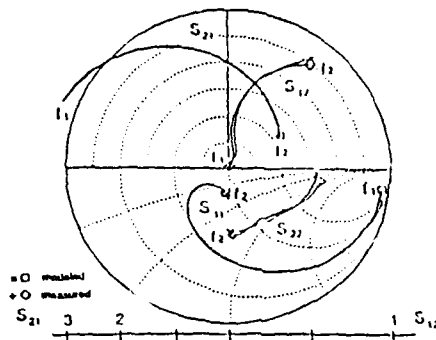


Fig. 4: Measured and modeled S-Parameter in single side grounded configuration (SSG).

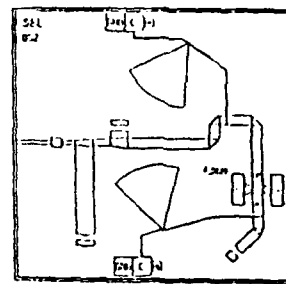


Fig. 5: Layout of the Oscillator.

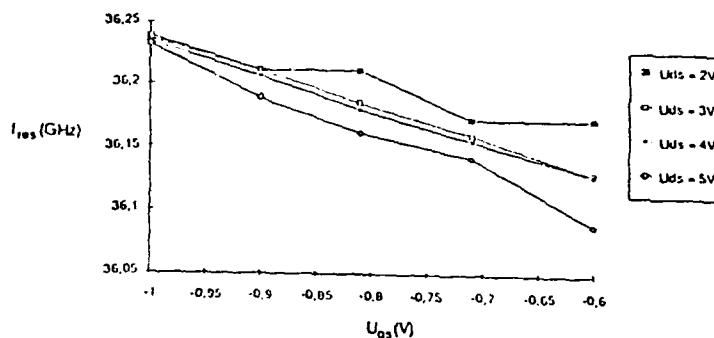


Fig. 6: Resonance frequency vs gate- and drain voltage.

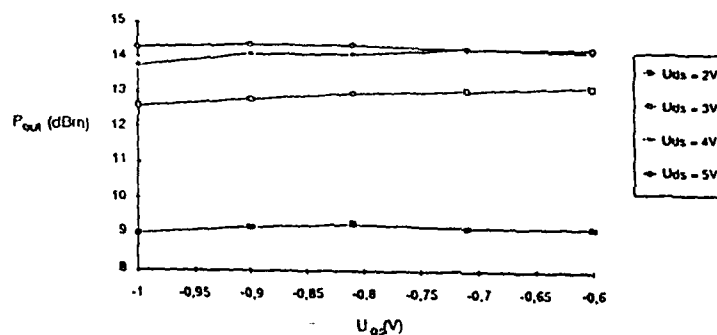


Fig. 7: Output power vs gate- and drain voltage.

References:

- /1/ W. Heinrich, "Limits of FET Modelling by Lumped Elements", *Electronics Letters*, vol. 22, no. 12, S. 630-632, Juni 1986
- /2/ H.P. Feldle, "Klein- und Großsignal-CAD-Modelle von GaAs MESFETs mit verteilten Elementen", Dissertation Universität Karlsruhe, 1987
- /3/ G. Baumann, R. Hierl, "Modular FET model with distributed source configuration for a single and double side source grounded MESFET", *Electronics Letters*, vol. 27, no. 13, S. 1128-1129, Juni 1991
- /4/ K. Kurokawa, "Some Basic Characteristics of Broadband Negative Resistance Oscillator Circuits", *The Bell System Technical Journal*, Juli- August, 1969
- /5/ George D. Vendelin, *Design of Amplifiers and Oscillators by the S-Parameter Method*, John Wiley and Sons, Inc., 1982